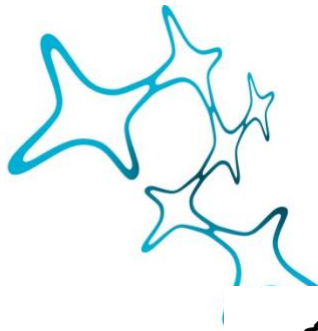


INTERPRETABLE APPROACHES FOR CELLULAR ORGANISATION AND MOLECULAR PROFILES USING (SPATIAL) OMICS DATA IN HEALTH AND DISEASE

Mayar Ali



Graduate School of
Systemic Neurosciences
LMU Munich



Dissertation at the
Graduate School of Systemic Neurosciences
Ludwig-Maximilians-Universität München

December 12, 2024

First Supervisor and Reviewer: Prof. Dr. Ali Ertürk
Institute for Intelligent Biotechnologies
Helmholtz Munich

Second Reviewer: Dr. Hannah Spitzer
Klinikum der Universität München,
Institute for Stroke and Dementia Research

Date of Submission: 12.12.2024

Date of Defense: 02.06.2025

Abstract

Deciphering cellular organisation and how molecular expression patterns vary across tissues is fundamental to gaining insights into biological processes and disease mechanisms. Advances in omics technologies, particularly spatial omics, have revolutionised our ability to investigate these patterns at unprecedented resolution and dimensionality. While various statistical and machine-learning approaches have emerged to analyse these complex data sets, critical gaps remain in our understanding of the differential cellular organisation and tissue characteristics across different conditions. Furthermore, the field typically lacks robust tools for a three-dimensional, holistic view of tissues, which is crucial for comprehending disease dynamics. In this thesis, I present a suite of mathematical approaches to analyse diverse omics data, focusing on spatial omics, with various resolutions, throughputs, and dimensionalities to reveal crucial insights into differential changes in molecular expression and cellular organisation across conditions. First, as part of a large multimodal comprehensive study, I expanded on our understanding of cell heterogeneity, the distinctive proteome signatures in the skull bone marrow, and its role in immunological responses to neurological disorders. Second, increasing the complexity and advancing into the spatial omics domain, I advanced the current approaches to quantitatively analyse the cellular organisation across multiple scales, from individual cell types and tissue niches to whole tissue revealing condition-specific tissue changes. Third, I proposed graph models and comprehensive multimodal ablation studies to understand the tissue traits contributing to patient outcomes and associate them with tissue architecture motifs to enhance our understanding of disease progression. Fourth, moving into three-dimensional space, I used our new technology, DISCO-MS, to explore the proteome changes in amyloid-beta plaques in Alzheimer's disease to capture very early (6 weeks) and late-stage dynamics and region-specific variations, providing a holistic view of the plaques' microenvironment. Collectively, these approaches represent a comprehensive effort and advancement in our ability to study the differential changes in molecular expression, cellular organisation, and tissue traits across different physiological and pathological conditions while further extending into three-dimensional volumes for a more holistic understanding of biological systems.

Abbreviations

A β plaques: Amyloid-beta plaques
BBB: Blood-brain barrier
cDNA: Complementary DNA
CNS: The central nervous system
CODEX: Co-Detection by Indexing
DDA: Data-dependent acquisition
DIA: Data-independent acquisition
DISCO: 3D imaging of solvent-cleared organs
DNA: Deoxyribonucleic acid
FDA: False discovery rate
FISH: Fluorescent in situ hybridisation
FISSEQ: Fluorescent in situ sequencing
FFPE: Formalin-fixed paraffin-embedded
GAN: Generative adversarial network
GAT: Graph attention network
GCN: Graph convolutional network
GIN: Graph isomorphism network
GNN: Graph neural network
IBC: Invasive breast cancer IMC: Image mass cytometry
ISH: In situ hybridisation
ISS: In situ sequencing
kNN: k-nearest neighbours
LCM: Laser capture microdissection
LC-MS: Liquid chromatography-mass spectrometry
MC: Mass cytometry
MS: Mass spectrometry
MERFISH: Multiplexed error robust FISH
NGS: Next-generation sequencing
PCR: Polymerase chain reaction
RI: Refractive index
RNA: Ribonucleic acid
RNA-seq: RNA-sequencing
scRNA-seq: Single-cell RNA-sequencing
SMC: Skull-meninges connection
smFISH: Single-molecule Fluorescent in situ hybridisation
TDA: Topological data analysis
UMI: Unique molecular identifier

Contents

| | Page |
|---|------------|
| 1 General Introduction | 1 |
| 1.1 Basic Principles of Cell Biology and Neuroimmunology | 1 |
| 1.1.1 Cell and tissue biology | 1 |
| 1.1.2 Immune system and the defensive role of bone marrow | 2 |
| 1.1.3 Central nervous system and role of calvaria in neuroimmunology | 4 |
| 1.2 Optical tissue clearing - DISCO technologies | 5 |
| 1.2.1 Optical tissue clearing: definition and principles | 5 |
| 1.2.2 DISCO technologies | 5 |
| 1.3 High-throughput and resolution biology: Omics technologies | 6 |
| 1.3.1 Transcriptomics | 7 |
| 1.3.2 Proteomics | 7 |
| 1.4 Spatial omics | 7 |
| 1.4.1 Spatial transcriptomics | 8 |
| 1.4.2 Spatial Proteomics | 10 |
| 1.4.3 Analysis of Spatial Omics | 11 |
| 2 Computational Methods | 14 |
| 2.1 Differential expression analysis | 14 |
| 2.2 Representation of tissue as a graph of cells | 14 |
| 2.3 Graph neural networks | 16 |
| 3 Aim | 18 |
| 4 Studies | 19 |
| 4.1 Study 1: GraphCompass: spatial metrics for differential analyses of cell organi- sation across conditions. | 19 |
| 4.2 Study 2: Graph neural networks learn tissue phenotypes from spatial molecular profiles. | 32 |
| 4.3 Study 3: Distinct molecular profiles of skull bone marrow in health and neuro- logical disorders. | 61 |
| 4.4 Study 4: Spatial proteomics in three-dimensional intact specimens. | 112 |
| 5 General Discussion | 152 |
| 5.1 Main findings | 152 |
| 5.1.1 Skull bone marrow molecular profile differs from other bones | 152 |
| 5.1.2 GraphCompass uncovers cellular organisation and tissue architecture across different conditions | 153 |
| 5.1.3 Graph neural networks reveal tissue traits and predictive factors across pathological stages using spatial omics | 153 |
| 5.1.4 DISCO-MS: advances in 3D spatial proteomics | 153 |
| 5.2 Key implications | 154 |

| | | |
|-------|--|-----|
| 5.2.1 | Skull bone marrow molecular profiles differ from other bones | 154 |
| 5.2.2 | Spatial omics as graphs - what we can learn about cellular organisation in different conditions | 155 |
| 5.2.3 | Spatial proteomics goes 3D | 157 |
| 5.3 | Limitations | 159 |
| 5.3.1 | Technical limitations | 159 |
| 5.3.2 | Biological limitations | 161 |
| 5.4 | Outlook | 162 |
| 5.4.1 | Leveraging multi-omics and spatial omics for a deeper understanding of the brain-skull axis and disease targeting | 162 |
| 5.4.2 | Advancing graph-based methods in spatial omics | 162 |
| 5.4.3 | Combining 3D spatial proteomics and graph models | 163 |
| 5.5 | Conclusion | 164 |

References

165

1 General Introduction

1.1 Basic Principles of Cell Biology and Neuroimmunology

1.1.1 Cell and tissue biology

Cells are the fundamental functional units of life, essential for carrying out all biological processes. They exhibit diverse structures and functions, from liver cells' metabolic activities to neurons' electrical excitability. In multicellular organisms, cells are building blocks for tissues, organs, and the entire body. This progression reflects the hierarchical organisation of life, where specialised clusters of cells collaborate to form tissues, and tissues integrate to build organs that function as part of interconnected body systems. These systems, such as vascularisation, innervation, and the immune system, interlink organs, synchronise their functions and mediate remote effects during pathological conditions. The bone marrow is an example of such systemic coordination, where haematopoietic cells contribute to immune system functionality and respond to signals from other body systems (Bandyopadhyay *et al.*, 2024). Such interconnections highlight the body's reliance on synchronised systems to maintain homeostasis and respond dynamically to disease.

Each cell is defined by its molecular profiles, encompassing not only genes transcribed into RNA and subsequently translated into proteins but also additional layers of complexity, such as modifications in the epigenome, which play a crucial role in regulating its function and state. Such molecular information is a useful indicator of its functionality. The distinct physical nature of cells, with a lipid cell membrane acting as a defining boundary of each cell, is crucial for maintaining the integrity of the cell and allows for physical separation between them. This has led researchers to view cells as membrane-bound molecular bags (Quake, 2021). The distinct nature of cells facilitates their study in a dissociated manner within tissues, making it feasible to investigate individual cells in diverse experimental settings. This, in turn, contributes to our understanding of cell types, states, and interactions within the tissue in health and disease. However, cells do not function as single entities, and the precise spatial arrangement, interactions, and distribution of cells within tissue play a critical role in determining the physiological state of tissues within the organism (Illustration 1). For example, the spatial organisation of cells is crucial for understanding the various underlying functions in different brain structures such as the cerebral cortex and the hippocampus (Chen *et al.*, 2023a; Qiu *et al.*, 2024). In addition, an imbalance in these interactions, or a change in the distribution, structure, or organisation of different cell types within tissue, can lead to loss of functions and disease (Palla *et al.*, 2022a; Rao *et al.*, 2021).

Understanding how molecular and spatial characteristics of cells contribute to higher-order tissue functions provides critical insights into the emergent properties of biological systems. For example, in cancer research, examining the tumour microenvironment reveals how the interplay between cancer cells and their surrounding stroma drives tumour growth, metastasis, and resistance to therapeutics (Wang *et al.*, 2023). Moreover, investigating the spatial context of amyloid-beta plaques in neuroscience has advanced our understanding of Alzheimer's disease pathogenesis (Wang *et al.*, 2024). Therefore, studying the interplay between individual

cells' behaviour and the constraints imposed by their spatial context is essential to gain deeper insights into these complex interactions (Polychronidou *et al.*, 2023).

Taking a holistic approach to studying biological systems and combining the diverse information provided by modern technologies is crucial for an unbiased understanding of health and disease (Kirschner, 2005). Therefore, studying both homeostasis and disturbances in the cellular organisation is not only essential to gain insights into the emergent properties and underlying mechanisms of tissue in different physiological and pathological states but also for our understanding of tissue biology and enhancing diagnostic and therapeutic strategies.

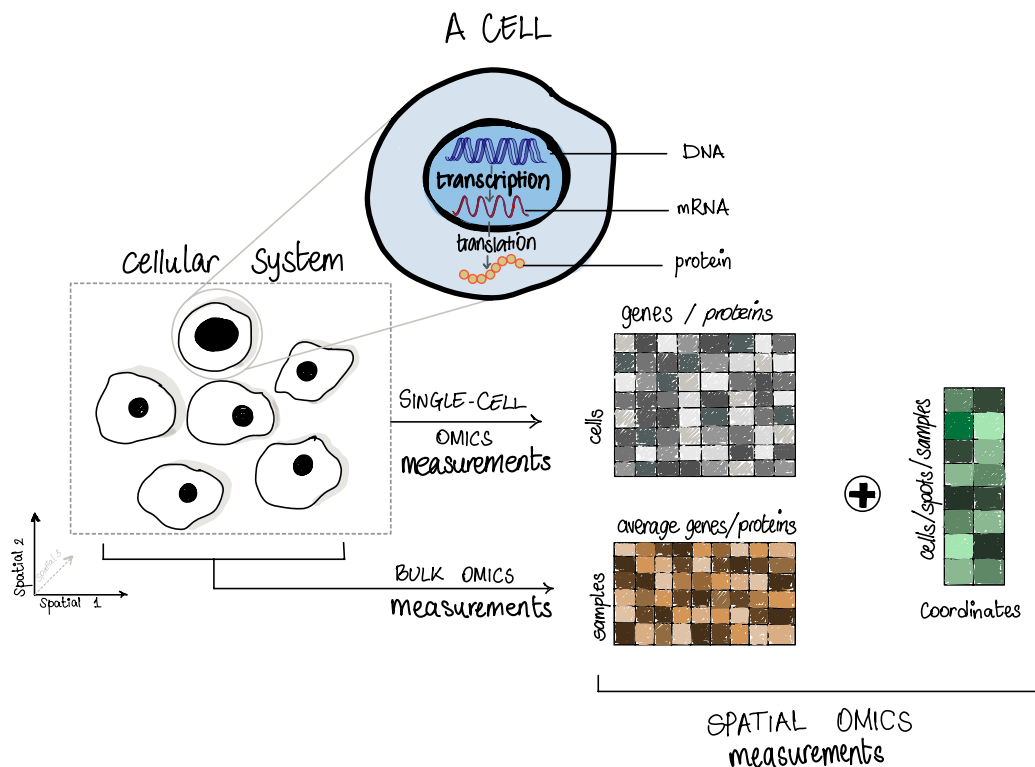


Illustration 1. From Cell Biology to Spatial Omics: Mapping Cells in Context. The cell contains DNA in the nucleus which is transcribed to mRNA. This mRNA is then translated in the cytoplasm, resulting in protein synthesis. Cells interact together in a three-dimensional space forming a cellular system. Molecular measurements from cells can be captured at different levels: from individual cells, single-cell omics measurements (cell x gene/protein) or from collection of cells, bulk omics measurements (sample x gene/protein). Since cells exist within a spatial context, the field of spatial omics has emerged, combining single-cell or bulk omics measurements with their spatial coordinates to study cells in situ.

1.1.2 Immune system and the defensive role of bone marrow

The immune system plays a pivotal role in maintaining the body's defence mechanisms and ensuring homeostasis by recognising and responding to pathogens while preserving the integrity of tissues. An important immune system component is the bone marrow, a primary lymphoid organ and the principal site of haematopoiesis that produces blood and immune cells (Leimkühler and Schneider, 2019). Among these immune cells, macrophages, lymphocytes, and neutrophils are crucial drivers of inflammatory responses (Illustration 2a). In addition to its role as a cell production site, the bone marrow also functions as a reservoir for immune cells that are mobilised in response to systemic or localised infections and injuries. This highlights

the bone marrow's importance as both a producer and regulator of immune cells, providing critical links between systemic immune function and localised immune responses, including those in the central nervous system.

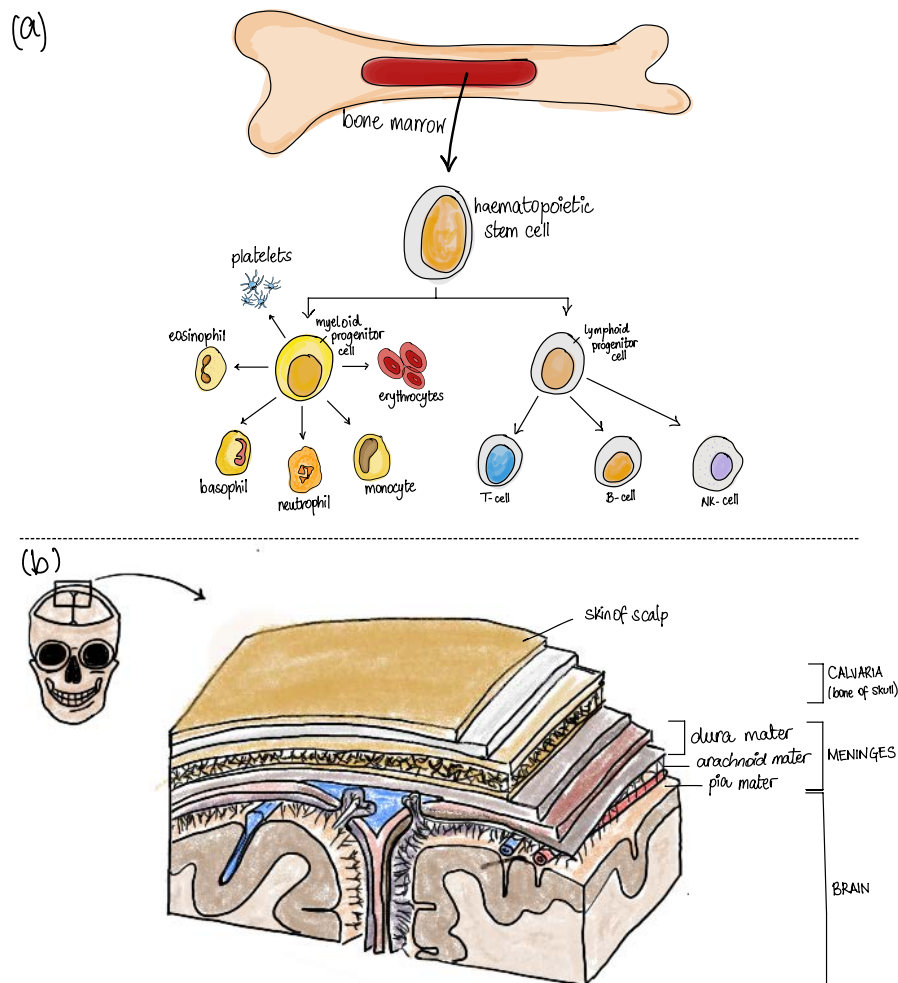


Illustration 2. Overview of Immune Cell Types and the Protective Structures of the Brain. (a) Immune cell types originate in the bone marrow and undergo differentiation from hematopoietic stem cells. They further differentiate into either myeloid or lymphoid progenitor cells. Myeloid progenitor cells give rise to erythrocytes, monocytes, neutrophils, basophils, eosinophils, or platelets. Lymphoid progenitor cells differentiate into T cells, B cells, or NK cells, which are components of the adaptive immune system. (b) There are multiple layers protecting the brain from the outside. Starting from the outermost layers, these include the skin of the scalp, followed by the calvaria (the bone of the skull). Next are the meningeal layers: dura mater, arachnoid mater, and pia mater, leading finally to the brain.

1.1.3 Central nervous system and role of calvaria in neuroimmunology

The central nervous system (CNS) is a major communication network in the body that dynamically interacts with the immune system in health and disease. For a long time, the CNS was considered an immunologically privileged site that is isolated from the peripheral immune system by the blood-brain barrier (BBB). The BBB, a specialised vascular structure, acts as a protective shield, preventing most immune cells and substances in the bloodstream from entering the brain while selectively allowing essential molecules (Carson *et al.*, 2006; Alves de Lima *et al.*, 2020). This concept of immune privilege, however, has been challenged over the past few decades.

Recent studies have revealed breaches in the BBB during inflammatory diseases such as stroke, Alzheimer's disease, and multiple sclerosis which allow immune cells to invade the brain. Pathways such as the choroid plexus and other mechanisms facilitate the migration of leukocytes into the CNS, demonstrating active interactions between the brain and the immune system (Solár *et al.*, 2020). Furthermore, the discovery of skull-meninges connections (SMCs), microscopic channels between the skull bone marrow and the meninges, has provided compelling evidence of immune cell migration during pathological conditions such as stroke (Cai *et al.*, 2019). These findings not only reshape our understanding of CNS-immune interactions but also highlight the importance of studying the two systems together as an interconnected whole. For example, studies have shown active interactions between the CNS and the peripheral immune system, through the discovery of routes for the migration of leukocytes into the CNS, which regulate immune responses (Ransohoff *et al.*, 2003).

The immune system's role in CNS health and disease is further underscored by the calvaria, or skull bones, which actively contribute to neuroimmunology. The skull and brain are separated by the meninges, three protective membranes (dura mater, arachnoid mater, and pia mater) that house immune cells crucial for brain health. Studies have shown that the skull bone marrow supplies immune cells such as monocytes and B-cells to the meninges during both homeostasis and disease (Cugurra *et al.*, 2021; Brioschi *et al.*, 2021) (Illustration 2b). This unique proximity of the skull to the brain positions it as a key site for immune-CNS communication, raising critical questions about how these interactions influence CNS pathology. For example, does the skull's immune composition uniquely impact neuroinflammatory responses compared to other skeletal sites? Profiling the calvaria's molecular and structural features is essential for answering these questions and understanding its distinct role in health and disease.

Understanding CNS pathology requires a holistic approach that considers not only cellular and molecular profiles within the brain but also interactions with the immune system. Neurodegenerative diseases such as Alzheimer's and Parkinson's highlight the complexity of these interactions, where disruptions in cellular organisation and composition lead to systemic effects (Jeong, 2017). For example, amyloid-beta ($A\beta$) plaques, a hallmark of Alzheimer's disease, illustrate the importance of studying molecular profiles, interactions, and spatial organisation within the brain microenvironment. Investigating these aspects can uncover critical mechanisms underlying disease progression and identify new therapeutic targets.

Advancements in high-throughput omics technologies (Section 1.3) have revolutionised the study of molecular and cellular biology by enabling the measurement of molecular profiles at unprecedented scale and resolution. These technologies, particularly spatial omics (Section 1.4), integrate molecular and spatial information to provide a comprehensive view of cellular organisation and interactions within tissues. Applying such tools to CNS pathology is crucial for linking molecular and structural data to the observed functional outcomes, offering insights

into complex disease mechanisms and facilitating the development of novel diagnostics and therapeutics.

The interplay between the CNS and the immune system shows the complexity of biological systems. Studying the brain in isolation is no longer sufficient; instead, a holistic approach that integrates molecular, cellular, and structural perspectives is necessary. Investigating the calvaria's unique role, pathways like the choroid plexus and SMCs, and the broader systemic interactions will deepen our understanding of CNS pathology and advance therapeutic strategies. As part of this thesis, these questions will be explored to leverage current technological advances and deepen our understanding of CNS-immune interactions within the broader context of biological systems (Kolabas *et al.*, 2023).

1.2 Optical tissue clearing - DISCO technologies

Studying large tissues (and even full bodies) in three dimensions is necessary for a comprehensive understanding of spatial relationships and interactions within complex biological systems. However, imaging large tissues while maintaining their structural integrity is challenging with the common high-resolution histological and microscopy imaging techniques without the loss of valuable information. On the other hand, whole-body imaging techniques such as positron emission tomography (PET) or magnetic resonance imaging (MRI) lack cellular-level resolution (Cai *et al.*, 2023). Although high-resolution histological and microscopy techniques provide cellular detail, they often require sectioning which can disrupt spatial organisation and lead to information loss. To address these challenges, optical tissue clearing has emerged as a transformative approach, allowing three-dimensional imaging of intact tissues while preserving their structural and cellular integrity (Ertürk *et al.*, 2012).

1.2.1 Optical tissue clearing: definition and principles

Optical tissue clearing is a term that describes a rapidly developing process of making biological tissue transparent by removing light-scattering components such as lipids and water while preserving the integrity of the tissue structure and maintaining the spatial cellular organisation within the tissue. This process enables high-resolution three-dimensional imaging of intact tissues and avoids the loss of information that can result from sectioning techniques. The key principle for achieving tissue transparency in tissue clearing methods is homogenising the refractive index (RI), which reduces the scattering of light in the medium allowing deeper penetration and therefore rendering transparent tissue (Cai *et al.*, 2023; Molbay *et al.*, 2021). The basic workflow of tissue clearing consists of three main principles: fixation, dehydration, and clearing of the tissue. First, the tissue is fixed to maintain the structural integrity. Dehydration usually follows fixation, which is the process of replacing water in the tissue with organic solvents such as methanol and ethanol. After the tissue is dehydrated, it is placed in a reagent with a matching RI to achieve maximum penetration of light and therefore transparency. After these steps are completed, the transparent tissue is then imaged using light sheet fluorescence microscopy providing an unbiased, holistic view to study with cellular resolution the biology at the tissue, system and whole-body scales.

1.2.2 DISCO technologies

Various tissue-clearing protocols have been developed over the past decade. These different protocols can be clustered into three categories: hydrogel-based, hydrophilic (aqueous-based) and hydrophobic (solvent-based) clearing. This thesis focuses on hydrophobic (solvent-based) tissue clearing, specifically 3D imaging of solvent-cleared organs (DISCO) technologies. The solvent-based clearing methods are considered the oldest clearing methods dating back to the

19th century (Molbay *et al.*, 2021). These methods use solvents to remove light-scattering molecules from tissue while preserving tissue integrity. However, the use of solvents results in tissue shrinkage, which, while beneficial for imaging large tissues, is an irreversible process that deforms the tissue and disrupts spatial cellular organisation. Therefore, these techniques are performed gradually to minimise shrinkage and deformation of the tissue. Examples of solvent-based clearing methods include; 3DISCO (Ertürk *et al.*, 2012), uDISCO (Pan *et al.*, 2016) which minimises the shrinkage of tissue, iDISCO (Renier *et al.*, 2014) which employs immunolabelling, vDISCO which uses nanobodies for labelling (Cai *et al.*, 2019, 2023), and SHANEL which can be applied to intact human organs (Zhao *et al.*, 2020).

Tissue clearing has been widely used in various applications to reveal new biological insights at the systems level and whole-organism scale. With their ability to preserve tissue integrity during imaging, tissue clearing methods offer a powerful approach to studying three-dimensional structural information at a microscopic scale and uncovering new anatomical connections. Some of these applications include the visualisation of neural circuits (Ertürk *et al.*, 2012) and inflammation (Liu *et al.*, 2015), the quantification of cancer cells that have been targeted by therapeutic antibodies (Pan *et al.*, 2019), visualisation of the whole-body neural projections in the adult mouse, and discovering short vascular connections (skull-meninges channels) between the skull bone marrow and the brain meninges, which were previously considered to be isolated (Cai *et al.*, 2019). The preservation of intact three-dimensional tissue, as well as the cellular resolution imaging of cleared tissues, facilitates the unbiased, holistic analysis of biological systems and even entire organisms, opening a wide range of applications in various biological research fields, from neuroscience and immunology to cancer and developmental biology. The next natural step for enhancing our understanding of biological systems and gaining deeper insights into their underlying mechanisms is to combine molecular information with three-dimensional spatial cellular information obtained through tissue clearing. This approach will pave the way for groundbreaking discoveries and significantly enhance our understanding of various research fields. The development of technologies to study cellular properties and organisation in three dimensions on a large scale is essential for providing new insights into how cells in their spatial context are affected in different pathological states, such as neurodegenerative diseases. These advancements are explored as part of this thesis (Bhatia *et al.*, 2022).

1.3 High-throughput and resolution biology: Omics technologies

Omics technologies have transformed biological research by enabling high-throughput analysis of molecular and cellular properties. These technologies encompass various fields, such as genomics, transcriptomics, proteomics, and metabolomics, each focusing on distinct aspects of biological complexity. By profiling molecular components like DNA, RNA, proteins, and metabolites, omics studies provide insights into the mechanisms underlying biological functions and diseases.

In the last decades, molecular profiling relied on bulk analysis which captures the average molecular information of hundreds or thousands of cells. Despite the effectiveness of targeted probing of specific molecular targets, bulk methods often ignore cell-specific heterogeneity which is a key aspect of many biological processes. The continuous advancements of high-throughput technologies have expanded the throughput and resolution of molecular studies which enabled single-cell analysis that uncovers the diversity of molecular states across tissues with unprecedented granularity (Li and Wang, 2021) (Illustration 1).

Overall, single-cell (and bulk) omics technologies have enhanced our understanding of bio-

logical systems by enabling genome-wide profiling of individual (or collection of) cells. These methods have facilitated breakthroughs in immunology, such as characterising immune cell heterogeneity and discovering novel cell types (Macosko *et al.*, 2015; Pijuan-Sala *et al.*, 2019). Furthermore, large-scale initiatives, like the Human Cell Atlas, leverage single-cell omics to create comprehensive maps of human tissues and organs (Regev *et al.*, 2017).

1.3.1 Transcriptomics

Transcriptomics focuses on the study of RNA molecules within cells, providing insights into gene expression patterns and functional elements of the genome. RNA-sequencing (RNA-seq) has become a gold standard of transcriptomic analysis, advancing from bulk approaches to single-cell resolution. Bulk RNA-seq measures average gene expression across large cell populations, which captures an overview of the molecular expression but fails to specify cell-specific variations. Single-cell RNA-seq (scRNA-seq) has revolutionised the field by enabling the profiling of individual cells, facilitating the discovery of rare cell types, cellular heterogeneity, and gene expression dynamics across tissues (Macosko *et al.*, 2015; Pijuan-Sala *et al.*, 2019).

The RNA-seq process involves extracting RNA from cells, reverse-transcribing it into complementary DNA (cDNA), and sequencing the resulting fragments (Sanger *et al.*, 1977; Heumos *et al.*, 2023). This technique provides genome-wide expression data, revealing cellular states and their roles in health and disease. Single-cell RNA-seq is particularly relevant in immunology, where it helps decipher the adaptive and innate immune systems, track gene mutations during development, and study immune responses in pathological conditions (Stubbington *et al.*, 2017). However, while single-cell approaches offer high resolution, they lack the spatial information of the cells they capture, which requires complementary methods to understand cell interactions in their native contexts.

1.3.2 Proteomics

Proteomics investigates protein levels and post-translational modifications, essential for understanding cellular functionality and tissue dynamics. Traditional antibody-based methods, such as Western blotting (Mahmood and Yang, 2012) and ELISA (Butler, 2000), provide targeted but low-throughput analysis, typically detecting tens to hundreds of proteins per experiment. These methods excel in studying specific pathways but lack the capacity for comprehensive proteome analysis.

Mass spectrometry (MS), on the other hand, has emerged as a powerful tool in proteomics, offering high-throughput analysis of thousands of proteins in complex samples (Bennett *et al.*, 2023). MS-based methods provide both qualitative and quantitative data, enabling the identification of protein interactions, modifications, and abundance. However, these methods predominantly operate on bulk samples, as single-cell proteomics remains technically challenging due to the low abundance of proteins and the difficulty of amplifying signals. While early advancements in single-cell proteomics show promise (Brunner *et al.*, 2022; Mund *et al.*, 2022; Petrosius *et al.*, 2023), further development is required to achieve broader applicability in biological research.

1.4 Spatial omics

Biological processes happen in a spatial context and three-dimensional alignments of cells within the tissue are necessary for the various functions. Therefore, information on both the spatial context of cells and their molecular profiling is crucial for deciphering the behavioural changes within the tissue across different conditions. Single-cell experiments performed on

disassociated cells lack this spatial information. Therefore, the development of a new field of technologies that captures spatial profiling of gene and protein expression to the resolution of single cells within the tissue was necessary. This field is referred to as "Spatial omics" (Bressan *et al.*, 2023) (Illustration 1).

Current spatial omics technologies can measure proteins and mRNA. Unlike single-cell technologies, which reached high levels of throughput, spatial omics face a trade-off between spatial resolution and both throughput and experimental time (Chen *et al.*, 2023b; Bressan *et al.*, 2023). Since the development of spatially resolved technologies, and despite their current limitations, these methods have greatly advanced biological research. Notably, spatially resolved transcriptomics was selected as *Nature's Method of the Year 2020* (Marx, 2021), and spatial proteomics received the same recognition as *Nature's Method of the Year 2024* (Nat, 2024). Spatial technologies have already contributed to a better understanding of the correlation between the tumour microenvironment and patient outcome in various breast cancer studies (Ali *et al.*, 2020; Jackson *et al.*, 2020), developmental stages and brain structures in different animal models (Moffitt *et al.*, 2018; Zhang *et al.*, 2021; Wei *et al.*, 2022). Furthermore, the human cell atlas initiative is expanding to include spatial omics to provide spatial atlases for the various human organs. However, it remains unclear how these spatial data will be standardised, as a common coordinate system is still needed to accurately map and compare cellular locations across tissues (Regev *et al.*, 2017).

In addition to advancements in individual modalities, there is a growing focus on multi-omics approaches that integrate spatial transcriptomics and proteomics, particularly using targeted methods. Recent innovations, such as combining DBiT-seq (Liu *et al.*, 2020) and CODEX (Goltsev *et al.*, 2018; Black *et al.*, 2021) (Section 1.4.2) technologies, highlight the potential of these multi-omics strategies to provide deeper insights into tissue organisation and function by simultaneously profiling RNA and protein abundance within spatial contexts (Enniful *et al.*, 2024).

Spatial omics datasets covered in this thesis (Ali *et al.*, 2024; Fischer *et al.*, 2022) can be divided into two modalities, (i) spatial transcriptomics datasets, which measure the abundance of genes at different resolutions (from multi-cells to subcellular) and different throughput (dozens of genes to genome-wide expression profiles), and (ii) spatial proteomics datasets, which measure the protein abundances within the cells. Methods used to acquire data from each modality can be further categorised based on the technologies and protocols to extract the molecular and spatial information as elaborated below.

1.4.1 Spatial transcriptomics

Current spatial transcriptomics methods still face trade-offs in terms of resolution, sensitivity, throughput and cost of use. Most of the commonly used spatial omics methods operate on 2-dimensional histological slices of tissues of different thicknesses. There have been significant advancements in spatial omics strategies in terms of profiling and tissue handling. This section describes in brief three of these strategies; (i) spatial barcoding, where RNA and DNA at specific locations in the tissue are linked to predetermined "barcodes", (ii) multiplexed in situ hybridisation, which relies on the hybridisation of labelled probes to their complementary RNA sequences within the tissue, and (iii) in situ sequencing of mRNA molecules.

Spatial barcoding

Spatial barcoding is a widely used approach in spatial transcriptomics, that resulted in the generation of vast amounts of spatial data. The core principle of this category of technologies is

the use of unique barcodes that correspond to specific locations on the tissue. These barcodes are attached to the RNA molecules in the tissue, therefore allowing the mapping of gene expression back to their exact spatial position. In addition, each RNA molecule is tagged to a unique molecular identifier (UMI), which helps to correct for polymerase chain reaction (PCR) amplification bias, or in other words, distinguish between the original RNA sequence and any duplicate that might arise during amplification. The resulting library is then prepared and sequenced using standard next-generation sequencing (NGS) techniques. This technique provides a highly accurate quantification and localisation of gene expressions in the tissue (Bressan *et al.*, 2023).

Different methods and technologies of spatial barcoding have been developed in the last decades. These methods can be categorised based on their underlying technology and resolution. First, there are *array-based methods*, such as 10x Genomics Visium and ST (Ståhl *et al.*, 2016), which capture RNA from tissue sections using arrays of spatially indexed barcoded spots. This category of methods provides transcriptome-wide coverage while maintaining high speed and supporting parallelisation. However, one major drawback of such methods is the low resolution (50-100 μm). The most recent advancement of Visium HD (10x Genomics) improves on this by reducing the spot size by using $2 \times 2 \mu\text{m}$ barcoded squares without gaps, offering finer spatial resolution. Second, there are *bead-based methods*, such as Slide-seq (Rodrigues *et al.*, 2019), which improved the resolution enabling near single-cell resolution. These methods rely on attaching barcoded DNA to densely packed nano-beads instead of directly on the slide surface, reaching high spatial density (10 μm). The second version of Slide-seq (Slide-seqV2) achieves higher resolution and sensitivity (RNA capture efficiency ~ 10 -fold greater than Slide-seq) (Stickels *et al.*, 2021). Finally, some methods provide ultra-high resolution and push the boundaries of spatial transcriptomics even further, using nano-meter-scale barcoding to achieve fine detailed spatial gene expression mapping. For example, Stereo-seq (Chen *et al.*, 2022). These methods provide great spatial resolution, though at the cost of complex experimental setups and high costs.

Multiplexed in situ hybridisation-based approaches

Multiplexed *in situ* hybridisation (ISH) methods are developed on the foundation of *single-molecule Fluorescent in situ hybridisation (FISH)* (smFISH) techniques and are used to capture individual mRNA molecules and their spatial context within tissue (Bressan *et al.*, 2023). These methods use multiple probes to hybridise mRNA molecules and can capture low-abundance transcripts at the single-molecule level. The main principles of these methods to enable spatial transcriptome mapping, revolve around repeated cycles of (1) association of barcodes to a transcript by hybridisation of short DNA probes, (2) reading of the barcodes by fluorescent imaging, (3) signal detection, and (4) signal reset and probe removal.

In the last few years, several multiplexed in situ hybridisation-based methods have been developed and enhanced to increase transcriptome coverage and improve the handling of challenging tissues. For instance, one of the main multiplexed in situ hybridisation-based methods is *multiplexed error robust FISH* (MERFISH) (Chen *et al.*, 2015), which has recently been commercialised, and is continuously being extended and enhanced with features like signal amplification, simultaneous mRNA and protein measurement as well as the incorporation of tissue embedding and clearing (Moffitt *et al.*, 2016). Another widely used method that is quite similar to MERFISH is seqFISH (Lubeck and Cai, 2012; Lubeck *et al.*, 2014) and its extension seqFISH+ (Eng *et al.*, 2019) which covers transcriptome-wide profiling. Furthermore, there are other quite different hybridisation-based methods such as ourboros smFISH (osmFISH) which replaces barcoding with a simpler protocol allowing the detection of fewer transcripts per cycle

(Codeluppi *et al.*, 2018) and SCRINSHOT, which is tailored to detect dozens of transcripts in challenging formalin-fixed paraffin-embedded (FFPE) tissues (Sountoulidis *et al.*, 2020). Another commercialised technology that is widely spreading is Xenium (10x Genomics), which combines multiplexed *in situ* hybridisation and single molecule imaging and therefore captures RNA expressions simultaneously from targets within the tissue enabling the profiling of up to 5000 genes. Notably, Xenium can also be applied to FFPE tissues. The diversity of hybridisation methods available for exploring spatial gene expression offers a range of options for various research needs, meeting the different experimental constraints like throughput, sensitivity, coverage, tissue types, and cost.

***In situ* sequencing-based approaches**

Another stream of spatial transcriptomics methods is based on *in situ* sequencing, which performs high-throughput sequencing directly within histological sections. Unlike traditional methods, *in situ* sequencing mostly uses sequencing by ligation rather than synthesis which is used in next-generation sequencing (NGS) (Bressan *et al.*, 2023). This sequencing (by ligation) method is better suited for complex tissue sections. Various *in situ* sequencing-based approaches have been developed, from early developments, such as *in situ* sequencing (ISS) (Larsson *et al.*, 2010) and *fluorescent in situ sequencing* (FISSEQ) (Lee *et al.*, 2015), to more optimised and sensitive approaches such as BaristaSeq (Chen *et al.*, 2018). In addition, further advancement of the approach combines ISS with untargeted FISSEQ and expansion microscopy. This hybrid approach enabled full-length, long-read sequencing with subcellular resolution, which is used in mapping complex tissues, such as mouse hippocampus and breast cancer human tissues (Alon *et al.*, 2021). However, despite these advancements, *in situ* sequencing approaches are challenging as they require precise imaging with profiling depth dependent on the cell size.

1.4.2 Spatial Proteomics

Single-cell proteomic technologies are still in the early stages in comparison to single-cell RNA-sequencing technologies, even for dissociated cells without spatial information. One of the reasons for that is that, unlike RNA, proteins cannot be directly amplified. This limitation makes detecting and quantifying proteins at the single-cell level more difficult and therefore delays the advancements in the field (Chen *et al.*, 2023a). This section briefly describes the common technologies used to detect proteins, particularly mass spectrometry, and their adaptation to go spatial.

Mass spectrometry

Mass spectrometry (MS) is one of the most widely used high-throughput proteomics technologies for identifying and quantifying proteins, and it can be applied to various tissue types, from fresh-frozen to FFPE tissues. This technology primarily works by ionising protein samples and then consequently measuring the mass-to-charge (m/z) ratio of the resulting ions. MS-based proteomics can be approached from two angles: top-down and bottom-up approaches. In top-down methods, the full-length protein is fragmented inside the MS and the masses of the fragments are directly analysed. On the other hand, in bottom-up methods, the proteins are broken down into peptides and fed to the MS, in this case, separation of peptides is not necessary (Cui *et al.*, 2022). One of the most widely used bottom-up mass spectrometry techniques is *liquid chromatography-mass spectrometry* (LC-MS). In this technique, proteins are first digested into peptides, which are then separated by liquid chromatography before being ionised and analysed by the mass spectrometer to determine their mass-to-charge ratios (m/z) (Aebersold and Mann, 2003). This method allows for the precise identification and quantification of proteins in

complex biological samples. Within the LC-MS workflow, there are two main acquisition methods: *data-dependent acquisition* (DDA) and *data-independent acquisition* (DIA). DDA targets the most abundant peptide ions providing in-depth quantification of those selected peptides while missing lower abundant ions. On the other hand, DIA fragments all ions within a selected (m/z) range simultaneously, providing comprehensive proteome coverage. Notably, the MS data in the projects covered in this thesis are acquired using LC-MS and DIA approaches. Despite the wide range of biological applications and the development of MS over the last decades, achieving single-cell level resolution is still quite significantly challenging due to the difficulty in efficiently delivering peptides from single-cell to mass spectrometry instruments (Cui *et al.*, 2022). However, efforts towards combining laser capture microdissection (LCM) with mass spectrometry are being developed to overcome these limitations, enabling more sensitive and spatially resolved proteomic analyses. Extending mass spectrometry-based proteomics approaches to go spatial and include three-dimensional information is also a focus of this thesis (Bhatia *et al.*, 2022).

Multiplexing antibody-based approaches

A more recent generation of mass spectrometry is mass cytometry (MC), which uses antibodies labelled with stable heavy metal isotopes, which are then detected by a time-of-flight mass spectrometer. This allows for the simultaneous measurement of multiple proteins in each cell (Bandura *et al.*, 2009). To extend the high multiplexing capacity of mass cytometry to include spatial context, mass cytometry is combined with spatial resolution by using laser ablation to ionise labelled proteins directly from tissue sections. *Image mass cytometry (IMC)* (Giesen *et al.*, 2014) and *multiplexed ion beam imaging (MIBI)* (Angelo *et al.*, 2014) are examples of widely successful methods leveraging this technique. Despite the high resolution of these methods, they can measure only around 30 to 50 proteins since they are limited by the number of discriminated masses and the availability of sufficiently pure metals. Another antibody multiplexing approach is *Co-Detection by Indexing* (CODEX) which uses DNA barcoded antibodies to label proteins and subsequent imaging cycles to reveal the spatial distribution of these proteins within tissues (Goltsev *et al.*, 2018; Black *et al.*, 2021). These multiplexing techniques provide greater capabilities compared to traditional mass spectrometry and offer a powerful avenue to study proteomic changes within tissues with high spatial and molecular resolution (Bressan *et al.*, 2023).

Spatial omics technologies are rapidly growing, to ideally spatial profile the entire molecular content of the cell at subcellular resolution within a short time for the entire image. Mostly, the spatial profiling is done on 2-dimensional slices. However, a shift towards the 3-dimensional space is necessary to be able to capture the true spatial heterogeneity of the tissues. Therefore, efforts are directed towards extending the current spatial technologies to 3-dimensional profiling of tissues (Bressan *et al.*, 2023).

1.4.3 Analysis of Spatial Omics

The rapid growth of spatial omics technologies and the massive increase in the generated data has led to the urge to develop computational tools to handle and analyse these data to discover spatial heterogeneity in disease states, identify spatial expression biomarkers in different tissue stages, and compare spatial niches and cell-type interactions under various conditions. Therefore, tools to store, integrate, and visualise the vast diversity of spatial data are continuously being developed (Palla *et al.*, 2022b; Marconato *et al.*, 2024). Spatial omics methods vary in the technologies they use for spatial profiling, from non-microscopic methods such as mass spectrometry to DNA sequencing and barcoding. Therefore, the diversity of data acquisition techniques results in a diversity of data forms, in terms of resolution (multiple cells

to subcellular), multiplexing (10s of features to genome-wide expression profiles) and modality (transcriptomics, proteomics) (Palla *et al.*, 2022b; Bressan *et al.*, 2023). Thus, computational tools that can handle such a diversity of data are essential to harness the richness of the spatial data.

Preprocessing is an essential step in the analysis pipeline of spatial omics data to convert raw data into interpretable formats, such as cell-by-gene or cell-by-protein matrices (Illustration I). This step includes image segmentation (for microscopy-based methods), spatial registration, normalisation, and quality control. Although segmentation has been a focus for spatial transcriptomics, spatial proteomics methods, such as imaging mass spectrometry or CODEX, require additional steps such as peak alignment and spectral deconvolution to resolve protein abundances at the cellular or subcellular levels. These preprocessing steps provide a foundation for downstream analyses.

Other important steps to prepare the spatial omics data for the downstream analyses are annotation and deconvolution which are critical for identifying cell types and dissecting the molecular composition of mixed populations. For spatial transcriptomics, annotation leverages reference transcriptomic datasets to classify cells. In spatial proteomics, similar efforts are emerging which combine reference proteomes with spatially resolved protein expression data. Imputation techniques, which is a necessary step especially in proteomics data, are also valuable across modalities, helping to address data sparsity, particularly in regions with incomplete molecular profiles due to experimental limitations.

Statistical and machine learning models are continuously being developed for spatially resolved omics data. Whether by adapting established single-cell omics methods to spatial omics data or by developing new approaches to incorporate spatial information, the goal is to understand spatial molecular profile patterns, cellular organisation, and cell-cell interactions within the tissue (Zeng *et al.*, 2022). Various statistical models have been developed to understand the spatial pattern variation of gene expressions. For instance, Gaussian process regression was utilised in SpatialDE to decompose the spatial and non-spatial components of gene expression, to explain the spatial variance and to identify the significantly variable genes within the tissue (Svensson *et al.*, 2018). Other work utilised CellPhoneDB (Efremova *et al.*, 2020), a repository for ligand-receptor interactions, to study the cell-cell interactions between cells within close spatial proximity using permutation tests (Palla *et al.*, 2022b). In addition, further studies have looked into spatial clustering of spatial data and spatial niches analysis using Bayesian methods (Zhao *et al.*, 2021) and Gaussian mixture models (Varrone *et al.*, 2024). Such clustering-based spatial niche methods are useful for comparing the spatial niches across various conditions, however, they are parameter-dependent, for instance, the number of clusters, and therefore require hyperparameter tuning. Graphs have been widely used to represent spatial omics data, as further elaborated in Section 2.2. Therefore, besides the typical statistical methods, graph neural networks have also been widely used to investigate and obtain new insights from spatial omics data. For instance, graph models have been utilised to study cell-cell communications and detect indirect interactions (Fischer *et al.*, 2023; Yuan and Bar-Joseph, 2020). Furthermore, the correlation between patient outcome and cellular organisation has been investigated using graph neural networks (GNNs) to study the disease progression and tumour microenvironments in various cancer datasets (Wu *et al.*, 2022; Hu *et al.*, 2024). The growth of the zoo of models to analyse and investigate the spatial omics data is still booming. The investigation of cellular organisation and the spatial structure of tissues across various pathological and physiological states remains a crucial area of research, that will benefit significantly from the continued development of both statistical and machine learning-based models to unravel new biological insights. Multiple parts of this the-

sis underscore the importance of continuing to develop statistical and machine learning-based approaches to unravel the complexities of cellular organisation and tissue structure. These methods will pave the way for deeper biological insights in both health and disease (Ali *et al.*, 2024; Fischer *et al.*, 2022).

2 Computational Methods

In this section, I discuss the main computational and mathematical modelling approaches I used in this thesis to analyse molecular profiles and cellular organisation across various conditions using different omics technologies.

2.1 Differential expression analysis

Some omics data is produced as an average of molecular profiles of a collection of cells in the tissue, the number of cells in the collection can vary from dozens of cells to hundreds and even thousands in some technologies like common mass spectrometry. Besides being bulk, the data generated from mass spectrometry is mostly non-spatial. Therefore, pairwise statistical methods are utilised to compare the molecular profiles of tissues across different conditions, to identify differentially expressed proteins or genes in one condition versus the other.

In differential expression analysis, the *t-test* is the standard statistical method for the means of molecular expressions between two conditions or groups to evaluate whether the difference is significant or occurred at random. However, the distributions of omics data present additional complexities. For instance, RNA-seq data is often modelled as count data, assuming a negative binomial distribution due to its overdispersed nature, which contrasts significantly with the assumptions of a standard t-test. Tools such `scanpy` (Wolf *et al.*, 2018) incorporate these distributional assumptions to perform robust differential expression testing. For protein abundance data, assumptions may vary based on whether the data is log-transformed or modelled directly as counts or continuous intensities. In addition, in omics studies, thousands of genes or proteins are analysed simultaneously, and this in turn increases the likelihood of false positives when identifying genes or proteins as differentially expressed. Therefore, multiple testing approaches, such as the Benjamini-Hochberg (BH) method (Benjamini and Hochberg, 1995), are used to control the false discovery rate (FDR) and adjust p-values, reducing the chances of false positives while still identifying truly differentially expressed genes or proteins, this ensures that the analysis results are statistically robust and reliable, and thus preventing incorrect conclusions from being drawn.

We should carefully consider the underlying distribution of the data and apply statistical models that account for these characteristics so that differential expression analysis can provide accurate insights into the molecular changes associated with different conditions and thus prevent incorrect conclusions from being drawn.

2.2 Representation of tissue as a graph of cells

In the realm of spatial omics, tissues can be viewed as graphs, with nodes representing either individual cells or collections of cells (or defined spots) and edges representing the proximity between these nodes (Illustration 3). This concept has been widely adopted across different spatial omics studies (Dries *et al.*, 2021; Palla *et al.*, 2022a; Wu *et al.*, 2022). In other words, a tissue can be represented as a graph $G = (V, E)$, where V is the set nodes (or cells, or spots in the tissue) and E is the set of edges, which represent how the cells are connected in the tissue.

Graphs are flexible mathematical representations and therefore open wide possibilities to apply various statistical and deep learning approaches to analyse spatial relationships, investigate cell-cell interactions, and identify patterns within the tissues of a specific pathological condition or across different conditions (Fischer *et al.*, 2023; Wu *et al.*, 2022). In addition, representing the tissue as a graph allows us to leverage well-established graph and topological methods in the spatial omics field, providing deeper insights into tissue architecture and the underlying biological processes.

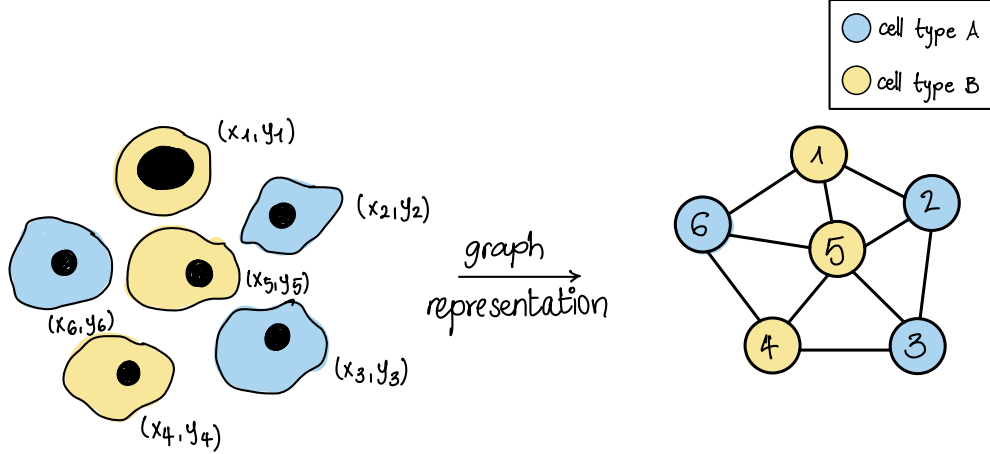


Illustration 3. Representation of Tissue as a Graph of Cells. The cells of the tissue can be represented as a mathematical graph, where the nodes represent the cells and the edges represent their spatial proximity. The graph is constructed based on the spatial coordinates of the cells. Node features can encode different properties of the cells, such as cell type.

Depending on the resolution of the spatial omics technology used to acquire the data, the nature of the nodes of the graph representing the tissue differs. As discussed in Section 1.4, some spatial omics methods, such as IMC, CODEX, and Stereo-seq, can reach single-cell resolution profiling, while others, like 10x Genomics Visium, can only capture the average molecular profiles of dozens of cells. Therefore, the nature of the nodes (whether single-cell or spot-based data) needs to be taken into consideration while constructing the graph of tissue.

Another aspect that one needs to consider when constructing the graphs from the spatial omics data, is how to construct the edges between the cells (or spots). For spot-based approaches with regular grids, such as 10x Genomics Visium, the edges are typically assigned between the neighbouring spots, representing a grid layout. However, for irregular single-cell-based approaches, there are several ways to construct the edges to represent the proximity of cells within the tissue. Some of these methods include:

1. *Distance thresholding*: In this approach, edges are constructed between cells that are within a certain distance from each other. This distance threshold is determined based on the spatial resolution of the data and the biological context to ensure that only cells in close proximity, which are more likely to interact, are connected in the graph. However, the choice of threshold can significantly affect the resulting network structure and thus needs to be carefully selected.
2. *K-nearest neighbours*: This method involves connecting each cell to its k nearest neighbours, where k is a predefined parameter. This approach ensures that each cell is connected to a fixed number of nearby cells to capture the local spatial relationships. This method is particularly useful in dense tissues where cells are uniformly distributed.

However, it may introduce connections that are less biologically relevant in regions with variable cell density (Guo *et al.*, 2003).

3. *Delaunay triangulation*: This is a geometric method that connects cells in such a way that no cell lies inside the circumcircle of any triangle in the triangulation. This method is often used to create edges that respect the overall spatial distribution of cells without relying on arbitrary distance thresholds. Delaunay triangulation is particularly useful in cases where the goal is to create a network that reflects the natural topology of the tissue and provides a more accurate representation of spatial relationships in irregularly distributed cell populations. Another advantage of this method is that it is parameter-free and easy to use (Lee and Schachter, 1980).

It is essential to consider the nature of the spatial omics data and the type of tissue before constructing the graphs. This ensures the appropriate methods are chosen for creating the nodes and edges and in turn, allows the flexibility of the graph to be leveraged effectively for understanding the underlying tissue structure and spatial molecular relationships and leading to valuable biological insights.

2.3 Graph neural networks

Graphs are considered flexible mathematical representations that capture nodes and their relationship with edges. Additionally, graphs can represent non-Euclidean data, which is valuable in representing 3-dimensional real-world data. Due to these advantages and with the extension of deep neural networks to non-Euclidean domains, the field of geometric deep learning has been rapidly emerging (Zhou *et al.*, 2020). As mentioned briefly in Section 2.2, a graph can be denoted as $G = (V, E)$, where $|V| = N_v$ is the number of nodes and $|E| = N_e$ is the number of edges that form the graph. $A \in \mathbb{R}^{N_v \times N_v}$ is the adjacency matrix representing the relationship between the nodes in the graph. Moreover, features on nodes and edges can be represented as $X_v \in \mathbb{R}^{N_v \times H_f}$ where H_f is the dimension of node features and $X_e \in \mathbb{R}^{N_e \times H_e}$ where H_e is the dimension of edge features.

Graph neural networks (GNNs) are neural networks that operate on graphs, utilising message passing to aggregate information about neighbouring nodes. The flexibility of GNNs allows them to be used for various tasks at different graph levels which in turn affect the choice of the loss function and the training setting of the model, supervised, semi-supervised and unsupervised. Additionally, graph learning tasks can be divided into three categories, (i) *node-level tasks*, which include node classification and regression problems in which node categorical labels or node continuous features are predicted, (ii) *edge-level tasks*, which include classifying edges or predicting links between nodes, and (iii) *graph-level tasks*, which learns the graph representations for graph classification or graph regression problems (Zhou *et al.*, 2020).

Various GNN architectures have been developed in the last few decades to address specific challenges and optimise performance. Among these architectures are graph convolutional networks (GCN) (Kipf and Welling, 2016), which generalise the concept of convolutions to graphs and aggregate information from each node's neighbours using convolution-like operation, with layer-wise propagation rule,

$$\mathbf{H} = \tilde{\mathbf{D}}^{-\frac{1}{2}} \tilde{\mathbf{A}} \tilde{\mathbf{D}}^{-\frac{1}{2}} \mathbf{X} \mathbf{W}$$

where $\tilde{\mathbf{A}} = \mathbf{A} + \mathbf{I}_N$ with \mathbf{A} is the adjacency matrix, $\tilde{\mathbf{D}}_{ii} = \sum_j \tilde{\mathbf{A}}_{ij}$ with $\tilde{\mathbf{D}}$ is degree of matrix $\tilde{\mathbf{A}}$, \mathbf{X} is the input matrix, and $\mathbf{W} \in \mathbb{R}^{F \times F'}$ is the free parameter with F and F' are input and output dimensions respectively. $\mathbf{H} \in \mathbb{R}^{N_v \times F'}$.

Another GNN architecture that efficiently captures the structure of graphs by focusing on the

ability to distinguish different graph structures is the graph isomorphism network (GIN). This model generalises the Weisfeiler-Lehman test and therefore can maximise the discriminative power of GNNs (Xu *et al.*, 2018) making it a powerful yet simple GNN. The node representation update rule of GIN is,

$$h_v^l = \text{MLP}^l((1 + \epsilon^l) \cdot h_v^{l-1} + \sum_{u \in \mathcal{N}(v)} h_u^{l-1})$$

where MLP^l is a multi-layer perceptron, ϵ^l is a learnable or fixed scalar, h_v^l is features of node v , and $\mathcal{N}(v)$ is the set of neighbours of node v .

There exist several other GNN architectures introducing various approaches to addressing different problems, some incorporate attention mechanisms into the propagation step like the graph attention networks (GAT) (Veličković *et al.*, 2017) while others employ generative adversarial networks (GAN) (Pan *et al.*, 2018). Therefore, the choice of the graph model architecture, as well as the graph learning task and training setting is crucial for effectively addressing the problem at hand.

3 Aim

The focus of this thesis is on uncovering the differences in cellular organisation and molecular profiles across various pathological and physiological conditions, to shed new light on how these variations influence health and disease. The work presented in this thesis is aimed towards, (1) developing tools and methodologies to address existing gaps in spatial omics, and (2) investigating complex biological systems to answer a range of research questions. The aims are detailed as follows:

1. Apply proteomics analyses to investigate the cellular heterogeneity of skull bone marrow (calvaria) and its uniqueness compared to other bone marrow as well as understand its role in neuroimmunological responses to neurological disorders (Kolabas *et al.*, 2023).
2. Develop computational tools and spatial metrics to analyse and compare cellular organisation across conditions to quantitatively understand differential changes in tissue architecture in health and disease using spatial omics data (Ali *et al.*, 2024).
3. Utilise graph-based models to explore how tissue traits and spatial patterns, such as cellular organisation and tissue architecture, contribute to patient outcomes and disease progression using spatial omics data (Fischer *et al.*, 2022).
4. Advance the study of tissue architecture in 3D by combining tissue clearing with mass spectrometry to map protein distributions in intact tissues, and to understand stage- and region-specific changes in neurological disorders such as Alzheimer's disease (Bhatia *et al.*, 2022).

Together, this thesis represents a comprehensive effort from method development to data analysis to enhance our ability to study the cellular organisation, tissue traits, and their implications for health and disease, spanning two-dimensional spatial omics slices and extending into three-dimensional volumes for a more holistic understanding of the different biological systems.

4 Studies

4.1 Study 1: GraphCompass: spatial metrics for differential analyses of cell organisation across conditions.

The paper “GraphCompass: spatial metrics for differential analyses of cell organisation across conditions.” was accepted for presentation at ISMB 2024 conference and published in the journal *Bioinformatics*. The full citation is:

Mayar Ali*, Merel Kuijs*, Soroosh Hedyeh-zadeh, Tim Treis, Karin Hrovatin, Giovanni Palla, Anna C Schaar, Fabian J Theis, GraphCompass: spatial metrics for differential analyses of cell organisation across conditions, *Bioinformatics*, Volume 40, Issue Supplement_1, July 2024, Pages i548–i557, <https://doi.org/10.1093/bioinformatics/btae242>

Summary:


Spatial omics technologies have been rapidly emerging combining spatial information and molecular profiles of cells within the tissue. Many tools have been developed to study the spatial variation within the tissue in disease and health. However, there was still a lack of computational tools to quantitatively compare the cellular organisation within samples across different pathological and physiological conditions. We tackled this gap by developing the `GraphCompass` package.

In this work, we modelled the tissue as graphs of cells to facilitate differential analysis of phenotypes. We adapted several graph metrics that are used in the graph theory field to the omics domain to quantitatively evaluate and compare cellular organisation in samples across different conditions at various levels of abstraction: individual cell types, niches, and samples. Some of the metrics we introduced in our package are novel to the omics field, such as the Wasserstein Weisfeiler–Lehman (WL) kernel and filtration curves, which provided new insights into the data. In addition, we adapted and optimised `GraphCompass` to handle various omics technologies (transcriptomics and proteomics) and different resolutions (multi-cell spot or single-cell).

We have implemented the package on top of the widely used spatial omics toolbox `Squidpy`, in a way that allows easy integration to other current spatial omics workflows. Furthermore, we have enriched the package with various visualisation functions to provide valuable insights into the data. We have also focused on developing the package in a user-friendly way to be equally usable to biologists and computational scientists.

Lastly, we have shown the capabilities of `GraphCompass` through its application on three different pathological, developmental and regeneration datasets: breast cancer, myocardial infarction, and axolotl brain regeneration, with data obtained from different omics technologies with various resolutions: MIBI-TOF, Visium and Stereo-seq respectively. These datasets can also be considered as benchmark datasets for further method development. With these analyses, we highlighted the biological insights that can be obtained from the various metrics implemented in `GraphCompass`.

GraphCompass: spatial metrics for differential analyses of cell organization across conditions

Mayar Ali ^{1,2,3,†}, Merel Kuijs ^{1,4,†}, Soroor Hadiyah-zadeh ^{1,5,‡}, Tim Treis ^{1,5,‡}, Karin Hrovatin ^{1,5}, Giovanni Palla ^{1,5}, Anna C. Schaar^{1,4,6}, Fabian J. Theis ^{1,4,5,*}

¹Institute of Computational Biology, Helmholtz Munich, Neuherberg, 85764, Germany

²Institute for Tissue Engineering and Regenerative Medicine, Helmholtz Munich, Neuherberg, 85764, Germany

³Graduate School of Systemic Neurosciences, Ludwig Maximilian University of Munich, Planegg-Martinsried, 82152, Germany

⁴Department of Mathematics, TUM School of Computation, Information and Technology, Technical University of Munich, Munich, 80333, Germany

⁵TUM School of Life Sciences, Technical University of Munich, Freising, 85354, Germany

⁶Munich Center for Machine Learning, Technical University of Munich, Munich, 80333, Germany

*Corresponding author. Institute of Computational Biology, Helmholtz Munich, Ingolstaedter Landstrasse 1, D-85764 Neuherberg, Germany.

E-mail: fabian.theis@helmholtz-munich.de (F.J.T.)

[†]Equal contribution as first authors.

[‡]Equal contribution as second authors.

Abstract

Summary: Spatial omics technologies are increasingly leveraged to characterize how disease disrupts tissue organization and cellular niches. While multiple methods to analyze spatial variation within a sample have been published, statistical and computational approaches to compare cell spatial organization across samples or conditions are mostly lacking. We present GraphCompass, a comprehensive set of omics-adapted graph analysis methods to quantitatively evaluate and compare the spatial arrangement of cells in samples representing diverse biological conditions. GraphCompass builds upon the *Squidpy* spatial omics toolbox and encompasses various statistical approaches to perform cross-condition analyses at the level of individual cell types, niches, and samples. Additionally, GraphCompass provides custom visualization functions that enable effective communication of results. We demonstrate how GraphCompass can be used to address key biological questions, such as how cellular organization and tissue architecture differ across various disease states and which spatial patterns correlate with a given pathological condition. GraphCompass can be applied to various popular omics techniques, including, but not limited to, spatial proteomics (e.g. MIBI-TOF), spot-based transcriptomics (e.g. 10x Genomics Visium), and single-cell resolved transcriptomics (e.g. Stereo-seq). In this work, we showcase the capabilities of GraphCompass through its application to three different studies that may also serve as benchmark datasets for further method development. With its easy-to-use implementation, extensive documentation, and comprehensive tutorials, GraphCompass is accessible to biologists with varying levels of computational expertise. By facilitating comparative analyses of cell spatial organization, GraphCompass promises to be a valuable asset in advancing our understanding of tissue function in health and disease.

1 Introduction

The spatial arrangement and interactions of cells under different physiological and pathological states provide insights into the underlying mechanisms of tissue function and disease progression. Understanding cell spatial organization is not only essential for deciphering physiological processes but also for advancing diagnostic and therapeutic strategies (Rao *et al.* 2021, Palla *et al.* 2022a, Williams *et al.* 2022).

Spatial omics have emerged as a powerful technology for profiling cellular phenotypes in their tissue context. Spatial transcriptomics methods such as 10x Genomics Visium (Stahl *et al.* 2016) and Stereo-seq (Chen *et al.* 2022), as well as spatial proteomics methods such as CODEX (Goltsev *et al.* 2018) and multiplexed ion beam imaging by time of flight (MIBI-TOF) (Keren *et al.* 2019), can measure molecular profiles while maintaining information about the locations of cells, therefore enabling the study of cell–cell communication (Fischer *et al.* 2023) and tissue architecture (Fischer *et al.* 2022, Wu *et al.* 2022). Spatial omics technologies have been increasingly leveraged by researchers

interested in delineating mechanisms that disrupt tissue homeostasis and cellular niches in diseased individuals. For example, spatial transcriptomics data has been instrumental in deciphering spatial dysregulation in ischemic hearts (Kuppe *et al.* 2022). Additionally, spatial proteomics data has been used to elucidate cellular neighborhoods associated with disease progression and response to therapy in breast cancer (Risom *et al.* 2022).

Related work has looked into identifying cell interactions (Fischer *et al.* 2023), spatial clusters (Zhao *et al.* 2021, Varrone *et al.* 2023), and niche composition in individual samples (Bernstein *et al.* 2023). However, methods to compare spatial organization across different sample groups are still lacking. Such methods would be instrumental in elucidating how the arrangement of cell types influences the overall state of a tissue.

In this work, we model spatial omics samples as graphs of cells to enable differential analysis of phenotypes. We focus on providing easy-to-use graph metrics and statistical methods for the comparative analysis of cell spatial organization.

Studying changes in niche composition and tissue architecture is essential to unlock new insights into the role of tissue organization in prognosis and diagnosis (Rao *et al.* 2021, Palla *et al.* 2022a, Williams *et al.* 2022).

We introduce GraphCompass (*Graph Comparison Tools for Differential Analyses in Spatial Systems*), a Python-based framework that brings together a robust suite of graph analysis and visualization methods, specifically tailored for the analysis of cell spatial organization using spatial omics data. Developed on top of Squidpy (Palla *et al.* 2022b) and AnnData (Virshup *et al.* 2021), our methods are easily integrated into existing spatial omics analysis workflows. The framework's modular design ensures adaptability and compatibility with various single-cell data analysis packages (Fig. 1a). Available for community use and collaboration, GraphCompass can be accessed at <https://github.com/theislabs/graphcompass/>, where we provide extensive function documentation and tutorials. We adapted the methods to make them flexible enough to handle large feature spaces (>20 000 genes), different resolutions (e.g. spot or single-cell), and multiple modalities of spatial omics data (Fig. 1b). To showcase the broad applicability of the methods in our suite, we curate datasets from three different spatial omics techniques and show that our methods recapitulate experimental results, additionally providing novel insights into the global changes in tissue organization under different disease

and developmental stages. The collection of omics-adapted methods we present are an effective hypothesis-generating tool that may inform the development of new diagnostic methods and therapeutic targets.

To the best of our knowledge, GraphCompass is the first method to enable differential analysis of spatial organization across conditions at three levels of abstraction: cell-type-specific subgraphs (Fig. 1d), multi-cell niches (Fig. 1e), and entire graphs (Fig. 1f). Though other methods, such as CellCharter (Varrone *et al.* 2023) and MENDER (Supplementary Table S1), also attempt to differentiate samples based on their neighborhood composition, they rely on clustering algorithms, and hence a well-chosen number of clusters. Here, we propose to perform differential niche analysis by studying enriched pairs of neighbor cells. We also present approaches that have never been applied to spatial omics before, such as the Wasserstein Weisfeiler-Lehman (WL) kernel and filtration curves. We adapt them to large continuous feature spaces, a typical characteristic of spatial omics data, and show that these metrics are powerful tools to compare samples and sample groups, capturing both local and global information. In this manuscript, we demonstrate the capacity of our methods to reproduce results consistent with previously published findings, as well as provide novel mechanistic hypotheses. To date, GraphCompass is the most comprehensive toolkit aimed at differential neighborhood

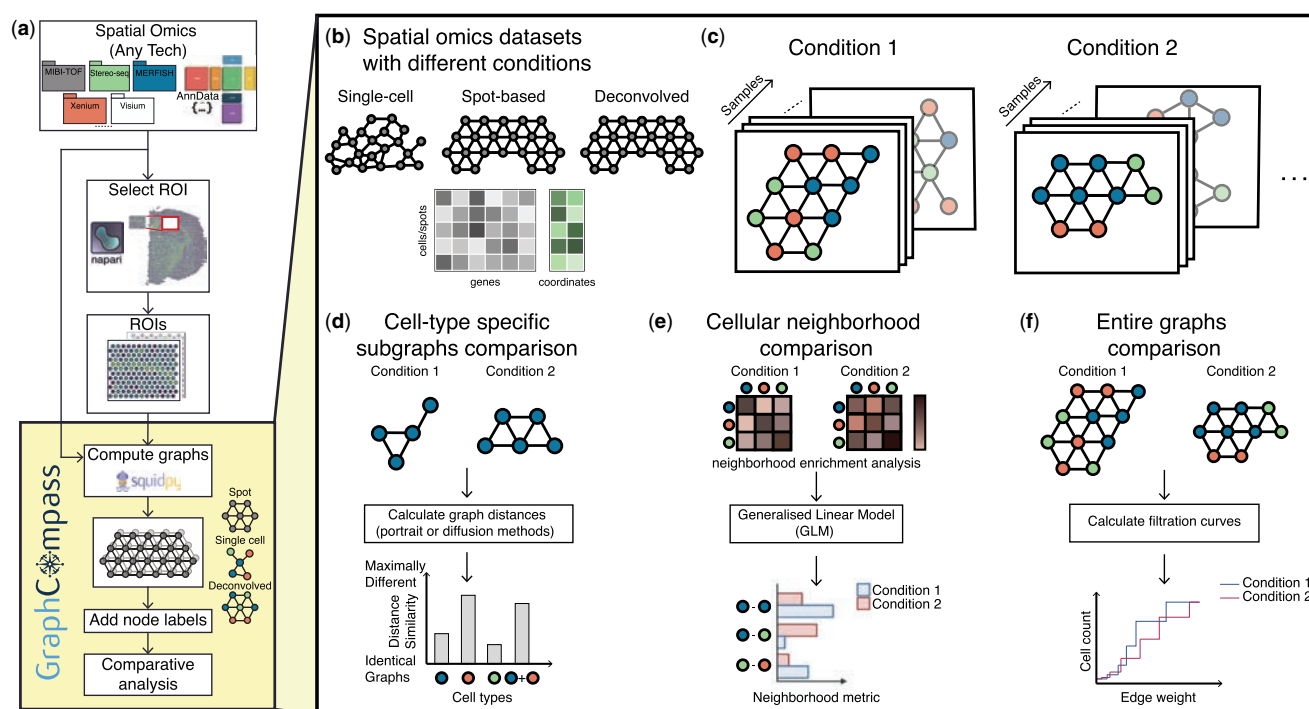


Figure 1. GraphCompass offers graph and statistical analysis methods to compare the spatial organization of cells across different conditions. (a) GraphCompass workflow. All spatial omics datasets that are stored as AnnData objects are currently supported. Support for SpatialData objects (Marconato *et al.* 2024) will be added in the near future. Select a region of interest (ROI) with napari (<https://github.com/napari/napari>) or use the entire tissue section. We use Squidpy to encode spatial omics measurements as graphs. If available, add node labels, such as cell types. Then, compare graphs across conditions or samples using any of the methods implemented in GraphCompass. (b) The example datasets covered here represent various technologies and different modalities. (c) In our framework, samples are represented as cellular graphs in which nodes correspond to cells or spots and edges denote spatial proximity. Nodes may be labeled (colored) based on their cell type and samples representing the same condition are grouped together to account for sample variation. (d–f) GraphCompass integrates multiple spatial metrics to find statistically significant differences in spatial organization across experimental conditions, utilizing spatial information at various abstraction levels. (d) Analyse graphs that consist of a single cell type and compare them between conditions using graph distance metrics (cell-type-specific subgraphs comparison). (e) Perform neighborhood analysis by retrieving cell-type neighbors enriched in one condition compared to another (cellular neighborhood comparison). (f) Using a holistic approach, compare entire graphs representing data obtained under two or more conditions (entire graphs comparison).

composition and spatial organization analysis in the context of spatial omics technologies applied to disease studies. We hope that this framework will empower significant advancements in understanding the complexities of cell organization within the spatial context of tissues, both in health and disease.

2 Materials and methods

2.1 Graph construction

Spatial omics data can be represented as graphs, where nodes in the graph represent either individual cells or predefined spots, and edges represent proximity between cells or spots (Dries et al. 2021, Palla et al. 2022a, Wu et al. 2022, Fischer et al. 2023). The nature of the node depends on the type of spatial omics technology used:

- 1) Cell-Based Data: For single-cell resolution techniques, each node corresponds to an individual cell. Every node is associated with a node attribute, namely the cell's transcriptomic profile.
- 2) Spot-Based Data: Technologies like Visium provide data at the level of spots, which are predefined, regularly spaced areas on a tissue section, each containing multiple cells. In this scenario, each spot, with its aggregated gene expression information, forms a node.

Edges represent spatial proximity between nodes. The edge construction method depends on the data's layout:

- 1) Grid Layout: In spot-based technologies like Visium, where spots are arranged in a fixed grid, edge construction is relatively straightforward. Graph edges are typically defined based on direct neighbors in this grid, leading to a structured, regular graph topology (Dries et al. 2021, Palla et al. 2022b, Sona et al. 2023).
- 2) Irregular Layouts: For data not laid out in a grid, defining node adjacency requires more sophisticated methods. Delaunay triangulation is a common approach used here. It involves creating a triangulated mesh such that no node lies inside the circumcircle of any triangle. This method effectively captures the proximity between irregularly spaced cells (Dries et al. 2021, Palla et al. 2022b, Zhang et al. 2022). Though distance thresholds and k -nearest neighbors have also been used to generate graphs from irregularly spaced nodes, they require that users tune the threshold or k appropriately, which necessitates prior knowledge of the average size of cells in the profiled tissue, for example. Delaunay triangulation, on the other hand, is parameter-free and hence straightforward to use.

Once the graph is constructed, it serves as a foundational structure for various differential analyses: comparing cell-type-specific subgraphs, cellular neighborhoods, and entire graphs between experimental conditions, developmental stages, or disease states. We use existing methods within Squidpy to compute a spatial graph from various types of spatial omics data. These graphs serve as the input for the analysis and visualization algorithms implemented in our package. We describe these analysis functions in the next sections. Broadly speaking, our criteria for our choice of methods are versatility, ease of use, and interpretability. Each

method returns a different and complementary type of information, which we explain in greater detail below. Most are parameter-free, eliminating the need for hyperparameter tuning.

2.2 Comparing cell-type-specific subgraphs

We introduce two graph distance metrics to compare cell-type-specific graphs between different conditions: portrait and diffusion methods (Supplementary Data A.1).

2.2.1 Portrait method

This method creates a so-called “portrait” of a graph, which is a way to represent the overall structure of the graph (Bagrow and Bollt 2019). The portrait of a graph typically includes information about the distribution of distances between nodes and degree distribution. The idea behind the portrait method is to capture the essence of the graph's topology in a comprehensive snapshot. The portrait method is robust to graph size and computationally efficient, focusing on the global graph structure. These characteristics make it suitable for handling cell-type-specific graphs of different sizes. Moreover, the portrait method offers an information-theoretic interpretation, facilitating the extraction of biological insights.

Given two graphs G and G' , we first define the network portrait B of each graph as an array with $l \times k$ elements, such that

$$B_{lk} = |(v_i, v_j) : D_{ij} = l, \text{degree}(i) = k|. \quad (1)$$

Here, (v_i, v_j) are node pairs of graph G such that the shortest path between v_i and v_j , D_{ij} , equals l . The degree of a node is defined as the number of edges incident to that node. We do not compare G and G' directly. Instead, we compare their network portraits B and B' , such that $\Delta(G, G') \equiv \Delta(B, B')$ (that is, such that the difference between the network portraits approximates the difference between the graphs). To compare the network portraits, we calculate the weighted distributions $P(k, l)$ and $Q(k, l)$, such that

$$P(k, l) = \frac{kB_{lk}}{\sum_c n_c^2}, \quad (2)$$

$$Q(k, l) = \frac{kB'_{lk}}{\sum_c n_c^2},$$

where n_c represents the number of nodes within a given connected component c , and $\sum_c n_c = N$, with N being the total number of nodes in the graph. We subsequently compare the two distributions using the Jensen–Shannon divergence:

$$D_{JS} = \frac{1}{2}KL(P||M) + \frac{1}{2}KL(Q||M), \quad (3)$$

where KL is the Kullback–Leibler divergence and $M = \frac{1}{2}(P+Q)$. $0 \leq D_{JS} \leq 1$ is the dissimilarity score between the cell-type-specific graphs G and G' , each representing a different experimental condition or co-variate. Here, a high dissimilarity score implies maximally different graphs, and a low score implies that graphs are highly similar. This comparison is repeated for every cell type present in both graphs. Cell-type-specific dissimilarity scores are jointly visualized to

determine which cell types are most similarly organized across both conditions.

2.3 Comparing cellular neighborhoods

Neighborhood analysis allows users to compare the count and composition of niches between samples, accounting for batch effects. To this end, we leverage interpretable linear models and Generalized Linear Models (GLMs). These models allow us to determine statistically significant changes in the neighborhood enrichment (i.e. the enrichment of spatial proximity between two cell types) across multiple conditions, offering a deeper understanding of the spatial density and distribution of specific cell types relative to others under a given condition. Here, we refer to a pair of cell types as “enriched” if they neighbor each other more often than we would expect based on random chance. We first compute neighborhood enrichment in each sample separately using Squidpy’s `nhood_enrichment` function. This function calculates the observed number of each cell type pair, which is then compared against the expected frequency. This expected frequency is determined through permutation tests.

The `nhood_enrichment` function returns a $n \times n$ matrix Z containing enrichment z -scores. Z_{ij} represents the enrichment of the pair that consists of cell type i and cell type j . Since this matrix is symmetric, we extract the upper triangular portion, which we flatten to obtain a row vector of shape $1 \times n(n+1)/2$ representing neighborhood enrichment in a single sample. Given m samples, we concatenate their corresponding vectors to obtain an $m \times n(n+1)/2$ enrichment score matrix. By default, we fit a linear model to the neighborhood enrichment z -scores. However, if one or more pairs of cell types are sparse, we instead fit a Quasi-Poisson model to the *count* of each observed cell type pair. Both the linear model and the Quasi-Poisson GLM include a fixed linear term to account for the “batch/subject/patient” co-variate, and an interaction term between all levels of the condition and cell type pair factors. The model functions perform a t -test to test if the coefficient for a given predictor is significant. In neighborhood analysis figures, we report the P -values of the significant interaction terms.

2.4 Comparing entire graphs

We present two methods to perform holistic graph comparisons: filtration curves and WL graph kernels. Both methods result in graph embeddings that can be compared against one another to obtain a broad measure of tissue architecture similarity.

2.4.1 Filtration curves

In the context of Topological Data Analysis (TDA), filtrations are a fundamental concept used to understand the shape of data (O’Bray *et al.* 2021). The basic idea is to gradually “grow” or “filter” the data and observe how topological features such as connected components, holes, and voids evolve. Filtration curves capture both differential abundance and density, providing users an overall understanding of tissue homogeneity. We define a graph filtration as a sequence of nested subgraphs $\emptyset \subseteq G_1 \subseteq G_2 \dots G_m \subseteq G$, ordered by edge weights. Let $G = (V, E, w)$ be a weighted graph, where $w : E \rightarrow \mathbb{R}$ is the weight function assigning a real number to each edge, here defined as the Euclidean distance between the gene expression matrices associated with neighboring nodes (O’Bray *et al.* 2021). To generate the filtration curve, we order the edges based on their weights, obtaining a series of

weights $w_1 \leq w_2 \dots w_{m-1} \leq w_m$. O’Bray *et al.* (2021) define the i th graph in the filtration, G_i , as the subgraph that includes all edges whose weight is less than or equal to w_i as well as all nodes connected by said edges. Since our distance function can take on any positive real number, we compute 10 threshold values from the collection of edge weights to restrict the algorithm’s computation time. We define the threshold values as the 10th, 20th, ..., 90th, and 100th percentile. At every filtration step, the algorithm analyzes the properties of the subgraph by evaluating a graph descriptor function. Assuming every node has been assigned a node label (i.e. a cell type), we can simply compute the number of each cell type present in the subgraphs. Computing and comparing filtration curves is an efficient approach for representing graphs and contrasting two graphs or sets of graphs.

2.4.2 Weisfeiler–Lehman graph kernels

The WL graph kernel is a powerful technique used in graph theory and machine learning, particularly in the context of graph classification and similarity analysis. Boris Weisfeiler and Andrei Lehman introduced it in the late 20th century as a graph isomorphism test (Weisfeiler and Leman 1968). Though it has been shown that there are non-isomorphic graphs that cannot be distinguished by this algorithm, it has been successfully implemented as a graph similarity measure (Shervashidze *et al.* 2011). Broadly speaking, the algorithm consists of three steps: node label augmentation, iteration, and kernel computation. In each iteration, the node label of a given node is transformed into an augmented label, or multi-set of labels, that contains the original label as well as the labels of the given node’s neighbors. The augmented label is subsequently hashed, resulting in a new, compressed node label. Given a graph $G = (V, E)$, where V is a set of nodes (vertices) and E is a set of edges, we can define the node label augmentation step as

$$a^{b+1}(v) = \text{hash}(a^b(v), \mathcal{N}^b(v)), \quad (4)$$

We define $a^b(v)$ as the compressed label of node v at iteration b . Similarly, $\mathcal{N}^b(v)$ represents the neighbor labels at iteration b . Lastly, we define $a^0(v)$ as the original label of node v . The node labeling step is repeated for a pre-specified number of iterations. After the iteration process, the labels assigned to the nodes are used to compute a kernel matrix. This matrix quantifies the structural similarity between pairs of graphs. The original formulation of the algorithm restricts its use to graphs with discrete labels. However, some of the more common spatial omics methods, most notably Visium, do not produce single-cell-resolved data. Each spot may contain more than one cell, complicating cell type assignment. The spot is best represented by its associated gene expression matrix. The Wasserstein WL kernel (Togninalli *et al.* 2019) extends the WL kernel from the discrete to the continuous case. We define $a^b(v)$ as the attribute of node v at iteration b . Let $w(v, u)$ be the weight of the edge between nodes v and u . Then, the updated node attribute at iteration $b+1$ is computed as

$$a^{b+1}(v) = \frac{1}{2} \left(a^b(v) + \frac{1}{\deg(v)} \sum_{u \in \mathcal{N}(v)} w(v, u) \cdot a^b(u) \right). \quad (5)$$

Once the maximum number of iterations has been reached, the algorithm evaluates the distance between pairs of nodes

(v_i, v'_j) for each $v_i \in V$ and each $v'_j \in V'$, resulting in distance matrix \mathcal{D} . Here, we set the number of iterations to three as suggested by the original authors (Togninalli et al. 2019) and define the distance between nodes v_i and v'_j as the Euclidean distance between their corresponding gene expression matrices (O'Bray et al. 2021). Lastly, the algorithm quantifies the similarity of graphs G and G' by measuring the Wasserstein distance between them as

$$W = \min_{T \in \Gamma} \langle T, \mathcal{D} \rangle, \quad (6)$$

where $T \in \Gamma$ is a transport matrix and $\langle \cdot, \cdot \rangle$ is the Frobenius dot product. Note that the Wasserstein WL kernel can be applied to data obtained at single-cell resolution as well as spot-based data. It does not require cell type annotations and provides a global view of tissue architecture similarity.

3 Results

In the next sections, we demonstrate the utility of GraphCompass methods by analyzing three datasets derived from three different technologies and spatial systems [MIBI-TOF breast cancer (Risom et al. 2022), 10x Genomics Visium heart (Kuppe et al. 2022), and Stereo-seq axolotl (Wei et al. 2022)]. We only use analysis and visualization functions implemented in GraphCompass, highlighting what can be learned from each function.

3.1 Spatial organization of the tumor microenvironment and breast cancer progression

Risom et al. (2022) used MIBI-TOF (Keren et al. 2019) with a 37-plex antibody staining panel to study changes in the tumor microenvironment during the transition from ductal carcinoma in situ (DCIS) to invasive breast cancer (IBC), allowing them to identify spatial and functional changes in various cell types, including myoepithelial cells (MYOEP), fibroblasts, and immune cells (Fig. 2a). They compared normal samples to both DCIS samples and IBC patient samples. DCIS samples can be further divided into progressors (samples that progress from DCIS to IBC) and non-progressors. The subset of data we analyze consists of 67 samples ($N_{\text{Normal}} = 9$, $N_{\text{Progressors}} = 14$, $N_{\text{Non-progressors}} = 44$). As part of their effort to identify features that distinguish transitioning samples from non-transitioning samples, the authors used a masking approach to gauge the thickness and continuity of the myoepithelial barrier in multiplexed images. An important, yet surprising, finding of this experiment is that myoepithelial disruption occurs in lesions that did *not* become invasive (non-progressors), while the myoepithelium of DCIS patients that *do* develop IBC (progressors) stayed mostly intact. A robust myoepithelial barrier is a key feature of healthy breast tissue, meaning that progressor samples more closely resemble normal breast samples in terms of myoepithelial robustness than non-progressor samples do. Risom et al. (2022) suggest that myoepithelial disruption may be a protective mechanism against progression to invasive cancer.

We employed GraphCompass to further investigate the downstream effects of myoepithelial disruption on breast tissue architecture at different scales. We first used a holistic approach, WL Graph Kernels (Section 2.4.2), to assess the overall similarity between the architecture of normal breast tissue and the spatial organization of non-progressor and progressor samples. Based on this holistic view of breast

cellular organizational structure, we find that normal tissue resembles non-progressor samples more closely than progressor samples (Fig. 2b). Next, we generated cell-type-specific subgraphs and calculated the dissimilarity scores of the subgraphs using the portrait distance method (Section 2.2.1). These subgraphs indeed suggest that the spatial organization of MYOEP in normal breast tissue is significantly more similar to that in progressor tissue than that in non-progressor tissue ($p = 7.9e^{-4}$, Student's t -test comparing Wasserstein distance means between (i) normal versus progressor and (ii) normal versus non-progressor) (Fig. 2c). GraphCompass was thus able to confirm the previously reported finding that non-progressor tissue is characterized by its compromised myoepithelial layer, distinguishing it from healthy and progressor tissue.

To further attempt to explain the protective quality of the disintegrating myoepithelial barrier, we executed a neighborhood analysis (Section 2.3) to determine which types of cells are more likely to co-occur in non-progressor samples than in progressor samples and normal breast samples. To this end, we fit a linear model to the cell type pair enrichment scores. Interestingly, immune cells were more likely to neighbor other immune cells in non-progressor samples compared to normal breast samples, indicating that non-progressors mount an immune response to the tumor, recruiting T lymphocytes (TCELL), B lymphocytes (BCELL), and dendritic cells (DC) to the site of the tumor. Indeed, CD4T-CD4T, CD4T-CD8T, B cell-T cell, and CD4T-DC were all enriched in non-progressor samples compared to normal samples (Fig. 2f). Notably, we did not observe an enrichment of these neighbor pairs in progressor samples. We hence hypothesize that a thinner myoepithelial barrier protects against the transition to IBC by contributing to the development of a “hot” tumor, i.e. a tumor that presents with a microenvironment characterized by heightened immune activity, often featuring tumor-infiltrating lymphocytes (Duan et al. 2020). The “temperature” of immune environments has indeed been shown to play a crucial role in shaping the trajectory of disease progression from pre-invasive lesions to invasive cancer (Galon et al. 2010, Fridman et al. 2017). The compromised myoepithelial barrier in non-progressor samples may allow immune cells, particularly T lymphocytes, greater access to the tumor microenvironment, increasing their presence around tumors. Our analysis suggests that these tumor-infiltrating T cells may eventually trigger cancer cell death, preventing progression to IBC.

In addition, we found that monocyte (MONO) organization in normal tissue is more similar to monocyte organization in non-progressors than that in progressors ($p = 7.6e^{-3}$, Student's t -test comparing Wasserstein distance means between (i) normal versus progressor and (ii) normal versus non-progressor) (Fig. 2c). Furthermore, the filtration curves (Section 2.4.1) show that the average number of macrophages (MACS) is higher in progressor samples than in non-progressors and control samples (Fig. 2e). In mouse models of cancer, monocytes have been observed to migrate to the site of the tumor, where they differentiate into tumor-associated macrophages (TAMs). Multiple independent breast cancer studies have identified the TAM signature and density as markers of tumor progression (Lin et al. 2003, Arwert et al. 2018, Cassetta et al. 2019). Our results suggest that progressor monocytes have differentiated into macrophages, which may affect progressor prognosis (Fig. 2d and

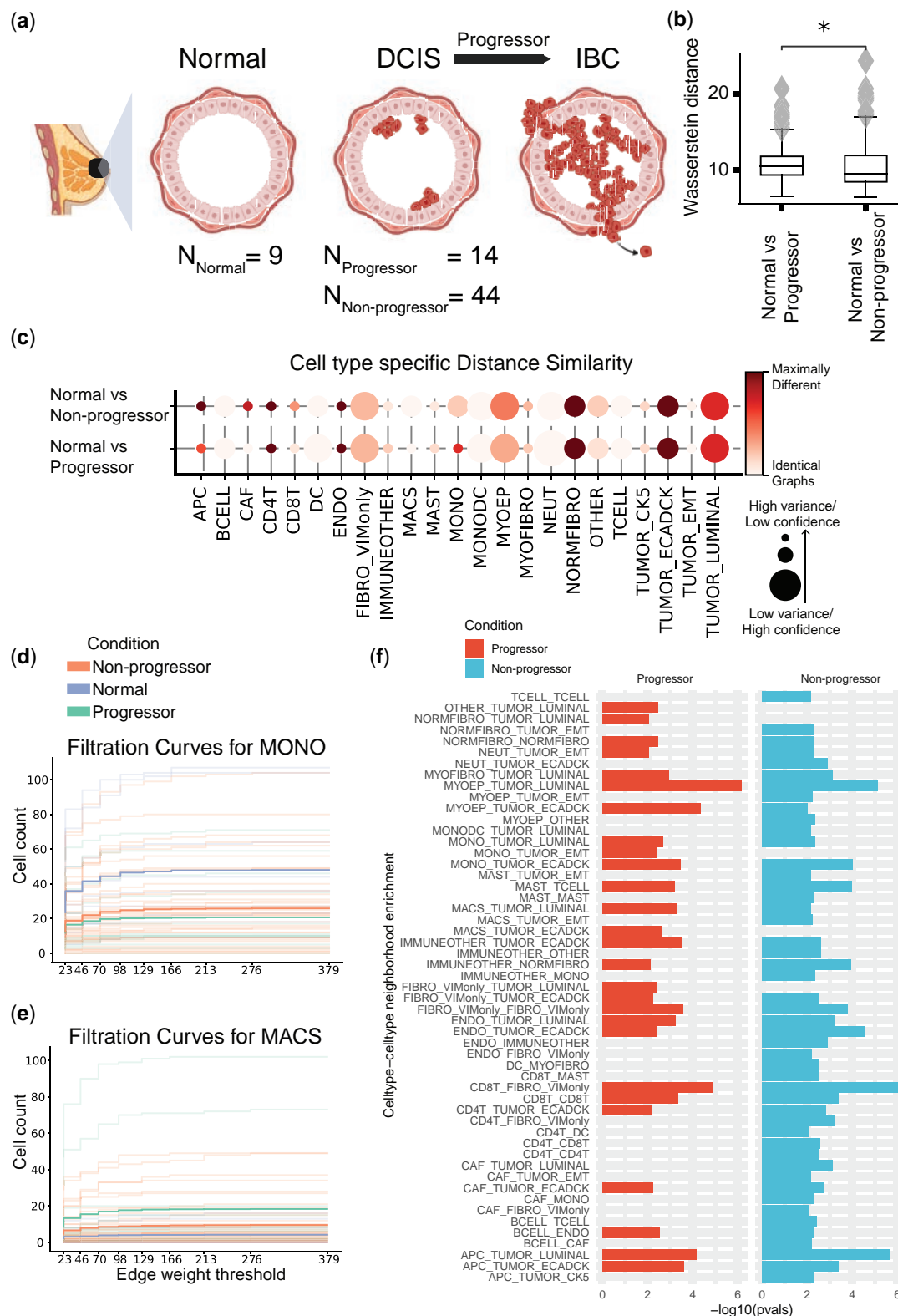


Figure 2. MIBI-TOF dataset studying the role of the tumor microenvironment (TME) in breast cancer progression. (a) Schematic figure describing the different biological conditions investigated in this study. (b) Comparing entire tissue samples, using Weisfeiler-Lehman Graph Kernels, to show the overall similarity in spatial organization across two conditions (normal versus non-progressors and normal versus progressors). The smaller the Wasserstein distance, the more similar the spatial organization is under the two compared conditions. (c) Cell-type-specific subgraphs comparison, using the portrait method, across condition pairs (normal versus non-progressors and normal versus progressors). The size of the dot is indicative of the dissimilarity score variance over samples. The larger the dot size, the lower the score variance and the higher the score confidence is. (d, e) Filtration curves (Normal, Non-progressor, and Progressor) for (d) Monocytes and (e) Macrophages. We plot a filtration curve for every sample, as well as the mean curve for every condition, which can be identified by the thicker, darker lines. Large vertical steps towards the left of the plot indicate high density, whereas large vertical steps towards the right of the plot indicate low density. (f) Enrichment of various cell type pairs in progressors and non-progressors, where the control condition acts as a baseline.

e). We could not establish differences in the organization of luminal tumor cells between progressors and non-progressors (Fig. 2c). Therefore, tumor spatial organization neither seems to cause nor appears to be immediately affected by myoepithelial integrity.

Understanding and manipulating the immune environment is essential for developing targeted therapeutic strategies to enhance immune responses and restrain cancer progression. Though further experimental validation is beyond the scope of our manuscript, we have shown that the algorithms implemented in GraphCompass generate results consistent with previously published findings, namely that myoepithelial barrier disintegration is associated with favorable disease outcomes. We have also demonstrated the use of GraphCompass as a hypothesis-generating tool, offering a potential explanation as to why myoepithelial loss protects against tumor progression.

3.2 Myocardial tissue reorganization following ischemic injury

Kuppe et al. (2022) conducted a comprehensive study to examine the changes that occur in the cardiac transcriptome and epigenome following a heart attack. They integrated data from three different modalities: single-cell RNA-seq, chromatin accessibility data, and spatial transcriptomics data generated by the Visium platform (Stahl et al. 2016). Their data contain samples from patients who experienced myocardial infarction and healthy individuals. Samples were taken from different physiological zones of the myocardium (RZ, remote zone; BZ, border zone; IZ, ischemic zone; FZ, fibrotic zone) (Fig. 3a). Here, we focus on the experiments that were based on spatial transcriptomics data. These experiments show changes in the organization of cardiomyocytes and myeloid cells after ischemic injury.

To study the effect of ischemic injury beyond the initial site of the injury, we performed a comparison of samples taken from three physiological regions: the IZ, the unaffected left ventricular myocardium (RZ), and control cardiac tissue ($N_{IZ} = 8$, $N_{RZ} = 5$, $N_{Control} = 4$). We focused our analysis on these three regions to better understand whether RZ is affected by the ischemic injury and therefore more similar to the IZ or is protected from the injury and thus more similar to control tissue. Using the entire graph comparison approach (Section 2.4.2), we show that the spatial arrangement of the RZ is not significantly more similar to the arrangement of the IZ than that of the control (Fig. 3b). This indicates that the remote zone might not be impacted, or only partially impacted, by the myocardial infarction. To further study the effects of ischemic injury at the cellular organization level, we utilized the cell-type-specific portrait method (Section 2.2.1). We found that the organization of cardiomyocytes in the RZ differed from that in the normal tissue samples. It also differed from cardiomyocyte organization in the IZ. Overall, the spatial arrangement of cardiomyocytes in the RZ is slightly more similar to the arrangement in the control samples than to the arrangement in the IZ, though the effect is not significant ($P = .25$, Student's *t*-test comparing Wasserstein distance means between (i) RZ versus control and (ii) RZ versus IZ) (Fig. 3c). This finding indicates that the cardiomyocytes in the remote ventricular myocardium are impacted by the injury, though to a lesser extent than the cardiomyocytes in the IZ. Our results also suggest that the arrangement of myeloid cells in the RZ is significantly more similar to that in the

control tissue than that in the IZ ($p = 2.2e^{-7}$, Student's *t*-test comparing Wasserstein distance means between (i) RZ versus control and (ii) RZ versus IZ) (Fig. 3c). This supports the notion that the damage inflicted by ischemic injury on myeloid cells is localized at the injury site. The filtration curves also show that cardiomyocyte organization in the RZ is affected by the injury (Fig. 3d), while myeloid organization is not (Fig. 3e). In particular, the curves show that both the number and density of cardiomyocytes in the RZ have been impacted by the infarction.

Collectively, our results support the finding that myocardial infarction can have localized or systemic impacts on different cell types. Though damage typically originates in a specific area of the heart, we observe that the consequences can extend beyond the initial site of injury. Indeed, experimental studies have suggested that the size of the infarct depends on the post-infarct inflammatory response (Frangogiannis 2014).

3.3 Restoration of axolotl brain function upon injury: comparing healthy and regenerated brains

Wei et al. (2022) used the Stereo-seq technology (Chen et al. 2022) to generate spatial omics data spanning six axolotl developmental stages and seven regeneration phases. The axolotl is a type of salamander, known for its remarkable ability to regenerate lost body parts. This ability makes them an invaluable model for studying tissue regeneration and wound healing, potentially offering insights applicable to human medicine (Fig. 4a). To shed light on the molecular events that precede regeneration, the authors removed a part of the brain and then collected spatial transcriptomics data 2, 5, 10, 15, 20, 30, and 60 days post-injury. They claim that 60 days post-injury, brain cell composition, and the spatial distribution of cell types are restored.

To assess tissue restoration success, we focused on studying the last two regenerative stages using two samples collected 30 and 60 days post-injury (30 DPI and 60 DPI). We compared the 60 DPI sample against the 30 DPI sample as well as a control adult sample from the development dataset ($N_{30DPI} = 1$, $N_{60DPI} = 1$, $N_{Adult} = 1$). The aim of our analysis is to understand whether, after 60 days, the regenerating axolotl brain is more similar to the unharmed adult brain or the 30 DPI brain. If the axolotl brain has indeed completely regenerated, we would expect to see that both the distribution of cell types and their spatial organization have been restored, mimicking that of the control adult sample. Comparing the 30 DPI, 60 DPI, and control sections at the sample level (Section 2.4.2), we show that the 60 DPI brain is slightly more similar to the 30 DPI brain than to the adult brain, indicating that the arrangement of cells has not been fully restored post-injury (Fig. 4b), though the differences are subtle.

Comparison of the cell-type-specific subgraphs further supports our conclusion that the spatial organization of the regenerated brain differs from the organization of the healthy brain. Indeed, the portrait graph (Section 2.2.1) indicates that the organization of multiple cell types in the 60 DPI sample resembles the 30 DPI organization more so than the adult brain organization. For example, one cell type that is arranged similarly in the 30 DPI and 60 DPI samples is the telencephalon neuroblast (tlNBL), which has been shown to have a role in telencephalon neurogenesis during regeneration (Lust et al. 2022) (Fig. 4c), indicating that regeneration may

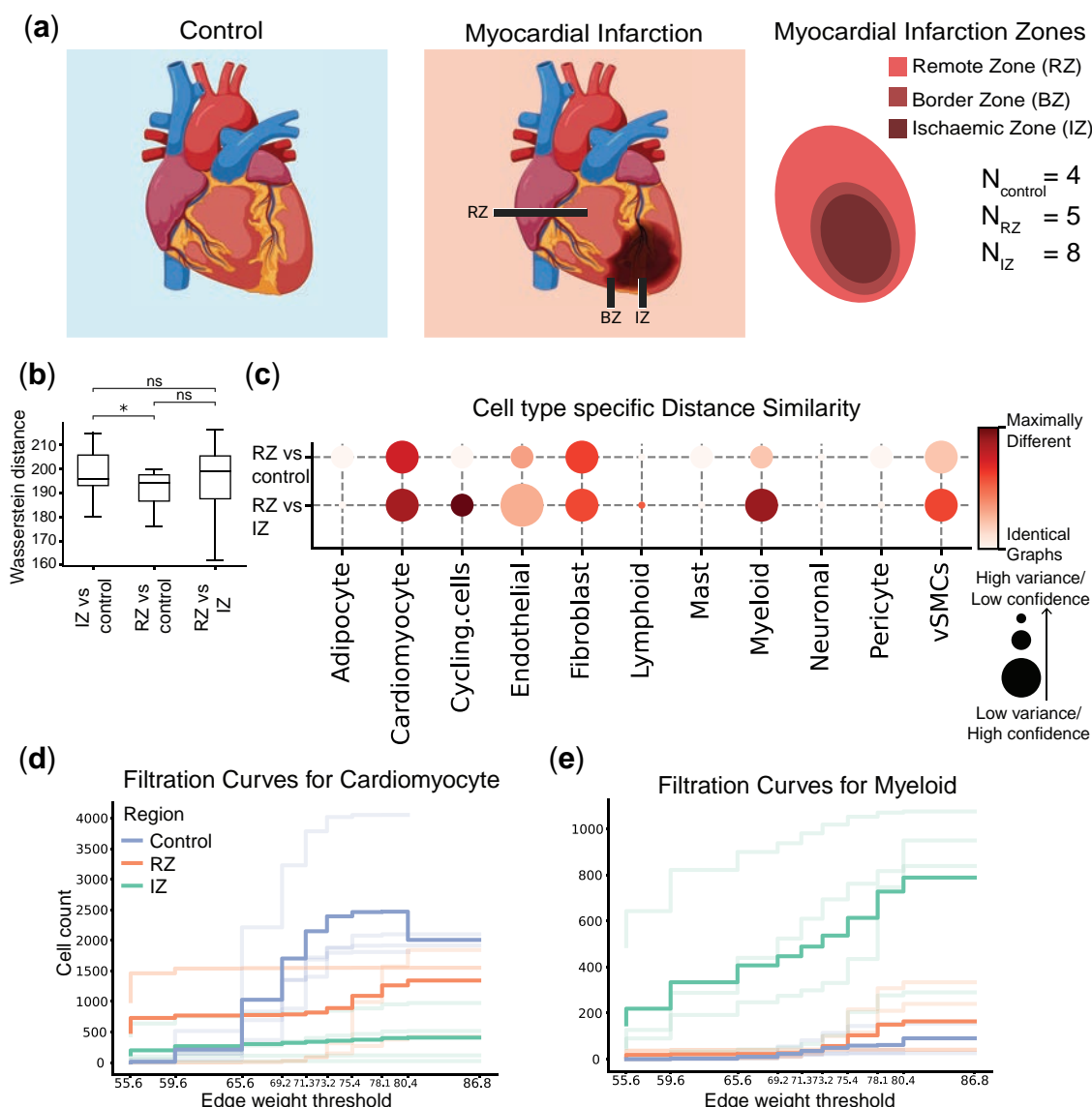


Figure 3. Visium dataset studying myocardial tissue architecture following ischemic injury. (a) Schematic figure describing the different physiological zones studied: the ischaemic zone (IZ), border zone (BZ), the unaffected left ventricular myocardium (remote zone, RZ), and control samples. (b) Comparing entire tissue samples, using Weisfeiler–Lehman Graph Kernels, to show the overall similarity in spatial organization across two conditions (RZ versus control and RZ versus IZ). The smaller the Wasserstein distance, the more similar the spatial organization is under the two compared conditions. (c) Cell-type-specific subgraphs comparison, using the portrait method, across condition pairs (RZ versus control and RZ versus IZ). The size of the dot is indicative of the dissimilarity score variance. The larger the dot size, the lower the score variance and the higher the score confidence is. (d, e) Filtration curves (RZ, IZ, and Control) for (d) Cardiomyocytes and (e) Myeloid cells. We plot a filtration curve for every sample, as well as the mean curve for every condition, which can be identified by the thicker, darker lines. Large vertical steps towards the left of the plot indicate high density, whereas large vertical steps towards the right of the plot indicate low density.

not yet be complete 60 days after the injury. However, the portrait plot also shows several cell types in the 60 DPI sample whose spatial organization is similar to that of adult cells. These cell types include dorsal pallium excitatory neurons (dpEX) and Sfrp+ ependymal glial cells (sfrpEGC). This suggests that the arrangement of dpEX and sfrpEGC cells is restored 60 days post-injury.

Wei *et al.* (2022) observe that development and regeneration are characterized by many of the same processes, including neuronal differentiation and migration, but that several pathways were uniquely upregulated in regenerating brains. In addition, they identify two subtypes of ependymal cells (EGCs), one of which is present in the developing brain, while the other is found only in the regenerating brain. It is

possible that these biological differences underlie the incomplete restoration of cell spatial organization in regenerating brains, but more data is needed to draw robust conclusions.

To summarize, we find that the arrangement of some cell types is successfully restored in the 60 days following brain injury. However, we also highlighted differences in the organization of the 60 DPI brain and the healthy adult brain, indicating that the former had not been fully regenerated at the 60-day mark.

4 Discussion

GraphCompass is a comprehensive graph analysis framework that provides quantitative methods to compare cell spatial

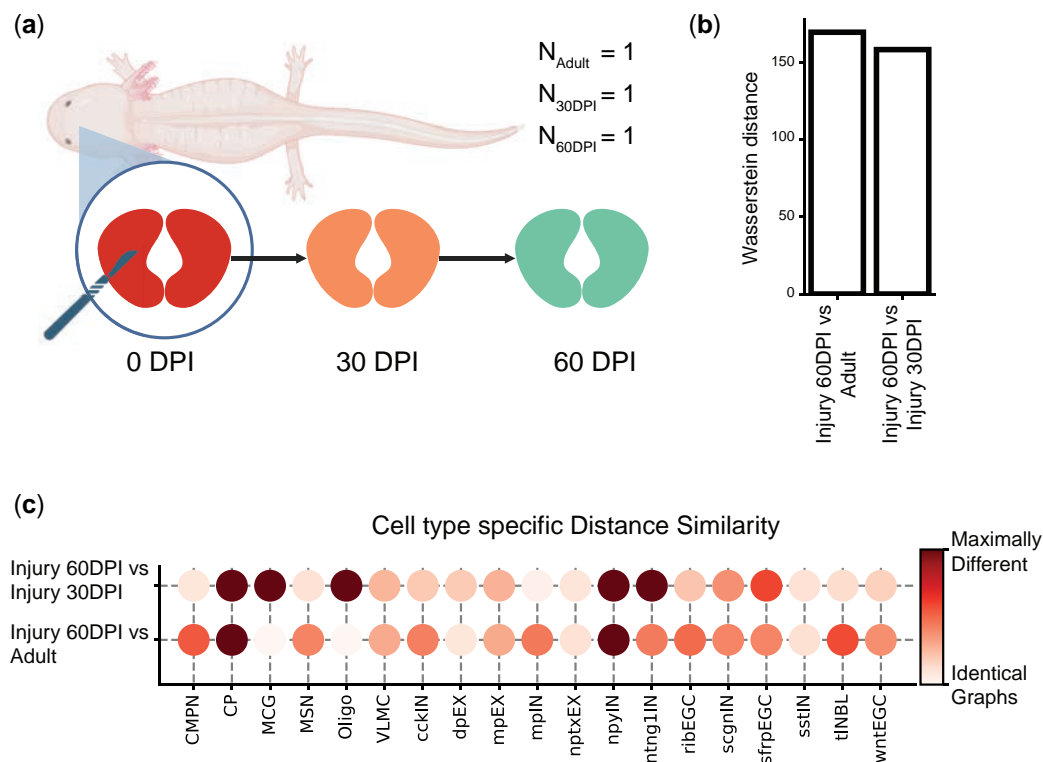


Figure 4. Stereo-seq dataset studying the axolotl brain during development and regeneration. (a) Schematic figure describing the subset of regeneration stages we investigated. On the day of injury (0 days post-injury, DPI), a section of the brain was removed. We compared a tissue sample collected 30 days post-injury (30 DPI) with a section obtained 60 days post-injury (60 DPI) and a control sample from an unharmed adult axolotl. (b) Comparing entire tissue samples, using Weisfeiler–Lehman Graph Kernels, to show the overall similarity in spatial organization across two stages (Injury 60 DPI versus Adult and Injury 60 DPI versus Injury 30 DPI). The smaller the Wasserstein distance, the more similar the spatial organization is under the two compared conditions. (c) Cell-type-specific subgraphs comparison, using the portrait method, across condition pairs (Injury 60 DPI versus Adult, Injury 60 DPI versus Injury 30 DPI).

organization across physiological systems, pathological states, and developmental stages. Compatible with spatially resolved transcriptomics and proteomics data, GraphCompass integrates multiple graph-based and statistical approaches for investigating spatial graphs at three different levels of abstraction: individual cell types, multi-cell neighborhoods, and entire samples. These methods were adapted for spatial omics data, such that they can handle high-dimensional features, flexible node identities (spot or single cell), and variable edge weight definitions.

Differences in cell spatial organization can be indicators of disease states, or correlate with how patients respond to treatments. Studying cell spatial organization across individuals can provide insights into developmental and regenerative processes, which can guide the development of engineered tissues and organoids. We believe that GraphCompass will significantly advance our understanding of the role of tissue architecture in healthy development, disease onset, and recovery.

In this manuscript, we have demonstrated the capabilities of GraphCompass through its application to datasets derived from diverse technologies, highlighting the biological insights that can be obtained from the various metrics it implements. Developed in Python, GraphCompass interfaces seamlessly with Squidpy and AnnData, enhancing its scalability and the potential for expansion with new methodologies. With GraphCompass, our aim is to offer the computational biology community user-friendly and accessible graph comparison methods, empowering both experimental and

computational scientists in the analysis and interpretation of tissue architecture differences across different biological phenotypes.

Acknowledgements

The authors thank Bastian Rieck for his valuable suggestions.

Supplementary data

[Supplementary data](#) are available at *Bioinformatics* online.

Conflict of interest

F.J.T. consults for Immunai Inc., Singularity Bio B.V., CytoReason Ltd, and Cellarity, and has ownership interest in Dermagnostix GmbH and Cellarity.

Funding

This work was supported by the European Union (ERC, DeepCell—101054957) and the Helmholtz Association’s Initiative and Networking Fund through CausalCell Dynamics (Interlabs-0029) to F.J.T.; and the Joachim Herz Stiftung via Add-on Fellowships for Interdisciplinary Life Science and the Helmholtz Association under the joint research school “Munich School for Data Science” to K.H.

Data availability

All the datasets used in this work are publicly available through open-access repositories. The Stereo-seq axolotl data (Wei *et al.* 2022) are available in the Spatial Transcriptomics DataBase (STOmics DB) under <https://db.cngb.org/stomics/artista/>. The MIBI-TOF breast cancer data (Risom *et al.* 2022) are available in a public Mendeley data repository: <https://data.mendeley.com/datasets/d87vg86zd8>. The Visium heart data (Kuppe *et al.* 2022) are available in the Zenodo data repository under <https://zenodo.org/record/6578047>.

Code availability

All spatial metrics described here are implemented in a Python package available at <https://github.com/theislab/graphcompass/>. Code documentation and tutorial notebooks can also be found on GitHub.

References

- Arwert EN, Harney AS, Entenberg D *et al.* A unidirectional transition from migratory to perivascular macrophage is required for tumor cell intravasation. *Cell Rep* 2018;23:1239–48.
- Bagrow JP, Boltt EM. An information-theoretic, all-scales approach to comparing networks. *Appl Netw Sci* 2019;4:1–15.
- Bernstein MN, Scott D, Hession CC *et al.* Monkeybread: a Python toolkit for the analysis of cellular niches in single-cell resolution spatial transcriptomics data. *bioRxiv*, 2023:2023–09, preprint: not peer reviewed. <https://doi.org/10.1101/2023.09.14.557736>.
- Cassetta L, Fragkogianni S, Sims AH *et al.* Human tumor-associated macrophage and monocyte transcriptional landscapes reveal cancer-specific reprogramming, biomarkers, and therapeutic targets. *Cancer Cell* 2019;35:588–602.e10.
- Chen A, Liao S, Cheng M *et al.* Spatiotemporal transcriptomic atlas of mouse organogenesis using DNA nanoball-patterned arrays. *Cell* 2022;185:1777–92.e21.
- Dries R, Zhu Q, Dong R *et al.* Giotto: a toolbox for integrative analysis and visualization of spatial expression data. *Genome Biol* 2021; 22:78.
- Duan Q, Zhang H, Zheng J *et al.* Turning cold into hot: firing up the tumor microenvironment. *Trends Cancer* 2020;6:605–18.
- Fischer DS, Ali M, Richter S *et al.* Graph neural networks learn emergent tissue properties from spatial molecular profiles. *bioRxiv*, 2022:2022–12, preprint: not peer reviewed. <https://doi.org/10.1101/2022.12.08.519537>.
- Fischer DS, Schaar AC, Theis FJ. Modeling intercellular communication in tissues using spatial graphs of cells. *Nat Biotechnol* 2023; 41:332–6.
- Frangogiannis NG. The inflammatory response in myocardial injury, repair, and remodeling. *Nat Rev Cardiol* 2014;11:255–65.
- Fridman WH, Zitvogel L, Sautès-Fridman C *et al.* The immune contexture in cancer prognosis and treatment. *Nat Rev Clin Oncol* 2017; 14:717–34.
- Galon J, Dieu-Nosjean M, Tartour E *et al.* Immune infiltration in human tumors: a prognostic factor that should not be ignored. *Oncogene* 2010;29:1093–102.
- Goltsev Y, Samusik N, Kennedy-Darling J *et al.* Deep profiling of mouse splenic architecture with CODEX multiplexed imaging. *Cell* 2018; 174:968–81.e15.
- Keren L, Bosse M, Thompson S *et al.* MIBI-TOF: a multiplexed imaging platform relates cellular phenotypes and tissue structure. *Sci Adv* 2019;5:eaa5851.
- Kuppe C, Ramirez Flores RO, Li Z *et al.* Spatial multi-omic map of human myocardial infarction. *Nature* 2022;608:766–77.
- Lin EY, Jones JG, Li P *et al.* Progression to malignancy in the polyoma Middle T oncoprotein mouse breast cancer model provides a reliable model for human diseases. *Am J Pathol* 2003;163:2113–26.
- Lust K, Maynard A, Gomes T *et al.* Single-cell analyses of axolotl telencephalon organization, neurogenesis, and regeneration. *Science* 2022;377:eabp9262.
- Marconato L, Palla G, Yamauchi KA *et al.* Spatialdata: an open and universal data framework for spatial omics. *Nat Methods* 2024; 1–5. <https://doi.org/10.1038/s41592-024-02212-x>.
- O’Bray L, Rieck B, Borgwardt K. Filtration curves for graph representation. In: *Proceedings of the 27th ACM SIGKDD Conference on Knowledge Discovery & Data Mining, Virtual Event, Singapore*. New York, NY, United States: Association for Computing Machinery, 2021, 1267–75.
- Palla G, Fischer DS, Regev A *et al.* Spatial components of molecular tissue biology. *Nat Biotechnol* 2022a;40:308–18.
- Palla G, Spitzer H, Klein M *et al.* Squidpy: a scalable framework for spatial omics analysis. *Nat Methods* 2022b;19:171–8.
- Rao A, Barkley D, França GS *et al.* Exploring tissue architecture using spatial transcriptomics. *Nature* 2021;596:211–20.
- Risom T, Glass DR, Averbukh I *et al.* Transition to invasive breast cancer is associated with progressive changes in the structure and composition of tumor stroma. *Cell* 2022;185:299–310.e18.
- Shervashidze N, Schweitzer P, Van Leeuwen EJ *et al.* Weisfeiler-Lehman graph kernels. *J Mach Learn Res* 2011;12:2539–61.
- Sona S, Bradley M, Ting AH. Protocols for single-cell RNA-seq and spatial gene expression integration and interactive visualization. *STAR Protoc* 2023;4:102047.
- Ståhl PL, Salmén F, Vickovic S *et al.* Visualization and analysis of gene expression in tissue sections by spatial transcriptomics. *Science* 2016;353:78–82.
- Togninalli M, Ghisu E, Llinas-López F *et al.* Wasserstein Weisfeiler-Lehman graph kernels. *Adv Neural Inf Process Syst* 2019; 32:6439–49.
- Varrone M, Tavernari D, Santamaria-Martínez A *et al.* CellCharter reveals spatial cell niches associated with tissue remodeling and cell plasticity. *Nat Genet* 2023;56:74–84.
- Virshup I, Rybakov S, Theis FJ *et al.* AnnData: annotated data. *bioRxiv*, 2021:2021–12, preprint: not peer reviewed. <https://doi.org/10.1101/2021.12.16.473007>.
- Wei X, Fu S, Li H *et al.* Single-cell Stereo-seq reveals induced progenitor cells involved in axolotl brain regeneration. *Science* 2022; 377:eabp9444.
- Weisfeiler B, Leman A. The reduction of a graph to canonical form and the algebra which appears therein. *NTI Series* 1968;2:12–6.
- Williams CG, Lee HJ, Asatsuma T *et al.* An introduction to spatial transcriptomics for biomedical research. *Genome Med* 2022;14:68–18.
- Wu Z, Trevino AE, Wu E *et al.* Graph deep learning for the characterization of tumour microenvironments from spatial protein profiles in tissue specimens. *Nat Biomed Eng* 2022;6:1435–48.
- Yuan Z, Li Y, Shi M *et al.* SOTIP is a versatile method for microenvironment modeling with spatial omics data. *Nat Commun* 2022; 13:7330.
- Zhang K, Feng W, Wang P. Identification of spatially variable genes with graph cuts. *Nat Commun* 2022;13:5488.
- Zhao E, Stone MR, Ren X *et al.* Spatial transcriptomics at subspot resolution with BayesSpace. *Nat Biotechnol* 2021;39:1375–84.

A. Supplementary Methods

A.1. Diffusion Method

Diffusion, in the context of graphs, refers to the process of spreading a certain amount of an imaginary substance (like information, heat, etc.) across the nodes of a graph over time. Diffusion on graphs can be intuitively understood through the analogy of balls connected by springs. When you impart energy to one ball in the system (for example, by hitting or pushing it), this energy is represented by the ball's movement. As the ball starts moving, it stretches or compresses the springs connected to it (the edges in the graph). This, in turn, transfers energy to the balls (nodes) at the other ends of these springs. Balls directly connected to the moving ball receive the energy first, and then the energy propagates to others in a ripple-like effect. The overall structure of the graph (how balls are connected by springs) affects the energy diffusion pathway and rate. Diffusion on graphs is implemented by NetLSD [Tsitsulin et al., 2018], a Python library that encodes a so-called “trace signature” to capture the energy diffusion process. The trace signature is computed as follows: Given graph G , calculate its normalized Laplacian as

$$\mathcal{L} = I - D^{-\frac{1}{2}} A D^{-\frac{1}{2}}. \quad (7)$$

A and D are the adjacency and degree matrix of G , respectively. Next, we compute the closed-form solution to the heat equation associated with the normalized Laplacian, which is defined as

$$\frac{\partial u_t}{\partial t} = -\mathcal{L}u_t, \quad (8)$$

where u_t represents the imaginary “energy” of a given node at time t . The solution to the heat equation is then computed as

$$H_t = e^{-t\mathcal{L}} = \sum_{j=1}^n e^{-t\lambda_j} \phi_j \phi_j^T. \quad (9)$$

Here, $H_{i,j,t}$ quantifies the amount of energy transferred from node v_i to node v_j at time t . λ_j and ϕ_j represent the j^{th} eigenvalue and eigenvector, respectively, of the Laplacian with Dirichlet boundary conditions. As a last step, we compute the heat trace h_t as the trace of H_t , such that

$$h_t = \text{tr}(H_t) = \sum_j e^{-t\lambda_j}. \quad (10)$$

To compare two graphs, we simply compute the L_2 distance between the corresponding heat traces computed at different times t ,

$$d(G, G') = \sqrt{\sum_{t=1}^n (h_t - h'_t)^2}. \quad (11)$$

Alternatively, we can cluster the heat traces to reveal sample-level similarities. The clusters can be visualized using, for example, a UMAP. Samples that cluster together are similar in terms of spatial organization.

Table 1. Comprehensive overview of methods for differential analysis of cellular organization in spatial omics data across conditions.

| Method | Cell-type Abundance | Cell-type Organization | Neighborhood/ Niche Analysis | Tissue-level Architecture | Code Availability | Comments |
|--|------------------------|---------------------------|------------------------------------|------------------------------|----------------------|---|
| Cluster-based | | | | | | |
| CellCharter [Varrone et al., 2023] | | | X | | X | Requires hyperparameter tuning |
| MENDER [Yuan, 2024] | | | X | | X | Requires hyperparameter tuning |
| SOTIP [Yuan et al., 2022] | | | X | X | X | Unflexible predefined neighborhood shapes and sizes; potential for false negatives |
| Image-based | | | | | | |
| Qualitative image analysis [Risom et al., 2022] | X | | X | | | Dataset-specific analysis; not generalizable or reproducible |
| Simple statistics | | | | | | |
| Qualitative niche analysis [Kuppe et al., 2022] | X | | X | | X | Dataset-specific analysis; not generalizable |
| Cell-type composition analysis [Wei et al., 2022] | X | | | | X | Dataset-specific analysis; not generalizable |
| Graph-based | | | | | | |
| Graph neural networks (GNN) [Wu et al., 2022, Hu et al., 2024] | X | | X | X | X | Computationally expensive; requires GPU and a large sample size |
| GraphCompass | X | X | X | X | X | Resource efficient, optional hyperparameter tuning, no need for GPU; comprehensive documentation and tutorials; insightful visualization functions |

4.2 Study 2: Graph neural networks learn tissue phenotypes from spatial molecular profiles.

The paper “Graph neural networks learn tissue phenotypes from spatial molecular profiles.” was published in 2022 as a preprint on bioRxiv. The full citation is:

Mayar Ali*, Sabrina Richter*, Ali Ertürk, David S. Fischer, Fabian Theis, 2022, Graph neural networks learn emergent tissue properties from spatial molecular profiles, bioRxiv 2022.12.08.519537; <https://doi.org/10.1101/2022.12.08.519537>

Summary:

Advancements in spatial omics enable the capture of spatial patterns within tissue niches, which in turn facilitates the study of tissue traits and their associations with patient outcomes. In this study, we analysed different cancer datasets: colorectal and breast cancer datasets, to investigate confounding tissue traits influencing patient outcomes and associate these traits with tissue architecture motifs.

We modelled tissues as cell graphs and applied graph neural networks (GNNs) to integrate spatial and single-cell data. We also designed a comprehensive multimodal ablation study to compare pseudobulk, single-cell, and spatially informed models to understand tissue traits contributing to patient outcomes. Our results showed that spatial information is encoded in global gene expression, which suggests that simpler models may be sufficient in data-limited regimes. However, we believe that larger datasets may reveal more complex relationships. However, we showed that graph neural networks capture hidden tissue architecture motifs relevant to disease progression and patient survival.

We further extended our ablation study to explore immune cell organisation and identified tissue traits influencing outcomes. In colorectal cancer, tissue architecture was the main confounding factor, while in breast cancer, cell organisation and cell-type frequencies contributed to cancer grade. In addition, we developed interpretation methods that highlighted the contributions of different tissue neighbourhoods to patient outcomes.

Our study showed that GNNs provide a powerful framework for integrating cellular organisation and tissue architecture. To the best of our knowledge, we presented in this study the most comprehensive multimodal ablation study to investigate the different tissue traits contributing to the disease stage. These insights can enhance our understanding of disease progression and support the treatment of pathological states.

Graph neural networks learn emergent tissue properties from spatial molecular profiles

Mayar Ali^{1,4,5,*}, Sabrina Richter^{1,2,*}, Ali Ertürk^{4,7}, David S. Fischer^{1,2,3,+}, Fabian Theis^{1,2,6,+}

¹Institute of Computational Biology, Helmholtz Zentrum München, 85764 Neuherberg, Germany

²TUM School of Life Sciences Weihenstephan, Technical University of Munich, 85354 Freising, Germany

³Eric and Wendy Schmidt Center at the Broad Institute, Cambridge, MA, 02142, USA

⁴Institute for Tissue Engineering and Regenerative Medicine, Helmholtz Zentrum München, 85764 Neuherberg, Germany

⁵Graduate School of Systemic Neurosciences, Ludwig Maximilian University of Munich, 80539 Munich, Germany

⁶Department of Mathematics, Technical University of Munich, 85748 Garching bei München, Germany

⁷Institute for Stroke and Dementia Research, Klinikum der Universität München, Ludwig-Maximilians-Universität LMU, 81377 Munich, Germany

+ correspondence to fabian.theis@helmholtz-munich.de

* These authors contributed equally

Tissue phenotypes, such as metabolic states, inflammation, and tumor properties, emerge from both molecular states of individual cells and their spatial organization. Spatial molecular assays provide an unbiased view of cellular spatial patterns, enabling both phenotype prediction and insights into tissue architecture. Graph models offer a natural framework for analyzing spatial proteomics data by integrating molecular expression profiles with tissue structure. Here, we apply graph neural networks (GNNs) to classify tissue phenotypes based on spatial cell patterns. We show that, for relatively simple classification tasks such as tumor grading in breast cancer, incorporating spatial context does not significantly improve predictive performance over models trained on single-cell or pseudobulk representations. However, GNNs effectively capture biologically meaningful spatial patterns, retaining prognostic signals beyond categorical tumor labels, highlighting tumor-grade-specific cell type interactions, and uncovering complex immune infiltration patterns in colorectal cancer that are not readily detectable with traditional statistical approaches. These findings suggest that, while spatial dependencies may not always enhance classification performance in small datasets, GNNs can serve as valuable tools for characterizing tissue organization and microenvironmental interactions. This study establishes GNNs as powerful tools for analyzing tissue architecture in spatial omics data, while also highlighting their current limitations in predictive modeling due to dataset constraints.

The high molecular resolution provided by single-cell RNA-seq (scRNA-seq) has put the cell as a functional unit in the focus of recent advances in tissue biology¹. However, interactions between cells and properties of the tissue beyond the length scale of a cell are largely lost in assays that are based on dissociated tissues. Highly multiplexed imaging technologies such as Imaging mass cytometry (IMC)¹⁹ and co-detection by indexing (CODEX)²⁰ enable the simultaneous measurement of dozens of protein markers at subcellular resolution within intact tissues. These technologies are particularly valuable in oncology and immunology, where they help characterize the tumor microenvironment and study how spatial organization of cells shapes disease progression and therapeutic responses^{21,22}. By capturing the coordinated behavior of malignant, immune, and stromal cells in different tumor phenotypes, these datasets provide insights into mechanisms of effective versus ineffective tumor control, ultimately advancing immunotherapies^{23,24}.

In order to analyze tissue organization, single-cell spatial omics data can be modeled as spatial graphs, where nodes represent individual cells and edges encode spatial proximity. This representation enables computational models to capture tissue architecture and cellular interactions explicitly²⁻⁴. Graph neural networks (GNNs) have emerged as a powerful tool for integrating spatial, molecular, and cellular information. Recent studies suggest that GNNs can identify disease-relevant tissue structures and even outperform traditional clinical metrics in certain prognostic tasks⁵⁻⁷. However, the extent to which GNNs effectively leverage spatial context for prediction, and whether their learned representations faithfully capture biologically meaningful features, remains unclear.

Here, we systematically evaluate the predictive performance and interpretability of GNNs for tumor phenotype classification using spatial omics data. We first conduct a comparative multi-model ablation study to assess the individual and combined contributions of spatial context and single-cell features to predictive performance. Second, we perform in-depth interpretability analyses of graph models to understand the underlying factors driving model

predictions and to better understand the biological relevance of the learned representations. Specifically, we address two key questions: (1) Does spatial context enhance predictive performance compared to single-cell or bulk representations? (2) Can graph models yield biologically meaningful insights into tissue organization? To this end, we explore several model interpretation strategies, including learned sample embeddings, attention-based interaction patterns, and saliency maps, to determine whether GNNs capture relevant biological structures. Our findings aim to clarify the role of spatial information in tumor phenotype prediction and highlight the potential of graph-based models as interpretable tools for spatial omics and tissue biology.

Results

Graph neural networks model tissue phenotypes

To investigate the role of tissue architecture in tumor phenotype prediction, we perform a multi-model ablation study to assess the performance of graph neural networks (GNNs) across multiple spatial omics datasets. Our goal is to determine how spatial context and single-cell information contribute to predictive accuracy, and whether graph-based models can capture meaningful biological patterns across different cancer types and imaging platforms (Figure 1a,b).

We first evaluate the performance of GNNs in predicting tumor phenotypes from spatial omics data, specifically examining the influence of spatial context and single-cell resolution. For this, we consider three distinct datasets with graph-level supervision tasks: a cohort of CODEX samples from colorectal cancer biopsies (*CODEX - colorectal cancer*⁹, 140 images from 35 patients), and two cohorts of imaging mass cytometry (IMC) breast cancer biopsy data (*IMC - Jackson*¹⁰, 559 images from 350 patients and *IMC - METABRIC*¹¹, 500 images from 454 patients). For the *CODEX - colorectal cancer* dataset, we focus on predicting binary anatomic labels, specifically the presence of tertiary lymphoid structures. For the *IMC - Jackson* and *IMC - METABRIC* datasets, we predict tumor grades, distinguishing between grades 1, 2, and 3 tumors. In all cohorts, hold-out splits are defined by patient to avoid leakage of batch information (Methods).

We represent the data as spatial graphs, where each node corresponds to an individual cell and is annotated with single-cell features. Spatial graphs are constructed by connecting cells with an edge if their Euclidean distance fell below a fixed threshold radius, with neighborhood sizes (resolutions) determined based on the average node degree distribution³ (Supp. Fig. 1). This representation enables the modeling of both cellular attributes and spatial relationships within the tissue. GNNs operate on these graphs by iteratively aggregating information from neighboring nodes and ultimately pooling the learned cell-level representations into a single graph-level embedding, which serves as the basis for tissue phenotype prediction.

Ablating over tissue architecture motives in spatial omics for tumor phenotype prediction

To disentangle the contribution of spatial context and single-cell resolution to model performance, we designed a comprehensive ablation study building on the spatial graph framework described above. In this setting, we constructed spatial graphs where each node represents an individual cell and is annotated with its molecular profile, such as protein or gene expression levels, while edges represent spatial proximity as previously described. To benchmark the utility of spatial context and single-cell resolution, we compared three scenarios: (1) the full molecular profiles of cells within their spatial context encoded via spatial proximity graphs (Spatial Tissue Architecture), (2) molecular profiles of *in silico* dissociated single cells without any encoding of potential interactions (Single Cell), and (3) pseudobulk profiles computed as the mean molecular expression across all cells in a tissue image (Bulk) (Figure 1c). For each of these inputs, we applied tailored machine learning models: graph convolutional networks (GCN) and graph isomorphism networks (GIN) for the spatial graphs, multi-instance learning (MI) models for the single-cell input, and multi-layer perceptrons (MLPs), logistic regression and random forests (RF) for the pseudobulk-level representation. We optimized all models using hyperparameter grid searches within a nested cross-validation framework (Table 1-2), and performance was evaluated using the area under the precision-recall curve (AUPR) to account for class imbalances (Methods).

We found that GNNs trained on spatial graph representations of tissue images did not significantly outperform multi-instance learning (MI) models trained solely on single-cell expression vectors for all datasets ($\Delta\text{AUPR}=0.052$ and $p=0.21$, $\Delta\text{AUPR}=0.036$ and $p=0.086$, $\Delta\text{AUPR}=0.014$ and $p=0.56$ for *CODEX - colorectal cancer*, *IMC - Jackson* and *IMC - METABRIC*, respectively, Fig. 2a,b,f). In addition, the single-cell resolution modelled by the MI models offered no substantial improvement over pseudobulk representations ($\Delta\text{AUPR}=-0.012$ and $p=0.71$, $\Delta\text{AUPR}=0.005$ and $p=0.80$, $\Delta\text{AUPR}=-0.021$ and $p=0.31$ for *CODEX - colorectal cancer*, *IMC - Jackson* and *IMC - METABRIC*, respectively, Fig. 2a,b,f, Supp. Fig. 2). Notably, only in the *IMC - Jackson* breast cancer dataset did the spatial model significantly outperform the pseudobulk-level representation ($\Delta\text{AUPR}=0.041$ and $p=0.019$). These findings suggest that the added value of spatial context or single-cell resolution for tumor phenotype prediction is limited in current spatial omics datasets, which comprise only up to a few hundred images. The strong performance of pseudobulk representations likely reflects their ability to smooth out cell-to-cell variability and emphasize dominant molecular signals at the tissue level. In contrast, more complex spatial or single-cell models may require larger datasets, or more complex phenotypes that are tightly coupled to spatial organization, to fully leverage the additional layers of information they encode.

Spatially-aware graph embeddings reveal clinically meaningful tissue representations

The ability of graph neural networks (GNNs) to explicitly model cellular interactions and tissue architecture offers unique opportunities for capturing biologically meaningful spatial features that may not directly translate into classification performance. Despite the comparable predictive performances of GNNs to the baseline models, it remains worthwhile to explore what these models learn about tissue organization and whether their learned representations reflect relevant biological structures or processes. Therefore, we analyzed the graph-level embeddings learned by the GNNs. These embeddings, obtained after node-pooling, provide spatially-aware representations of entire tissue samples and can be interpreted as a continuous patient manifold (Methods). Interestingly, the embeddings revealed biologically meaningful patterns beyond the separation required for tumor phenotype classification. For the two breast cancer datasets, we found that the graph embeddings recapitulated the sequential ordering of tumor grades (1, 2, and 3), even though the categorical multi-class loss function does not enforce such ordering. For the *IMC - Jackson* dataset, the embeddings showed a clear gradient of tumor grades, progressing from grade 1 through grade 2 to grade 3, as reflected in the increasing pairwise distances between grades (Fig. 2c,e). In the *IMC - METABRIC* dataset, although the distance between grade 1 and grade 3 embeddings was not significantly greater than that between grade 2 and grade 3, the median distance from grade 1 to grade 3 was still higher, suggesting a partial preservation of grade ordering (Fig. 2i). This interpretation is further supported by principal component analysis of the learned embeddings. The first principal component (PC1) revealed a graded separation across tumor grades: grade 3 samples were shifted toward the positive end of PC1, grade 1 clustered toward the negative end, and grade 2 was distributed between them. This suggests that the model captures a latent, continuous trajectory consistent with tumor severity (Fig. 2g). Furthermore, to assess whether the learned embeddings also captured prognostic signals, we examined the association between the first principal component and disease-specific patient survival, and indeed found a correlation even within samples of the same tumor grade (Fig. 2d,h). This was reflected in the right-censored concordance index, which yielded median values consistently above 0.5 across cross-validation runs of the selected model (*IMC - Jackson*: 0.55, 0.54, 0.57 for grades 1, 2, and 3; *IMC - Metabric*: 0.86, 0.62, 0.53; Supp. Fig. 3a,b). These analyses show that the graph models learned meaningful, even clinically interesting, sample representations that go beyond the separation of labels they were trained on and offer two important implications: (1) the multifaceted utility of these embeddings suggests that the models base their predictions on biologically meaningful features and may generalize to further interpretation tasks, and that (2) the continuous nature of the learned representations reflects gradual variability across tumor grades and patient subgroups, highlighting their potential for future studies to explore clinical outcomes along such latent trajectories.

Uncovering spatial patterns of immune cell distribution in breast cancer with graph neural networks

These results suggest that gene expression states, the input node states in the presented ablation study, contain significant information about the tissue labels, even in the absence of information about spatial connectivity. However, the cell-wise gene expression states themselves are functions of the spatial context^{3,25}, thus potentially confounding this ablation result. To address this potential limitation in the capture of spatial patterns of cells that are predictive of tissue labels, we set out to perform a similar ablation study in which the input node states are discrete cell type labels.

These cell type labels do not resolve fine-grained gene expression variability within cell types that is often confounded by spatial context³ but may still represent relevant spatial patterns in the tissue: for example, the spatial distribution of immune cells within tumors in a spatial graph of cells that has cell type labels as node states. To specifically query immune cell distributions, we reused the previously described graph representation of tissue images, replacing molecular expression profiles with binary immune versus non-immune cell representations as node features.

To determine whether GNNs pick up tumor phenotype specific spatial patterns of immune infiltration into the tumor, we designed a second ablation study to compare their classification performance against baseline models. Specifically, we compared: (1) the graph tissue representation with binary node features of immune vs non-immune cell ("Spatial Tissue Architecture" model), (2) tissue density structure, using either the graph skeleton or the histogram of node degrees without cell phenotype information ("Density" model), and (3) the cell type fractions (immune vs. non-immune) only ("Cell Type Fractions" model) (Figure 1c). As an additional control, we trained GNNs on data with randomly permuted node labels ("Permuted Spatial Tissue Architecture" model) to test whether predictions relied on specific immune-tumor spatial arrangements, while keeping the adjacency matrices and cell type fractions fixed (Methods).

Notably, we found that GIN models trained on the spatial immune cell distribution of the IMC - Jackson breast cancer dataset significantly outperformed all other models. This included models trained solely on cell type fractions, tissue density features, and permuted node labels ($\Delta\text{AUPR} = 0.072$, $p = 0.019$ for Cell Type Fractions; $\Delta\text{AUPR} = 0.16$, $p = 5.47\text{e-}6$ for Density; $\Delta\text{AUPR} = 0.047$, $p = 0.041$ for Permuted, Figure 3a). Therefore, we conclude that the GIN model successfully captured distinctive spatial patterns of immune cell invasion associated with different tumor grades. In contrast, for IMC - METABRIC dataset, graph models did not outperform baseline models trained solely on immune cell fractions, although they did outperform both the tissue density-based and permuted graph baselines ($\Delta\text{AUPR}=0.052$ and $p=0.14$ for Cell Type Fractions, $\Delta\text{AUPR}=0.12$ and $p=6.69\text{e-}6$ for Density, $\Delta\text{AUPR}=0.088$ and $p=9.72\text{e-}3$ for Permuted, Figure 3b). The generally low performance on this dataset, close to random baseline levels, may explain why modeling complex spatial patterns failed to improve prediction performance. This finding highlights the current limitations imposed by small sample sizes in spatial omics datasets. Together, these findings show that while spatial modeling of immune cell organization can enhance phenotype prediction in certain settings, its effectiveness likely depends on dataset size, signal strength, and the degree to which immune spatial patterns are linked to the target phenotype.

To further explore the ability of GNNs to retrieve spatial patterns, we trained a graph attention network (GAT) on the IMC - METABRIC dataset and analyzed the learned interactions between neighboring cell types in the context of tumor grades (Figure 3c-e, Supp. Fig. 4). Interpreting the weight matrix of the first graph convolutional layer (Methods), similar to how convolutional filters are visualized in image recognition models, revealed biologically meaningful interactions. Specifically, setting the convolutional filters in context with the learned attention mechanism between cell types (Figure 3c), we found that the proximity of fibroblasts around tumor cells to be indicative of grade 1 tumors, while the occurrence of macrophages next to tumor cells rather indicated grade 3 tumors (Figure 3c,d). This observation aligns with the increased presence of macrophages near tumor cells in grade 3 tumors and the higher prevalence of fibroblast-tumor cell interactions in grade 1 tumors¹¹ (Figure 3e).

In summary, our findings demonstrate that GNNs applied to immune cell patterns within tumor tissue can identify distinctive spatial patterns of immune infiltration relevant for tumor grade prediction, as shown in the IMC - Jackson dataset. We further demonstrated a way to extract such patterns from fitted models. Our findings emphasize the value of GNNs in integrating diverse factors contributing to phenotype prediction and to uncover subtle spatial patterns that hold promise for advancing our understanding of tumor microenvironments and informing targeted therapeutic strategies.

Graph neural networks capture complex immune infiltration patterns in colorectal cancer

Previous studies have shown that the spatial distribution of immune cells in colorectal cancer is predictive of disease outcomes and is used to stratify tumors.^{5,9} This motivated us to investigate whether spatial immune infiltration

patterns could again be found to distinguish between tumor cores with tertiary lymphoid structures (TLS) and those with diffuse immune infiltrates (DII).

To model these spatial patterns, we represented tissues again as spatial proximity graphs where nodes were categorized as either immune or non-immune cells. Surprisingly, GNNs trained on this representation did not significantly outperform models trained on permuted node labels, where cell type identities were randomly shuffled ($\Delta\text{AUPR} = 0.004$, $p = 0.88$, Figure 4a). This suggests that immune cell identity contributed little to the model's predictive performance in this setting. Moreover, models trained on the graph structure alone, without any node feature information, outperformed graph models that included either immune status or full molecular profiles as node features ($\Delta\text{AUPR} = 0.023$, $p = 0.44$ for Spatial Tissue Architecture (immune/non-immune features); $\Delta\text{AUPR} = 0.027$, $p = 0.45$ for Spatial Tissue Architecture (molecular features), Figure 4a, Supp. Fig. 2). This indicates that the underlying spatial arrangement of cells, independent of their molecular or immune identity, may be the dominant predictive signal in this dataset. Supporting this, even random forest classifiers trained on node degree histograms achieved comparable performance in distinguishing tumor areas with tertiary lymphoid structures from those with diffuse immune infiltrates ($\Delta\text{AUPR} = 0.071$, $p = 0.12$, Figure 4a).

The relevance of tissue density in modelling colorectal cancer also explains the strong performance differences between GCN and GIN models in this setting. While GCNs normalize node degrees during message passing, GINs preserve node degree information through sum aggregation. Modifying GCNs to use sum aggregation restored their performance to match GINs ($\Delta\text{AUPR}=0.17$ and $p=1.49\text{e-}4$ GIN vs. GCN, $\Delta\text{AUPR}=0.015$ and $p=0.51$ GIN vs. GCN with sum aggregation, Supp. Figure 5d). This finding highlights the significance of preserving tissue density structure in models of cellular organization.

We note that tissue density may be confounded by local cell type composition, thus not guaranteeing that the density model is indeed an ablation that is free of spatial information. To understand if the GIN model captured immune-related spatial features in these settings in which it did not outperform the density model, we employed a gradient-based interpretability approach, calculating the gradient of the model's output with respect to node-level inputs to estimate the contribution of individual cells. Positive gradient values indicated features characteristic of TLS regions, while negative values pointed toward the DII label. First, stratified cells by their node degree and the immune-to-non-immune cell ratio in their local neighborhood and computed average gradient values. Interestingly, while node degree alone was sufficient to achieve high predictive performance, the model clearly incorporated immune identity into its predictions. For instance, cells with node degrees between 10 and 15 and high immune fractions were strong indicators of TLS regions, whereas cells with similar degree but lower immune content were associated with DII regions (Figure 4b). This level of discrimination could not be achieved by models relying only on tissue density. Next, we asked whether cells within similar local features, same node degree and immune fraction, were used differently by the model depending on whether they point towards TLS or DII regions. For this, we compared the average gradient values between cells from TLS and DII images (Figure 4e,f). The gradient values revealed a specific subset of cells (with node degree 10-20, immune cell fraction >80%) that emerged as key determinants of TLS classification. However, the presence of these cells alone did not fully explain the model's predictions; cells with identical local properties exhibited substantially lower gradient values when they originated from DII images. This suggests that the model leveraged broader spatial context beyond local density and immune abundance. To further investigate potential sources of this contextual difference, we analyzed the neighborhood compositions of these predictive cells, using annotations from the original dataset (Figure 4c,d,g). We found that cells linked to TLS regions were most often situated in follicle- or T cell-enriched neighborhoods, while the same cell types in DII regions were more frequently embedded in granulocyte- or macrophage-enriched neighborhoods. Even among cells residing in T cell-enriched neighborhoods, gradient values differed markedly between TLS and DII images (Figure 4h,i), further supporting that the model captures subtle, higher-order spatial cues that distinguish immune microenvironments.

These findings suggest that the graph models capture spatial organization patterns beyond local tissue density, immune cell composition, and immediate neighborhood context. Despite cells having the same node degree, immune fraction, and neighborhood annotation, the model assigns distinct importance depending on whether they originate from TLS or DII regions. This indicates that the model leverages more complex spatial relationships within the tissue subgraph to distinguish between these phenotypes. Such patterns are difficult to capture with conventional models,

highlighting the strength of graph-based approaches in learning subtle, context-dependent features of tissue architecture. It is also important to keep in mind that tissue density may still embed some spatial context due to confounding with local cell composition, which may partly account for the performance of the density-based models relative to the graph models.

Cell type encodings enable interpretability in graph representation learning despite lower prediction accuracy

Cell type labels are a coarsening of vector-shaped cell-wise mean gene expression observations. One would expect the increased feature complexity of gene expression states compared to cell type labels to translate to overall improved predictive ability of models that use these node states in the input. Indeed, graph models were significantly better when trained on gene expression vectors as opposed to one-hot encoded cell type node representations on the breast cancer datasets, *IMC - Jackson* data and *IMC - METABRIC* data ($p=7.22e-4$ and $p=3.59e-3$, respectively, Supp. Fig. 5a-c). Nonetheless, cell type encodings offer a lower-dimensional and interpretable representation of tissue, which can be particularly valuable for identifying structural patterns and supporting mechanistic studies, such as those modeling immune infiltration.

Introducing additional prediction tasks to combat overfitting

Overfitting is of particular concern in relatively small cohorts of hundreds of observations as those that we considered here, especially when working with high-dimensional molecular feature spaces. We introduced an auxiliary self-supervision task (Methods) to the graph model, where the graph neural network predicts the cell type composition of neighboring spectral clusters, to constrain the node embeddings, and compared the resulting performance with standard graph models. However, this task did not improve overall performance of the graph models (Supp. Fig. 6). We added further sample-level labels in a multi-task setup to the GCNs trained on the *IMC - Jackson* and *IMC - METABRIC* datasets but did not find this to improve the prediction accuracy on test data (Supp. Fig. 7). These results highlight the challenges of training expressive graph models on limited data and point to the need for larger, more diverse datasets to fully leverage their potential.

Discussion

In this study, we evaluated the ability of GNNs to capture tissue phenotypes from spatial molecular profiling data, leveraging their capacity to implicitly integrate multiple layers of biological information: spatial organization of cells, overall cell type composition, molecular expression profiles as well as structural tissue features such as cellular density patterns. We found that for relatively simple classification tasks, such as predicting tumor grade in breast cancer, the inclusion of spatial context did not improve phenotype classification performance, likely due to the limited dataset sizes of a few hundred images. However, despite this, GNNs successfully captured biologically meaningful spatial patterns, revealing insights beyond what traditional statistical approaches could extract. For instance, GNN-derived sample representations contained clinically relevant signals beyond categorical tumor grade labels. Using Graph Attention Networks, we identified tumor-grade-specific cell type interactions in one of the breast cancer datasets, and in colorectal cancer, GNNs uncovered complex immune infiltration patterns that would not have been apparent through simple statistical analyses. Even in cases where these patterns did not enhance classification accuracy, their successful retrieval suggests that GNNs could serve as valuable tools for spatial data analysis, helping to characterize tissue organization principles and microenvironmental interactions.

As datasets grow in size and phenotype complexity, graph-based approaches remain a promising avenue for modeling spatial molecular data. With richer and more extensive datasets, there will be greater flexibility to explore more sophisticated model architectures. While our study was constrained to relatively simple GCN and GIN models due to dataset size limitations, future work could benefit from models with higher capacity, such as Graph Attention Networks¹³ or spatially aware message-passing architectures, which may be more sensitive to subtle tissue niche motifs. Additionally, hierarchical pooling strategies could enhance information aggregation in larger graphs⁵, which may for example become available in the context of tissue clearing¹⁶. Integrating spatial profiling with high-resolution single-cell RNA sequencing may further improve the molecular input space for GNNs¹⁴, allowing for a more detailed characterization of tissue organization.

Beyond methodological advancements, the ability of GNNs to extract spatially structured biological signals suggests potential applications beyond classification tasks. In research settings, such models could aid in identifying microenvironmental features associated with disease progression or treatment response, offering an interpretable framework for studying tissue organization. In the long term, if trained on sufficiently large and diverse datasets, GNN-based models could contribute to biomarker discovery or aid in stratifying patients based on spatially defined phenotypic traits. However, realizing these possibilities will require not only larger and more comprehensive datasets but also careful validation to ensure robustness and clinical applicability. Taken together, our findings highlight both the current limitations and future promise of GNNs for spatial molecular profiling data, positioning them as a powerful tool for studying the complex interplay between tissue structure and molecular state.

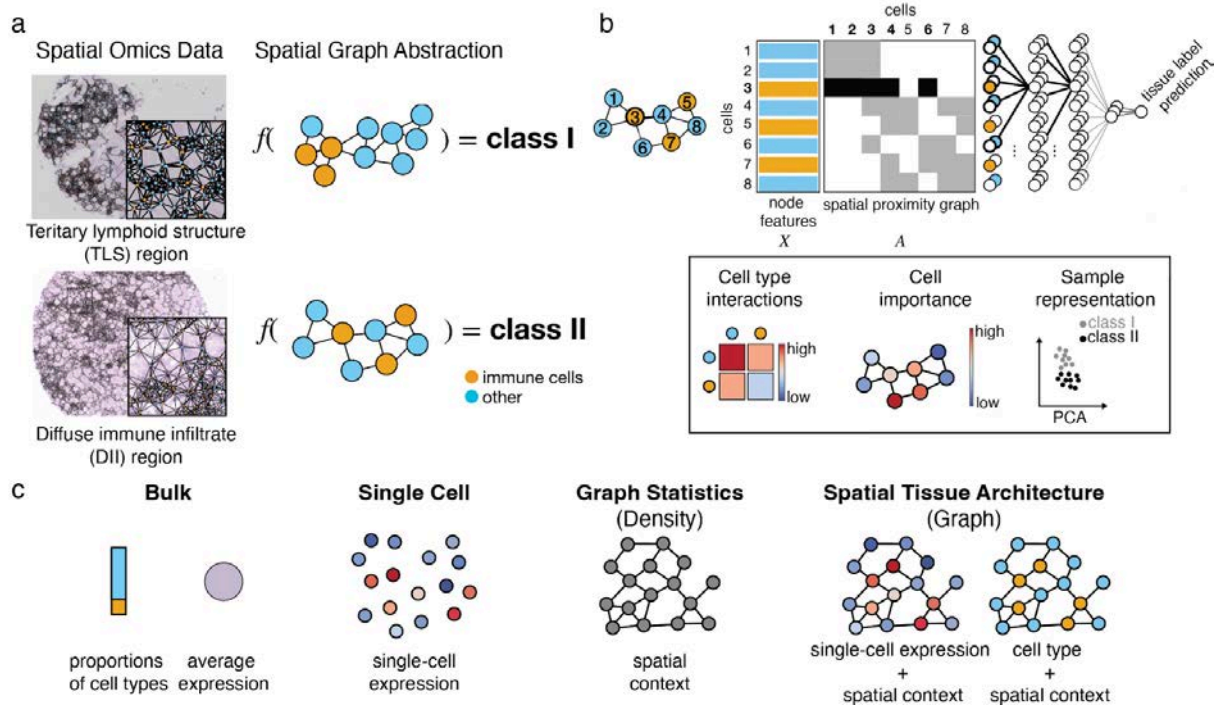
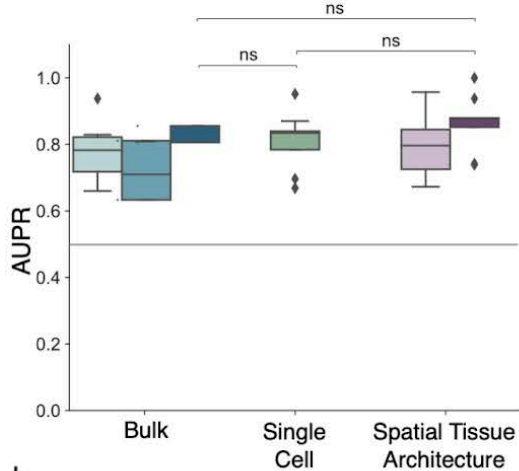


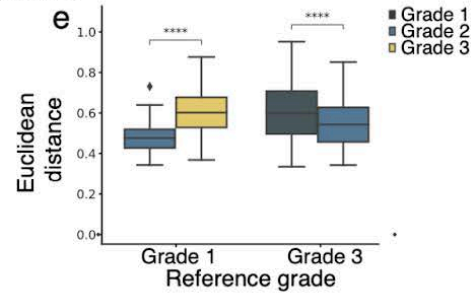
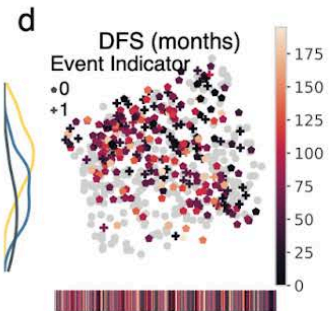
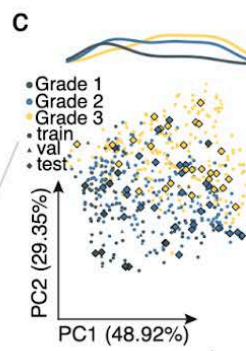
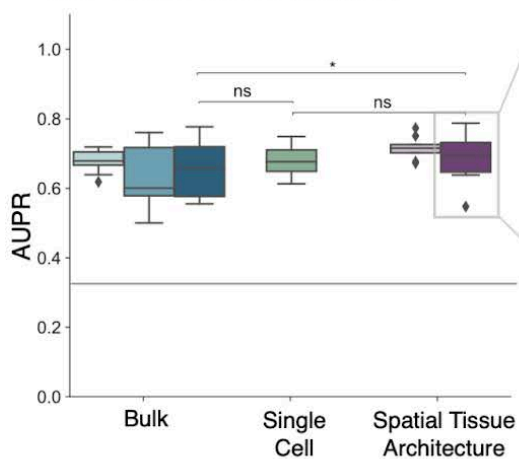
Figure1. Overview of spatial graph framework and ablation design for phenotype prediction. (a) Tissue-level phenotypes are functions of the architecture of the tissue. In this case, two immune infiltration regions, Tertiary lymphoid structure (TLS) region and diffuse immune infiltrate (DII) region, can be distinguished based on the spatial distribution of immune cells. This anatomical label cannot be inferred based on frequencies of cell types that would be available in dissociation-based protocols, but only based on the spatial distribution of cells⁹. One example image from the *CODEX - colorectal cancer* dataset for each class. (b) (top) The spatial context of each cell can be formally represented by a graph in which edges are weighted based on the distance between nodes. Each sample can be represented as one such graph, where nodes are colored by the measured cell features. Node features and the proximity graph are input to the model. We perform prediction with a model that consists of graph neural network layers to produce node embeddings, followed by pooling over nodes and a final classification network that outputs a tissue-level label. (bottom) Different downstream tasks and interpretation approaches can be performed using the graph embeddings, such as cell-type interactions or neighborhood analysis, cell importance to the phenotype prediction, and sample representation where the spatially-aware graph embeddings can be visualized with a PCA in which each point reflects one graph (image) and depicts separation of samples by the tissue-level class. (c) Design of the ablation study. *Bulk* models only have access to the average node feature vector of the graph whether proportions of cell types or average molecular expression. *Single Cell* models have access to single-cell-resolved but *in silico* dissociated data from the observed spatial graph. *Graph Statistics* are spatially aware models that have access to the full spatially resolved data, but reduce it to simpler summary statistics such as tissue density represented by node degree. Finally, *Spatial Tissue Architecture* which are represented by graph models, have access to node features and the spatial proximity graph.

a CODEX - colorectal cancer



Model Type
 ■ Multilayer Perceptron (MLP)
 ■ Logistic Regression
 ■ Random Forest (RF)
 ■ Multiple Instance (MI)
 ■ Graph Convolutional Network (GCN)
 ■ Graph Isomorphism Network (GIN)
 — random predictor

b IMC - breast cancer (Jackson)



f IMC - breast cancer (METABRIC)

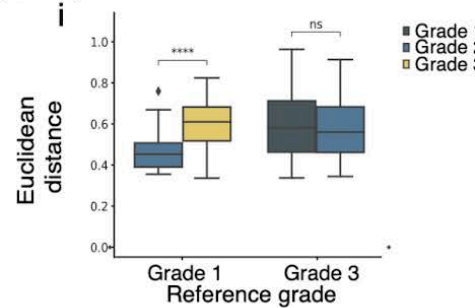
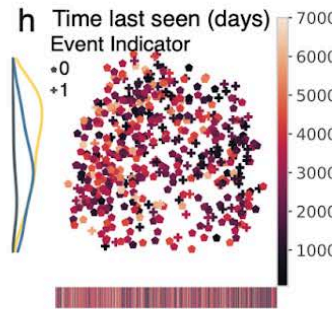
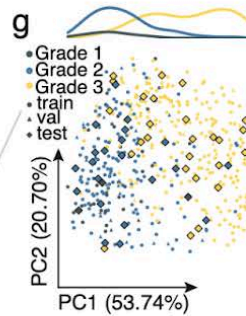
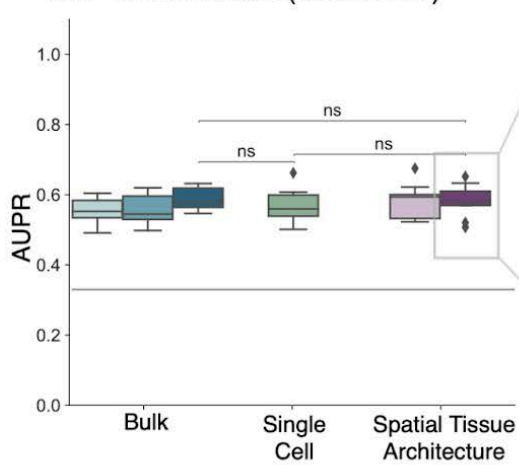


Figure 2: Graph networks capture latent biological signals related to breast cancer grade and patient survival. (a,b,f) Multi-modal ablation study on tumor phenotype classification performance using molecular cell representations. Shown is the area under the precision-recall curve (AUPR) across three-fold nested cross-validation for the best performing hyper-parameter set per test split selected based on the train loss for (a) CODEX - colorectal cancer and the validation loss for (b) IMC - Jackson, and (f) IMC - METABRIC. Bulk represents the pseudobulk expression per sample, Single Cell is the set of molecular expression vectors per tissue image and Spatial Tissue Architecture represents the spatial tissue graph representation. The mean positive class prevalence across the 9 cross validation splits is included as a random predictor (grey line). (c-e) and (g-i) show analyses on the graph embeddings from the GIN models for IMC - Jackson and IMC - METABRIC, respectively. (c, g) PCA of the graph embeddings obtained from a GIN model of training, validation, and test data with class labels superimposed. (d, h) Clinical disease-free survival (DFS) annotations. Gray points indicate graphs without recorded survival annotations. (e, i) The average euclidean distances between graph embedding vectors from different classes.

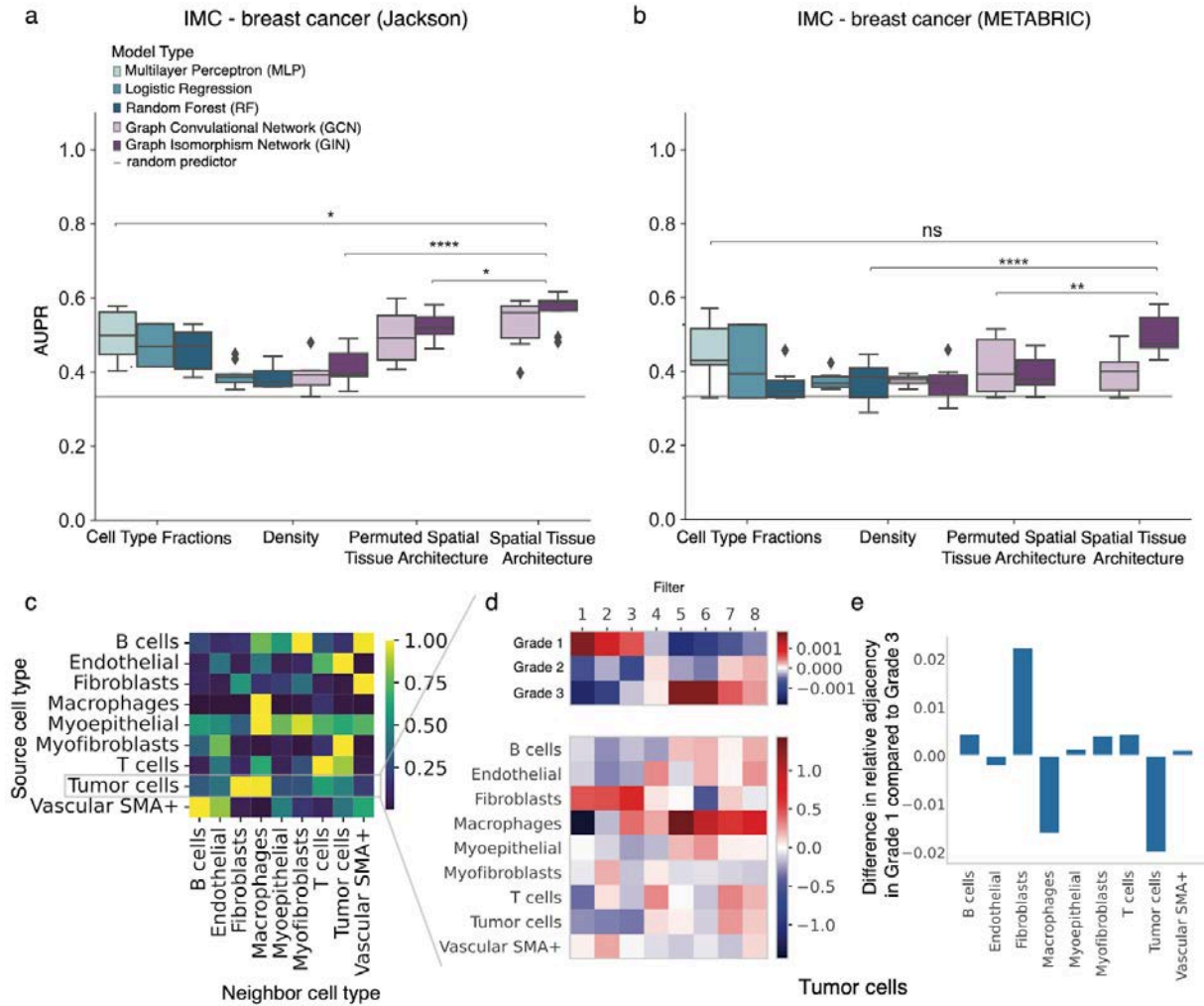


Figure 3: Graph neural networks capture tumor microenvironment features beyond cell type proportions or tissue density. (a, b) Multi-modal ablation study on breast cancer tumor grade classification performance using binary cell types feature space for (a) *IMC - Jackson*, and (b) *IMC - METABRIC*. Shown is the area under the precision-recall curve (AUPR) across three-fold nested cross-validation for the best performing hyper-parameter set per test split selected based on the validation loss. *Cell Type Fractions* represent the ratio between immune vs non-immune cells per sample, *Density* is represented either as the histogram of node degrees within a sample, or it is the full graph structure without node features. *Permuted Tissue Spatial Architecture* refers to a spatial tissue graph representation with cell identities randomly permuted across the graph and *Tissue Spatial Architecture* represents samples via their spatial tissue graphs. The mean positive class prevalence across the 9 cross validation splits is included as a random predictor (grey line). (c-e) Interpretation of the attention mechanism of a GAT model (Methods) trained on the *IMC - METABRIC* dataset with cell type input. (c) Heatmap of the attention weights between different pairs of key and query cell types. (d, e) Neighborhood analysis on tumor cells. (d) Heatmap of the filter weight matrix of the first convolutional node embedding layer weighted by the attention weights for Tumor query cells (bottom) set into global context by the averaged gradients of the different graph labels wrt. the filter activation scores (top). (e) Difference in neighborhood frequency between tumor cells and other cell types in cancer grade 1 versus grade 3, showing the average differences between the neighboring environment of tumor cells during disease progression.

CODEX - colorectal cancer

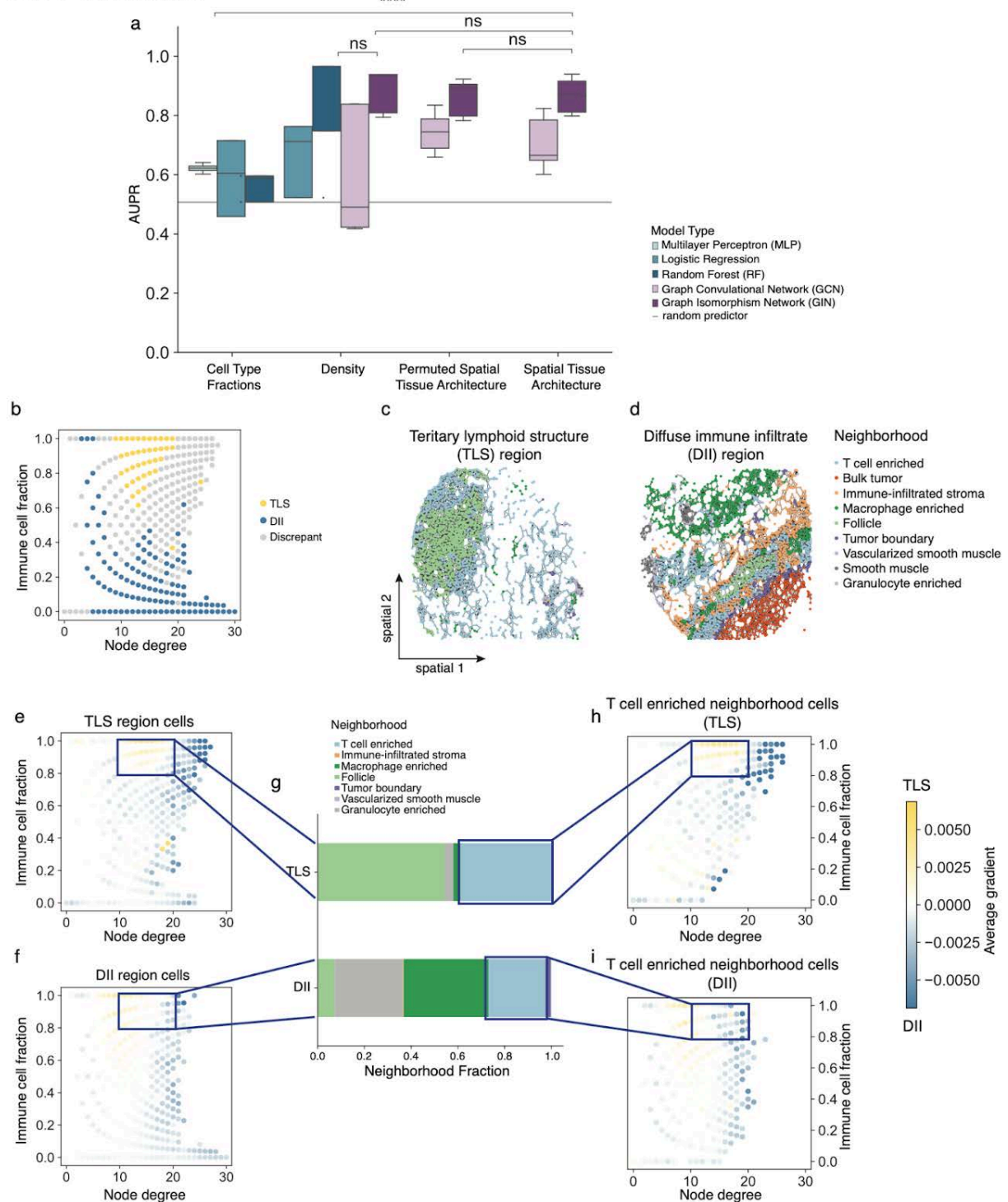


Figure 4: Graph neural networks model complex spatial immune infiltration patterns in colorectal cancer. (a) Multi-modal ablation study on colorectal cancer anatomical phenotype prediction using binary immune vs. non-immune cell feature space. Shown is the area under the precision-recall curve (AUPR) across three-fold nested cross-validation for the best performing hyper-parameter set per test split selected based on the train loss. *Cell Type Fractions* represent the ratio between immune vs non-immune cells per sample, *Density* is represented either as the histogram of node degrees within a sample, or it is the full graph structure without node features. *Permuted Spatial*

Tissue Architecture refers to a spatial tissue graph representation with cell identities randomly permuted across the graph and *Spatial Tissue Architecture* represents samples via their spatial tissue graphs. The mean positive class prevalence across the 9 cross validation splits is included as a random predictor (grey line). **(b)** Cells stratified by node degree and fraction of immune cells in the immediate neighborhood colored by agreement between enrichment of a cell category within one phenotype class and the average model saliency using GIN model. **(c, d)** Spatial plots of the spatial tissue graphs colored by the neighborhood cell annotation from the original publication from samples with different anatomical phenotypes, **(c)** TLS region and **(d)** DII regions. **(e-i)** Cell saliency analysis based on the GIN model. **(e,f)** Average cell saliencies stratified by node degree and fraction of immune cells in the immediate neighborhood for cells from **(e)** TLS samples and **(f)** DII samples. Saliencies are computed as the gradient of the output wrt. the input cell representations (yellow: TLS, blue: DII). **(g)** Neighborhood composition of the cells highlighted in **(e)** and **(f)**. **(h,i)** Same as **(e, f)** of cells annotated as T cell enriched neighborhoods.

Methods

Data

IMC - Jackson (breast cancer)

The breast cancer dataset (Jackson *et al.*¹⁰ with 559 images from 350 patients) was measured with IMC. The dataset consists of samples from three breast cancer grades, grade 1 (114 images), grade 2 (214 images) and grade 3 (231 images). Here, 34 proteins in a panel specific to breast cancer microenvironment were simultaneously measured. We used the segmentation provided by Jackson *et al.*. We used the following channels: 1021522Tm169Di EGFR, 1031747Er167Di ECadhe, 112475Gd156Di Estroge, 117792Dy163Di GATA3, 1261726In113Di Histone, 1441101Er168Di Ki67, 174864Nd148Di SMA, 1921755Sm149Di Vimentin, 198883Yb176Di cleaved, 201487Eu151Di cerbB, 207736Tb159Di p53, 234832Lu175Di panCyto, 3111576Nd143Di Cytoker, Nd145Di Twist, 312878Gd158Di Progest, 322787Nd150Di cMyc, 3281668Nd142Di Fibrone, 346876Sm147Di Keratin, 3521227Gd155Di Slug, 361077Dy164Di CD20, 378871Yb172Di vWF, 473968La139Di Histone, 651779Pr141Di Cytoker, 6967Gd160Di CD44, 71790Dy162Di CD45, 77877Nd146Di CD68, 8001752Sm152Di CD3epsi, 92964Er166Di Carboni, 971099Nd144Di Cytoker, 98922Yb174Di Cytoker, phospho Histone, phospho S6, phospho mTOR, Area. Jackson *et al.* annotated the following cell types: B cells, T and B cells, T cells, macrophages, T cells, macrophages, endothelial, vimentin hi stromal cell, small circular stromal cell, small elongated stromal cell, fibronectin hi stromal cell, large elongated stromal cell, SMA hi vimentin hi stromal cell, hypoxic tumor cell, apoptotic tumor cell, proliferative tumor cell, p53+ EGFR+ tumor cell, basal CK tumor cell, CK7+ CK hi cadherin hi tumor cell, CK7+ CK+ tumor cell, epithelial low tumor cell, CK low HR low tumor cell, CK+ HR hi tumor cell, CK+ HR+ tumor cell, CK+ HR low tumor cell, CK low HR hi p53+ tumor cell and myoepithelial tumor cell. We coarsened the cell types into B cells, T and B cells, T cells, macrophages, T cells, macrophages, endothelial, stromal cells (vimentin hi stromal cell, small circular stromal cell, small elongated stromal cell, fibronectin hi stromal cell, large elongated stromal cell, SMA hi vimentin hi stromal cell) and tumor cells (hypoxic tumor cell, apoptotic tumor cell, proliferative tumor cell, p53+ EGFR+ tumor cell, basal CK tumor cell, CK7+ CK hi cadherin hi tumor cell, CK7+ CK+ tumor cell, epithelial low tumor cell, CK low HR low tumor cell, CK+ HR hi tumor cell, CK+ HR+ tumor cell, CK+ HR low tumor cell, CK low HR hi p53+ tumor cell, myoepithelial tumor cell). We binarized the cell types into immune cells (B cells, T cells, macrophages) and non immune cells (endothelial, vimentin hi stromal cell, small circular stromal cell, small elongated stromal cell, fibronectin hi stromal cell, large elongated stromal cell, SMA hi vimentin hi stromal cell, hypoxic tumor cell, apoptotic tumor cell, proliferative tumor cell, p53+ EGFR+ tumor cell, basal CK tumor cell, CK7+ CK hi cadherin hi tumor cell, CK7+ CK+ tumor cell, epithelial low tumor cell, CK low HR low tumor cell, CK+ HR hi tumor cell, CK+ HR+ tumor cell, CK+ HR low tumor cell, CK low HR hi p53+ tumor cell, myoepithelial tumor cell). We used the disease-free survival annotations censored in the cases where the disease-free survival equaled the overall survival to perform survival analysis.

IMC - METABRIC (breast cancer)

The breast cancer METABRIC cohort (Ali *et al.*¹¹ with 500 images from 467 patients) was collected with IMC. Here, 37 proteins in formalin-fixed, paraffin-embedded breast tumor samples were measured. METABRIC dataset consists of images from three breast cancer grades, grade 1 (50 images), grade 2 (181 images) and grade 3 (269 images). Ali *et al.* segmented the single cells in the images using random forest classifier and then the expression of proteins in single cells was quantified. The mean protein expression of the segmented cells are used as the node features of the spatial graph. We used the following channels: HH3_total, CK19, CK8_18, Twist, CD68, CK14, SMA, Vimentin, c_Myc, HER2, CD3, HH3_ph, Erk1_2, Slug, ER, PR, p53, CD44, EpCAM, CD45, GATA3, CD20, Beta_catenin, CAIX, E_cadherin, Ki67, EGFR, pS6, Sox9, vWF_CD31, pmTOR, CK7, panCK, c_PARP_c_Casp3, DNA1, DNA2, H3K27me3, CK5, Fibronectin. Ali *et al.* annotated the following cell types: B cells, Basal CKlow, Endothelial, Fibroblasts, Fibroblasts CD68+, HER2+, HR+ CK7-, HR+ CK7- Ki67+, HR+ CK7- Slug+, HR- CK7+, HR- CK7-, HR- CKlow CK5+, HR- Ki67+, HRlow CKlow, Hypoxia, Macrophages Vim+ CD45low, Macrophages Vim+ Slug+, Macrophages Vim+ Slug-, Myoepithelial, Myofibroblasts and T cells, Vascular SMA+. We coarsened the cell types into B cells, Endothelial, Fibroblasts (Fibroblasts, Fibroblasts CD68+), Macrophages (Macrophages Vim+ CD45low, Macrophages Vim+ Slug+, Macrophages Vim+ Slug-), Myoepithelial, Myofibroblasts, T cells, Vascular SMA+ and Tumor cells (HER2+, HR+ CK7-, HR+ CK7- Ki67+, HR+ CK7- Slug+, HR- CK7+, HR- CK7-, HR- CKlow CK5+, HR- Ki67+, HRlow CKlow, Hypoxia). We binarized the cells types into immune cells (B cells, Macrophages Vim+ CD45low,

Macrophages Vim+ Slug+, Macrophages Vim+ Slug-": "immune cells, T cells) and non-immune cells (Basal CKlow, Endothelial, Fibroblasts, Fibroblasts CD68+, HER2+, HR+ CK7-, HR+ CK7- Ki67+, HR+ CK7- Slug+, HR- CK7+, HR- CK7-, HR- CKlow CK5+, HR- Ki67+, HRlow CKlow, Hypoxia). We used the disease-specific survival that is the time until the last follow-up or death censored according to the disease specific death indicator to perform survival analysis.

CODEX - colorectal cancer

The colorectal cancer dataset (Schürch *et al.*⁹ with 140 images from 35 patients) was measured with CODEX. The dataset consists of two patient groups, one group with Crohn's-like reaction (CLR) represented in 68 images and one group with diffuse inflammatory infiltration (DII) represented in 72 images. Four regions were sampled from each patient: from patients in the CLR groups, two regions containing a tertiary lymphoid structure (TLS) and two diffuse immune infiltrate regions (DII) were sampled per patient, while from patients in the DII group, four diffuse immune infiltrate regions were sampled per patient. The sample-specific anatomic label (with tertiary lymphoid structure or diffuse immune infiltrate, Figure 2) Patients from the CLR group have higher overall survival than patients classified as DII. Here, 57 proteins specific to the tumor microenvironment were measured. We used the segmentation previously performed by Schürch *et al.*. The molecular abundance per cell segment and the coordinates of the center of each cell were used to construct the spatial graph. We used the following channels: CD44, FOXP3, CD8A, TP53, GATA3, PTPRC, TBX21, CTNNB1, HLA-DR, CD274, MKI67, PTPRC, CD4, CR2, MUC1, TNFRSF8, CD2, VIM, MS4A1, LAG3, ATP1A1, CD5, IDO1, KRT1, ITGAM, NCAM1, ACTA1, BCL2, IL2RA, ITGAX, PDCD1, GZMB, EGFR, VISTA, FUT4, ICOS, SYP, GFAP, CD7, CD247, CHGA, CD163, PTPRC, CD68, PECAM1, PDPN, CD34, CD38, SDC1, HOECHST1:Cyc_1_ch_1, CDX2, COL6A1, CCR4, MMP9, TFRC, B3GAT1, MMP12. Schürch *et al.* annotated the following cell types: B cells, CD11b+ monocytes, CD11b+CD68+ macrophages, CD11c+ DCs, CD163+ macrophages, CD3+ T cells, CD4+ T cells, CD4+ T cells CD45RO+, CD4+ T cells GATA3+, CD68+ macrophages, CD68+ macrophages GzmB+, CD68+CD163+ macrophages, CD8+ T cells, NK cells, Tregs, adipocytes, dirt, granulocytes, immune cells, immune cells / vasculature, lymphatics, nerves, plasma cells, smooth muscle, stroma, tumor cells, tumor cells / immune cells and undefined, vasculature. We binarized the cell types into immune cells (B cells, CD11b+ monocytes, CD11b+CD68+ macrophages, CD11c+ DCs, CD163+ macrophages, CD3+ T cells, CD4+ T cells, CD4+ T cells CD45RO+, CD4+ T cells GATA3+, CD68+ macrophages, CD68+ macrophages GzmB+, CD68+CD163+ macrophages, CD8+ T cells, NK cells, Tregs, granulocytes, immune cells, immune cells / vasculature, lymphatics and tumor cells / immune cells) and non-immune cells (adipocytes, dirt, nerves, plasma cells, smooth muscle, stroma, tumor cells, undefined and vasculature).

Spatial proximity graphs

We considered spatial neighborhood graphs built with fixed kernel radii across all images. In all datasets considered here, pixel dimensions are fixed across images so that radii defined in pixels correspond to consistent spatial distances across images. We defined a raw adjacency matrix A for each image with entries a_{ij} based on a radius r of a kernel between the position of two cells i, j in 2D space z_i, z_j :

$$a_{ij} = 1 \text{ if } \|z_i - z_j\|_2 < r \text{ else } 0.$$

Spectral clustering

We applied spectral clustering to the spatial graphs by first constructing a k -nearest neighbor (kNN) graph using the spatial coordinates $\{z_i\}_{i=1}^n$ of the cells, with $k = 10$. The kNN graph is undirected, where an edge exists between two nodes i and j if either i is among the k nearest neighbors of j or vice versa.

Label preparation for the self-supervision task

For each spectral cluster C_i , we define the local self-supervision label $y_i \in \mathbb{R}^d$, where d is the number of cell types, as the normalized cell type frequency vector computed over all cells in the neighboring clusters $\mathcal{N}(C_i)$, where the neighborhood is defined using cluster connectivity in the original kNN graph.

| dataset | learning rate | l2 | radius | number of clusters |
|--------------------------------|--------------------|-----------------|---------------|--------------------|
| IMC - breast cancer (Jackson) | {5e-2, 5e-3, 5e-4} | {0, 1e-6, 1e-3} | {10, 20, 50} | {5, 10, 20} |
| IMC - breast cancer (METABRIC) | {5e-2, 5e-3, 5e-4} | {0, 1e-6, 1e-3} | {10, 20, 55} | {5, 10} |
| CODEX - colorectal cancer | {5e-2, 5e-3, 5e-4} | {0, 1e-6, 1e-3} | {25, 50, 120} | {5, 10} |

Table 1: Hyperparameters related to training and data processing screened in grid search for each dataset.

| dataset | depth feature embedding | width feature embedding | depth node embedding | width node embedding | depth graph embedding | width graph embedding |
|--------------------------------|-------------------------|-------------------------|----------------------|----------------------|-----------------------|-----------------------|
| IMC - breast cancer (Jackson) | {1, 2, 3} | {4, 8, 16, 32, 64} | {1, 2, 3} | {4, 8, 16, 32, 64} | {1, 2, 3} | {16, 64} |
| IMC - breast cancer (METABRIC) | {1, 2, 3} | {4, 8, 16, 32, 64} | {1, 2, 3} | {4, 8, 16, 32, 64} | {1, 2, 3} | {16, 64} |
| CODEX - colorectal cancer | {1, 2, 3} | {4, 8, 16, 32, 64} | {1, 2, 3} | {4, 8, 16, 32, 64} | {1, 2, 3} | {16, 64} |

Table 2: Hyperparameters related to model topology for models with molecular features as input screened in grid search for each data set. *node embedding*: The node embedding describes transformations of node-wise feature vectors and is used in MI and GCN/GIN models. All layers have the same width. *graph embedding*: The graph embedding describes the layer stack that transforms the graph representation to a graph label prediction. The input representation derives from an aggregation over nodes for MI and GCN/GIN models and is the input feature vector for MLP models. All layers have the same width.

Hold-out definitions

We implemented a nested cross validation. For each study, the datasets were split into training (80%), validation (10%) and test (10%) datasets, except for CODEX - colorectal cancer study which was split into only training and test datasets due to the limited number of samples. The split was performed on the patients domain, ensuring that images from the same patients are grouped together in the split. In the nested cross validation, we used 3 random tests and 3 validation splits. The same splits were used for all the models to ensure fair comparison. We used early stopping on the validation loss for the two breast cancer datasets and fixed number of epochs for colorectal cancer dataset. The best models were selected based on their performance in terms of the lowest validation loss (or training loss in case of CODEX - colorectal cancer). To evaluate the models, we compared based on Area Under Precision-Recall curve (AUPR) (section Evaluation metrics). This metric provides an overall assessment of the models' ability to distinguish between the tissue phenotype and capture the balance between precision and recall. To determine the optimal hyperparameters, we employed a grid search strategy where different combinations of hyperparameters were explored as shown in Tables 1 and 2.

Evaluation

Evaluation metrics: We used the area under the precision-recall curve (AUPR): as a metric for classification performance across all classes considered.

$$AUPR = \sum_i (R_i - R_{i-1}) P_i$$

where R_i and P_i are recall and precision respectively for threshold i . The score for multi-class is calculated using macro average.

Evaluation comparison: We used a two-sided t-test to assess the statistical significance of performance differences between independent scenarios. For each scenario, we identified the best-performing model class by comparing the mean AUPR across repeated runs. p-values below 0.05 were considered statistically significant.

Models

All neural network models used in this study are feed-forward architectures designed to perform graph-level classification. The models take graph-structured inputs or reduced representations thereof and predict phenotype-level outcomes. Depending on the experiment, models were trained using either a cell type feature space (one-hot-encoded categorical input) or a molecular feature space (continuous gene expression values).

In molecular feature space models, we first embed the input node features into a lower-dimensional latent space using a fully connected multilayer perceptron (MLP) with non-linear activation, $h_i = MLP(x_i)$ where x_i are the raw features of node i , and h_i is the resulting node embedding.

For graph models, node embeddings are passed through graph neural network (GNN) layers, including GCN, GIN, or Graph Attention Networks, to propagate information through the graph structure. The final graph representation is obtained by pooling node embeddings via mean; in our experiments, we used mean pooling.

Each model is trained for graph-level supervision (e.g., tumor class prediction) using the appropriate loss function depending on the task type: categorical cross-entropy (CCE) for classification, mean squared error (MSE) for regression, binary cross-entropy with logits (BCE) for proportion outputs, and a custom right-censored MSE loss for survival prediction.

All models share a consistent data structure and training pipeline to ensure comparability. Node and graph features are accessed as standardized batch tensors, and predictions are generated through the shared forward API. Optimization is performed using the Adam optimizer with learning rate scheduling.

In addition, we implemented random forest and logistic regression baselines using scikit-learn, trained on the same aggregated graph-level feature representations used by the MLP models.

Bulk models

Pseudobulk multi-layer perceptron networks (MLP): We implemented a pseudobulk reference model by aggregating cell-wise feature vectors into a single vector per image. For models using the molecular feature space, we computed the mean of each feature across all cells in the image. In the case of models using the cell type feature space, we computed a compositional representation by normalizing the distribution of one-hot encoded cell types across the image, resulting in a frequency-based encoding per cell type. The aggregated input vector passed through a fully connected neural network as described in Table 2 (graph embedding) to obtain the graph-level prediction $y = f(x)$.

Pseudobulk random forest (RF) and logistic regression models: Using the same aggregated input representations described above, we trained scikit-learn random forest and logistic regression classifiers for graph-level prediction. Model performance was monitored using log-loss on a validation set.

Single-cell models

Multi-instance networks (MI): For the multi-instance reference model, each node's features $x_i \in \mathbb{R}^d$ were independently transformed using a stack of fully connected layers with non-linear activation functions. At each layer l , the transformation is given by, $h_i^{(l+1)} = \phi(h_i^{(l)} W^{(l)} + b^{(l)})$, where ϕ is a non-linear activation, $W^{(l)} \in \mathbb{R}^{d \times d_{l+1}}$ is a learnable weight matrix, and $b^{(l)}$ is a bias term. After the final layer, the node embeddings $h_i^{(L)}$ are aggregated using a pooling operation (mean, max, or sum) to form a graph-level representation, $z = \text{Pool}(\{h_i^{(L)}\}_{i=1}^N)$. This graph embedding z was then passed through a multilayer perceptron to generate the graph-level prediction $y = f(z)$, as detailed in Table 2.

Correlation Network: We constructed a correlation network by generating k-nearest neighbor (KNN) graphs based on gene expression similarities instead of spatial proximity. We applied a log transformation to the expression matrix and used Scanpy's `sc.pp.neighbors` to compute the correlation-based adjacency matrix.

Spatially-aware models

Node degree models (Density): To explore the impact of spatial information on the tissue-level phenotype classification, we implemented two models: a random forest and logistic regression. To generate the node degree distributions, we computed the histogram of node degrees from 0 to 14, with an additional bin for nodes with a node degree exceeding 14. The resulting histogram was normalized to obtain the proportion of nodes within each bin. These normalized node degree distributions were then used as input features for the random forest and logistic regression models. By incorporating the full distribution of node degrees per graph, we aim to capture the spatial information within each graph which play a significant role in the graph structure and should be able to provide insights about the tissue-level phenotypes.

Graph models

Graph convolutional networks (GCN): The node embedding layers for the Graph Convolutional Network are defined as: $H^{(l+1)} = \phi(A^* H^{(l)} W^{(l)})$, where ϕ is a Leaky ReLU activation function with negative slope factor 0.1, $H^{(l)} \in \mathbb{R}^{n \times d}$ is the input node feature matrix of dimensions (number of nodes x input features), $W^{(l)} \in \mathbb{R}^{d \times d'}$ is a learnable weight

matrix is a weight matrix of dimensions (input features x output features) and A^* is the symmetrically normalized adjacency matrix: $A^* = D^{-\frac{1}{2}} A D^{-\frac{1}{2}}$ where A is the raw adjacency matrix and D is the degree matrix of A . The resulting node embeddings were aggregated using a pooling layer and passed through a multilayer perceptron (MLP) to obtain graph-level predictions. We additionally implemented a GCN variant with sum aggregation (GCN_SUM) to assess its performance relative to other graph models (Supp. Fig. 5d).

Graph isomorphism networks (GIN): We used GIN as a graph neural network model for tissue-level classification, designed to capture global graph structures through aggregation-invariant operations and non-linear transformations. The node embedding layers for the GIN models at layer l are defined as:

$$h_i^{(l)} = \text{MLP}((1 - \epsilon) h_i^{(l-1)} + \sum_{j \in \mathcal{N}(i)} h_j^{(l-1)})$$

where $h_i^{(l-1)}$ denotes the node feature embeddings vector node i at layer $l - 1$, $\mathcal{N}(i)$ denotes the set of neighbors of nodes and ϵ is a learnable scalar (fixed to 0 in our implementation). To form the graph-level representation, node embeddings from all GIN layers are concatenated, $h_i = \text{CONCAT}(h_i^{(0)}, h_i^{(1)}, \dots, h_i^{(L)})$, where L is the number of GIN layers. These concatenated node embeddings are then aggregated across all nodes using mean pooling $h = \frac{1}{N} \sum_{i=1}^N h_i$. The graph-level representation h then passed through a fully connected network to learn the tissue-level phenotype classification $y = f(h)$, where y is the classification output.

Graph convolutional networks with self-supervision (GNN-SS): We introduced an auxiliary self-supervision task to the graph neural networks. For each pre-computed spectral cluster in the graph, the model predicts the cell type composition of all neighboring clusters combined. After the graph embedding layers, node embeddings within each cluster are pooled and passed through a one-layer neural network to produce the predicted composition. A mean squared error (MSE) loss is computed between the predicted and true composition vectors and added to the main graph-level loss during training.

GNN-Permuted: We used the described Graph Neural Networks (GNN) but trained them with randomly permuted node features, preserving the adjacency matrix to maintain the graph structure.

Graph attention networks (GAT): We implemented Graph attention networks with dot-product attention to allow for actual incorporation of both partners in the attention value computation. Instead of computing scalar scores for all nodes and taking pairwise sums to weight the information transfer between two nodes, here, the attention score is computed as

$$\alpha_{ij} = \text{softmax}_j(x_i^T W_Q W_K^T x_j),$$

with W_Q and W_K being weight matrices corresponding to linear embeddings for the query and key nodes, respectively, and softmax being computed over all neighbors of a query node after subtracting the maximum value. We used 4 dimensional key and query embeddings for the dot product computation. The message passing step is then performed as

$$x_i^k = \sigma(W_V^T (\sum_{j \in \mathcal{N}_i} \alpha_{ij} x_j)),$$

with a node feature embedding matrix W_V and σ as a Leaky ReLU activation function with negative slope factor 0.1. Node embeddings were then aggregated using a mean pooling layer followed by a simple MLP for final graph-level predictions.

Other baselines

Random predictor: showing the expected value of the random predictor, which is the mean positive class prevalence plotted per class across the cross validation folds.

Downstream analyses and model interpretations

Tissue graph embeddings

For the sample representation analyses, we computed the graph embeddings for the whole dataset as obtained as activations after the global node pooling step within the respective GNN. These latent graph representations were then quantile normalized to follow feature-wise uniform distributions as implemented in `sklearn.preprocessing.quantile_transform`, followed by a PCA transformation.

Survival analysis

To assess the signal of the disease-free survival covariate in the graph embedding space, we used the loadings of the first principal component as predictor and quantified the performance using the concordance index for right-censored data. This concordance index computes the fraction of comparable data pairs, that is pairs where at least the earlier event occurred, that were predicted in the correct order.

Graph attention network interpretation

We visualized the learned attention weights between nodes of different cell types in the case of one-hot encoded cell type identities as node input features as follows: First, we computed $\tilde{\alpha}_{ij} = x_i^T W_Q W_K^T x_j$ for all combinations of cell types, then subtracted the maximum value per key cell type, and exponentiated these values to mimic the softmax transformation. For visualization purposes, these values were additionally divided by the maximum value per key cell type. Secondly, inspired by interpretation methods from image recognition, we looked into the learned filter weights of the first convolutional node embedding layer. We retrieved the node embedding weight matrix W_V and scaled it according to the transformed attention scores corresponding to the key cell type of interest. To set the individual filters into context, we computed the average gradients of the model outputs with respect to the activations of the individual filters. We computed the frequencies of the different cell types as neighbors of a cell type of interest per image and averaged those values over the images per cancer grade to validate findings from interpreting the filter weights. Plotted in Fig. 3e and Supp. Fig. 4b are the differences of these averaged frequencies between grade 1 and grade 3.

Cell saliency analysis

To determine how much individual cells influence the GNNs predictions, we calculated gradients of the model outputs with respect to the cell type indicators of the input nodes. We deemed cells with positive gradients corresponding to a specific tissue phenotype class as indicative for that phenotype.

Code and data availability

We used published datasets provided in the original studies. We summarized all models, training and interpretation mechanisms discussed here in a python package centered around graph-level supervision on spatial single-cell graphs, <https://github.com/theislabs/tissue>.

Author contributions

M.A., D.S.F., S.R. and F.J.T. conceived the study. M.A., S.R. and D.S.F. implemented the overall software and performed the analyses. M.A., D.S.F., S.R., A.E. and F.J.T. wrote the manuscript.

Acknowledgements

We would like to thank Jana R. Fischer, Jonas Windhager, and Prof. Dr. Bernd Bodenmiller for assistance with the discussed breast cancer datasets and for discussion on the topic of graph convolutional networks and cancer grade prediction. We would like to thank Eeshit Dhaval Vaishnav Prof. Dr. Aviv Regev for discussion on spatial molecular profiling data. We would like to thank Anna Schaar for discussions about the model and the code base and Louis B. Kümmerle for feedback to the manuscript.

This work was supported by the German Federal Ministry of Education and Research (BMBF) under Grant No. 01IS18036B and No. 01IS18053A, by the Wellcome Trust Grant 108413/A/15/D and by the Helmholtz Association's Initiative and Networking Fund through Helmholtz AI [grant number: ZT-I-PF-5-01]. D.S.F. acknowledges support from a German Research Foundation (DFG) fellowship through the Graduate School of Quantitative Biosciences Munich (QBM) [GSC 1006 to D.S.F.] and by the Joachim Herz Foundation. This work was supported in part by funding from the Eric and Wendy Schmidt Center at the Broad Institute of MIT and Harvard. S. R. is supported by the Helmholtz Association under the joint research school "Munich School for Data Science" — MUDS.

Conflicts of interest

F.J.T. consults for Immunai Inc., Singularity Bio B.V., CytoReason Ltd, and Omniscope Ltd, and has ownership interest in Dermagnostix GmbH and Cellarity.

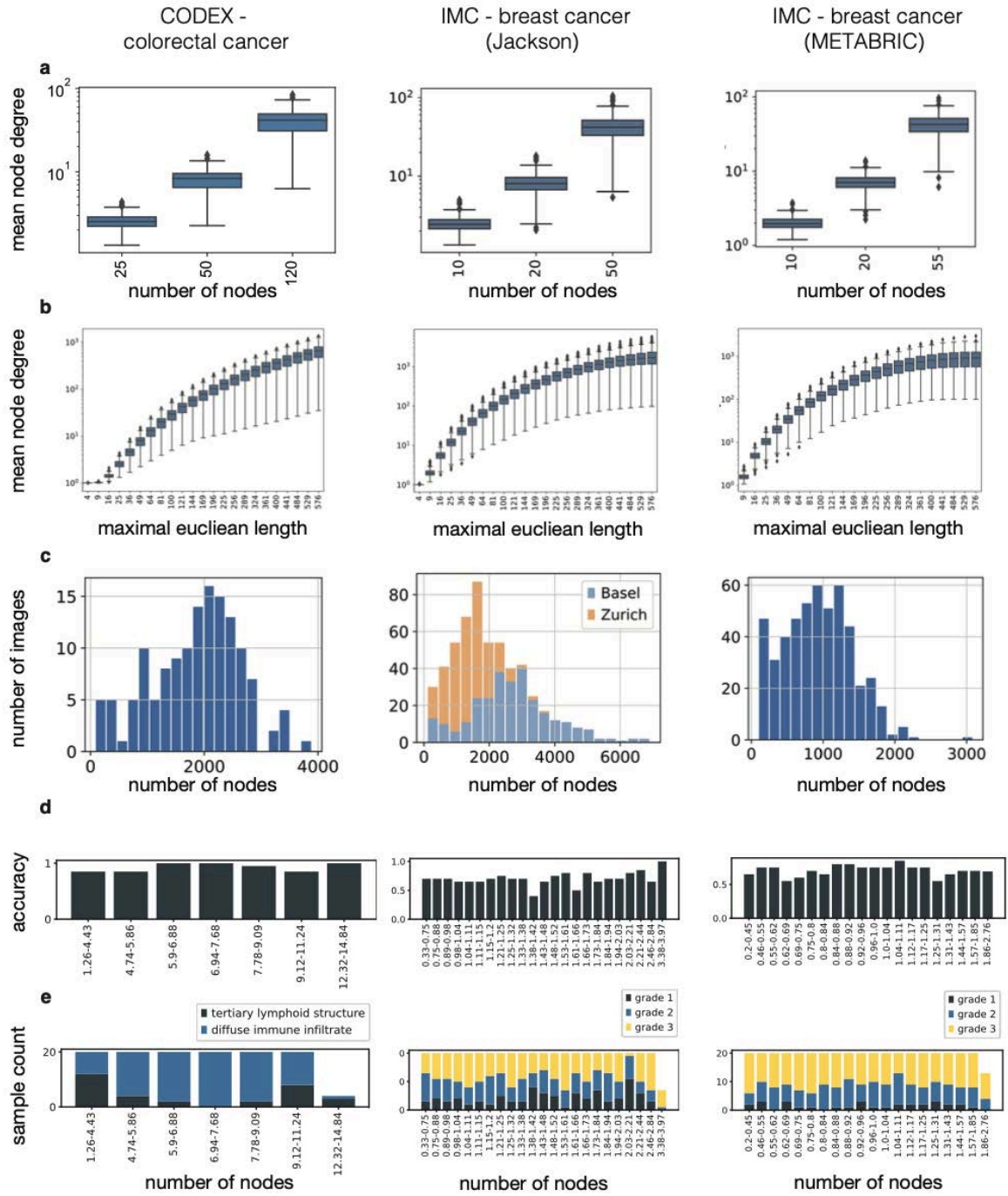
1. Wagner, A., Regev, A. & Yosef, N. Revealing the vectors of cellular identity with single-cell genomics. *Nat. Biotechnol.* **34**, 1145–1160 (2016).
2. Palla, G., Fischer, D. S., Regev, A. & Theis, F. J. Spatial components of molecular tissue biology. *Nat. Biotechnol.* (2022) doi:10.1038/s41587-021-01182-1.
3. Fischer, D. S., Schaar, A. C. & Theis, F. J. Modeling intercellular communication in tissues using spatial graphs of cells. *Nat. Biotechnol.* 1–5 (2022).
4. Hetzel, L., Fischer, D. S., Günnemann, S. & Theis, F. J. Graph Representation Learning for Single Cell Biology. *Current Opinion in Systems Biology* (2021) doi:10.1016/j.coisb.2021.05.008.
5. Wu, Z. et al. Graph deep learning for the characterization of tumour microenvironments from spatial protein profiles in tissue specimens. *Nat Biomed Eng* (2022) doi:10.1038/s41551-022-00951-w.
6. Hu, Y., Rong, J., Xu, Y., Xie, R., Peng, J., Gao, L., & Tan, K. (2024). Unsupervised and supervised discovery of tissue cellular neighborhoods from cell phenotypes. *Nature Methods*, 21(2), 267-278.
7. Wang, Y. et al. Cell graph neural networks enable the precise prediction of patient survival in gastric cancer. *NPJ Precis Oncol* **6**, 45 (2022).
9. Schürch, C. M. et al. Coordinated Cellular Neighborhoods Orchestrate Antitumoral Immunity at the Colorectal Cancer Invasive Front. *Cell* **182**, 1341–1359.e19 (2020).
10. Jackson, H. W. et al. The single-cell pathology landscape of breast cancer. *Nature* **578**, 615–620

(2020).

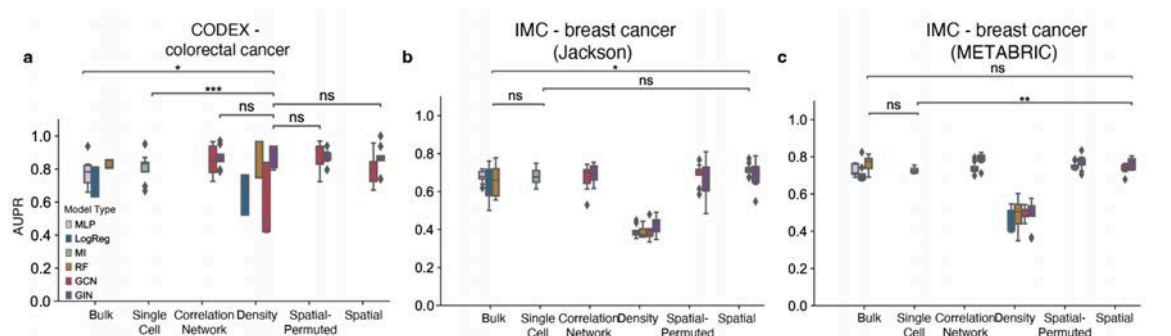
11. Ali, H. R. *et al.* Imaging mass cytometry and multiplatform genomics define the phenogenomic landscape of breast cancer. *Nat Cancer* **1**, 163–175 (2020).
13. Veličković, P. *et al.* Graph Attention Networks. *arXiv [stat.ML]* (2017).
14. Biancalani, T. *et al.* Deep learning and alignment of spatially resolved single-cell transcriptomes with Tangram. *Nat. Methods* **18**, 1352–1362 (2021).
15. Luecken, M. D. *et al.* Benchmarking atlas-level data integration in single-cell genomics. *Nat. Methods* **19**, 41–50 (2022).
16. Bhatia, H. S. *et al.* Spatial proteomics in three-dimensional intact specimens. *Cell* **185**, 5040–5058.e19 (2022).
18. Schaar, A. C., Tejada-Lapuerta, A., Palla, G., Gutgesell, R., Halle, L., Minaeva, M., ... & Theis, F. J. (2024). Nicheformer: a foundation model for single-cell and spatial omics. *bioRxiv*, 2024-04.
19. Giesen, C., Wang, H. A., Schapiro, D., Zivanovic, N., Jacobs, A., Hattendorf, B., ... & Bodenmiller, B. (2014). Highly multiplexed imaging of tumor tissues with subcellular resolution by mass cytometry. *Nature methods*, *11*(4), 417-422.
20. Goltsev, Y., Samusik, N., Kennedy-Darling, J., Bhate, S., Hale, M., Vazquez, G., ... & Nolan, G. P. (2018). Deep profiling of mouse splenic architecture with CODEX multiplexed imaging. *Cell*, *174*(4), 968-981.
21. Keren, L., Bosse, M., Marquez, D., Angoshtari, R., Jain, S., Varma, S., ... & Angelo, M. (2018). A structured tumor-immune microenvironment in triple negative breast cancer revealed by multiplexed ion beam imaging. *Cell*, *174*(6), 1373-1387.
22. Phillips, D., Matusiak, M., Gutierrez, B. R., Bhate, S. S., Barlow, G. L., Jiang, S., ... & Nolan, G. P. (2021). Immune cell topography predicts response to PD-1 blockade in cutaneous T cell lymphoma. *Nature communications*, *12*(1), 6726.
23. Li, M., Wang, L., Cong, L., Wong, C. C., Zhang, X., Chen, H., ... & Yu, J. (2024). Spatial proteomics of immune microenvironment in nonalcoholic steatohepatitis-associated hepatocellular carcinoma.

Hepatology, 79(3), 560-574.

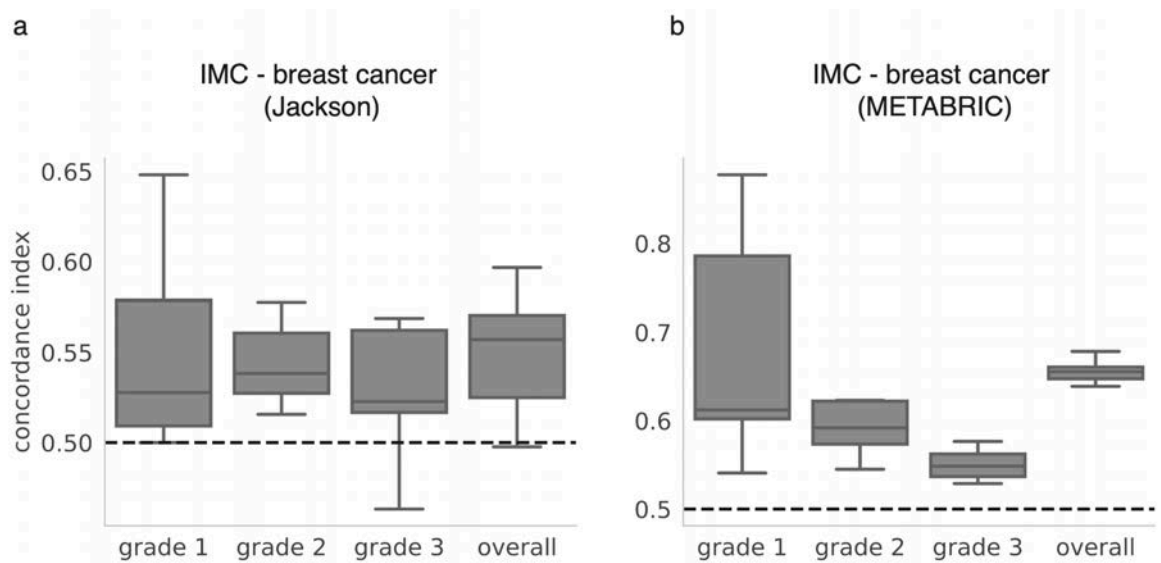
24. Chevrier, S., Levine, J. H., Zanotelli, V. R. T., Silina, K., Schulz, D., Bacac, M., ... & Bodenmiller, B. (2017). An immune atlas of clear cell renal cell carcinoma. *Cell*, 169(4), 736-749.
25. Haviv, D., Remšík, J., Gatie, M., Snopkowski, C., Takizawa, M., Pereira, N., ... & Pe'er, D. (2024). The covariance environment defines cellular niches for spatial inference. *Nature Biotechnology*, 1-12.



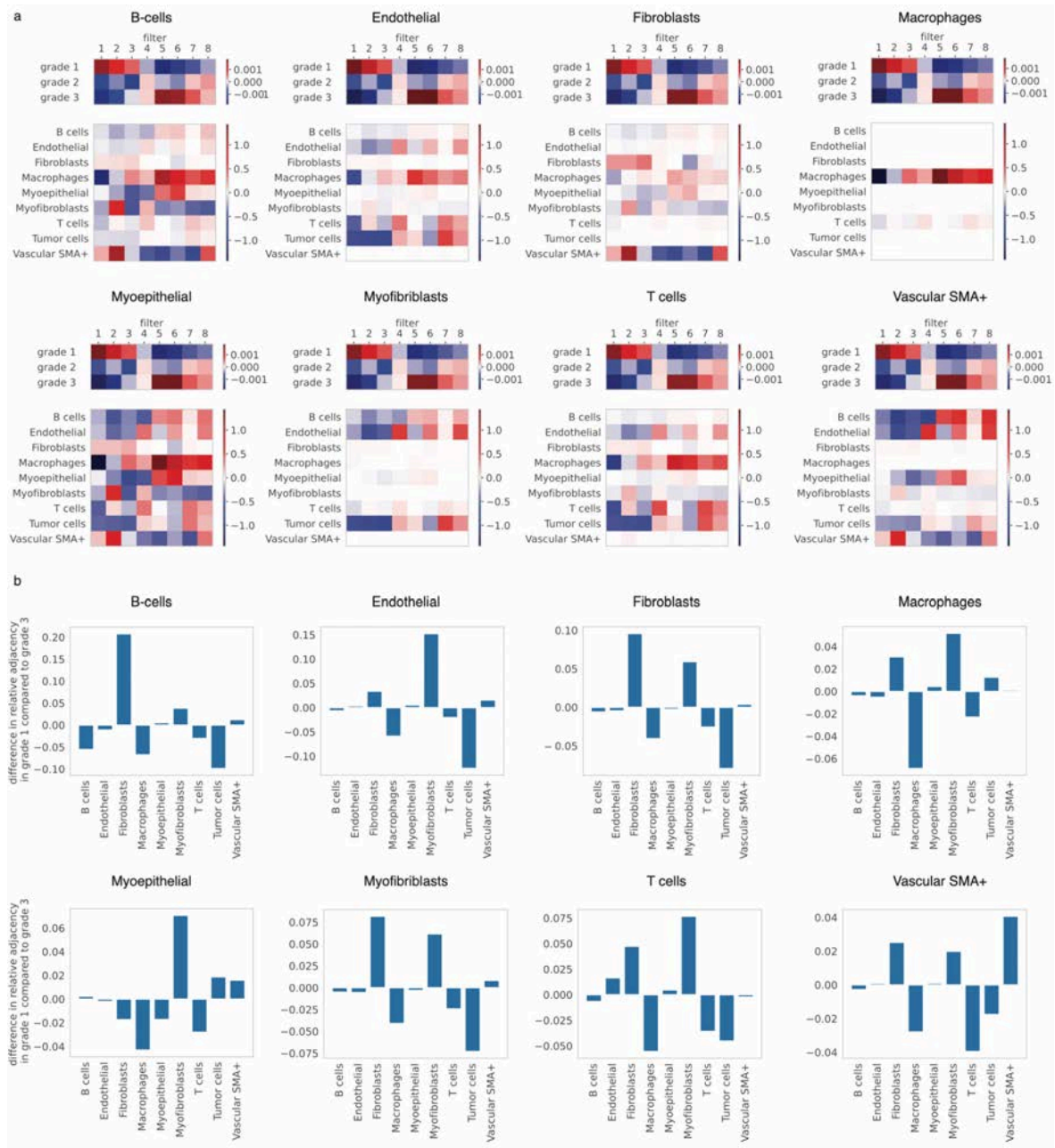
Supp. Figure 1: Graph summary statistics of analyzed data. Mean node-degree per image by radius length used in benchmarks (a) and in a scan across (b), number of nodes per image (c), binned accuracy by number of nodes in graph (d) and label distribution over graph size bins (e) for CODEX - colorectal cancer (left), IMC - breast cancer (Jackson) (middle) and IMC - breast cancer (METABRIC) (right) datasets.



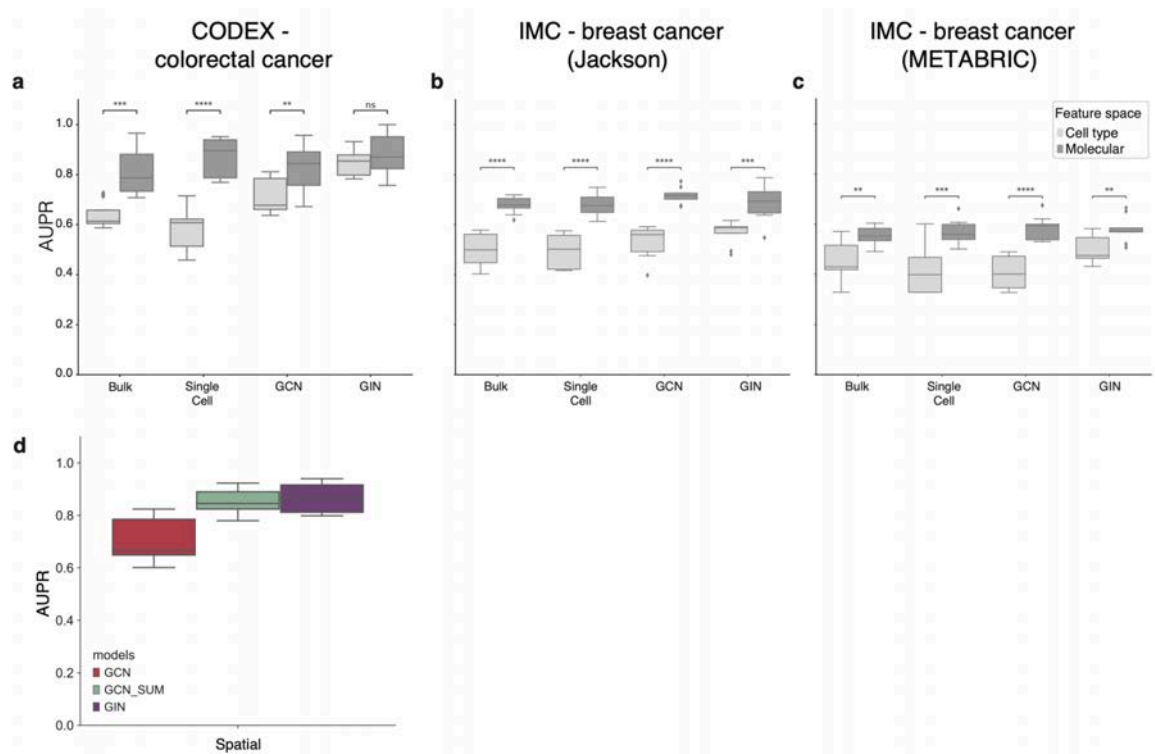
Supp. Figure 2: Baseline models for graph neural networks on molecular feature space. (a-c) Three separate applications of graph neural networks to predict tumor phenotypes on the IMC - breast cancer (Jackson), IMC - breast cancer (METABRIC) and anatomical label on the CODEX - colorectal cancer datasets. The neural networks are a multi-layer perceptron in Bulk, a multi-instance (MI) in Single Cell, and a GCN and GIN in the Graph scenario GNN. Baseline models are random forests (RF) and regression models (Logistic regression) trained on the mean feature value across the graph (Bulk), the node degree distribution per graph (Density), or the correlation network of k-nearest neighbor (KNN) graphs based on gene expression similarities (Methods).



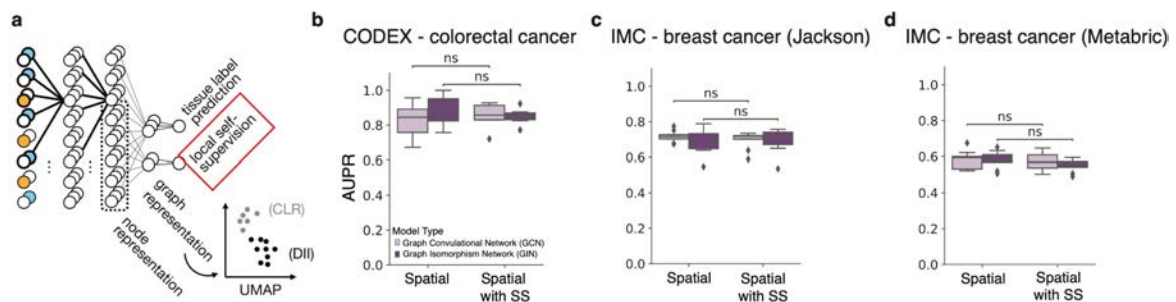
Supp. Figure 3: Patient survival analysis based on graph embeddings. Boxplots showing the censored concordance index values computed based on the first principal component of the graph embeddings for all 9 cross-validation splits, for breast cancer datasets, (a) IMC - Jackson and (b) IMC - METABRIC.



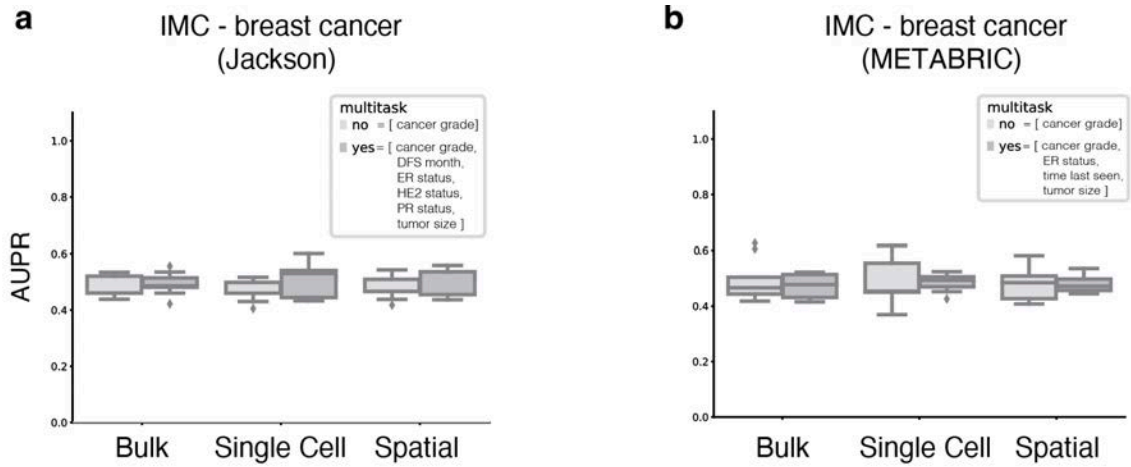
Supp. Figure 4: Attention filters from graph attention (GAT) model. The analyses presented concern the IMC - breast cancer (METABRIC) dataset. **(a)** Attention filters from the GAT model for the eight different cell types across the cancer grades. **(b)** Bar plots of the differences in relative adjacency for the different cell type neighbors in grade 1 compared to grade 3.



Supp. Figure 5: Training of models that predict anatomical labels and cancer grade based on cell type and molecular feature space. (a-c) Comparison between the performance of the molecular and binary cell types features for the different datasets: (a) CODEX - colorectal cancer, (b) IMC - breast cancer (Jackson), and (c) IMC - breast cancer (METABRIC). (d) Comparison of different aggregation functions for graph models on colorectal cancer dataset. GCN with default aggregation function (GCN), GCN with sum aggregation function (GCN_SUM) and GIN with default aggregation function (GIN).



Supp. Figure 6: Graph models with self-supervision. (a) The spatial context of each cell can be formally represented by a graph in which edges are weighted based on the distance between nodes. Each sample can be represented as one such graph, where nodes are colored by the measured cell features. We perform prediction with a model that consists of graph neural network layers to produce node embeddings, followed by pooling over nodes and a final classification network. In addition, the node embeddings of connected components of nodes on the spatial proximity graph can be aggregated for local self-supervision tasks, such as reconstruction of adjacent clusters' cell type composition. *dotted line*: connected component of nodes on spatial proximity graph. (b-d) Comparison of performance of graph models with and without self-supervision task on the different datasets: (b) CODEX - colorectal cancer, (c) IMC - breast cancer (Jackson), and (d) IMC - breast cancer (METABRIC) trained on molecular features using different measures (N=9 nested cross validations per method and dataset).



Supp. Figure 7: Multitask learning models. On breast cancer datasets, **(a, b)** shown is the accuracy on test set based on number of tasks (upper panel) and epoch-wise training of multi-tasking models (lower panel) on **(a)** IMC - breast cancer (Jackson) dataset, and **(b)** IMC - breast cancer (METABRIC). *target* with only the cancer grade and *multitask* with cancer grade, disease-free survival (DFS) month, estrogen receptor (ER) status HER2 status, progesterone receptor (PR) status and tumor size.

4.3 Study 3: Distinct molecular profiles of skull bone marrow in health and neurological disorders.

The paper “Distinct molecular profiles of skull bone marrow in health and neurological disorders.” was published in 2023 in the journal *Cell* as a resource article. The full citation is:

Zeynep Ilgin Kolabas*, Louis B. Kuemmerle*, Robert Perneczky*, Benjamin Förster*, Selin Ulukaya, **Mayar Ali**, ..., Fabian J. Theis, Ali Ertürk, “Distinct molecular profiles of skull bone marrow in health and neurological disorders.” 2023, *Cell* 186.17 (2023): 3706-3725. <https://doi.org/10.1016/j.cell.2023.07.009>

Summary:

In this study, we investigated the molecular profile of the skull and its connection to the meninges. In addition, we studied the response of the skull to neurodegenerative disorders. We have combined various technologies: single-cell RNA-seq, mass spectrometry-based proteomics, tissue clearing, light sheet fluorescence microscopy, confocal microscopy, 2-photon microscopy, scanning electron microscope, and translocator protein positron emission tomography (TSPO-PET), to have a comprehensive study of the skull bone marrow in different pathological conditions and comparison to the different bone marrow in mouse and human.

My collaborators generated a vast amount of molecular and imaging data for this study. For molecular data, they generated single-cell RNA-seq and mass spectrometry-based proteomics data from five bones in addition to the skull, meninges and brain in mice with three different conditions, naïve, sham-operated, and stroke. In addition, they generated single-cell RNA-seq data from one human skull and mass spectrometry-based proteomics data from the skull, vertebrae, and pelvis from twenty samples. For the imaging data, they imaged mouse skulls at different time points before and after stroke (up to 72 hours after stroke) using 2-photon microscopy. Moreover, they were able to detect more than 500 skull-meninges connections (SMCs) in different locations in the human skull using various microscopy.

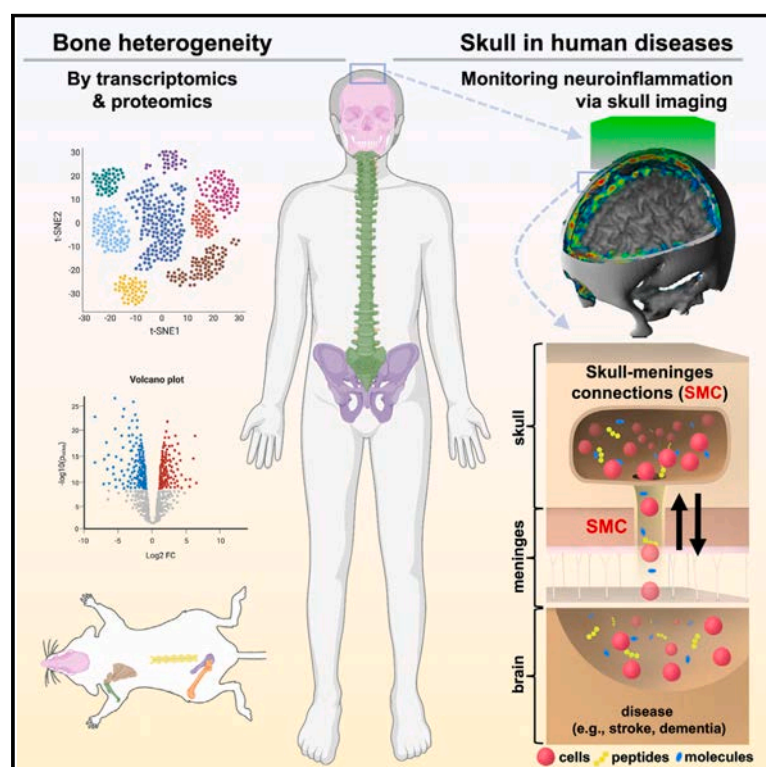
My collaborators analysed the single-cell RNA-seq data, while I developed the software and analysed the proteomics data from the various bones (5 bones, skull, meninges, and brain) in different conditions (naïve, sham-operated, and stroke) in mice, as well as human proteome data from the three bones (skull, vertebrae, and pelvis), highlighting the distinct molecular profiles of the skull to the other bones.

Finally, by analysing TSPO-PET images of human skulls from patients with various neurological disorders, we reported spatial and temporal inflammatory responses that highlight brain inflammation.

This study may be viewed as a resource, with a large collection of data, for further studies investigating the role of the skull in neurological conditions.

Distinct molecular profiles of skull bone marrow in health and neurological disorders

Graphical abstract



Authors

Zeynep Ilgin Kolabas,
Louis B. Kuemmerle,
Robert Perneczky, ..., Matthias Brendel,
Fabian J. Theis, Ali Erturk

Correspondence

ali.erturk@helmholtz-munich.de

In brief

The bone marrow of the skull has a unique molecular and functional composition, as well as disease-specific inflammatory responses that can be observed through human translocator protein positron emission tomography (TSPO-PET) imaging, suggesting that it has potential as a site for brain disease diagnosis, monitoring, and treatment.

Highlights

- Bone marrow across the body display molecular heterogeneity in mice and humans
- Calvaria cells have a distinct profile that is relevant to brain pathologies
- Structural details of human skull-meninges connections are revealed
- TSPO-PET imaging of human skulls can be a proxy of neuroinflammation in the brain



Kolabas et al., 2023, Cell 186, 3706–3725
August 17, 2023 © 2023 The Author(s). Published by Elsevier Inc.
<https://doi.org/10.1016/j.cell.2023.07.009>

Resource

Distinct molecular profiles of skull bone marrow in health and neurological disorders

Zeynep Ilgin Kolabas,^{1,2,3,39} Louis B. Kuemmerle,^{1,4,39} Robert Perneczky,^{5,6,7,8,9,39} Benjamin Förstera,^{1,2,39} Selin Ulukaya,¹ Mayar Ali,^{1,3,4} Saketh Kapoor,¹ Laura M. Bartos,¹⁰ Maren Büttner,⁴ Ozum Sehnaz Caliskan,¹¹ Zhouyi Rong,^{1,2,12} Hongcheng Mai,^{1,2,12} Luciano Höher,¹ Denise Jeridi,¹ Muge Molbay,¹ Igor Khalin,² Ioannis K. Deligiannis,¹³ Moritz Negwer,¹ Kenny Roberts,¹⁴ Alba Simats,² Olga Carofiglio,² Mihail I. Todorov,^{1,2} Izabela Horvath,^{1,15} Furkan Ozturk,¹ Selina Hummel,^{6,10} Gloria Biechele,¹⁰ Artem Zatcepin,^{6,10} Marcus Unterrainer,^{10,16} Johannes Gnörich,¹⁰ Jay Roodselaar,^{17,18} Joshua Shrouder,² Pardis Khosravani,¹⁹ Benjamin Tast,¹⁹ Lisa Richter,¹⁹ Laura Díaz-Marugán,² Doris Kaltenecker,^{1,20} Laurin Lux,¹ Ying Chen,² Shan Zhao,^{1,2} Boris-Stephan Rauchmann,^{5,9,21} Michael Sterr,^{22,23} Ines Kunze,^{22,23} Karen Stanic,^{1,2} Vanessa W.Y. Kan,²⁴ Simon Besson-Girard,^{2,3} Sabrina Katzdobler,^{6,25} Carla Palleis,^{6,25} Julia Schädler,²⁶ Johannes C. Paetzold,^{1,27} Sabine Liebscher,^{8,24,32} Anja E. Hauser,^{17,18} Ozgun Gokce,^{2,8} Heiko Lickert,^{22,23,30} Hanno Steinke,²⁸ Corinne Benakis,² Christian Braun,²⁹ Celia P. Martinez-Jimenez,^{13,30} Katharina Buerger,^{2,6} Nathalie L. Albert,¹⁰ Günter Höglinger,^{6,25} Johannes Levin,^{6,8,25} Christian Haass,^{6,8,31}

(Author list continued on next page)

- ¹Institute for Tissue Engineering and Regenerative Medicine (iTERM), Helmholtz Center, Neuherberg, Munich, Germany
²Institute for Stroke and Dementia Research, LMU University Hospital, Ludwig-Maximilians University Munich, Munich, Germany
³Graduate School of Systemic Neurosciences (GSN), Munich, Germany
⁴Institute of Computational Biology, Helmholtz Zentrum München, German Research Center for Environmental Health, Neuherberg, Germany
⁵Division of Mental Health in Older Adults and Alzheimer Therapy and Research Center, Department of Psychiatry and Psychotherapy, University Hospital, Ludwig Maximilian University Munich, 80336 Munich, Germany
⁶German Center for Neurodegenerative Diseases (DZNE) Munich, Munich, Germany
⁷Ageing Epidemiology (AGE) Research Unit, School of Public Health, Imperial College London, London, UK
⁸Munich Cluster for Systems Neurology (SyNergy), Munich, Germany
⁹Sheffield Institute for Translational Neuroscience, University of Sheffield, Sheffield, UK
¹⁰Department of Nuclear Medicine, University Hospital, Ludwig-Maximilians-Universität München, Munich, Germany
¹¹Institute for Diabetes and Obesity, Helmholtz Center Munich and German Center for Diabetes Research (DZD), 85764 Neuherberg, Germany
¹²Munich Medical Research School (MMRS), 80336 Munich, Germany
¹³Helmholtz Pioneer Campus (HPC), Helmholtz Munich, Neuherberg, Germany
¹⁴Wellcome Sanger Institute, Cambridge, UK

(Affiliations continued on next page)

SUMMARY

The bone marrow in the skull is important for shaping immune responses in the brain and meninges, but its molecular makeup among bones and relevance in human diseases remain unclear. Here, we show that the mouse skull has the most distinct transcriptomic profile compared with other bones in states of health and injury, characterized by a late-stage neutrophil phenotype. In humans, proteome analysis reveals that the skull marrow is the most distinct, with differentially expressed neutrophil-related pathways and a unique synaptic protein signature. 3D imaging demonstrates the structural and cellular details of human skull-meninges connections (SMCs) compared with veins. Last, using translocator protein positron emission tomography (TSPO-PET) imaging, we show that the skull bone marrow reflects inflammatory brain responses with a disease-specific spatial distribution in patients with various neurological disorders. The unique molecular profile and anatomical and functional connections of the skull show its potential as a site for diagnosing, monitoring, and treating brain diseases.

INTRODUCTION

The complex interplay between immune cells at the central nervous system (CNS) borders and the CNS resident immune sys-

tem has become the subject of intensive research.¹ The dura mater of the meninges is directly connected to the adjacent skull bone marrow via skull-meninges connections (SMCs) that allow the trafficking of immune cells^{2–5} and might facilitate the



Anna Kopczak,² Martin Dichgans,^{2,6,8} Joachim Havla,^{24,32} Tania Kümpfel,^{24,32} Martin Kerschensteiner,^{8,24,32} Martina Schifferer,^{6,8} Mikael Simons,^{6,8} Arthur Liesz,^{2,3,8} Natalie Krahmer,¹¹ Omer A. Bayraktar,¹⁴ Nicolai Franzmeier,² Nikolaus Plesnila,^{2,8} Suheda Erener,¹ Victor G. Puelles,^{33,34,35,36} Claire Delbridge,³⁷ Harsharan Singh Bhatia,^{1,2} Farida Hellal,^{1,2,8} Markus Elsner,¹ Ingo Bechmann,²⁸ Benjamin Ondruschka,²⁶ Matthias Brendel,^{6,8,10} Fabian J. Theis,^{4,38} and Ali Erturk^{1,2,3,8,40,*}

¹⁵School of Computation, Information and Technology (CIT), TUM, Boltzmannstr. 3, 85748 Garching, Germany

¹⁶Department of Radiology, University Hospital, LMU Munich, Munich, Germany

¹⁷Charité - Universitätsmedizin Berlin, Department of Rheumatology and Clinical Immunology, Berlin, Germany

¹⁸Immune Dynamics, Deutsches Rheuma-Forschungszentrum (DRFZ), a Leibniz Institute, Berlin, Germany

¹⁹Biomedical Center (BMC), Core Facility Flow Cytometry, Faculty of Medicine, LMU Munich, Munich, Germany

²⁰Institute for Diabetes and Cancer, Helmholtz Munich, Munich, Germany

²¹Institute of Neuroradiology, University Hospital LMU, Munich, Germany

²²Institute of Diabetes and Regeneration Research, Helmholtz Diabetes Center, Helmholtz Zentrum München, Neuherberg, Germany

²³Institute of Stem Cell Research, Helmholtz Zentrum München, Neuherberg, Germany

²⁴Institute of Clinical Neuroimmunology, University Hospital Munich, Ludwig-Maximilians University Munich, Munich, Germany

²⁵Department of Neurology, Ludwig-Maximilians-Universität München, Munich, Germany

²⁶Institute of Legal Medicine, University Medical Center Hamburg-Eppendorf, Hamburg, Germany

²⁷Department of Computing, Imperial College London, London, UK

²⁸Institute of Anatomy, University of Leipzig, 04109 Leipzig, Germany

²⁹Institute of Legal Medicine, Faculty of Medicine, LMU Munich, Germany

³⁰TUM School of Medicine, Technical University of Munich, Munich, Germany

³¹Metabolic Biochemistry, Biomedical Center (BMC), Faculty of Medicine, Ludwig-Maximilians-Universität München, Munich, Germany

³²Biomedical Center (BMC), Medical Faculty, Ludwig-Maximilians Universität Munich, Munich, Germany

³³III. Department of Medicine, University Medical Center Hamburg-Eppendorf, Hamburg, Germany

³⁴Hamburg Center for Kidney Health (HCKH), University Medical Center Hamburg-Eppendorf, Hamburg, Germany

³⁵Department of Clinical Medicine, Aarhus University, Aarhus, Denmark

³⁶Department of Pathology, Aarhus University Hospital, Aarhus, Denmark

³⁷Institute of Pathology, Department of Neuropathology, Technical University Munich, TUM School of Medicine, Munich, Germany

³⁸Department of Mathematics, Technische Universität München, Garching bei München, Germany

³⁹These authors contributed equally

⁴⁰Lead contact

*Correspondence: ali.erturk@helmholtz-munich.de

<https://doi.org/10.1016/j.cell.2023.07.009>

preferential recruitment of immune cells to the meninges from the skull bone marrow.^{5–7}

In mice, high-throughput, multidimensional techniques, such as flow and mass cytometry and single-cell RNA sequencing (scRNA-seq), have provided a detailed map of the cell-type composition and molecular profiles of meningeal immune cells.^{8–12} CNS border-derived cells can be functionally distinct from blood-derived cells of the same type⁵ and cells from different regions of the CNS borders.^{12,13}

By contrast, little functional and multidimensional molecular data are available for the skull bone marrow and how it relates to other bones. For example, Herisson et al.⁴ found a higher influx of monocytes and neutrophils from the skull than from the tibia after brain injury, and Cugurra et al.⁵ showed that dural monocytes and neutrophils are mainly directly derived from the skull bone marrow. Basic scRNA-seq data of the unperturbed skull in comparison to the tibia marrow were obtained by Mazzitelli et al.¹⁴ Proteome-wide characterization of the bone marrow in mice has focused on individual cell types and bones in homeostasis^{15–18} or has used antibody-based methods.¹⁹ For the skull bone marrow, profiling has been limited to small flow or mass cytometry panels.^{6,9,10} Thus, it remains unclear whether the expression profiles of skull bone marrow cells are distinct from those of other bones and whether different types of bone marrow react differently to brain injury.

In humans, the functional roles and molecular makeups of the skull bone marrow, and other bone marrow are even less well characterized. A limited number of ‘omics studies of the human bone marrow have been presented,^{20–23} but a systematic characterization of potential differences among different bone marrow under different conditions is yet to be performed. Even on an anatomical level, although the presence of human SMCs has been suggested using microcomputed tomography (microCT),⁴ their detailed conformation at the cellular level remains elusive.

Here, we performed a systematic and comprehensive molecular analysis of the RNA and protein expression profiles of diverse bone marrow cells in mice and humans. In mice, we performed bulk and scRNA-seq and bulk proteomics on cells from six different bones, the dura, and the brain in three conditions (naive, middle cerebral artery occlusion [MCAo], and sham-operated animals). Our data show that different bones have distinct molecular profiles, with the skull calvaria bone displaying the highest number of differentially expressed genes (DEGs) and ligand-receptor (LR) pairs, mainly related to migration and inflammation.

For studies in humans, we collected post-mortem samples from the skull, vertebra, and pelvis of 20 deceased individuals and performed proteomic analysis, again showing a unique molecular profile of the skull. Using optical clearing on human

skull + meninges + brain specimens, we characterized the anatomical details of SMCs at the cellular level. Using functional imaging in patients, we found disease-specific increases in 18 kDa translocator protein (TSPO) positron emission tomography (PET) signal in different parts of the skull in numerous neurological diseases and a strong correlation between changes in the brain and skull TSPO-PET signal in patients with Alzheimer's disease (AD) and stroke in longitudinal data. These data provide a critical link between the skull and neurological diseases in humans.

RESULTS

Skull is a dynamic site that responds to stroke

To test the skull marrow's involvement in the response to brain injury, we used MCAo as a model for stroke in mice.²⁴ In MCAo, the mice first undergo a neck incision to expose the carotid artery before the occlusion of the middle cerebral artery (Figure 1A). A sham-operation procedure without MCAo mimics a local injury without inducing stroke.^{24–26}

Two-photon imaging on the skull after stroke ($n = 3$ for naive and sham, $n = 5$ for MCAo) at baseline and 2, 24, and 72 h post injury showed that both sham and MCAo groups had a significant decrease of LysM⁺ cells (mostly myeloid cells) (Figure S1A, $p = 0.004$ in sham and $p \leq 0.0001$ in MCAo). Furthermore, there was a higher efflux of myeloid cells from the skull after stroke (Figure S1B), similar to what was observed for Ly6C^{hi} monocytes and neutrophils.⁴

Next, we studied immune cells in the skull marrow and brain using KikGR mouse model.^{5,27} We used ultraviolet laser illumination to convert a photoconvertible protein to RFP in the skull area above the ischemic brain region (Figures S1C–S1E). We detected RFP⁺ B, T, and myeloid cells in the ipsilateral brain 1 and 6 h after photoconversion (Figure S1C), indicating that immune cells from the skull marrow are recruited to the brain after injury.^{2,4–6}

Expression differences between cells of different bone marrows

Next, we assessed if/how skull cells might be different. To this end, we performed scRNA-seq analysis on three flat bones (calvaria, scapula, and pelvis [ilium]), two long bones (humerus and femur), and one irregular bone (vertebra from thoracic level T5 to lumbar L3), along with dura mater and brain samples in naive, sham-operated, and MCAo-operated animals (Figure 1A).

Single-cell transcriptomics of >100,000 cells across the bones and conditions revealed 17 coarse and 50 fine cell types (Figures 1B–1D). We found a bone-specific abundance of the coarse cell types, whereas meninges and brain-specific cells were separated (Figure 1B). We detected large numbers of neutrophils (~25%) and erythroid cells (~30%) along with other expected cell types (Figures 1E and S1F). Neutrophil populations were clearly separated between the conditions (Figure 1C). Standard cell-type proportions were homogeneously distributed among different bones (Figures 1E, 1F, S1G–S1J, and S2). Cell-type proportions were validated per mouse by deconvolving pooled samples with SNPs and flow cytometry, with an overall correlation of 0.88 (Figure 1F).

To investigate changes in absolute cell numbers, we imaged whole mouse bodies at cellular resolution using vDISCO tissue clearing²⁸ and found that the number of total cells (propidium iodide [PI]-labeled cells) increased in the calvaria marrow of mice after stroke compared with controls (Figures S3A–S3C; Video S1). The overall increase in cell number contrasts with the decrease in LysM⁺ cells quantified by live imaging (Figure S1A), suggesting the mobilization of specific cell types out of the skull, whereas there is an overall increase in immune cell numbers as a response to injury.

Hierarchical clustering showed that the long bones, femur, and humerus clustered together with the pelvis. Likewise, the two flat bones, scapula and calvaria, clustered together. The irregular vertebral bone branched with the flat bones in naive condition and after MCAo surgery and with the long bones and pelvis in sham condition (Figure 1G). Calvaria clustered with scapula in naive and sham conditions. Notably, it formed its own branch in MCAo condition, indicating a skull-specific immune reaction to brain injury.

To assess how strongly the gene expression profiles of one bone's population diverge from the other bones' pooled population for each cell type, we used principal component regression analysis (Figure 2A). The calvaria's neutrophils diverged most from the neutrophils of the other bones in all three conditions.

On analyzing DEGs, we found the highest number in the calvaria for all conditions (Figure 2B; Table S1, tabs 5–13): in naive condition, 96; sham condition, 15; and MCAo condition, 62 genes were upregulated, whereas 138, 538, and 62 were downregulated, respectively. In all three conditions, most of the differentially downregulated genes in the calvaria were observed in progenitor cells such as pro-neutrophils, granulocyte-monocyte progenitors, and erythroid progenitors, whereas the upregulated genes were mostly in the myeloid lineage (Figure 2B).

In naive condition calvaria myeloid cell DEGs related to the regulation of apoptotic processes and programmed cell death pathways (Table S1, tabs 5–7), and calvaria-unique DEGs were mostly transcription factors, immediate early genes, and taxis-related genes (Figure 2C; Table S1, tabs 5–7). Transcription factors included *Nr4a1* and *Nr4a2* involved in cellular proliferation, apoptosis, metabolism, and T cell regulation,²⁹ with an anti-inflammatory and damage-limiting role after ischemic stroke.³⁰ Taxis-related DEGs include chemokines and chemokine receptors, e.g., *Cxcr4*, *Ccr12*, *Ccl4*, and *Cxcl2*. Finally, the calvaria exhibited DE pro- and anti-inflammatory genes mostly in neutrophils, such as *Il1b*,³¹ *Ptgs2*,³² and *Thbs2*,³³ of which some are also involved in cell adhesion and migration. In sham-condition calvaria, some genes were common with naive differentially upregulated genes (DUGs) such as *Nr4a1* and *Egr1* in addition to some distinct ones such as *Btg2* (anti-proliferation factor).³⁴

In MCAo-condition calvaria, neutrophils harbored most DUGs. Some DUGs were in common with other conditions such as *Nr4a1*, *Cxcl2*, *Ccr12*, and *Egr1*, whereas others were unique to stroke, such as *Cd69* (T cell migration),³⁵ *Gpr35* (inflammation regulation),³⁶ and *Nr4a3* (T cell and progenitor proliferation)²⁹ (Figure 2C). We validated the upregulation of *Nr4a1* in the calvaria using tissue clearing and immunostaining (Figures 2D and 2E) and RNAscope³⁷ (Figure 2F).

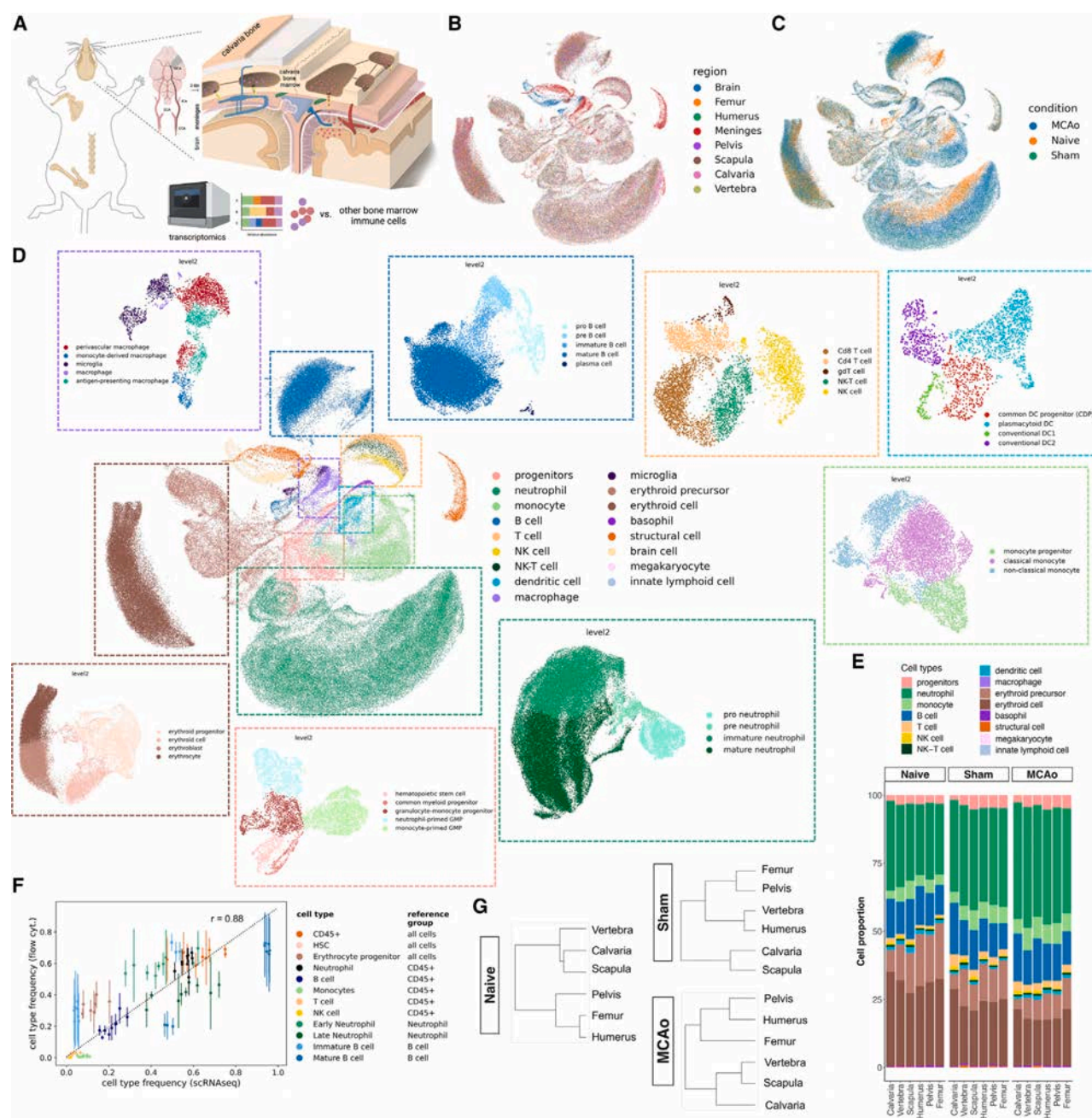


Figure 1. Bones diverge based on transcriptional signature of cell types

(A) Experimental design of single-cell RNA sequencing of bones, dura, and brain, and a schematic of the middle cerebral artery occlusion (MCAO) model of stroke. (B–D) Uniform manifold approximation and projection (UMAP) distribution of scRNA-seq colored by (B) region, (C) condition: naive, sham-operated, and MCAO, and (D) cell type with fine annotated cell types in the surrounding with matching color. (E) Relative proportions of the coarse cell types. (F) Correlation between relative proportions of the cell types in scRNA-seq and independent animals measured by flow cytometry using 15 color panel. Mean Pearson correlation over conditions and bones is 0.875. (G) Dendrograms for naive, sham, and MCAO conditions. (n = 3 pooled animals for sham and n = 6 pooled animals for MCAO.). See also [Figures S1](#) and [S2](#).

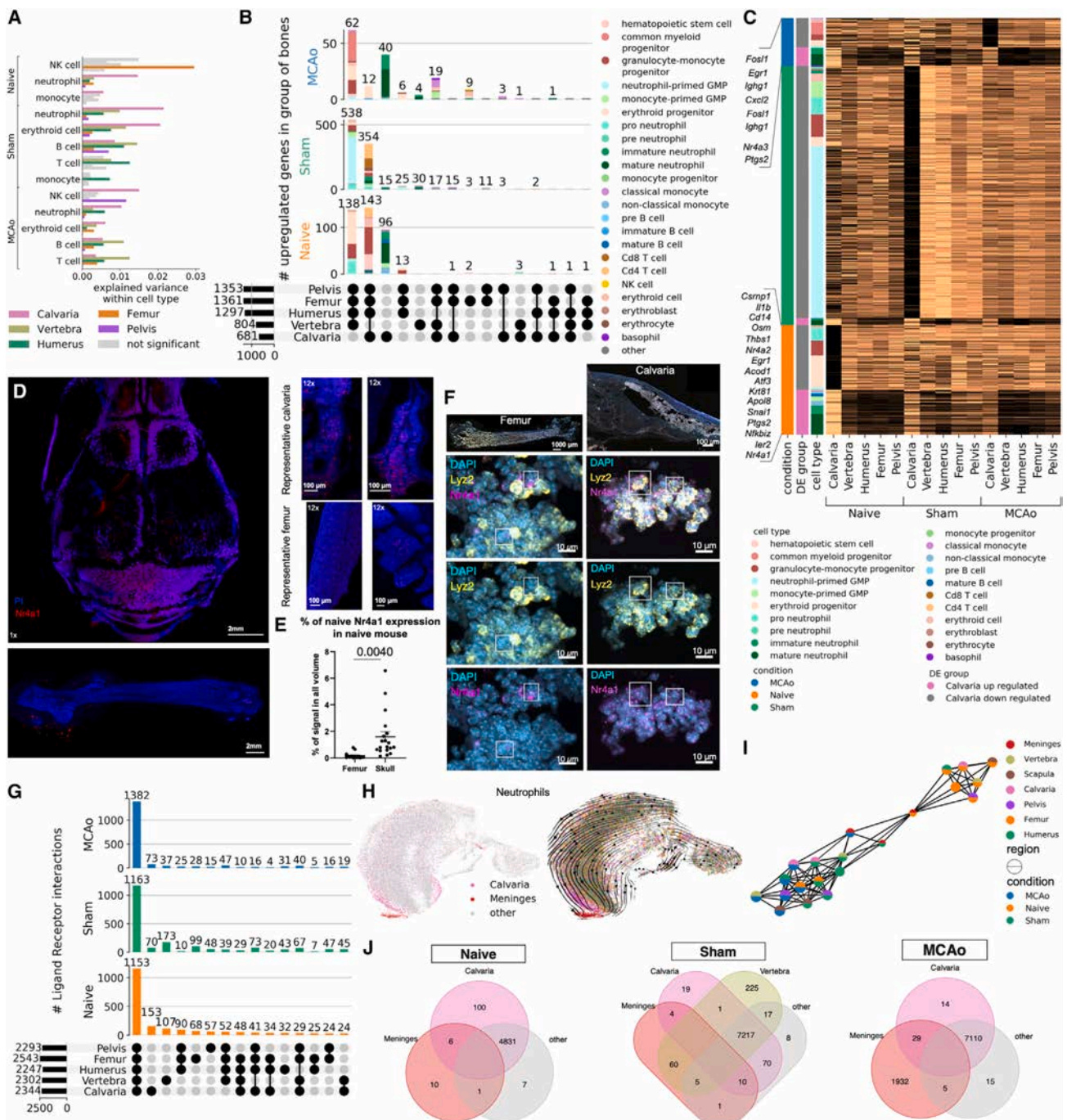


Figure 2. Different cell types show unique differentially expressed genes and ligand-receptor pairs between bones

(A) PC regression plot shows how strongly each bone's cell population diverges from the pooled population of other bones by variance explained for each coarse cell type. Only significant differences are shown for level 1 annotations. (permutation test, $p < 0.0001$)

(B) Differentially expressed genes in naive, sham, and MCAo conditions ($p < 0.05$, LFC > 1 threshold). Each bar represents the fine cell-type color the genes are upregulated in. Fine cell annotations are used.

(C) Calvaria-unique upregulated genes in the three conditions. ($p < 0.05$, LF change > 1)

(D) Representative images of *Nr4a1* labeling after clearing and light-sheet fluorescent microscopy, $n = 3$.

(E) Threshold based quantification of 12x scans of *Nr4a1* ($p = 0.0040$). *Nr4a1*+ voxels as % of total volume. Data represented as \pm SEM.

(F) *Nr4a1* transcript is shown to colocalize with *Lyz2* and *Mpo*, myeloid cell marker and progenitor marker, respectively, using RNAscope.

(G) Ligand-receptor interactions in three conditions on coarse cell-type annotations. (permutation test, 1000 permutations, $p = 0$)

(legend continued on next page)

Focusing on the damage-associated molecular patterns (DAMPs) in CD45+ immune cells, known to guide the immune response in trauma and infection,³⁸ we found calvaria-specific expressions of *Trem1*, *Trpm2*, *Nlrp3*, *Trem2*, and *Cgas* (Figure S3D). The skull was unique in downregulating *Trem1* and *Tlr2* in response to MCAo (Figure S3E).

On investigating the LR interactions using CellPhoneDB,³⁹ we identified bone-type unique interactions (Figure 2G; Table S1, tabs 14–28). In each of the three conditions, we found a core module of LR interactions common to all bones. The numbers of common LR pairs increased for MCAo (naive, 1,153; sham, 1,163; and MCAo, 1,382 pairs). Among the unique interactions, calvaria had the most for naive and MCAo (153 and 73, respectively), whereas vertebra had the most in sham (173).

Gene ontology (GO)-term analysis showed that common pairs to all bones in all conditions were mostly involved in cell migration, cytokine production, and immune regulation such as *Pecam1*-*Cd177*,⁴⁰ *Cd74*-*Mif*,⁴¹ and *Lgals9*-*Cd47* (Table S1, tabs 18, 23, and 28). The calvaria-unique pairs included *Il1b*-*Adrb2* and *Ccl4*-*Ccr5* in naive, *Ccl4*-*Cnr2* in sham, and *Cxcl2*-*Dpp4* and *Cd28*-*Cd86* in MCAo conditions. Naive LR pairs had GO terms mostly related to taxis, cell motility, and cytokine production whereas sham had immune activity-related terms (Figure S3F; Table S1, tabs 18, 23, and 28). Skull-unique LR pairs in MCAo were mostly related to cell migration, chemotaxis, or immune cell activation (Figure S3F).

In conclusion, calvaria displayed the highest number of DUGs and LR pairs among the bones tested, suggesting a distinct molecular profile related to migration and inflammation, especially in the myeloid lineage. This unique signature might underly the differential cell recruitment from the skull bone marrow to the brain.^{2,4–6}

Skull and meningeal neutrophils share unique similarities

As most of the calvaria-specific genes were in neutrophils (Figure 2B), we next examined their developmental trajectories using RNA velocity⁴² in its scVelo⁴³ implementation and pseudotime,⁴⁴ which aligned well with the RNA velocity trajectory (Figures 2H and S3G). Our analysis revealed a subset of mature neutrophils from calvaria clustering next to a group of neutrophils found in the dura (Figure 2H). Along the trajectory, we observed a higher percentage of late neutrophils in the calvaria compared with other bones (Figure S3G). Upon injury, we observed a shift toward late neutrophils in the dura, most prominently in MCAo (Figure S2A). A representative phase portrait of a calcium-binding gene *S100a6* confirmed the validity of our scVelo trajectory analysis (Figure S3H).

To investigate the similarity of mature neutrophils in the calvaria and dura, we performed branching trajectory analysis

using partition-based graph abstraction (PAGA).⁴⁵ We observed a clear distinction between the naive vs. injury groups with the dura positioned in the middle (Figure 2I). The meningeal neutrophils from the naive condition connected with almost all bones in the naive condition, whereas the sham and MCAo meningeal neutrophils connected to the calvaria's sham and MCAo, revealing a similarity between their late-stage neutrophil population profiles. The number of common DEGs between the dura and the calvaria also increased from 6 upregulated and 7 downregulated genes in naive (Figures 2J and S3I–S3K) to 29 upregulated to 15 downregulated genes in MCAo (Figure S3K).

The calvaria displayed the highest pro-inflammatory signature among bones in all conditions (Figure S3L) with neutrophils having the highest pro-inflammatory signature in the calvaria and B cells having the lowest (Figures S3L and S3M). Comparing the pro- and anti-inflammatory scores of the meningeal immune cells with those of the bones, we saw a stronger inflammatory response to injury and especially to MCAo in the meningeal cells, mainly in monocytes and neutrophils.

We validated our scRNA-seq results using bulk RNA-seq for the same bones. Uniform manifold approximation and projection (UMAP) showed similar trends as we saw in scRNA-seq data (Figure S4A). The overall mean correlation of gene expression values between the bulk dataset and a pseudo-bulk created from the scRNA-seq dataset was $r = 0.81$ (Figure S4B). 69 of the 98 genes in naive, 19 of the 78 genes in sham, and 48 of the 62 genes significantly upregulated in calvaria in the pseudo-bulk scRNA-seq data showed the same trend in both datasets (Figure S4C). 9, 4, and 21 of these genes showed the same trend and were also significant in both samples for naive, sham, and MCAo conditions, respectively (Figure S4C; Table S1, tabs 31–34).

We also sequenced CD45+ cells in 6-month-old 5xFAD AD model mice vs. littermates using smart-Seq2 ($n = 3$ per group) (Figures S4D and S4E). Comparing smart-Seq2 data from wild-type calvaria and femur with our scRNA-seq dataset, we found that 15 of the 23 upregulated genes showed the same trend in both (Figure S4F; Table S1, tab 35).

Overall, our data show that bones change their transcriptome in pathologies, and the calvaria holds a distinct profile mostly close to meninges.

Protein-level bone heterogeneity in mice

After transcriptomics, we also investigated proteome profiles in mouse bones, meninges, and brain using mass spectrometry proteomics (three biological replicates) (Figures 3A and S5). We quantified 9,597 proteins in total, 4,172 present in at least half of the samples (Figure S5A) and at least 5,000 proteins were present in at least one sample of each bone (Figures S5B–S5D).

(H) Left: in the neutrophil subpopulation, calvaria, and dura neutrophils are highlighted in region-based UMAP. Right: projected developmental trajectory of MCAo neutrophils subset using scVelo.

(I) PAGA analysis on the neutrophils subpopulation demonstrates separation of samples based on condition.

(J) DE genes (DEGs) among dura, calvaria, and other bones, in three conditions ($n = 3$ pooled animals for sham and $n = 6$ pooled animals for MCAo). ($p < 0.05$, LF change > 0.5)

See also Figures S3 and S4.

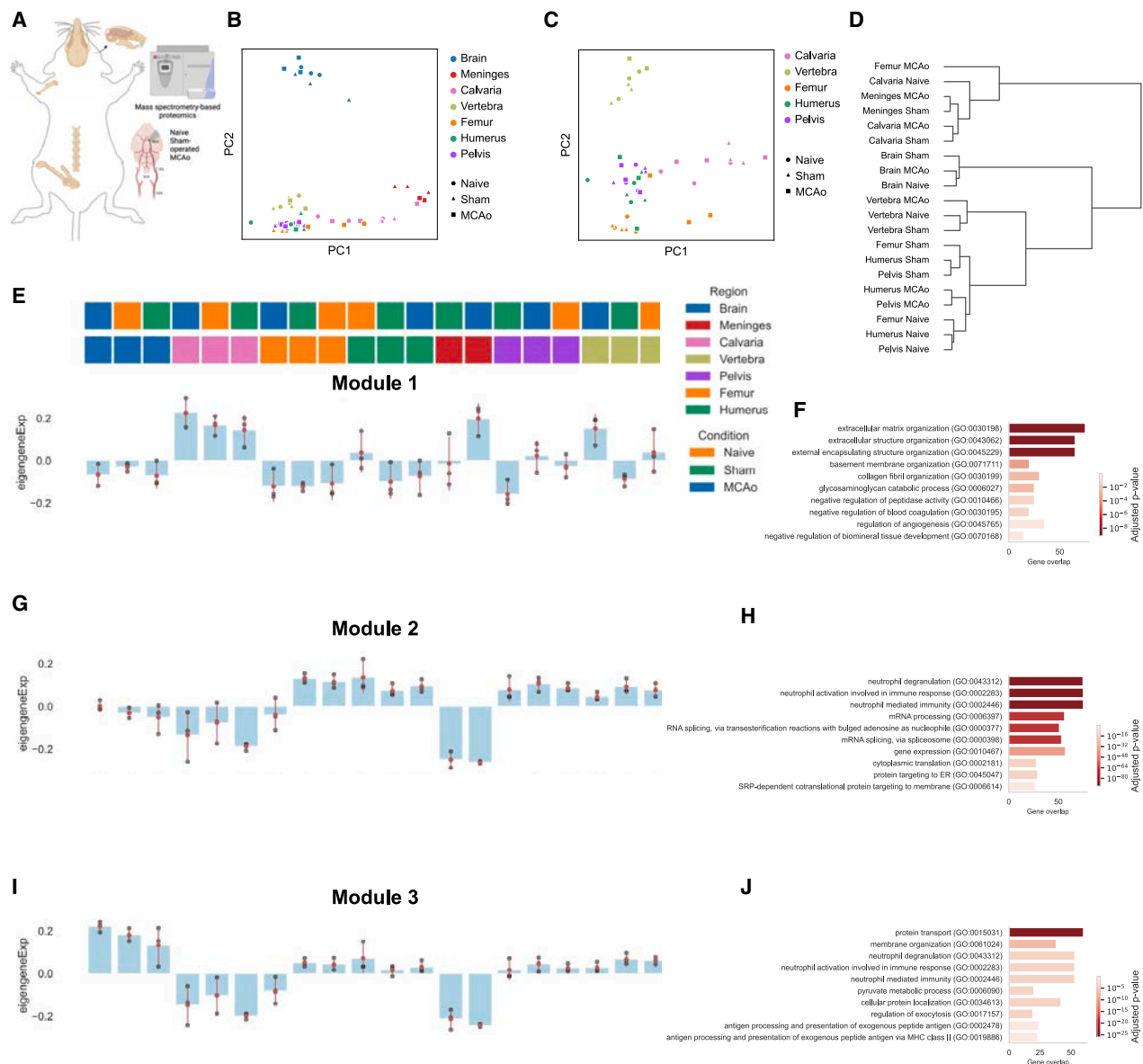


Figure 3. Proteomics identifies protein modules that characterize inter-bone expression differences

(A) Illustration of the experimental pipeline is shown: mouse calvaria, humerus, vertebra, pelvis, and femur from three animals were collected to perform mass spectrometry in three different conditions, that is, naive, sham-operated, and MCAo.

(B and C) Principal component analysis (PCA) of (B) six bones, dura, and brain and (C) six bones in naive, sham, and MCAo conditions.

(D) Dendrogram demonstrates the relation among bones and conditions.

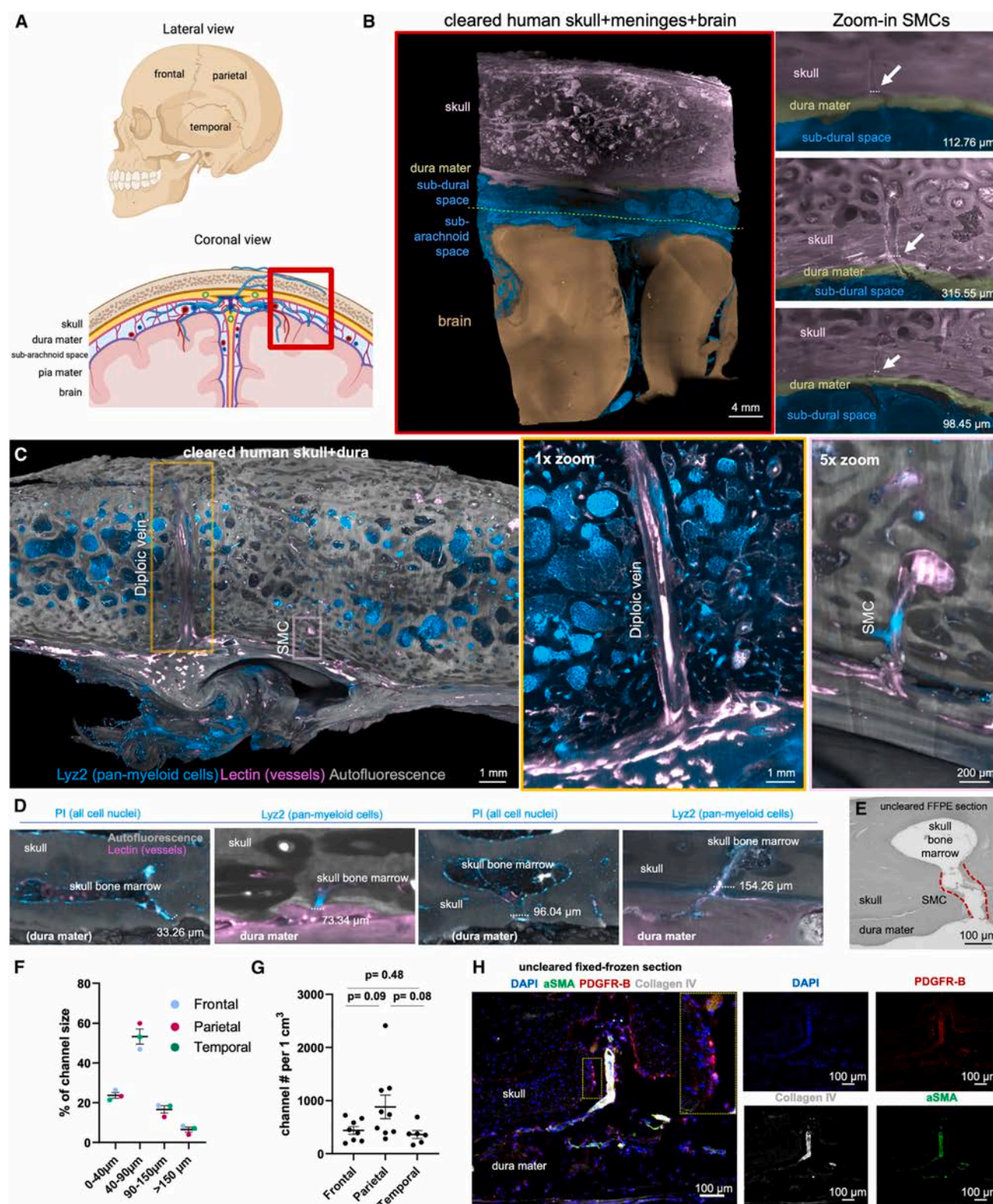
(E–J) Protein expression modules identified by WGCNA among bones, brain, and meninges. Module distributions are shown in the left-hand panels the corresponding GO terms in the right-hand panels ($n = 3$ independent samples each for bones and brain for all conditions, $n = 3$ for meninges MCAo and sham conditions).

See also Figure S5.

Principal component analysis (PCA) showed segregation of the brain and meninges from bones. Calvaria samples were distributed over the PC1, clustering closest to the meninges (Figure 3B) and closer to femur in MCAo conditions (Figure 3C). We did not observe any clustering based on conditions (Figures 3B and 3C). On comparing the calvaria's proteomic signature in sham and MCAo, we found 28 upregulated and 6 downregulated

proteins (Figure S5E; Table S2, tab 10). Prominent examples include complement proteins such as CFB, which regulates B cell differentiation⁴⁶ and cell adhesion factors including CD9⁴⁷ and NID2⁴⁸ (Table S2, tab 10).

A matrix plot and a dendrogram confirmed the segregation of calvaria, meninges, and femur MCAo samples from all other bones across all conditions (Figures 3D, S5C, and S5D). We



(legend on next page)

found 45 upregulated proteins in the calvaria in naive condition ($p < 0.005$, log fold change [LFC] > 1), 65 proteins in sham, and 67 proteins in MCAo compared with other bones, whereas we identified a higher number of downregulated proteins (Figures S5F–S5K; Table S2, tabs 1, 4, and 7).

Using weighted correlation network analysis (WGCNA), we identified three modules with calvaria-specific differences. Module 1 was (mostly related to extracellular matrix [ECM] organization) increased in calvaria samples for all three conditions as well as meninges MCAo and vertebra MCAo samples (Figures 3E and 3F). Module 2 (mainly involved in neutrophil degranulation and immunity, and mRNA processing) showed a decreased expression in brain, calvaria, and meninges (Figures 3G and 3H). Module 3 was also downregulated in calvaria and meninges (Figure 3I) with GO terms related to protein transport, neutrophil degranulation, and immune pathways (Figure 3J). Comparing the protein with scRNA-seq data for module 2, we found a Spearman correlation value of $R = 0.42$, suggesting that this phenomenon is recapitulated on the RNA level⁴⁹ (Figure S5L). Our proteomic analysis confirms neutrophils as a major source of the differences between calvaria and the other bones.

Characterization of SMCs in human samples

We next explored the relevance of our findings in humans. First, we characterized SMCs using tissue clearing and light-sheet fluorescent imaging in 23 skull + dura mater samples in frontal, parietal, and temporal regions coming from seven human skulls (Figures 4A and S5M). We used immunofluorescence to label myeloid cells (LY22) and macrophages (IBA1) (Figures S5N and S5O), PI to label cell nuclei, and lectin to label vasculature (Figures 4B–4D). Human SMCs most often transverse the dura mater, opening to the sub-dural space underneath to arachnoid granulations⁵⁰ (Figure 4B; Videos S2 and S3). We confirmed that SMCs transverse the dura using bright-field imaging of un-cleared formalin-fixed paraffin-embedded (FFPE) sections of decalcified human skull (Figure 4E).

We quantified more than 500 SMCs and found that they are mostly 40–90 μm wide (Figures 4F and S5P) as suggested.⁴ Some SMCs were $>150 \mu\text{m}$, which were often surrounding big blood vessels and occasionally diploic veins (Figure 4C; Video S3). Region-based analysis did not reveal significant differences (Figures 4G and S5Q). We next used graph analysis and found the average shortest path length from a bone marrow cavity to

SMC as $\sim 3,000 \mu\text{m}$, and the average radius along the shortest path as $\sim 37 \mu\text{m}$ (Figure S5R). Furthermore, using histology on skull + dura mater, we found that PDGFR-B signal was present both at the vessels and at the SMC lumen (Figure 4H). This suggests that the SMC lumen is lined with a layer of fibroblastic cells, known antigen-presenting cells,⁵¹ that might potentiate cerebrospinal fluid (CSF) sampling already at the beginning of the SMCs.

Finally, we performed scanning electron microscopy on human skull + dura mater (Figures S5S–S5W). We found similar structures as we identified using tissue clearing, immunohistochemistry (IHC), and as previously shown using microCT⁴ that were filled with fat/lipids. The SMC structure showed immune cells within, in addition to a fibroblastic cell layer (Figures S5S–S5W) as suggested by histology (Figure 4H). These findings suggest that human SMCs might be filled with fat, unlike those of mice,⁴ allowing immune trafficking while serving as an energy source to hematopoietic stem cells.^{52–54}

Human skull proteome is distinct from vertebra and pelvis

Next, we obtained 20 post-mortem human skull, vertebra, and pelvis samples from two independent autopsy centers for proteomic analysis (Figures 5A and S6A). We detected 8,526 protein groups before and 5,320 protein groups after filtering (Figure 5B).

The highest number of uniquely detected proteins was in the skull with 105 unique proteins (Figure 5C). GO analysis revealed 27 skull-specific synapse and synaptic signaling related terms. For example, the term “chemical synaptic transmission” was represented by proteins such as SYP, SYN3, SNAP25, and SLC17A7 (Figure 5D; Table S2, tabs 14–16). Mouse proteome also showed a positive trend in *Syp* and *Snap25* proteins in the calvaria (Figure S6B). This might suggest that skull is more involved in neuropeptide or neurotransmitter-based communication, compared with other bones.⁵⁵

The PC1 of PCA plot depicts the distinct nature of the skull, whereas PC2 demonstrates that the skull samples have a larger variance (Figure 5E). Euclidian distance between pairs showed the differences between skull and pelvis to be the highest and that between vertebra and pelvis to be the lowest (Figure 5F). Bone proteome differences were not driven by age, post-mortem interval, sex, or cause of death (Figure S6C). On the global proteomic scale, we observed a strong downregulation of proteins in the skull compared with other bones, few DE proteins between the vertebra and the other bones, and a strong

Figure 4. Tissue clearing enables a comprehensive characterization of human skull-meninges connections

(A) Frontal, parietal, and temporal regions of the skull and coronal view depicting the meningeal layers and the brain.
(B) Representative light-sheet microscopy image of cleared tissue corresponding to the red box in (A). The right panels show skull-meninges channels connecting the skull bone marrow to the sub-dural space and to the dura mater.
(C) Representative skull piece cleared and imaged for SMC quantification in different regions of the human skull. Diploic vein and an exemplary SMC are shown.
(D) Representative skull-meninges-channels in different sizes: ~ 33 , ~ 73 , ~ 96 , and $\sim 154 \mu\text{m}$. Autofluorescence in gray, lectin in magenta. Left panels are labeled with PI (cyan) and right panels with LY22 (cyan). Dura mater in some panels is not preserved in (D).
(E) Human SMC example from 1 μm thick FFPE embedded skull-dura section.
(F) Quantification for % of channel size in frontal, parietal, and temporal regions. Data represented as \pm SEM.
(G) Quantification for annotated channel numbers, normalized to 1 cm^2 (22 region of interests (ROIs) in total, >500 channels, from seven post-mortem samples, frontal vs. parietal $p = 0.09$, parietal vs. temporal $p = 0.08$, and frontal vs. temporal $p = 0.48$). Data represented as \pm SEM.
(H) Human SMC example with an artery passing to the skull from 8 μm thick fixed-frozen skull-dura section labeled with DAPI (blue), α SMA (green), PDGFR-B (red), and CollagenIV (gray).
See also Figure S5.

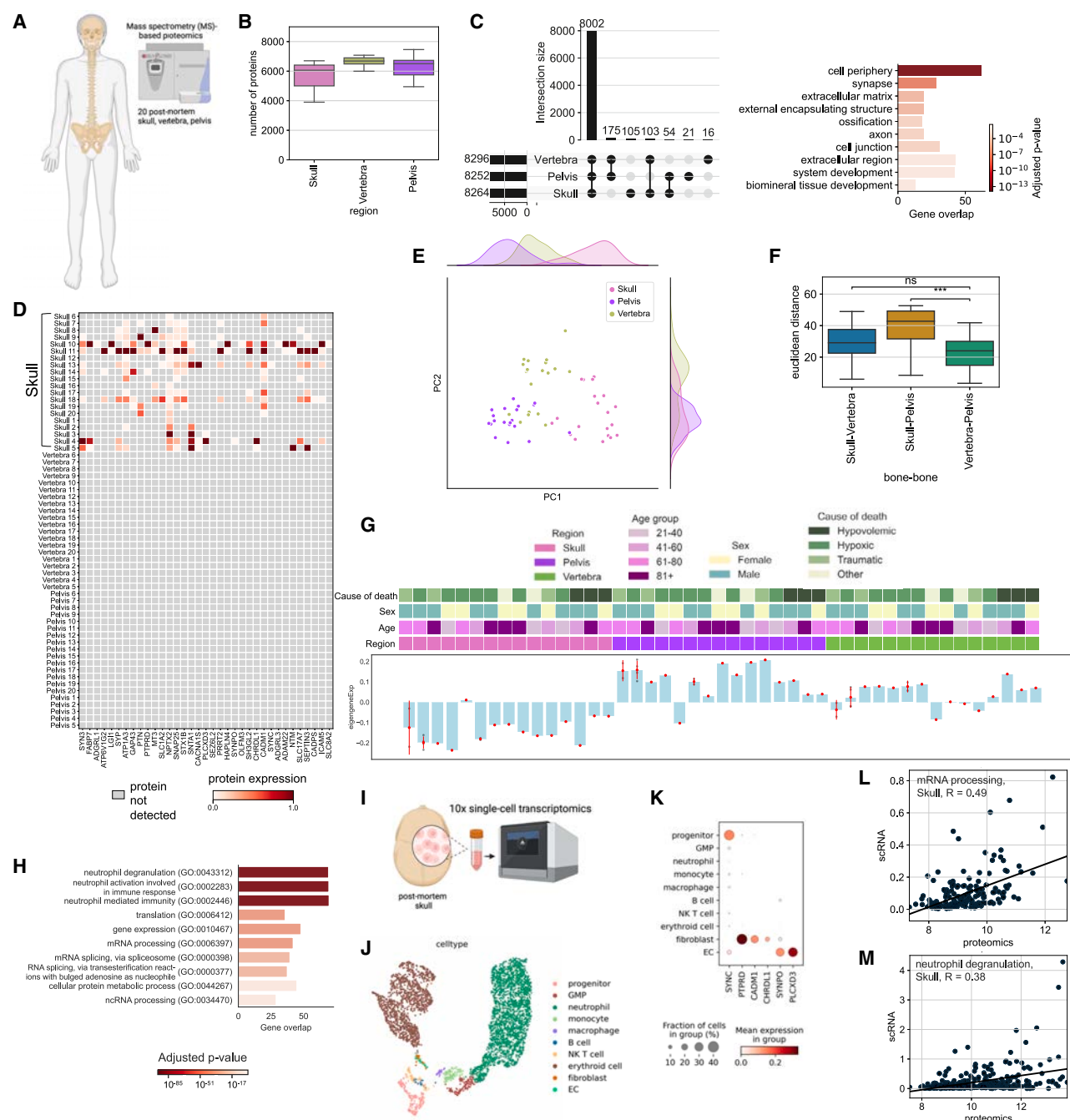


Figure 5. Human bones differentially express distinct protein modules

(A) Illustration of the experimental pipeline, 60 bones in total were collected to perform mass spectrometry-based proteomics on 20 skull, 20 vertebra, and 20 pelvis.

(B) The number of proteins detected from each bone is shown with a boxplot.

(C) The number of common proteins and unique proteins detected from different bones are shown with an upset plot. GO terms associated with unique skull proteins are shown at the bottom.

(D) Expression levels of a selection of proteins belonging to GO terms related to synapse term that were detected in more than half of the skull samples uniquely.

(E) Principal component analysis of the three bones analyzed.

(F) Boxplot depicts the Euclidean distances between pairs of bones using the first 2 principal components. ($p = 2.862 \times 10^{-4}$ for skull-pelvis vs. vertebra-pelvis, p value $\approx 2.862 \times 10^{-4}$ for skull-pelvis vs. vertebra-pelvis)

(G) WGCNA among bones reveal one significant module where calvaria genes are downregulated compared with two other bones with some exceptions. Biggest source of variance is the bone type.

(legend continued on next page)

upregulation of proteins in the pelvis (Figures S6D–S6I; Table S2, tabs 19–27).

Cellular processes such as translation, metabolism of RNA, and leukocyte activation-related terms were downregulated in the calvaria, whereas ECM organization-related terms were upregulated (Figure S6E; Table S2, tab 20). These differences are in line with our mouse scRNA-seq dataset, e.g., in the collagens *Col1a1* and *Col1a2* in naive ($p = 0.0004$ and $p = 0.0016$, respectively) and MCAo ($p = 0.00005$ and $p = 0.0002$, respectively) conditions. In mice, *COL1A1* and *COL1A2* were also among the top DE proteins in the calvaria (Table S2, tabs 1, 4, and 7). ECM strongly influences immune cell functions,⁵⁶ suggesting that the functional role of ECM differences should be investigated further. Additionally, the most abundant protein in our human skull dataset was *COL1A1*, a structural protein encapsulating blood vessels in bone marrow,⁵⁷ suggesting differences in the vascular organization of the skull bone marrow.

Using WGCNA, we identified a module that was downregulated in the skull samples of the human proteomics dataset (Figure 5G), whose GO terms were very similar to mouse proteome modules: most prominently neutrophil degranulation and mRNA processing (Figure 5H).

Overall, two notable groups of proteins showed interesting expression profiles between the bones. First, we identified several proteins unique to the skull that relate to synapses, and second, a downregulation of neutrophil degranulation and mRNA processing in the skull. To test how these differences would translate into the RNA level, we performed scRNA-seq of one human post-mortem skull (Figure 5I). After annotating 10 cell types (Figures 5J and S6J), we assessed the presence and expression levels of unique skull proteins (Figure 5C). Six of the 256 unique synapse-relevant genes were detected in the dataset, mostly in fibroblasts (Figure 5K). This allowed us to rule out immune cell expression as a source of the synapse-related terms. We speculate that the difference in synaptic protein levels could either hint at a denser or more active innervation of the skull bone marrow or it might reflect the immune surveillance of the brain that leads to a transport of peptides from brain to the skull.

The human scRNA-seq data supported the presence of the mRNA processing and neutrophil degranulation modules. Proteomics data and scRNA-seq data correlated with R values of $R = 0.49$ and $R = 0.38$ for the genes in these GO terms, respectively (Figures 5L and 5M). This correlation from both mouse and human datasets suggests a consistently low neutrophil degranulation and lower mRNA processing, based on previously reported correlations between mRNA-protein levels.^{58,59} Thus, we conclude that the human skull differs from other bones at both transcriptomic and proteomic levels.

TSPO signal in the skull is associated with inflammatory, ischemic, and neurodegenerative CNS diseases

Next, we examined the reaction of the skull to different neurological disorders in patients. TSPO is a protein markedly upregulated in the brain during neuroinflammation and is used as a PET biomarker.^{60,61} We also found significantly higher *Tspo* RNA levels in the calvaria in injury compared with naive mice (Figure S7A), especially in neutrophils. To confirm the ability of PET imaging to measure skull-specific TSPO-PET signals, we performed imaging on three living mice and immediately isolated the skulls. The isolated skulls had a strong association with the skull signal in the live animals confirming the skull origin of the TSPO signal (Figure S7B).

Next, we assessed TSPO-PET signals in 50 patients belonging to the AD continuum, 43 patients with 4-repeat tauopathies (4RTs),⁶² 10 patients in the post-acute phase of stroke, 15 patients with relapsing-remitting multiple sclerosis (RRMS),⁶³ and 14 patients with primary progressive multiple sclerosis (PPMS) (Table S3, tab 1). We used 3D surface projections on a CT template to show substantial relative TSPO-PET differences in patients belonging to the AD continuum compared with healthy controls (Figure 6A). We found a clear increase in TSPO-PET signals in calvaria regions adjacent to the frontal, parietal, and motor cortices of patients belonging to the AD continuum (Figures 6A–6F; Video S4). Similarly, elevated skull inflammation was observed in each cohort of patients with distinct patterns in different pathological conditions (Figures 6B–6F), e.g., a prominent temporal pole signal in stroke and multiple sclerosis patients (Figures 6B and 6E), in the skull base in RRMS and PPMS patients (Figure 6D), and in the skull adjacent to the prefrontal cortex and the motor area in 4RT patients (Figures 6C and 6D). In 5xFAD mouse model of AD, we observed a similar TSPO signal elevation in the fronto-parietal and temporal regions compared with controls (Figures S7C and S7D). These results indicate that TSPO-PET imaging of the skull can reveal distinct signal patterns in inflammatory, ischemic, and degenerative CNS conditions, at least at the cohort level.

In the AD continuum patients, the overall TSPO-PET signal was increased in females over males and was negatively associated with age in patients with AD (Figures S7E and S7F). We did not find statistically significant differences between male and female patients in the 4RT, stroke, and PPMS cohorts, although RRMS showed increased TSPO tracer uptake in males (Figure S7E). We did not find significant correlations with AD severity based on cognitive tests such as mini-mental-state examination (MMSE), the Consortium to Establish a Registry for AD (CERAD) neuropsychological test battery, and the clinical dementia rating (CDR) scale (Figure S7G). There were also no significant associations with specific clinical stages of AD such as in the

(H) GO terms from the module of skull downregulated proteins.

(I) Single-cell sequencing of post-mortem skull sample illustration.

(J) UMAP of single-cell sequencing of post-mortem skull sample ($n = 1$).

(K) Expression of unique skull detected proteins in the scRNA-seq data.

(L) Correlation plot of the module from (G), mRNA processing GO term. Protein expression vs. scRNA-seq. Spearman correlation, $R = 0.49$, $p < 0.0001$.

(M) Correlation plot of the module from (G), neutrophil degranulation GO term protein expression. Protein expression vs. scRNA-seq. Spearman correlation, $R = 0.38$, $p < 0.0001$.

See also Figure S6.

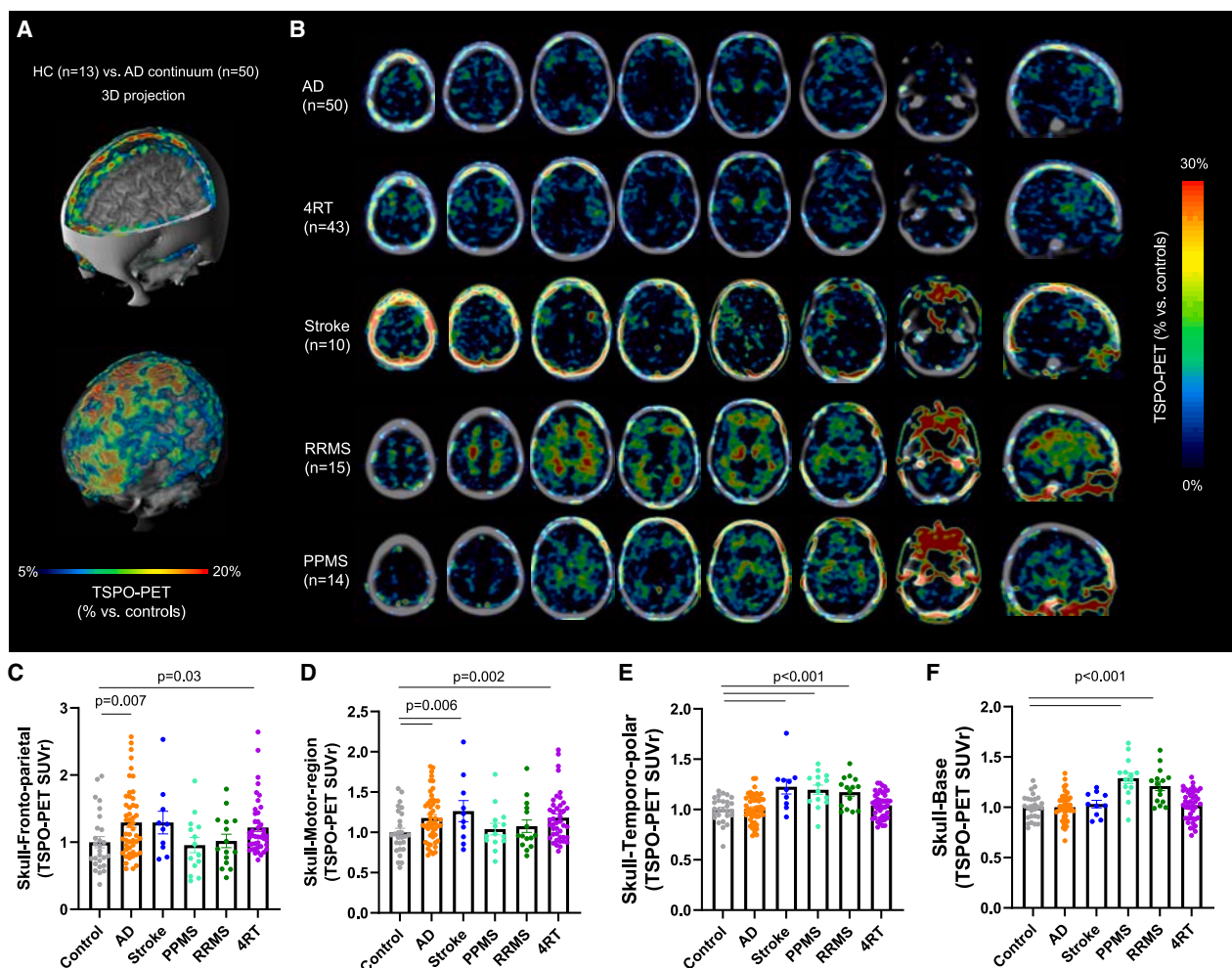


Figure 6. Distinct TSPO uptake patterns are observed in the skull of patients with inflammatory, ischemic, and degenerative CNS diseases (A) 3D surface projection (triple fusion with CT and MRI templates; quadrant cut [top]; transparent CT [bottom] displaying increased activity within skull) shows % -TSPO-PET differences between patients with AD and healthy controls at the group level. (B) Average TSPO-PET signal in Alzheimer's disease (AD), stroke, primary progressive multiple sclerosis (PPMS), relapsing-remitting multiple sclerosis (RRMS), and 4-repeat tauopathy (4RT) patients. (C–F) TSPO-PET signal quantifications in skull regions adjacent to different brain regions: (C) fronto-parietal area ($p = 0.007$ for control vs. AD, and $p = 0.03$ for control vs. 4RT), (D) motor area ($p = 0.006$ for control vs. AD and stroke, and $p = 0.002$ for control vs. 4RT), (E) temporo-polar area ($p < 0.001$ for control vs. stroke, PPMS, and RRMS), and (F) skull base ($p < 0.001$ for control vs. PPMS and RRMS). Data represented as \pm SEM. One-way ANOVA with Bonferroni post hoc correction (see STAR Methods for details). Data were normalized as described in the STAR Methods. Significant differences of disease vs. controls are indicated. Pairwise comparisons of all groups can be found in Table S3. See also Figure S7.

comparison of the prodromal stage characterized by subjective cognitive decline (SCD) or mild cognitive impairment (MCI) and the AD dementia stage (Figure S7H). Early and late clinical AD subgroups displayed a similar increase in the calvaria TSPO-PET signal (Figures S7G and S7H), suggesting that skull inflammation occurs during all stages of the AD continuum.

Notably, a significant correlation between the TSPO-PET signals in the calvaria and the brain was only observed in Braak stage VI regions, which can suggest an increasing skull inflammation with advanced tau spread (Figure S7I). TSPO-PET levels in the calvaria were associated with decreased β -amyloid₄₂ but

not β -amyloid₄₀ concentration in CSF (Figures S7J and S7K). Lower β -amyloid₄₂ in CSF is associated with more fibrillar amyloid deposits in the brain,⁶⁴ suggesting that β -amyloid is also a trigger for increasing skull inflammation. By comparison, the C2 bone of the vertebra had no significant increase compared with controls in any of our cohorts (Figure S7L).

Next, we performed longitudinal analysis on patients with stroke and AD. Our stroke patients were scanned again 3 months after the stroke, whereas patients with AD were imaged 18 months after their baseline scan. Time points were chosen based on clinical necessity. On comparing 13 patients with AD

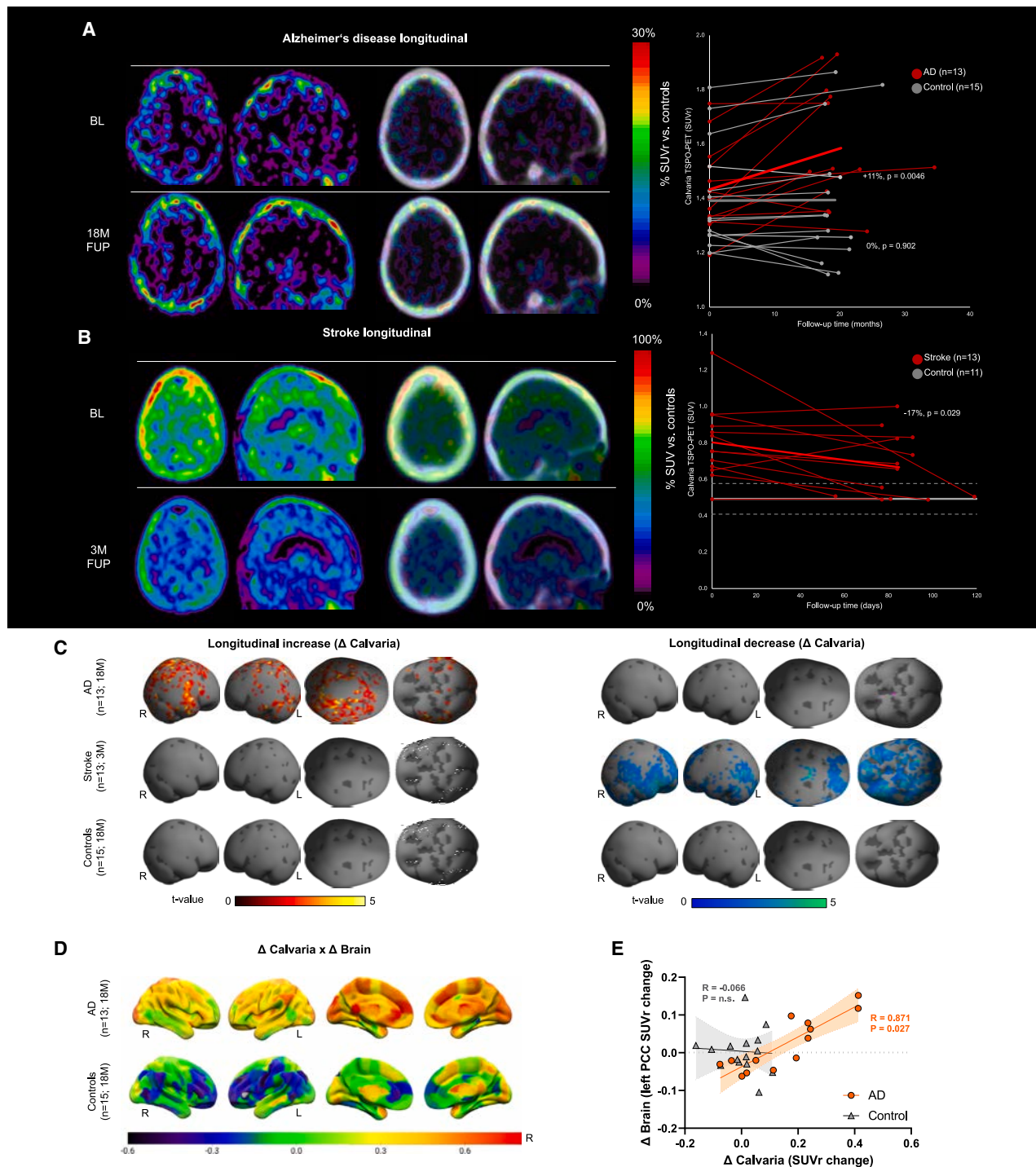


Figure 7. Serial calvaria TSPO-PET imaging of patients with Alzheimer's disease and stroke

(A and B) Axial and sagittal slices show %PET difference images of patients with Alzheimer's disease (AD, $n = 13$, A, +11%, $p = 0.0046$ in AD vs. 0%, $p = 0.902$ in controls) and stroke ($n = 13$, B, -17%, $p = 0.029$ in stroke) against age-matched healthy controls (normalized as described in the [STAR Methods](#)). Controls in (A) ($n = 15$) were imaged serially and controls in (B) ($n = 11$) were imaged at a single time point. %PET difference images are depicted with and without CT overlay. Right panels show individual time courses of calvaria TSPO-PET signals of (A) patients with Alzheimer's disease and healthy controls at a median follow-up

(legend continued on next page)

with 15 serially imaged age-matched healthy controls, we found, on average, an 11% increase in the skull TSPO-PET signal in patients with AD ($p = 0.0046$, paired t test), whereas healthy controls revealed no change ($p = 0.902$, paired t test, Figure 7A). By contrast, we observed a 17% decrease ($p = 0.029$, paired t test) in the skull TSPO-PET signal of stroke patients 3 months after the onset of their stroke (13 stroke patients, 11 controls) (Figure 7B).

After normalization (see STAR Methods), we generated surface projections to reflect the pattern of longitudinal TSPO-PET changes by statistical parametric mapping (SPM) (voxels with $p < 0.05$, uncorrected for multiple comparisons) (Figure 7C) on SPM12 skull surface template. We observed that signal increases in patients with AD were mainly observed in areas highly relevant to AD pathology such as the skull covering the temporal and parietal cortices⁶⁵ and were also in line with the regions we report as significantly higher in the baseline condition, i.e., motor area and fronto-parietal cortex (Figures 6C and 6D). In stroke patients, we observed a longitudinal decrease in the whole skull without specific regional preferences (Figure 7C).

We correlated TSPO-PET changes in 246 brain regions of the Brainnetome Atlas⁶⁶ with the overall skull TSPO-PET signal changes in patients with AD and found that regional increases of microglial activation in the brain are correlated with progressive overall skull inflammation (Figure 7D). This association was found for brain regions highly relevant to AD pathology, namely the posterior cingulate cortex (PCC), which remained statistically significant even after strict false discovery rate (FDR) correction for multiple comparisons (Figure 7E). Only weak correlations were found in controls (Figure 7D). These results suggest that skull responds to brain inflammation in AD and may serve as a proxy for monitoring neuroinflammation in humans.

DISCUSSION

Neuroinflammation is a significant factor in many CNS disorders. Recent findings suggest that studying the connections between the dura mater and neighboring calvaria marrow could provide insights into brain inflammation. Observing cells and molecules specifically associated with the calvaria-meninges-brain axis could be an effective way to monitor and understand this process.

Our study shows that there is a clear difference between the marrow cells suggesting localized functions for different bones. Our human proteomics analysis confirmed that human skull has a distinct molecular profile as in mice. As these proteomics data were obtained from post-mortem individuals with a wide

range of ages and pathologies, it suggests that the skull bone marrow remains distinct across a wide range of conditions. Moreover, the increased levels of brain-related, especially synaptic proteins, in the human skull suggests that communication along the skull-meninges-brain axis might occur in both directions.⁵⁵

Overall, our extensive data on human SMCs using tissue clearing of large samples of human skulls with attached dura mater suggest that they facilitate immune cell trafficking between the skull and meningeal surface of the brain similar to detailed observations provided in different studies in mice.^{2,4-6} Although the disruption of the blood-brain barrier after pathological conditions such as stroke as well as the infiltrating immune cells through blood has been well-documented,^{12,67,68} it is currently still unclear under which conditions and what fraction of immune cells reach the meninges or to the parenchyma from the calvaria compared with other routes.^{6,12,69}

Several studies demonstrated the clinical utility of TSPO-PET imaging in neurological diseases such as AD, Huntington's disease (HD), amyotrophic lateral sclerosis, Parkinson's disease, multiple sclerosis, and migraine.^{70,71} The correlations between brain and skull inflammation signal we observed with a third-generation TSPO-PET ligand [¹⁸F]GE-180⁷² suggest that the use of skull imaging for the early diagnosis and/or monitoring of brain pathologies should be further investigated. However, given the limited disease specificity of the TSPO signal, it is likely that different contrast agents and imaging modalities will be needed for clinical applications. Our data support the notion of chronic inflammation in patients with AD^{73,74} vs. resolving inflammation in stroke patients after acute trauma.^{75,76} As calvaria cells are localized very close to the surface, it could be easier and faster to image it by different modalities, for example, optoacoustic imaging technologies in the future, which are portable and less costly compared with MRI/PET imaging and could provide early point-of-care diagnosis.⁷⁷

TSPO is strongly upregulated in microglia and astrocytes upon activation and is also expressed on infiltrating macrophages in the brain.⁶⁰ However, its sources outside the brain are less understood as many immune cell types including neutrophils express TSPO.^{78,79} The increased cell numbers in the skull marrow in response to injury also suggest a mechanism for the increase in TSPO signals seen in mouse and human data for various diseases, although more detailed studies are needed to establish the sources of signal increase for each condition.^{80,81}

Our data suggest that different bones in the body have distinct molecular profiles. Notably, the response of the calvaria to neurological pathologies is different from other bones, indicating

interval of 18 months and (B) patients with stroke at a median follow-up interval of 84 days. Mean (thick line) and standard deviation (dashed lines) of calvaria TSPO-PET.

(C) Surface projections show statistical parametric mapping (SPM) of longitudinal TSPO-PET changes (left: increases, hot/right: decreases, cold) of patients with AD, patients with stroke, and healthy controls. Voxels with $p < 0.05$ (t value threshold 1.78, uncorrected for multiple comparisons) are projected on the SPM12 skull surface template.

(D) Brain surface projections show regional correlations (Pearson's correlation coefficient, R) of longitudinal TSPO-PET changes in calvaria with longitudinal TSPO-PET changes in brain of patients with AD and healthy controls.

(E) Correlation between calvaria and brain TSPO-PET changes in the left posterior cingulate cortex that survived false discovery rate correction for multiple comparison of 246 brain regions ($R = 0.871$, $p = 0.027$ in AD vs. $R = -0.066$, $p = \text{n.s.}$ in controls).

that the skull may be useful for monitoring and potentially controlling inflammation in various brain pathologies in the future.

Limitations of the study

Our data have limitations, despite the rich data on molecular analysis and imaging in mice and humans. We could not statistically compare transcriptomics differences in mice and humans due to the limited number of samples. We only focused on a selected number of bones in mice and humans. Also, for ethical reasons, we could not obtain bone samples from healthy humans for comparison with pathological states. Different causes of death might also be affecting the molecular profile of the samples.

Although our data provide leads for the molecules that might regulate the skull's response to disease, only future mechanistic studies can clarify their exact involvement. Future work must explore inter-individual differences and gene expression profile evolution over time in mice. Additional characterization of the specific contribution of skull immune cells compared with other bones and exact routes of trafficking is necessary to understand the neuroimmune axis. Although our study suggested B cell, T cell, and myeloid cell trafficking, it would be interesting to elucidate specific cell-type dynamics in certain disease cases. Finally, our detailed demonstration of skull inflammation in diverse diseases in humans suggests that it can be used for diagnosing or monitoring diseases in the future, but detailed clinical studies are needed to explore its clinical utility.

STAR★METHODS

Detailed methods are provided in the online version of this paper and include the following:

- **KEY RESOURCES TABLE**
- **RESOURCE AVAILABILITY**
 - Lead contact
 - Materials availability
 - Data and code availability
- **EXPERIMENTAL MODEL AND STUDY PARTICIPANT DETAILS**
 - Animals
 - Human samples and participants
- **METHOD DETAILS**
 - Middle cerebral artery occlusion (MCAo) model
 - Skull preparation for chronic imaging
 - Live Imaging
 - Behavioral experiments - Neuroscore
 - Perfusion, fixation and tissue preparation
 - vDISCO whole-body immunostaining, PI labeling and clearing
 - *Nr4a1* labeling and clearing of mice bones with SHANEL
 - Human skull labeling and clearing with SHANEL
 - Light sheet microscopy imaging
 - Reconstruction of whole-mouse body and mouse head scans
 - Fixed-formalin paraffin embedding, sectioning and H&E staining

- Human fixed frozen sections, immunohistochemistry and imaging
- Single-cell isolation for scRNAseq and proteomics
- Cell sorting and plate-based bulk RNA-sequencing
- Single-cell suspension isolation from the human bones for proteomics
- Single-cell isolation from human skull for scRNAseq
- scRNA sequencing – 10x Genomics
- Sample preparation for bulk RNA isolation
- Bulk RNA isolation, library preparation and sequencing
- Flow cytometry
- Multiplexed RNAscope smFISH
- High-resolution imaging
- Image stitching
- Scanning electron microscopy
- Proteomics Sample Preparation
- Liquid chromatography and mass spectrometry (LC-MS/MS)
- Proteomics data processing
- Small animal PET/MRI acquisition
- Human TSPO-PET imaging acquisition

● QUANTIFICATION AND STATISTICAL ANALYSIS

- Single-cell RNA data analysis
- Bulk RNA data analysis for 5xFAD dataset
- Bulk RNA data analysis for MCAo dataset
- Statistical analysis of KikGR animals
- Image Analysis
- Proteomics data analysis
- Small animal PET/MRI analysis
- Human TSPO-PET imaging analysis
- Statistics for human TSPO-PET imaging

● ADDITIONAL RESOURCES

SUPPLEMENTAL INFORMATION

Supplemental information can be found online at <https://doi.org/10.1016/j.cell.2023.07.009>.

ACKNOWLEDGMENTS

This project has received funding from the European Research Council (ERC) under the European Union's Horizon 2020 research and innovation program (ERC CoG no. 865323 to A.E. and ERC-StG 802305 to A.L.) and Nomis Foundation (A.E.). This work was further supported by Vascular Dementia Research Foundation, Deutsche Forschungsgemeinschaft (DFG, German Research Foundation) under Germany's Excellence Strategy within the framework of the Munich Cluster for Systems Neurology (EXC 2145 SyNergy, ID 390857198 and ID 390857198 [C.P.]), grant DI-722/16-1 (project ID: 428668490) and a dedicated grant to M. Brendel. (BR4580/1-1), to I. Khalin (457586042), ICARUS study (FOR 2879, ID 405358801), procurement of the MRI scanner (DFG, INST 409/193-1 FUGG), to N.K. and O.S.C. through Emmy Noether Programme (KR5166/1-1), and to A.E.H. (DFG SFB1444, Project 14, DFG HA5354/12-1). Additionally, C.P. supported by Friedrich-Baur-Stiftung, C.P. and S. Katzdobler. by Lüneburg Heritage Foundation, A.E.H. by the Einstein Foundation Berlin, project A 2019-559, V.G.P. by Novo Nordisk Foundation (Young Investigator Award; NNF21OC0066381), R.P. by the National Institute for Health and Care Research (NIHR) Sheffield Biomedical Research Centre (NIHR203321), and M. Brendel, B.-S.R., and R.P. by the Hirnliga e.V. (Manfred-Strohscheer-Stiftung) and the Alzheimer Forschung Initiative e.V. (project ID 19063p). GE Healthcare made GE-180 cassettes available through an early-access model. The BMBF has supported the work of J.L. by (FKZ: FKZ161L0214B, ClinspectM), J. Schädler and B.O. within the NATON

collaboration of the Network University Medicine (01KX2121) and V.G.P. by eMed Consortia “Fibromap.” A.L., Z.I.K., and M.A. are members of the GSN at the University of Munich. We acknowledge SFB-Project CCR1052-A9, the technical support of Core Facilities of Genomics at Helmholtz Munich and Flow cytometry at Biomedical Center Munich. We thank Uta Mamrak for performing MCAo surgeries; Alex Nazlidis for contribution to Figure 1A; Cornelia Niemann, Lucia Rodriguez, and Georg Kislinger for technical assistance for SEM experiments; and Giovanna Palumbo during PET imaging. The graphical abstract and experimental pipeline in Figures 1, 3, 4, and 5 were created with BioRender.com.

AUTHOR CONTRIBUTIONS

Conceptualization and management of whole project, A.E.; methodology, Z.I.K., L.B.K., B.F., B.T., L.R., I.H., and M.N.; software, L.B.K., M.A., M. Büttner, I.H., M.N., M.I.T., and J.C.P.; validation, Z.I.K., L.B.K., S.U., I.H., K.R., and O.A.B.; formal analysis, Z.I.K., L.B.K., M.A., M. Büttner, M. Brendel, N.F., L.M.B., G.B., S.H., J.G., M. Schifferer, A.S., L.H., I.H., M.N., M.I.T., L.L., J.C.P., S.U., S. Kapoor, O.S.C., and N.K.; investigation, Z.I.K., S.U., M. Sterr, I. Kunze, H.L., I.K.D., C.P.M.-J., M. Schifferer, A.S., O.C., L.D.-M., C. Benakis, A.L., P.K., K.R., O.A.B., D.J., M.M., F.O., J. Shrouder, J.R., A.E.H., S.Z., D.K., I. Khalin, N.P., B.F., H.S.B., Z.R., H.M., M.M., K.S., F.H., S.B.-G., O.G., S. Kapoor, O.S.C., N.K., V.W.Y.K., and S.L.; writing – original draft, Z.I.K., S.E., and A.E.; writing – review & editing, Z.I.K., M.E., and A.E.; funding acquisition, A.E.; visualization, Z.I.K., L.B.K., M.A., S.U., L.H., and A.Z.; resources, R.P., M. Brendel, H.S., I.B., C. Braun, C.D., J. Schädler, B.O., V.G.P., N.L.A., M.U., J.G., S. Katzdobler, C.P., A.K., K.B., J.L., C.H., M. Simons, M.D., G.H., J.H., T.K., and M.K.; project administration, Z.I.K.; supervision, F.H., S.E., H.S.B., F.J.T., M.E., and A.E.

DECLARATION OF INTERESTS

M. Brendel received speaker honoraria from GE healthcare, Roche, and Life Molecular Imaging and is an advisor of Life Molecular Imaging. J.H. reports personal fees, research grants, and non-financial support from Merck, Bayer, Novartis, Roche, Biogen, and Celgene and non-financial support of the Guthy-Jackson Charitable Foundation—none in relation to this study. C.P. is inventor in a patent “Oral Phenylbutyrate for Treatment of Human 4-Repeat Tauopathies” (EP 23 156 122.6) filed by LMU Munich. T.K. has received speaker honoraria and/or personal fees for advisory boards from Bayer Healthcare, Teva Pharma, Merck, Novartis, Sanofi/Genzyme, Roche, and Biogen as well as grant support from Novartis and Chugai Pharma—none in relation to this study. M.K. has been on advisory boards for Biogen, medDay Pharmaceuticals, Novartis, and Sanofi; has received grant support from Sanofi and Biogen; and has received speaker fees from Abbvie, Almirall, Biogen, medDay Pharmaceuticals, Merck Serono, Novartis, Roche, Sanofi, and Teva—none in relation to this study. R.P. has received speaker honoraria, research support, and consultancy fees from Janssen, Eli Lilly, Biogen, Wilmar Schwabe, Takeda, Novo Nordisk, and Bayer Healthcare. N.K. has received speaker honoraria from Novartis and Regeneron and research grants from Regeneron—none in relationship to this study. M.I.T., H.S.B., M.N., and A.E. received speaker honoraria from Miltenyi Biotec—none in relation to this study. A.E. is co-founder of Deep Piction and 1X1 Biotech.

INCLUSION AND DIVERSITY

We support inclusive, diverse, and equitable conduct of research. We worked to ensure sex balance in the selection of non-human subjects. We worked to ensure diversity in experimental samples through the selection of the genomic datasets. One or more of the authors of this paper self-identifies as an under-represented ethnic minority in their field of research or within their geographical location. One or more of the authors of this paper self-identifies as a gender minority in their field of research. One or more of the authors of this paper self-identifies as a member of the LGBTQIA+ community. We avoided “helicopter science” practices by including the participating local contributors from the region where we conducted the research as authors on the paper.

Received: December 6, 2021

Revised: April 24, 2023

Accepted: July 7, 2023

Published: August 9, 2023

REFERENCES

1. Rustenhoven, J., and Kipnis, J. (2022). Brain borders at the central stage of neuroimmunology. *Nature* 612, 417–429. <https://doi.org/10.1038/s41586-022-05474-7>.
2. Cai, R., Pan, C., Ghasemigharagoz, A., Todorov, M.I., Förster, B., Zhao, S., Bhatia, H.S., Parra-Damas, A., Mrowka, L., Theodorou, D., et al. (2019). Panoptic imaging of transparent mice reveals whole-body neuronal projections and skull-meninges connections. *Nat. Neurosci.* 22, 317–327. <https://doi.org/10.1038/s41593-018-0301-3>.
3. Cai, R., Pan, C., Ghasemigharagoz, A., Todorov, M.I., Förster, B., Zhao, S., Bhatia, H.S., Mrowka, L., Theodorou, D., Rempfler, M., et al. (2019). Panoptic vDISCO imaging reveals neuronal connectivity, remote trauma effects and meningeal vessels in intact transparent mice. Preprint at bioRxiv. <https://doi.org/10.1101/374785v1>.
4. Herisson, F., Frodermann, V., Courties, G., Rohde, D., Sun, Y., Vandoorne, K., Wojtkiewicz, G.R., Masson, G.S., Vinegoni, C., Kim, J., et al. (2018). Direct vascular channels connect skull bone marrow and the brain surface enabling myeloid cell migration. *Nat. Neurosci.* 21, 1209–1217. <https://doi.org/10.1038/s41593-018-0213-2>.
5. Cugurra, A., Mamuladze, T., Rustenhoven, J., Dykstra, T., Beroshvili, G., Greenberg, Z.J., Baker, W., Papadopoulos, Z., Drieu, A., Blackburn, S., et al. (2021). Skull and vertebral bone marrow are myeloid cell reservoirs for the meninges and CNS parenchyma. *Science* 373, eabf7844. <https://doi.org/10.1126/science.abf7844>.
6. Brioschi, S., Wang, W.-L., Peng, V., Wang, M., Shchukina, I., Greenberg, Z.J., Bando, J.K., Jaeger, N., Czepielewski, R.S., Swain, A., et al. (2021). Heterogeneity of meningeal B cells reveals a lymphopoietic niche at the CNS borders. *Science* 373, eabf9277. <https://doi.org/10.1126/science.abf9277>.
7. Wang, Y., Chen, D., Xu, D., Huang, C., Xing, R., He, D., and Xu, H. (2021). Early developing B cells undergo negative selection by central nervous system-specific antigens in the meninges. *Immunity* 54, 2784–2794.e6. <https://doi.org/10.1016/j.immuni.2021.09.016>.
8. Rustenhoven, J., Drieu, A., Mamuladze, T., de Lima, K.A., Dykstra, T., Wall, M., Papadopoulos, Z., Kanamori, M., Salvador, A.F., Baker, W., et al. (2021). Functional characterization of the dural sinuses as a neuro-immune interface. *Cell* 184, 1000–1016.e27. <https://doi.org/10.1016/j.cell.2020.12.040>.
9. Van Hove, H., Martens, L., Scheyltjens, I., De Vlaminc, K., Pombo Antunes, A.R., De Prijck, S., Vandamme, N., De Schepper, S., Van Isterdael, G., Scott, C.L., et al. (2019). A single-cell atlas of mouse brain macrophages reveals unique transcriptional identities shaped by ontogeny and tissue environment. *Nat. Neurosci.* 22, 1021–1035. <https://doi.org/10.1038/s41593-019-0393-4>.
10. Mrdjen, D., Pavlovic, A., Hartmann, F.J., Schreiner, B., Utz, S.G., Leung, B.P., Lelios, I., Heppner, F.L., Kipnis, J., Merkler, D., et al. (2018). High-dimensional single-cell mapping of central nervous system immune cells reveals distinct myeloid subsets in health, aging, and disease. *Immunity* 48, 380–395.e6. <https://doi.org/10.1016/j.immuni.2018.01.011>.
11. Jordão, M.J.C., Sankowski, R., Brendecke, S.M., Sagar, A., Locatelli, G., Tai, Y.-H., Tay, T.L., Schramm, E., Armbruster, S., Hagemeyer, N., et al. (2019). Single-cell profiling identifies myeloid cell subsets with distinct fates during neuroinflammation. *Science* 363, eaat7554. <https://doi.org/10.1126/science.aat7554>.
12. Schafflick, D., Wolbert, J., Heming, M., Thomas, C., Hartlehnert, M., Börsch, A.-L., Ricci, A., Martin-Salamanca, S., Li, X., Lu, I.-N., et al. (2021). Single-cell profiling of CNS border compartment leukocytes reveals that B cells and their progenitors reside in non-diseased meninges.

- Nat. Neurosci. 24, 1225–1234. <https://doi.org/10.1038/s41593-021-00880-y>.
13. Beuker, C., Schafflick, D., Strecker, J.-K., Heming, M., Li, X., Wolbert, J., Schmidt-Pogoda, A., Thomas, C., Kuhlmann, T., Aranda-Pardos, I., et al. (2022). Stroke induces disease-specific myeloid cells in the brain parenchyma and pia. *Nat. Commun.* 13, 945. <https://doi.org/10.1038/s41467-022-28593-1>.
14. Mazzitelli, J.A., Smyth, L.C.D., Cross, K.A., Dykstra, T., Sun, J., Du, S., Mamuladze, T., Smirnov, I., Rustenhoven, J., and Kipnis, J. (2022). Cerebrospinal fluid regulates skull bone marrow niches via direct access through dural channels. *Nat. Neurosci.* 25, 555–560. <https://doi.org/10.1038/s41593-022-01029-1>.
15. Zaro, B.W., Noh, J.J., Mascetti, V.L., Demeter, J., George, B., Zukowska, M., Gulati, G.S., Sinha, R., Flynn, R.A., Banuelos, A., et al. (2020). Proteomic analysis of young and old mouse hematopoietic stem cells and their progenitors reveals post-transcriptional regulation in stem cells. *eLife* 9, e62210. <https://doi.org/10.7554/eLife.62210>.
16. Ryan, D.G., Knatko, E.V., Casey, A.M., Hukelmann, J.L., Dayalan Naidu, S., Brenes, A.J., Ekkunagul, T., Baker, C., Higgins, M., Tronci, L., et al. (2022). Nrf2 activation reprograms macrophage intermediary metabolism and suppresses the type I interferon response. *iScience* 25, 103827. <https://doi.org/10.1016/j.isci.2022.103827>.
17. Chumak, V., Sielatycka, K., Ciechanowicz, A., Bujko, K., Ratajczak, M.Z., and Kucia, M. (2023). Proteomic analysis of murine bone marrow very small embryonic-like stem cells at steady-state conditions and after in vivo stimulation by nicotinamide and follicle-stimulating factor reflects their germ-lineage origin and multi germ layer differentiation potential. *Stem Cell Rev. Rep.* 19, 120–132. <https://doi.org/10.1007/s12015-022-10445-6>.
18. Guérit, D., Marie, P., Morel, A., Maurin, J., Verollet, C., Raynaud-Messina, B., Urbach, S., and Blangy, A. (2020). Primary myeloid cell proteomics and transcriptomics: importance of β -tubulin isoforms for osteoclast function. *J. Cell Sci.* 133, jcs239772. <https://doi.org/10.1242/jcs.239772>.
19. Andersson, S., Nilsson, K., Fagerberg, L., Hallström, B.M., Sundström, C., Danielsson, A., Edlund, K., Uhlen, M., and Asplund, A. (2014). The transcriptomic and proteomic landscapes of bone marrow and secondary lymphoid tissues. *PLoS One* 9, e115911. <https://doi.org/10.1371/journal.pone.0115911>.
20. Wang, D., Eraslan, B., Wieland, T., Hallström, B., Hopf, T., Zolg, D.P., Zecha, J., Asplund, A., Li, L.H., Meng, C., et al. (2019). A deep proteome and transcriptome abundance atlas of 29 healthy human tissues. *Mol. Syst. Biol.* 15, e8503. <https://doi.org/10.15252/msb.20188503>.
21. Hennrich, M.L., Romanov, N., Horn, P., Jaeger, S., Eckstein, V., Steeples, V., Ye, F., Ding, X., Poisa-Beiro, L., Lai, M.C., et al. (2018). Cell-specific proteome analyses of human bone marrow reveal molecular features of age-dependent functional decline. *Nat. Commun.* 9, 4004. <https://doi.org/10.1038/s41467-018-06353-4>.
22. Tonglin, H., Yanna, Z., Xiaoling, Y., Ruilan, G., and Liming, Y. (2021). Single-cell RNA-seq of bone marrow cells in aplastic anemia. *Front. Genet.* 12, 745483.
23. Ho, A.D., Horn, P., Hennrich, M., Jaeger, S., Romanov, N., Ding, X., Bork, P., Aloy, P., and Gavin, A.-C. (2016). Proteomics analysis of cellular network in human bone marrow reveals lineage skewing towards megakaryocytes and decrease in lymphoid development upon aging. *Blood* 128, 2658. <https://doi.org/10.1182/blood.V128.22.2658.2658>.
24. Lourdopoulos, A., Mamrak, U., Roth, S., Balbi, M., Shrouder, J., Liesz, A., Hellal, F., and Plesnila, N. (2017). Inadequate food and water intake determine mortality following stroke in mice. *J. Cereb. Blood Flow Metab.* 37, 2084–2097. <https://doi.org/10.1177/0271678X16660986>.
25. Liesz, A., Dalpke, A., Mracsko, E., Antoine, D.J., Roth, S., Zhou, W., Yang, H., Na, S.Y., Akhisaroglu, M., Fleming, T., et al. (2015). DAMP signaling is a key pathway inducing immune modulation after brain injury. *J. Neurosci.* 35, 583–598. <https://doi.org/10.1523/JNEUROSCI.2439-14.2015>.
26. Roth, S., Yang, J., Cramer, J.V., Malik, R., and Liesz, A. (2021). Detection of cytokine-induced sickness behavior after ischemic stroke by an optimized behavioral assessment battery. *Brain Behav. Immun.* 91, 668–672. <https://doi.org/10.1016/j.bbi.2020.11.016>.
27. Nowotschin, S., and Hadjantonakis, A.-K. (2009). Use of KikGR a photoconvertible green-to-red fluorescent protein for cell labeling and lineage analysis in ES cells and mouse embryos. *BMC Dev. Biol.* 9, 49. <https://doi.org/10.1186/1471-213X-9-49>.
28. Pan, C., Schoppe, O., Parra-Damas, A., Cai, R., Todorov, M.I., Gondi, G., von Neubeck, B., Böğürçü-Seidel, N., Seidel, S., Sleiman, K., et al. (2019). Deep learning reveals cancer metastasis and therapeutic antibody targeting in the entire body. *Cell* 179, 1661–1676.e19. <https://doi.org/10.1016/j.cell.2019.11.013>.
29. Herring, J.A., Elison, W.S., and Tessem, J.S. (2019). Function of Nr4a orphan nuclear receptors in proliferation, apoptosis and fuel utilization across tissues. *Cells* 8, 1373. <https://doi.org/10.3390/cells8111373>.
30. Strecker, J.-K., Liebmann, M., Revenstorff, J., Beuker, C., Schmidt-Pogoda, A., Hücke, S., Vogl, T., Roth, J., Thomas, C., Kuhlmann, T., et al. (2022). The nuclear receptor NR4A1 restrains neutrophil granulocyte mediated brain damage in cerebral ischemia. Preprint at bioRxiv. <https://doi.org/10.1101/2022.02.27.482146>.
31. Hewett, S.J., Jackman, N.A., and Claycomb, R.J. (2012). Interleukin-1 β in central nervous system injury and repair. *Eur. J. Neurodegener. Dis.* 1, 195–211.
32. Hellmann, J., Tang, Y., Zhang, M.J., Hai, T., Bhatnagar, A., Srivastava, S., and Spite, M. (2015). Atf3 negatively regulates Ptg2/Cox2 expression during acute inflammation. *Prostaglandins Other Lipid Mediat.* 116–117, 49–56. <https://doi.org/10.1016/j.prostaglandins.2015.01.001>.
33. Papageorgiou, A.-P., Swinnen, M., Vanhoutte, D., VandenDriessche, T., Chuah, M., Lindner, D., Verhesen, W., de Vries, B., D'hooge, J., Lutgens, E., et al. (2012). Thrombospondin-2 prevents cardiac injury and dysfunction in viral myocarditis through the activation of regulatory T-cells. *Cardiovasc. Res.* 94, 115–124. <https://doi.org/10.1093/cvr/cvs077>.
34. Kim, S.H., Jung, I.R., and Hwang, S.S. (2022). Emerging role of anti-proliferative protein BTG1 and BTG2. *BMB Rep.* 55, 380–388. <https://doi.org/10.5483/BMBRep.2022.55.8.092>.
35. Cibrián, D., and Sánchez-Madrid, F. (2017). CD69: from activation marker to metabolic gatekeeper. *Eur. J. Immunol.* 47, 946–953. <https://doi.org/10.1002/eji.201646837>.
36. MacKenzie, A.E., Lappin, J.E., Taylor, D.L., Nicklin, S.A., and Milligan, G. (2011). GPR35 as a novel therapeutic target. *Front. Endocrinol.* 2, 68.
37. Wang, F., Flanagan, J., Su, N., Wang, L.-C., Bui, S., Nielson, A., Wu, X., Vo, H.-T., Ma, X.-J., and Luo, Y. (2012). RNAscope: a novel in situ RNA analysis platform for formalin-fixed, paraffin-embedded tissues. *J. Mol. Diagn.* 14, 22–29. <https://doi.org/10.1016/j.jmoldx.2011.08.002>.
38. Gong, T., Liu, L., Jiang, W., and Zhou, R. (2020). DAMP-sensing receptors in sterile inflammation and inflammatory diseases. *Nat. Rev. Immunol.* 20, 95–112. <https://doi.org/10.1038/s41577-019-0215-7>.
39. Efremova, M., Vento-Tormo, M., Teichmann, S.A., and Vento-Tormo, R. (2020). CellPhoneDB: inferring cell–cell communication from combined expression of multi-subunit ligand–receptor complexes. *Nat. Protoc.* 15, 1484–1506. <https://doi.org/10.1038/s41596-020-0292-x>.
40. Deng, H., Hu, N., Wang, C., Chen, M., and Zhao, M.-H. (2018). Interaction between CD177 and platelet endothelial cell adhesion molecule-1 down-regulates membrane-bound proteinase-3 (PR3) expression on neutrophils and attenuates neutrophil activation induced by PR3-ANCA. *Arthritis Res. Ther.* 20, 213. <https://doi.org/10.1186/s13075-018-1710-0>.
41. Farr, L., Ghosh, S., and Moonah, S. (2020). Role of MIF cytokine/CD74 receptor pathway in protecting against injury and promoting repair. *Front. Immunol.* 11, 1273. <https://doi.org/10.3389/fimmu.2020.01273>.
42. La Manno, G., Soldatov, R., Zeisel, A., Braun, E., Hochgerner, H., Petukhov, V., Lidschreiber, K., Kastrioti, M.E., Lönnerberg, P., Furlan, A., et al.

- (2018). RNA velocity of single cells. *Nature* 560, 494–498. <https://doi.org/10.1038/s41586-018-0414-6>.
43. Bergen, V., Lange, M., Peidli, S., Wolf, F.A., and Theis, F.J. (2020). Generalizing RNA velocity to transient cell states through dynamical modeling. *Nat. Biotechnol.* 38, 1408–1414. <https://doi.org/10.1038/s41587-020-0591-3>.
 44. Haghverdi, L., Büttner, M., Wolf, F.A., Büttner, F., and Theis, F.J. (2016). Diffusion pseudotime robustly reconstructs lineage branching. *Nat. Methods* 13, 845–848. <https://doi.org/10.1038/nmeth.3971>.
 45. Saelens, W., Cannoodt, R., Todorov, H., and Saeys, Y. (2019). A comparison of single-cell trajectory inference methods. *Nat. Biotechnol.* 37, 547–554. <https://doi.org/10.1038/s41587-019-0071-9>.
 46. CFB protein expression summary - The Human Protein Atlas. <https://www.proteinatlas.org/ENSG00000243649-CFB>.
 47. Reyes, R., Cardenas, B., Machado-Pineda, Y., and Cabañas, C. (2018). Tetraspanin CD9: A key regulator of cell adhesion in the immune system. *Front. Immunol.* 9, 863.
 48. Nid nidogen 2 [Mus musculus (house mouse)] - Gene - NCBI. <https://www.ncbi.nlm.nih.gov/gene?Db=gene&Cmd=DetailsSearch&Term=18074>.
 49. Liu, Y., Beyer, A., and Aebersold, R. (2016). On the dependency of cellular protein levels on mRNA abundance. *Cell* 165, 535–550. <https://doi.org/10.1016/j.cell.2016.03.014>.
 50. Shah, T., Leurgans, S.E., Mehta, R.I., Yang, J., Galloway, C.A., de Mesy Bentley, K.L., Schneider, J.A., and Mehta, R.I. (2023). Arachnoid granulations are lymphatic conduits that communicate with bone marrow and dura-arachnoid stroma. *J. Exp. Med.* 220, e20220618. <https://doi.org/10.1084/jem.20220618>.
 51. Kündig, T.M., Bachmann, M.F., DiPaolo, C., Simard, J.J.L., Battagay, M., Lother, H., Gessner, A., Kuhlcke, K., Ohashi, P.S., Hengartner, H., et al. (1995). Fibroblasts as efficient antigen-presenting cells in lymphoid organs. *Science* 268, 1343–1347. <https://doi.org/10.1126/science.7761853>.
 52. Wang, H., Leng, Y., and Gong, Y. (2018). Bone marrow fat and hematopoiesis. *Front. Endocrinol.* 9, 694.
 53. Robles, H., Park, S., Joens, M.S., Fitzpatrick, J.A.J., Craft, C.S., and Scheller, E.L. (2019). Characterization of the bone marrow adipocyte niche with three-dimensional electron microscopy. *Bone* 118, 89–98. <https://doi.org/10.1016/j.bone.2018.01.020>.
 54. Tratwal, J., Rojas-Sutterlin, S., Bataclan, C., Blum, S., and Naveiras, O. (2021). Bone marrow adiposity and the hematopoietic niche: A historical perspective of reciprocity, heterogeneity, and lineage commitment. *Best Pract. Res. Clin. Endocrinol. Metab.* 35, 101564. <https://doi.org/10.1016/j.beem.2021.101564>.
 55. Shi, S.X., Shi, K., and Liu, Q. (2021). Brain injury instructs bone marrow cellular lineage destination to reduce neuroinflammation. *Sci. Transl. Med.* 13, eabc7029. <https://doi.org/10.1126/scitranslmed.abc7029>.
 56. Sutherland, T.E., Dyer, D.P., and Allen, J.E. (2023). The extracellular matrix and the immune system: A mutually dependent relationship. *Science* 379, eabp8964. <https://doi.org/10.1126/science.abp8964>.
 57. Ben Shoham, A., Rot, C., Stern, T., Krief, S., Akiva, A., Dadosh, T., Sabany, H., Lu, Y., Kadler, K.E., and Zelzer, E. (2016). Deposition of collagen type I onto skeletal endothelium reveals a new role for blood vessels in regulating bone morphology. *Development* 143, 3933–3943. <https://doi.org/10.1242/dev.139253>.
 58. Maier, T., Güell, M., and Serrano, L. (2009). Correlation of mRNA and protein in complex biological samples. *FEBS Lett.* 583, 3966–3973. <https://doi.org/10.1016/j.febslet.2009.10.036>.
 59. de Sousa Abreu, R., Penalva, L.O., Marcotte, E.M., and Vogel, C. (2009). Global signatures of protein and mRNA expression levels. *Mol. Biosyst.* 5, 1512–1526. <https://doi.org/10.1039/b908315d>.
 60. Guilarte, T.R., Rodichkin, A.N., McGlothlin, J.L., Acanda De La Rocha, A.M., and Azzam, D.J. (2022). Imaging neuroinflammation with TSPO: A new perspective on the cellular sources and subcellular localization. *Pharmacol. Ther.* 234, 108048. <https://doi.org/10.1016/j.pharmthera.2021.108048>.
 61. Werry, E.L., Bright, F.M., Piguet, O., Ittner, L.M., Halliday, G.M., Hodges, J.R., Kiernan, M.C., Loy, C.T., Kril, J.J., and Kassiou, M. (2019). Recent developments in TSPO PET imaging as a biomarker of neuroinflammation in neurodegenerative disorders. *Int. J. Mol. Sci.* 20, 3161. <https://doi.org/10.3390/ijms20133161>.
 62. Palleis, C., Sauerbeck, J., Beyer, L., Harris, S., Schmitt, J., Morenas-Rodríguez, E., Finze, A., Nitschmann, A., Ruch-Rubinstein, F., Eckenweber, F., et al. (2021). In vivo assessment of neuroinflammation in 4-repeat tauopathies. *Mov. Disord.* 36, 883–894. <https://doi.org/10.1002/mds.28395>.
 63. Unterrainer, M., Mahler, C., Vomacka, L., Lindner, S., Havla, J., Brendel, M., Böning, G., Ertl-Wagner, B., Kämpfel, T., Milenkovic, V.M., et al. (2018). TSPO PET with [18F]GE-180 sensitively detects focal neuroinflammation in patients with relapsing-remitting multiple sclerosis. *Eur. J. Nucl. Med. Mol. Imaging* 45, 1423–1431. <https://doi.org/10.1007/s00259-018-3974-7>.
 64. Hansson, O., Lehmann, S., Otto, M., Zetterberg, H., and Lewczuk, P. (2019). Advantages and disadvantages of the use of the CSF Amyloid β (A β) 42/40 ratio in the diagnosis of Alzheimer's disease. *Alzheimers Res. Ther.* 11, 34. <https://doi.org/10.1186/s13195-019-0485-0>.
 65. Braak, H., and Braak, E. (1991). Neuropathological staging of Alzheimer-related changes. *Acta Neuropathol.* 82, 239–259. <https://doi.org/10.1007/BF00308809>.
 66. Fan, L., Li, H., Zhuo, J., Zhang, Y., Wang, J., Chen, L., Yang, Z., Chu, C., Xie, S., Laird, A.R., et al. (2016). The human Brainnetome atlas: A new brain atlas based on connectome architecture. *Cereb. Cortex N. Y. NY*: 1991 26, 3508–3526. <https://doi.org/10.1093/cercor/bhw157>.
 67. Yang, C., Hawkins, K.E., Doré, S., and Candelario-Jalil, E. (2019). Neuroinflammatory mechanisms of blood-brain barrier damage in ischemic stroke. *Am. J. Physiol. Cell Physiol.* 316, C135–C153. <https://doi.org/10.1152/ajpcell.00136.2018>.
 68. Jickling, G.C., Liu, D., Ander, B.P., Stamova, B., Zhan, X., and Sharp, F.R. (2015). Targeting neutrophils in ischemic stroke: translational insights from experimental studies. *J. Cereb. Blood Flow Metab.* 35, 888–901. <https://doi.org/10.1038/jcbfm.2015.45>.
 69. Pulous, F.E., Cruz-Hernández, J.C., Yang, C., Kaya, Z., Wojtkiewicz, G., Capen, D., Brown, D., Wu, J.W., Vinegoni, C., Yamazoe, M., et al. (2021). Cerebrospinal fluid outflow through skull channels instructs cranial hematopoiesis. <https://doi.org/10.1101/2021.08.27.457954>.
 70. Barc, K., and Kuźma-Kozakiewicz, M. (2019). Positron emission tomography neuroimaging in neurodegenerative diseases: Alzheimer's disease, Parkinson's disease, and amyotrophic lateral sclerosis. *Neurol. Neurochir. Pol.* 53, 99–112. <https://doi.org/10.5603/PJNNS.a2019.0013>.
 71. Hadjikhani, N., Albrecht, D.S., Mainero, C., Ichijo, E., Ward, N., Granziere, C., Zürcher, N.R., Akeju, O., Bonnier, G., Price, J., et al. (2020). Extra-axial inflammatory signal in parameninges in migraine with visual aura. *Ann. Neurol.* 87, 939–949. <https://doi.org/10.1002/ana.25731>.
 72. Wadsworth, H., Jones, P.A., Chau, W.-F., Durrant, C., Fouladi, N., Passmore, J., O'Shea, D., Wynn, D., Morisson-Iveson, V., Ewan, A., et al. (2012). [18F] GE-180: A novel fluorine-18 labelled PET tracer for imaging translocator protein 18kDa (TSPO). *Bioorg. Med. Chem. Lett.* 22, 1308–1313. <https://doi.org/10.1016/j.bmcl.2011.12.084>.
 73. Rejc, L., Gómez-Vallejo, V., Joya, A., Arsequell, G., Egimendia, A., Castellnou, P., Ríos-Anglada, X., Cossio, U., Baz, Z., Iglesias, L., et al. (2022). Longitudinal evaluation of neuroinflammation and oxidative stress in a mouse model of Alzheimer disease using positron emission tomography. *Alzheimers Res. Ther.* 14, 80. <https://doi.org/10.1186/s13195-022-01016-5>.
 74. Fan, Z., Okello, A.A., Brooks, D.J., and Edison, P. (2015). Longitudinal influence of microglial activation and amyloid on neuronal function in

- Alzheimer's disease. *Brain* 138, 3685–3698. <https://doi.org/10.1093/brain/awv288>.
75. Thiel, A., Radlinska, B.A., Paquette, C., Sidel, M., Soucy, J.-P., Schirmacher, R., and Minuk, J. (2010). The temporal dynamics of poststroke neuroinflammation: A longitudinal diffusion tensor imaging-guided PET study with ¹¹C-PK11195 in acute subcortical stroke. *J. Nucl. Med.* 51, 1404–1412. <https://doi.org/10.2967/jnumed.110.076612>.
76. Shi, K., Tian, D.-C., Li, Z.-G., Ducruet, A.F., Lawton, M.T., and Shi, F.-D. (2019). Global brain inflammation in stroke. *Lancet Neurol.* 18, 1058–1066. [https://doi.org/10.1016/S1474-4422\(19\)30078-X](https://doi.org/10.1016/S1474-4422(19)30078-X).
77. Beziere, N., von Schacky, C., Kosanke, Y., Kimm, M., Nunes, A., Licha, K., Aichler, M., Walch, A., Rummeny, E.J., Ntziachristos, V., et al. (2014). Optoacoustic imaging and staging of inflammation in a murine model of arthritis. *Arthritis Rheumatol.* 66, 2071–2078. <https://doi.org/10.1002/art.38642>.
78. Largeau, B., Dupont, A.-C., Guilloteau, D., Santiago-Ribeiro, M.-J., and Arlicot, N. (2017). TSP0 PET imaging: from microglial activation to peripheral sterile inflammatory diseases? *Contrast Media Mol. Imaging* 2017, 6592139. <https://doi.org/10.1155/2017/6592139>.
79. Shah, S., Sinharay, S., Patel, R., Solomon, J., Lee, J.H., Schreiber-Stainthorpe, W., Basuli, F., Zhang, X., Hagen, K.R., Reeder, R., et al. (2022). PET imaging of TSP0 expression in immune cells can assess organ-level pathophysiology in high-consequence viral infections. *Proc. Natl. Acad. Sci. USA* 119, e2110846119. <https://doi.org/10.1073/pnas.2110846119>.
80. Bartos, L.M., Kirchleitner, S.V., Kolabas, Z.I., Quach, S., Blobner, J., Mueller, S.A., Ulukaya, S., Hoeher, L., Horvath, I., Wind-Mark, K., et al. (2023). Deciphering sources of PET signals in the tumor microenvironment of glioblastoma at cellular resolution. Preprint at bioRxiv. <https://doi.org/10.1101/2023.01.26.522174>.
81. Bartos, L.M., Kunte, S.T., Beumers, P., Xiang, X., Wind, K., Ziegler, S., Bartenstein, P., Choi, H., Lee, D.S., Haass, C., et al. (2022). Single-cell radiotracer allocation via immunomagnetic sorting to disentangle PET signals at cellular resolution. *J. Nucl. Med.* 63, 1459–1462. <https://doi.org/10.2967/jnumed.122.264171>.
82. Schindelin, J., Arganda-Carreras, I., Frise, E., Kaynig, V., Longair, M., Pietzsch, T., Preibisch, S., Rueden, C., Saalfeld, S., Schmid, B., et al. (2012). Fiji: an open-source platform for biological-image analysis. *Nat. Methods* 9, 676–682. <https://doi.org/10.1038/Nmeth.2019>.
83. Wolf, F.A., Angerer, P., and Theis, F.J. (2018). SCANPY: large-scale single-cell gene expression data analysis. *Genome Biol.* 19, 15. <https://doi.org/10.1186/s13059-017-1382-0>.
84. Percie du Sert, N.P., Hurst, V., Ahluwalia, A., Alam, S., Avey, M.T., Baker, M., Browne, W.J., Clark, A., Cuthill, I.C., Dirnagl, U., et al. (2020). The ARRIVE guidelines 2.0. The ARRIVE guidelines 2.0: Updated guidelines for reporting animal research. *PLoS Biol.* 18, e3000410. <https://doi.org/10.1371/journal.pbio.3000410>.
85. Xiang, X., Wind, K., Wiedemann, T., Blume, T., Shi, Y., Briel, N., Beyer, L., Biechele, G., Eckenweber, F., Zatcepin, A., et al. (2021). Microglial activation states drive glucose uptake and FDG-PET alterations in neurodegenerative diseases. *Sci. Transl. Med.* 13, eabe5640.
86. Schmitt, J., Palleis, C., Sauerbeck, J., Unterrainer, M., Harris, S., Prix, C., Weidinger, E., Katzdobler, S., Wagemann, O., Danek, A., et al. (2021). Dual-phase β -amyloid PET captures neuronal injury and amyloidosis in corticobasal syndrome. *Front. Aging Neurosci.* 13, 661284. <https://doi.org/10.3389/fnagi.2021.661284>.
87. Wang, T., Ouzounov, D.G., Wu, C., Horton, N.G., Zhang, B., Wu, C.-H., Zhang, Y., Schnitzer, M.J., and Xu, C. (2018). Three-photon imaging of mouse brain structure and function through the intact skull. *Nat. Methods* 15, 789–792. <https://doi.org/10.1038/s41592-018-0115-y>.
88. Khalin, I., Heimburger, D., Melnychuk, N., Collot, M., Groschup, B., Helal, F., Reisch, A., Plesnila, N., and Klymchenko, A.S. (2020). Ultrabright fluorescent polymeric nanoparticles with a stealth pluronic shell for live tracking in the mouse brain. *ACS Nano* 14, 9755–9770. <https://doi.org/10.1021/acsnano.0c01505>.
89. Cai, R., Kolabas, Z.I., Pan, C., Mai, H., Zhao, S., Kaltenecker, D., Voigt, F.F., Molbay, M., Ohn, T.L., Vincke, C., et al. (2023). Whole-mouse clearing and imaging at the cellular level with vDISCO. *Nat. Protoc.* 18, 1197–1242. <https://doi.org/10.1038/s41596-022-00788-2>.
90. Susaki, E.A., Tainaka, K., Perrin, D., Kishino, F., Tawara, T., Watanabe, T.M., Yokoyama, C., Onoe, H., Eguchi, M., Yamaguchi, S., et al. (2014). Whole-brain imaging with single-cell resolution using chemical cocktails and computational analysis. *Cell* 157, 726–739. <https://doi.org/10.1016/j.cell.2014.03.042>.
91. Zhao, S., Todorov, M.I., Cai, R., Maskari, R.A., Steinke, H., Kemter, E., Mai, H., Rong, Z., Warmer, M., Stanic, K., et al. (2020). Cellular and molecular probing of intact human organs. *Cell* 180, 796–812.e19. <https://doi.org/10.1016/j.cell.2020.01.030>.
92. Holzwarth, K., Köhler, R., Philipsen, L., Tokoyoda, K., Ladygina, V., Wählby, C., Niesner, R.A., and Hauser, A.E. (2018). Multiplexed fluorescence microscopy reveals heterogeneity among stromal cells in mouse bone marrow sections. *Cytometry A* 93, 876–888. <https://doi.org/10.1002/cyto.a.23526>.
93. Safaiyan, S., Besson-Girard, S., Kaya, T., Cantuti-Castelvetri, L., Liu, L., Ji, H., Schifferer, M., Gouna, G., Usifo, F., Kannaiyan, N., et al. (2021). White matter aging drives microglial diversity. *Neuron* 109, 1100–1117.e10. <https://doi.org/10.1016/j.neuron.2021.01.027>.
94. Picelli, S., Björklund, A.K., Reinius, B., Sagasser, S., Winberg, G., and Sandberg, R. (2014). Tn5 transposase and tagmentation procedures for massively scaled sequencing projects. *Genome Res.* 24, 2033–2040. <https://doi.org/10.1101/gr.177881.114>.
95. Pedersen, K.B., Williams, A., Watt, J., and Ronis, M.J. (2019). Improved method for isolating high-quality RNA from mouse bone with RNAlater at room temperature. *Bone Rep.* 11, 100211. <https://doi.org/10.1016/j.bonr.2019.100211>.
96. Bayraktar, O.A., Bartels, T., Holmqvist, S., Kleshchevnikov, V., Martirosyan, A., Polioudakis, D., Ben Haim, L., Young, A.M.H., Batiuk, M.Y., Prakash, K., et al. (2020). Astrocyte layers in the mammalian cerebral cortex revealed by a single-cell in situ transcriptomic map. *Nat. Neurosci.* 23, 500–509. <https://doi.org/10.1038/s41593-020-0602-1>.
97. Kislinger, G., Gnägi, H., Kerschensteiner, M., Simons, M., Misgeld, T., and Schifferer, M. (2020). ATUM-FIB microscopy for targeting and multi-scale imaging of rare events in mouse cortex. *STAR Protoc.* 1, 100232. <https://doi.org/10.1016/j.xpro.2020.100232>.
98. Bhatia, H.S., Brunner, A.-D., Öztürk, F., Kapoor, S., Rong, Z., Mai, H., Thielert, M., Ali, M., Al-Maskari, R., Paetzold, J.C., et al. (2022). Spatial proteomics in three-dimensional intact specimens. *Cell* 185, 5040–5058.e19. <https://doi.org/10.1016/j.cell.2022.11.021>.
99. Demichev, V., Messner, C.B., Vernardis, S.I., Lilley, K.S., and Ralser, M. (2020). DIA-NN: neural networks and interference correction enable deep proteome coverage in high throughput. *Nat. Methods* 17, 41–44. <https://doi.org/10.1038/s41592-019-0638-x>.
100. Overhoff, F., Brendel, M., Jaworska, A., Korzhova, V., Delker, A., Probst, F., Focke, C., Gildehaus, F.-J., Carlsen, J., Baumann, K., et al. (2016). Automated spatial brain normalization and hindbrain white matter reference tissue give improved [¹⁸F]-florbetaben PET quantitation in Alzheimer's model mice. *Front. Neurosci.* 10, 45. <https://doi.org/10.3389/fnins.2016.00045>.
101. Brendel, M., Probst, F., Jaworska, A., Overhoff, F., Korzhova, V., Albert, N.L., Beck, R., Lindner, S., Gildehaus, F.-J., Baumann, K., et al. (2016). Glial activation and glucose metabolism in a transgenic amyloid mouse model: A triple-tracer PET study. *J. Nucl. Med.* 57, 954–960. <https://doi.org/10.2967/jnumed.115.167858>.
102. Reifschneider, A., Robinson, S., van Lengerich, B., Gnörich, J., Logan, T., Heindl, S., Vogt, M.A., Weidinger, E., Riedl, L., Wind, K., et al. (2021). Loss of TREM2 reduces hyperactivation of progranulin deficient microglia but not lysosomal pathology. <https://doi.org/10.1101/2021.07.08.451574>.

103. Albert, N.L., Unterrainer, M., Fleischmann, D.F., Lindner, S., Vettermann, F., Brunegrat, A., Vomacka, L., Brendel, M., Wenter, V., Wetzel, C., et al. (2017). TSPO PET for glioma imaging using the novel ligand 18F-GE-180: first results in patients with glioblastoma. *Eur. J. Nucl. Med. Mol. Imaging* 44, 2230–2238. <https://doi.org/10.1007/s00259-017-3799-9>.
104. Luecken, M.D., and Theis, F.J. (2019). Current best practices in single-cell RNA-seq analysis: a tutorial. *Mol. Syst. Biol.* 15, e8746. <https://doi.org/10.15252/msb.20188746>.
105. Lun, A.T., Bach, K., and Marioni, J.C. (2016). Pooling across cells to normalize single-cell RNA sequencing data with many zero counts. *Genome Biol.* 17, 75. <https://doi.org/10.1186/s13059-016-0947-7>.
106. Wolf, F.A., Hamey, F.K., Plass, M., Solana, J., Dahlin, J.S., Göttgens, B., Rajewsky, N., Simon, L., and Theis, F.J. (2019). PAGA: graph abstraction reconciles clustering with trajectory inference through a topology preserving map of single cells. *Genome Biol.* 20, 59. <https://doi.org/10.1186/s13059-019-1663-x>.
107. Gulati, G.S., Sikandar, S.S., Wesche, D.J., Manjunath, A., Bharadwaj, A., Berger, M.J., Ilagan, F., Kuo, A.H., Hsieh, R.W., Cai, S., et al. (2020). Single-cell transcriptional diversity is a hallmark of developmental potential. *Science* 367, 405–411. <https://doi.org/10.1126/science.aax0249>.
108. Hie, B., Cho, H., DeMeo, B., Bryson, B., and Berger, B. (2019). Geometric sketching compactly summarizes the single-cell transcriptomic landscape. *Cell Syst.* 8, 483–493.e7. <https://doi.org/10.1016/j.cels.2019.05.003>.
109. Raudvere, U., Kolberg, L., Kuzmin, I., Arak, T., Adler, P., Peterson, H., and Vilo, J. (2019). g:profiler: a web server for functional enrichment analysis and conversions of gene lists (2019 update). *Nucleic Acids Res.* 47, W191–W198. <https://doi.org/10.1093/nar/gkz369>.
110. Huang, X., and Huang, Y. (2021). Cellsnp-lite: an efficient tool for genotyping single cells. *Bioinformatics* 37, 4569–4571. <https://doi.org/10.1093/bioinformatics/btab358>.
111. Huang, Y., McCarthy, D.J., and Stegle, O. (2019). Vireo: bayesian demultiplexing of pooled single-cell RNA-seq data without genotype reference. *Genome Biol.* 20, 273. <https://doi.org/10.1186/s13059-019-1865-2>.
112. Patro, R., Duggal, G., Love, M.I., Irizarry, R.A., and Kingsford, C. (2017). Salmon provides fast and bias-aware quantification of transcript expression. *Nat. Methods* 14, 417–419. <https://doi.org/10.1038/nmeth.4197>.
113. Patel, H., Ewels, P., Peltzer, A., Botvinnik, O., Sturm, G., Moreno, D., Vemuri, P., Silviamorins, A., Garcia, M.U., Pantano, L., et al. (2023). nf-core/rnaseq: nf-core/rnaseq v3.11.1—Plastered Radium Rhino. <https://doi.org/10.5281/zenodo.7789554>.
114. Love, M.I., Huber, W., and Anders, S. (2014). Moderated estimation of fold change and dispersion for RNA-seq data with DESeq2. *Genome Biol.* 15, 550. <https://doi.org/10.1186/s13059-014-0550-8>.
115. Berg, S., Kutra, D., Kroeger, T., Straehle, C.N., Kausler, B.X., Haubold, C., Schiegg, M., Ales, J., Beier, T., Rudy, M., et al. (2019). ilastik: interactive machine learning for (bio)image analysis. *Nat. Methods* 16, 1226–1232. <https://doi.org/10.1038/s41592-019-0582-9>.
116. Kuleshov, M.V., Jones, M.R., Rouillard, A.D., Fernandez, N.F., Duan, Q., Wang, Z., Koplev, S., Jenkins, S.L., Jagodnik, K.M., Lachmann, A., et al. (2016). Enrichr: a comprehensive gene set enrichment analysis web server 2016 update. *Nucleic Acids Res.* 44, W90–W97. <https://doi.org/10.1093/nar/gkw377>.
117. Rezaie, N., Reese, F., and Mortazavi, A. (2022). PyWGCNA: A Python package for weighted gene co-expression network analysis. <https://doi.org/10.1101/2022.08.22.504852>.
118. Rominger, A., Brendel, M., Burgold, S., Keppler, K., Baumann, K., Xiong, G., Mille, E., Gildehaus, F.-J., Carlsen, J., Schlichtiger, J., et al. (2013). Longitudinal assessment of cerebral β -amyloid deposition in mice over-expressing Swedish mutant β -amyloid precursor protein using 18F-florbetaben PET. *J. Nucl. Med.* 54, 1127–1134. <https://doi.org/10.2967/jnumed.112.114660>.
119. Hammers, A., Allom, R., Koeppe, M.J., Free, S.L., Myers, R., Lemieux, L., Mitchell, T.N., Brooks, D.J., and Duncan, J.S. (2003). Three-dimensional maximum probability atlas of the human brain, with particular reference to the temporal lobe. *Hum. Brain Mapp.* 19, 224–247. <https://doi.org/10.1002/hbm.10123>.
120. Finze, A., Biechele, G., Rauchmann, B.-S., Franzmeier, N., Palleis, C., Katzdobler, S., Weidinger, E., Guersel, S., Schuster, S., Harris, S., et al. (2022). Individual regional associations between A β -, tau- and neurodegeneration (ATN) with microglial activation in patients with primary and secondary tauopathies. Preprint at medRxiv. <https://doi.org/10.1101/2022.11.12.22282082>.

STAR★METHODS

KEY RESOURCES TABLE

| REAGENT or RESOURCE | SOURCE | IDENTIFIER |
|--|-------------------|----------------------------------|
| Antibodies | | |
| Atto647NconjugatedantiGFP nanobooster | Chromotek | Cat.#gba647n-100;RRID:AB_2629215 |
| Anti-NUR77 antibody | Abcam | Cat# ab153914 |
| anti-Lysozyme antibody | Abcam | Cat#ab108508; RRID:AB_10861277 |
| Goat anti-Rabbit IgG (H+L) Highly Cross-Adsorbed Secondary Antibody, Alexa Fluor 647 | Abcam | Cat#A-21245; RRID:AB_141775 |
| APC/Cyanine7 anti-mouse Ly-6G/Ly-6C (Gr-1) Antibody | Biolegend | Cat#108423; RRID:AB_2137486 |
| APC anti-mouse CD11c Antibody | Biolegend | Cat# 117309; RRID:AB_313778 |
| BD Horizon™ BUV395 Rat Anti-Mouse CD45 | BD Biosciences | Cat#565967; RRID:AB_2739420 |
| BD Horizon™ BV421 Rat Anti-Mouse CD117 | BD Biosciences | Cat# 562609; RRID:AB_11154585 |
| BD Pharmingen™ PerCP-Cy5.5 Rat Anti-Mouse F4/80 | BD Biosciences | Cat# 567202; RRID:AB_2916500 |
| Brilliant Violet 510™ anti-mouse I-A/I-E Antibody | Biolegend | Cat# 107635; RRID:AB_2561397 |
| Brilliant Violet 650™ anti-mouse TER-119/Erythroid Cells Antibody | Biolegend | Cat# 116235; RRID:AB_11204244 |
| Brilliant Violet 711™ anti-mouse NK-1.1 Antibody | Biolegend | Cat# 108745; RRID:AB_2563286 |
| Brilliant Violet 785™ anti-mouse/human CD11b Antibody | Biolegend | Cat# 101243; RRID:AB_2561373 |
| PE anti-mouse CD179a (VpreB) Antibody | Biolegend | Cat# 143603; RRID:AB_11147372 |
| PE/Dazzle™ 594 anti-mouse CD182 (CXCR2) Antibody | Biolegend | Cat# 149317; RRID:AB_2750072 |
| BD Pharmingen™ PE-Cy™7 Rat Anti-Mouse Ly-6A/E | BD Biosciences | Cat# 561021; RRID:AB_2034021 |
| BD Pharmingen™ Alexa Fluor® 700 Rat Anti-Mouse CD3 Molecular Complex | BD Biosciences | Cat# 561388; RRID:AB_10642588 |
| Brilliant Violet 605™ anti-mouse Ly-6C Antibody | Biolegend | Cat# 128035; RRID:AB_2562352 |
| BD Pharmingen™ PE-Cy™5 Rat Anti-Mouse CD45R/B220 | BD Biosciences | Cat#553091; RRID:AB_394621 |
| Donkey anti-Rabbit IgG (H+L) Highly Cross-Adsorbed Secondary Antibody, Alexa Fluor 647 | Invitrogen | Cat#A-31573; RRID:AB_2536183 |
| Alexa Fluor 594 Anti-alpha smooth muscle Actin antibody [1A4] | Abcam | Cat#ab202368;RRID:AB_2924381 |
| Anti-PDGFRB antibody produced in rabbit | Merck | Cat# HPA028499; RRID:AB_10602018 |
| Mouse Anti-Human Type IV Collagen-FITC (2F11) | SouthernBiotech | Cat#1460-02; RRID:AB_2794763 |
| Chemicals, peptides, and recombinant proteins | | |
| Methyl-beta-cyclodextrin | Sigma | Cat#332615 |
| Hydroxy-L-proline | Sigma | Cat#441562 |
| 4%paraformaldehyde(PFA) | Morphisto | Cat.#11762.05000 |
| Tetrahydrofuran | Sigma | Cat#186562 |
| Benzyl alcohol | Sigma | Cat#24122 |
| Benzyl benzoate | Sigma | Cat#W213802 |
| Ethylenediamine tetra acetic acid | Carl Roth | Cat#1702922685 |
| CHAPS | Roth | Cat# 1479.4 |
| Guanidine hydrochloride | Roth | Cat# 6069.3 |
| Acetic acid | Roth | Cat# T179.1 |
| TritonX-100 | PanReac Applichem | Cat.#A4975,1000 |
| N-Methyl-diethanolamine | Sigma | Cat.#471828 |
| Dichloromethane | Roth | Cat.#KK47.1 |
| RPE buffer | Qiagen | Cat#1018013 |

(Continued on next page)

Continued

| REAGENT or RESOURCE | SOURCE | IDENTIFIER |
|---|--------------|--------------|
| Propidium iodide | ThermoFisher | Cat.#P3566 |
| Lycopersicon Esculentum (Tomato) Lectin | Invitrogen | Cat.# L32470 |

Critical commercial assays

| | | |
|--|---------------------------------------|---|
| 10x Chromium Single Cell 3' Library & Gel Bead Kit v3 for mouse and v3.1 for human | 10x Genomics | https://www.10xgenomics.com/support/single-cell-gene-expression |
| RNAScope Multiplex Fluorescent Reagent Kit v2 Assay | Advanced cell Diagnostics, Bio-Techne | https://acdbio.com/rnascope-multiplex-fluorescent-v2-assay |

Deposited data

| | | |
|--|------------|---|
| Mass spectrometry raw data | This paper | PRIDE accession code: PXD041665 |
| All code used in this study | This paper | https://github.com/erturklab/skull_immune |
| Patient source file | This paper | Table S3 |
| Single-cell sequencing raw counts matrices and annotation and bulk RNA-sequencing data | This paper | NCBI's GEO: GSE192616 |

Experimental models: Organisms/strains

| | | |
|--|--------------------|--|
| LySM-GFP (Lyz2tm1.1 ^{Graf} , MGI: 2654931) | MMRC | Strain#012039-MU;RRID: MMRRC_012039-MU |
| 5xHAD (B6SJL-Tg(APPswF10n,PSEN1*M146L*L286V)6799Vas/Mmjax MGI:3693208) | Jackson Laboratory | Strain#034848-JAX;RRID: MMRRC_034848-JAX |
| KikGR33 (Tg(CAG-KikGR)33Had/J) | Jackson Laboratory | Strain#013753;RRID:IMSR_JAX:013753 |
| C57BL/6J mouse line | Jackson Laboratory | Strain#:000,664;RRID:IMSR_JAX:000,664 |
| C57BL/6NJ mouse line | Jackson Laboratory | Strain#:005304;RRID:IMSR_JAX:005304 |

Software and algorithms

| | | |
|----------------------------------|---------------------------------|---|
| ImSpector | MiltenyiBiotec | https://www.miltenyibiotec.com/DE-en/products/ultramicroscope-blaze.html |
| Imaris | Bitplane AG | https://imaris.oxinst.com/ |
| Vision4D | Arivis | https://www.arivis.com/de/ |
| Fiji | Schindelin et al. ⁸² | https://imagej.net/software/fiji/ |
| syGlass VR | syGlass | https://www.syglass.io |
| Scanpy v. 1. 6 | Wolf et al. ⁸³ | https://scanpy.readthedocs.io/en/stable/ |
| GraphPadPrism (8.2.1) | GraphPad software | https://www.graphpad.com |
| PMOD | Digilent | https://www.pmod.com/web/ |
| IBM SPSS Statistics version 22.0 | IBM | https://www.ibm.com/spss |
| Image analysis algorithm | This paper | https://github.com/erturklab/skull_immune |

Other

| | | |
|---|---------------------|---|
| 0.22 µm syringe filter | Sartorius | Cat#16532 |
| SCEM medium | Sectionlab | SCEM |
| 70 µm Falcon™ Cell Strainers | Falcon | Cat#08-771-2 |
| 35° ultra-diamond knife | Diatome | https://www.scienceservices.eu/tools-supplies/diamond-knives/ultra |
| EconoSpin(TM) All-in-1 Mini Spin Columns for DNA/RNA extraction | Epoch life sciences | Cat#1920-250 |

RESOURCE AVAILABILITY

Lead contact

Further information and requests for resources should be directed to and will be fulfilled by the lead contact, Ali Erturk (ali.erturk@helmholtz-munich.de).

Materials availability

This study did not generate new unique reagents.

Data and code availability

- Single-cell RNA sequencing data raw counts, matrices and annotation and bulk RNA datasets are available via NCBI's GEO (GSE192616), proteomic data is available on PRIDE, accession code: PXD041665 and patient source file human TSPO-PET imaging study can be found under [supplemental information](#). Imaging data is available upon request from the corresponding author.
- All code used in this study can be found as jupyter notebooks in the project github repository: https://github.com/erturklab/skull_immune.
- Any additional information required to reanalyze the data reported in this paper is available from the [lead contact](#) upon request.

EXPERIMENTAL MODEL AND STUDY PARTICIPANT DETAILS

Animals

Animal housing and experiments in this work were conducted in agreement with the institutional guidelines (Klinikum der Universität München/Ludwig Maximilian University of Munich, Technische Universität München, Regierung von Oberbayern and UK Home Office), after approval of the ethical review board of the government of Upper Bavaria (Regierung von Oberbayern, Munich, Germany), and in accordance with the European directive 2010/63/EU for animal research. The transgenic lines used in this study are C57BL/6, LySM-GFP (Lyz2tm1.1Graf, MGI: 2654931) and 5xFAD (B6SJL-Tg(APPswF1L0n,PSEN1*M146L*L286V)6799Vas/Mmjax MGI:3693208) acquired from Charles River and Jackson Laboratory. KikGR33 (Tg(CAG-KikGR)33Hadj/J) mice were kindly given to C.B. by Dr. Josef Anrather, Weill Cornell Medical College, New York. KikGR33 mice were bred and housed at the animal core facility of the Center for Stroke and Dementia Research (Munich, Germany), and for which male mice were used. 3-month-old male mice were used in study with the exception of bulk AD and 5xFAD TSPO-PET dataset, where the sex of the animals were female and the age were 6-months-old for bulk AD and 4.5-months-old for TSPO-PET dataset. In all in vivo experiments in this study, littermates of the same sex were randomly assigned to experimental groups, the animals were housed under a 12/12 h light/dark cycle, all animals were healthy in the beginning of the experiment, no drugs were given to animals during the time of data acquisition, no specific food, temperature and cage conditions were kept. All data are reported according to the ARRIVE.⁸⁴

Human samples and participants

All anatomy donors or next-of-kin gave their informed and written consent to explore the cadavers for research and educational purposes. The signed consents are kept at the institutes involved. Institutional approval was obtained in accordance to the Saxonian Death and Funeral Act of 1994, of the independent ethics committee of the Hamburg Chamber of Physicians (protocol 2020-10353-BO-ff) and the Ethics committee of Technical University of Munich (67/22S). The skull samples in this study are coming from the following sources: University Medical Center Hamburg-Eppendorf, Institute of Legal Medicine; Institut für Allgemeine Pathologie und Pathologische Anatomie, Technische Universität München and Anatomy Institute, University of Leipzig, Institut für Rechtsmedizin der Universität München. A detailed list of post-mortem samples used for light sheet imaging and proteomics samples are given in [Figures S5O](#) and [S7A](#).

Regarding human participants: ten patients with stroke, 29 patients with multiple sclerosis (15 with relapsing remitting multiple sclerosis and 14 with primary progressive multiple sclerosis), 43 patients with 4R tauopathies, 50 patients with AD and 27 age- and sex-matched individuals without objective cognitive impairment and with intact motor function were available for calvaria analysis of TSPO-PET. Sample sizes were determined in the specific study protocols, based on comparisons of TSPO-PET signals in brain between disease and controls. Power was set to 0.8 and alpha was set to 0.05 with the goal to achieve effect sizes of 1.0, also graded sufficient to test for differences in skull TSPO-PET signals. Allocation into study groups was determined by the clinical diagnosis. Severe neurological disorders other than the investigated diagnosis were excluded in the study protocols, assuming immunocompetence in all participants. All participants were naïve to TSPO-PET at study inclusion. In one set of analyses stroke, MS and 4R tauopathy patients were compared with controls, while the AD cohort, for which additional biomarkers were available, was analyzed separately. All patients with multiple sclerosis were investigated during observational studies. We included all baseline scans of therapy naïve patients with primary progressive multiple sclerosis (n=14) and patients with relapsing remitting multiple sclerosis (n=15; previously published in Unterrainer et al.⁶³) regardless of therapy regimes. However, patients who received steroid therapy < 4 weeks prior to PET as well as patients with additional CNS pathologies were excluded a priori. PET acquisition and PET data analyses of the multiple sclerosis cohort (ethics-application: 601-16) were approved by the local institutional ethics committee (LMU Munich) and the German radiation protection (BfS-application: Z 5 - 22463/2 - 2015 - 006) authorities. The 4R-tauopathy cohort⁶² was composed of patients with possible or probable β -amyloid negative corticobasal syndrome (n=29) and patients with possible or probable progressive supranuclear palsy Richardson syndrome (n=14) according to Armstrong Clinical Research and Movement Disorders Society criteria respectively. Detailed inclusion and exclusion criteria were published elsewhere.⁶² One case was excluded due to cropped skull. PET acquisition and PET data analyses of the 4R-tauopathy cohort (ethics-applications: 17-569 & 17-755) were approved by the local institutional ethics committee (LMU Munich) and the German radiation protection (BfS-application: Z 5 - 22464/2017-047-K-G) authorities. A total of 27 healthy controls deriving from the different cohorts were included to cover the whole age range of patients. PET acquisition and PET data analyses of the stroke cohort

(ethics-application: 19–428) were approved by the local institutional ethics committee of the LMU Munich (ethics-application: 19–428) and the German radiation protection authority (BfS-application: Z 5 - 22464/2019-163-G). To compare different patient cohorts, we used harmonized data from different PET imaging studies: All patients with acute ischemic stroke ($n=10$) were recruited from the ongoing ICARUS study which included a TSPO-PET up to 10 days after stroke onset. Inclusion criteria were an age ≥ 50 years, acute ischemic stroke as defined by an acute focal neurological deficit in combination with a corresponding infarct as documented by diffusion-weighted imaging (DWI)-positive lesion on brain MRI, presence of an infarct involving the cortex or a strictly subcortical infarct, written informed consent; and willingness to participate in study assessments including follow-up. Exclusion criteria were among others multiple infarcts, infratentorial infarcts affecting the brain stem or cerebellum, immunomodulatory therapies within the last 3 months, chronic inflammatory disease, and infectious diseases (< 7 days prior to stroke). The AD cohort was composed of nine cases with subjective cognitive decline due to AD, 13 cases with mild cognitive impairment due to AD, 18 cases with AD dementia, and 12 cases with corticobasal syndrome, dementia and underlying AD. Initial results of brain TSPO labeling in this cohort are published elsewhere.⁸⁵ Two patients with AD were excluded from the cross-sectional TSPO-PET group comparison due to limited field of view. Participants were enrolled in the interdisciplinary AD study "Activity of Cerebral Networks, Amyloid and Microglia in Aging and AD (ActiGliA)". In the AD cohort and its controls, A β -PET was performed in all participants using [18 F]flutemetamol.⁸⁶ PET acquisition and PET data analyses of the AD cohort (ethics-applications: 17-569 & 17-755) were approved by the local institutional ethics committee (LMU Munich) and the German radiation protection (BfS-application: Z 5 - 22464/2017-047-K-G) authorities. Longitudinal follow-up imaging within the ActiGliA cohort was available for 13 patients of the AD continuum and 15 controls at a median interval of 18 months. Additionally, 3 months follow-up imaging was available for 13 patients with stroke. Age, gender, SNP coding and medication status of participants are provided in [Table S3](#).

METHOD DETAILS

Middle cerebral artery occlusion (MCAo) model

The MCAo model was used to generate transient cerebral ischemic strokes by introducing an intraluminal filament through the carotid artery of mice anesthetized with isoflurane mixed with 30% O₂ and 70% N₂O. To initiate the occlusion the left common carotid artery and interna of the animal were permanently ligated and a silicon capped nylon suture (6/0) was introduced through a cut in the common carotid artery and advanced through the external carotid artery until it reached and obstructed the MCA for 30 minutes. Regional cerebral blood flow was monitored, in the bregma coordinates 2-mm posterior, 5-mm lateral, via transcranial laser Doppler flowmeter from the induction of stroke until 10 minutes after retraction of the filament and reperfusion took place. After the procedure, mice were left for recovery in temperature-controlled cages for two hours in order to minimize the risk of hypothermia. Sham-operated animals were subjected to the same procedure without the insertion of the filament. Body temperatures were kept constant throughout all surgeries with a feedback-controlled heating pad at 37.0 ± 0.5 °C. Animals were then kept in their home cages with facilitated access to water and food whilst being subjected to behavioral tests for three days. Mice were excluded in case of insufficient MCA occlusion (a reduction in blood flow to 15% of the baseline value) or blood flow recovery $>80\%$ within 10 min of reperfusion.

Skull preparation for chronic imaging

Experiments were carried out on 8–12 weeks old male LysM-GFP $-/+$ mice. Induction of anesthesia with buprenorphine (0.1 mg/kg Bw) and isoflurane (5%, 30s), was followed by maintenance anesthesia with 1.5–2.5% isoflurane in room air with 30% oxygen/70% air under continuous monitoring of body temperature 37.5 °C with a feedback-controlled heating pad. Glass window preparation was adapted from described method.⁸⁷ Mouse was placed on a stereotactic frame (RWD Life Science Co., LTD, Shenzhen, China) where head was fixed by ear bars and the eyes were covered with Bepanthen ointment (AG Bayer, Leverkusen, Germany). The left parietal bone was exposed after resection of the mouse scalp. Sterile saline was applied to the skull and the periosteum were gently removed with forceps. Then, Ultraviolet-curable glue Loctite 4305 (Henkel, Düsseldorf, Germany) was applied onto the parietal bone surface. A sterile round glass window of 3-mm diameter was placed on the skull followed by two by 1s exposures every 3s of ultraviolet light source UV301D UV 365NM Light Flashlight (LIGHTFE Lighting Co., Ltd., Shenzhen, China) to cure the glue. Then, skull surrounding the window was prepared for the dental cement application by putting for 1 min onto the surface of iBond Self Etch (Kulzer GmbH., Hanau, Germany) solution with subsequent curing by UV source for 5 s using Demi™ Ultra Dental Curing Lights (Kerr Corporation, Brea, CA, USA). Then on top of the etching solution the dental cement Tetric EvoFlow® (Ivoclar Vivadent, Schaan, Liechtenstein) was applied. Before UV curing, the titanium ring was placed on the skull to have the window in its center and then cement was cured with the same UV source (Demi™ Ultra Dental Curing Lights) for not more than 5 s including every side around the ring. Finally, a thin stripe of dental cement was applied onto the inner edge of the ring, with subsequent 5 s UV exposing, to fix the ring to the skull. Carprofen (4mg/kg every 24h) was administered i.p. for the following 72 hours.

Live Imaging

For multiphoton imaging, we used an upright Zeiss LSM710 confocal microscope equipped with a Ti:Sa laser (Chameleon Vision II) from Coherent (Glasgow, Scotland) and 2 external photomultiplier detectors for red and green fluorescence.⁸⁸ Anesthetized animals (1.5 % of isoflurane) were placed on a heating pad under the microscope. For visualization of the vasculature, 5 min prior to the

imaging, the fluorescent tracer Tetramethylrhodaminisothiocyanat-Dextran (TMR-Dextran), 3000 Da MW (Sigma-Aldrich, St. Luis, MI, UA) was injected subcutaneously. The scanning was performed with Z-stack, 50-100 μm depth, laser (900 nm) power from 6-8% till 12-16% depending on the region of interest (ROI) depth. GAASP detector with LP<570 nm filter for the GFP channel, LP>570 nm for the TMR channel, and NDD detector SP<485 nm for the bone visualization, all with master gain 600. Image size 1024x1024, 8 bit. Objective: W Plan-Apochromat 20x/1.0 DIC M27 75mm. For the series scanning, the laser power was 8-10%, 5 frames every 1 s. For each animal, 2-3 ROI was chosen which were imaged at baseline, 2, 24, and 72 hours post-stroke, or at the respective time point for naïve and sham-operated animals.

Behavioral experiments - Neuroscore

Neuroscore²⁴ was performed to assess each animal's general and focal deficits every day. The scoring was composed of general deficits (scores): fur (0 to 2), ears (0 to 2), eyes (0 to 4), posture (0 to 4), spontaneous activity (0 to 4), and epileptic behavior (0 to 12); and focal deficits: body asymmetry (0 to 4), gait (0 to 4), climbing on a surface inclined at 45° (0 to 4), circling behavior (0 to 4), fore-limb asymmetry (0 to 4), compulsory circling behavior (0 to 4), and whisker response to touch (0 to 4). This resulted in a score of 0 to 56 in total; up to 28 from general and up to 28 from focal deficits.

Perfusion, fixation and tissue preparation

After the mice were anesthetized with a mixture of midazolam, medetomidine and fentanyl (MMF) (1ml/100g of body mass for mice; i.p.), and showed no pedal reflex, they were intracardially perfused with 0.1 M PBS (combined with heparin, 10 U/ml, Ratiopharm). 100-125 mmHg pressure with a Leica 13 Perfusion One system was used for perfusion. PBS ran for 3-4 minutes for single-cell isolation experiment, 5-10 minutes for tissue clearing experiments to let the blood wash out at room temperature. For single-cell isolation experiments, bones were dissected as detailed in the Single cell isolation method section. For the tissue clearing experiments, PBS perfusion was followed by the administration of 4% paraformaldehyde (PFA) in 0.1 M PBS (pH 7.4) (Morphisto, 11762.01000) for 10-20 minutes. After removal of the skin and a washing step with PBS to clean the animal as much as possible, the animals were post-fixed by 4% PFA for the first 24 hours at 4°C and washed three times with 0.1M PBS before processing with the clearing protocol.

vDISCO whole-body immunostaining, PI labeling and clearing

The detailed protocol of vDISCO was described previously.^{2,89} The mouse bodies were placed inside a 300 ml glass chamber (Omnilab, 5163279), to be filled with the appropriate solution regarding the protocol to cover the entire body of the animal (~250-300ml). A transcardial-circulator system was established in order to allow peristaltic pumping of the solutions (ISMATEC, REGLO Digital MS-4/8 ISM 834; reference tubing, SC0266), with the pressure being set at 180-230 mmHg (50-60 rpm). The tubing was set to allow pumping of the solutions through the heart (attached to a perfusion needle (Leica, 39471024)) into the vasculature with the same entry point used for PBS and PFA perfusion steps described above. The other end of the tube was immersed into the chamber with a loose end to allow suction of the solution into the body. The samples were initially perfused with a decolorization solution (25% of CUBIC reagent 1⁹⁰ which is composed of 25 wt% urea (Carl Roth, 3941.3), 25 wt% N,N,N',N'-tetrakis (2-hydroxypropyl)ethylenediamine (Sigma, 122262) and 15 wt% Triton X-100 (AppliChem, A4975,1000) in 0.1 M PBS)) for 2 days, refreshing the solutions every 12h. Samples were washed with PBS for 3x2h. Then, decalcification solution (10 wt/vol% EDTA in 0.01 PBS, pH~8-9, Carl Roth, 1702922685) was perfused for 2 days followed by half a day with permeabilization solution composed of 0.5% Triton X-100, 1.5% goat serum (GIBCO, 16210072), 0.5 mM of Methyl-beta-cyclodextrin (Sigma, 332615), 0.2% trans-1-Acetyl-4-hydroxy-L-proline (Sigma, 441562), 0.05% sodium azide (Sigma, 71290) in 0.01 M PBS. To initiate the PI labeling and boosting, the setup was adjusted. The free end of the perfusion tube was connected to a 0.22 μm syringe filter (Sartorius, 16532) and an infrared lamp (Beuer, IL21) was aimed at the chamber to enable the solution's temperature to be around 26-28 °C. This setup was then left running for 6 days after the addition of 35 μl of nanobooster (stock concentration 0.5 – 1 mg/ml) and 290 μl of propidium iodide (stock concentration 1 mg/ml) which was added directly into the refreshed permeabilization solution. Next, the body was placed into a 50 ml tube (Falcon, 352070), with the same permeabilization and labeling solution, and an extra 5 μl of nanobooster was added. The tube was then put on a shaker at RT for 2 additional days for labeling. Atto647N conjugated anti GFP nanobooster (Chromotek, gba647n-100) and Propidium iodide (PI, Sigma, P4864), was used to boost the signal from the LysM animals and stain cell nuclei respectively in the study. Then, the animals were placed back into the initial perfusion setup, where the washing solution was perfused for 2x12h, which was composed of; 1.5% goat serum, 0.5% Triton X-100, 0.05% of sodium azide in 0.1 M PBS. 0.1 M PBS was used to wash the sample 3x2h. 3DISCO protocol was applied for whole body clearing. The animals were freed from the perfusion system, but kept in glass chambers and placed on top of shakers (IKA, 2D digital) at room temperature inside a fume hood. Glass chambers were sealed with parafilm and covered with aluminum foil along with the 3DISCO application. For dehydration, sequential immersion of tetrahydrofuran (THF) (Sigma, 186562) (50 Vol% THF, 70 Vol% THF, 80 Vol% THF, 100 Vol% THF and again 100 Vol% THF) was applied every 12 hours. Then three hours of dichloromethane (DCM) (Sigma, 270997) immersion for delipidation was followed by indefinite immersion in BABB (benzyl alcohol + benzyl benzoate 1:2, Sigma, 24122 and W213802) solution for refractive index matching.

Nr4a1 labeling and clearing of mice bones with SHANEL

Mouse heads and left femurs were collected from three-month-old, male, wild-type C57Bl6/J mice (n=3). After dissection to remove surrounding tissue, bones were decalcified in 20% (wt/vol) ethylenediamine tetraacetic acid (EDTA, pH=8.0, prepared in dH2O) for two

days at 37°C. EDTA was removed by washing in 0.1 M PBS for 3x2 hours. Bones were stained and cleared using the SHANEL protocol.⁹¹ Samples were dehydrated in 50–70–100% ethanol/dH₂O for 1 hour each, delipidated in dichloromethane/methanol (2:1) for 6 hours and rehydrated in sequence with the same dilutions backward. Next, they were incubated in acetic acid/dH₂O (30 mL/L) 2 hours for extracellular matrix hydrolyzation and washed with dH₂O for 3x15 minutes. Then, samples were incubated in extracellular matrix proteoglycan extraction solutions consist of 4 M guanidine hydrochloride, 0.05 M sodium acetate, and 2% Triton X-100 in 0.1 M PBS for 2 hours, washed first with dH₂O and then PBS for 3x15 minutes each, followed by incubation in 10% 3-[(3-Cholamidopropyl)-dimethylammonio]-1-propansulfonat (CHAPS) + 25% N-Methyldiethanolamine (NMDEA) in dH₂O at 37°C for further permeabilization and washed with dH₂O for 3x15 minutes. Blocking was performed with 0.2% TritonX-100, 10% DMSO, 10% goat serum in 0.1 M PBS (blocking solution) for 6 h at 37°C. Anti-NUR77 antibody (1:200, Abcam, ab153914) were added with 0.2% Tween-20, 5% dimethyl sulphoxide (DMSO), 5% goat serum, 0.001% heparin in 0.1 M PBS (primary antibody solution) and incubated for 2 days at 37°C. After washing with 0.2% Tween-20, 0.001% heparin in 0.1 M PBS (washing solution) 4x20 minutes, bones were incubated with Goat anti-Rabbit IgG (H+L) Highly Cross-Adsorbed Secondary Antibody, Alexa Fluor 647 (1:200, Abcam, A-21245) and propidium iodide (1:1000) in 0.2% Tween-20, 5% goat serum, 0.001% heparin in 0.1 M PBS (secondary antibody solution) for 2 days at 37°C, washed with washing solution. Clearing was performed by dehydrating the bones in dilutions of 50-70-100-100% ethanol/dH₂O for 12 h each, followed by delipidation of the samples in 100% dichloromethane (DCM) for 15 minutes. Finally, samples were kept in refractive index matching solution BABB (benzyl alcohol + benzyl benzoate 1:2, Sigma, 24122 and W213802). If not stated otherwise, steps were performed with constant shaking at room temperature inside a fume hood.

Human skull labeling and clearing with SHANEL

SHANEL protocol with extended incubation periods were performed on human post-mortem skull pieces. Bones were decalcified in 20% (EDTA, pH=8.0) for 1.5-2 months (until the bone becomes cuttable) at 37°C EDTA was removed by washing in 0.1 M PBS for 3x2 hours. Bones were incubated in 10% CHAPS + 25% NMDEA solution for 4 days at 37°C and washed with dH₂O for 3x20 minutes. Bones were dehydrated in 50-70-100% ethanol/dH₂O, each with overnight incubation, delipidated overnight in DCM/MeOH (2:1) and rehydrated. Then, samples were incubated in acetic acid for 4 hours, followed by incubation with 4 M guanidine hydrochloride, 0.05 M sodium acetate, and 2% Triton X-100 in 0.1 M PBS for 2 days and washed first with dH₂O and then PBS for 3x20 minutes. Samples were incubated in a blocking solution overnight at 37°C. Staining was performed in two groups: some samples were incubated with recombinant anti-Lysozyme antibody (1:250, Abcam, ab108508) in primary antibody solution for 10 days at 37°C, washed with washing solution 4x20 minutes, then stained with Lycopersicon Esculentum (Tomato) Lectin (LEL, TL), DyLight 649 (1:500, Invitrogen, L32470) for 7 days at 37°C, washed with washing solution 4x20 minutes, incubated with Goat anti-Rabbit IgG (H+L) Highly Cross-Adsorbed Secondary Antibody, Alexa Fluor 568 (1:200, A-11036, Thermo Fisher) and washed. The remaining samples were stained with Lycopersicon Esculentum (Tomato) Lectin and Propidium Iodide (1:1000, Sigma, P4864) in primary antibody solution, washed and proceeded with clearing. Clearing was performed by dehydrating the bones in dilutions of 50-70-100-100% ethanol/dH₂O for 12 h each, delipidated in 100% DCM for 15 minutes and incubated indefinitely in BABB (benzyl alcohol + benzyl benzoate 1:2, Sigma, 24122 and W213802). If not stated otherwise, steps were performed with constant shaking at room temperature inside a fume hood.

Light sheet microscopy imaging

Single plane illumination (light sheet) image stacks were acquired using an Ultramicroscope II and Ultramicroscope Blaze (Mitenyi BioTec). The available filter sets were ex 470/40 nm, em 535/50 nm; ex 545/25 nm, em 605/70 nm; ex 560/30 nm, em 609/54 nm; ex 580/25 nm, em 625/30 nm; ex 640/40 nm, em 690/50 nm. The filter sets used to capture the LysM signal and the PI labeling were 640/40 nm and 545/25 nm filter sets, respectively. Low magnification whole-body imaging of the LysM mice was performed with Ultramicroscope Blaze, with a 1.1x objective, 3x8 tiling with 35% overlap and 6 µm z-step. Exposure time was 120 ms, and laser power was 25% and 12% for LysM (647nm) and PI (594nm) channels, respectively. The depth of the scans was approximately 13 mm from dorsal and ventral surfaces, which were then reconstructed. The whole head images were taken with an Olympus MVX10 zoom body, which offered zoom-out and -in ranging from 0.63x up to 6.3x. The depth of the scans was approximately 4 mm and the z-step used was 6 µm combined with an exposure time of 200 ms. Human bone pieces were imaged with 1.1x magnification using LaVision BioTec MI PLAN 1.1x/0.1 NA (WD = 17 mm), with 1.66X zoom, as stacks, tiles were adjusted to cover all the bone surface with 25-35% overlap. The depth of scans was 1-1.5 cm. Higher magnification imaging of ROIs from mice bones were obtained with 12x magnification using PLAN 12x/0.53 NA (WD = 10 mm), LaVision 470 BioTec MI objective as 1 tile, step size of 6 µm. Depth of scans was 0.5-1 mm. Following settings were kept the same for all samples: Exposure time: 120 ms; light sheet width: 100%; and light sheet thickness: 7 µm (NA 0.31). Multiple tile scans were stitched with Fiji's stitching plugin (http://discotechnologies.org/SHANEL/manual_stitching.py) and visualized in 3D using Imaris (v.9.6 × 64, Imaris).

Reconstruction of whole-mouse body and mouse head scans

The image stacks were acquired and saved by ImSpector (Mitenyi BioTec) as 16-bit grayscale TIFF images for each channel separately. The whole-body tiled stacks were initially stitched utilizing Fiji/ImageJ to obtain stitching on the xy-axis (http://discotechnologies.org/SHANEL/manual_stitching.py). Next, Vision 4d (Arivis AG) was used to fuse the stacks in the z-axis. For heads, one tile stacks were acquired, hence stitching was not necessary. Imaris (Bitplane AG) was used to visualize both whole body and intact mouse heads.

Fixed-formalin paraffin embedding, sectioning and H&E staining

Fixed formalin paraffin-embedded samples were acquired from decalcified human skulls initially by using the Sakura Tissue-Tek VIP 6 AI machine. The samples were placed in holders and were sectioned as 1 μ m thick slices using Microm HM 355S microtome. Sections were then placed in the Sakura Tissue-Tek Prisma machine for H&E staining. The images were then acquired by a bright field microscope using 40x magnification.

Human fixed frozen sections, immunohistochemistry and imaging

Fixed samples were placed in 15% sucrose in PBS until they sunk and then in 30% sucrose overnight. Samples were frozen in SCEM medium (Sectionlab, Japan). 7 μ m cryosections were cut using Kawamoto's film method⁹² on a cryostat, which were then stored at -80°C until further use. For immunofluorescence, sections were thawed, rehydrated in PBS, blocked with 10% serum, and stained with antibodies in 1% serum in PBS containing DAPI for 1–2 h. Antibodies used were; anti-SMA-Alexa Fluor A594, 1A4, Abcam; Collagen-IV-FITC, 2F11, Southern Biotec; anti-PDGFRB, HPA028499, Merck; Donkey anti-Rabbit IgG (H+L) Highly Cross-Adsorbed Secondary Antibody, Alexa Fluor 647. Stained sections were washed and mounted with aqueous mounting medium (Fluoromount, Thermo Fisher, MA, US).

Sections were imaged with at a Zeiss LSM880 using a 20x objective.

Single-cell isolation for scRNAseq and proteomics

Single-cell isolation from the calvaria, brain, meninges, humerus, scapula, vertebra, femur and pelvis was done for one animal at a time. Three naïve, six MCAo-operated and three sham operated animals were pooled in threes for single-cell RNA sequencing. Another cohort of three animals for naïve, three animals for sham-operated and three MCAo-operated animals were not pooled and were treated separately for proteomic analysis. These experiments were performed on sham and MCAo animals that had the procedure three days prior to the single-cell isolation experiment. Separate equipment was utilized during the isolation to ensure high viability of cells free of contamination. The animals were anesthetized with Isoflurane and then with a Ketamine/Xylazine mixture (0.6 ml Ketamine + 0.3 ml Xylazine + 5.1 ml Saline, 0.2 ml for 20 gr animals). Then animals were transcardially perfused with 10 ml of ice-cold 0.1 M PBS. After the blood was rinsed, the calvaria bone, humerus, scapula, vertebra, femur, brain, meninges, and pelvis were dissected and processed by separate people to minimize the time required in order to keep the cell viability to a maximum and conditions comparable for all locations. The isolated cells were processed with 37 $^{\circ}\text{C}$ pre-warmed DMEM (Thermo Fischer, 21013024) with 10% heat inactivated fetal bovine serum (FBS) (Sigma Aldrich, F7524-100ML). For brain cell isolation; the brain was isolated from the calvaria and the rest of the body, then, the cortex was separated and the leptomeninges was removed from the surface, the final sample consisted of the injured region. The sample was placed in 5 ml of trypsin enzyme with 0.05% concentration and incubated in a pre-heated 37 $^{\circ}\text{C}$ water bath for 2 minutes. Following this, the reaction was stopped with 10 ml of 37 $^{\circ}\text{C}$ pre-warmed DMEM with 10% heat inactivated FBS, the cells were dissociated by gentle trituration with a 1000 μ l and 200 μ l pipette and filtered through 70 μ m Falcon™ Cell Strainers (08-771-2). For meningeal cell isolation; after the brain was removed, the meningeal dura layer that was attached to the calvaria bone, was plucked carefully using fine tipped dissection pincers (Dumont #55 Forceps, Dumostar, 11295-51, FST) under a dissection microscope. Leptomeninges was not isolated and therefore is not included in this study. The dissected meninges was placed in 37 $^{\circ}\text{C}$ pre-warmed DMEM with 10% heat-inactivated FBS solution, shredded with a fine scalpel, gently titrated with a 200 μ l pipette and filtered through a 70 μ m Falcon™ Cell Strainers (08-771-2). For humerus, vertebrae and femur cell isolation; the bone was dissected from the body and the muscles and connective tissue were meticulously cleared off. The bone marrow inside was flushed out to the collection tube with the help of a syringe (Braun, Injekt - F Solo 2-piece Fine Dosage Syringe 1 ml x 100), and further dissection of the bone was performed by fine pincers (Dumont #55 Forceps, Dumostar, 11295-51, FST). The remaining bone was cut into small pieces and added to the cell mix. This mixture was shortly vortexed with 37 $^{\circ}\text{C}$ warmed DMEM with 10% heat-inactivated FBS and filtered with 70 μ m (Falcon™ Cell Strainers, 08-771-2). Lastly, for the flat bones, calvaria, scapula and pelvis, after carefully clearing the non-bone parts in the sample i.e., muscles and connective tissue, they were cut into small pieces (Extra Fine Bonn Scissors, 14084-08, FST), and shortly vortexed and filtered through 70 μ m Falcon™ Cell Strainers (08-771-2). After all the samples were ready, they were centrifuged at 4 $^{\circ}\text{C}$, with 1000 rpm, for 5 minutes. The supernatant of all samples was then discarded and the remaining precipitate was put into small 1.5 ml Eppendorf tubes (Eppendorf Safe-Lock Tubes, 1.5 mL, Eppendorf Quality™, 0030120086) after resuspension with DMEM. Cell viabilities and numbers were checked with trypan blue by an automated cell counter (TC20™ Automated Cell Counter) and controlled by manual counting (Neubauer Cytometry Chamber, MARI0640031).

Cell sorting and plate-based bulk RNA-sequencing

6-month-old mice were used for this study (3 5XFAD, 3 wildtype littermates). Cell sorting for CD45 and CD11b positive cells, cDNA generation and library construction was performed as described previously.⁹³ Briefly, after cells were passed through a 70 μ m cell strainer, staining was performed for 15 min using 7AAD (Thermo Fisher, A1310, 25 μ g/ml) and the antibodies against CD45 (eFluor 450,30-F11, eBioscience, Cat.:48-0451-82, 1:200) and CD11b (PE/Cy7,M1/70, eBioscience, Cat:25-0112-82,1:200). Cells were then washed with PBS (Sigma, D8537). Viable (7AAD negative) immune cells (CD45 and CD11b positive cells) were sorted by flow cytometry (SH800; Sony) into the 96-well plates by groups of 50 cells per well (we acquired 69 samples). The 96-well plates were filled with 4 μ l lysis buffer containing 0.05% Triton X-100 (Sigma), ERCC (External RNA Controls Consortium) RNA spike-in Mix (Ambion,Life

Technologies) (1:24000000 dilution), 2.5 μ M oligo-dT, 2.5 mM dNTP and 2 U/ μ L of recombinant RNase inhibitor (Clontech). The plate was spun down and frozen at -80 °C.

cDNA and cDNA libraries were generated using an improved version of the Smart-seq2 protocol. The plates with the sorted pools were first thawed and then incubated for 3 min at 72 °C and immediately placed on ice. To perform reverse transcription (RT), we added to each well a mix of 0.59 μ L H₂O, 0.5 μ L SMARTScribe™ Reverse Transcriptase (Clontech), 2 μ L 5x First Strand buffer, 0.25 μ L Recombinant RNase Inhibitor (Clontech), 2 μ L Betaine (5 M Sigma), 0.5 μ L DTT (100 mM), 0.06 μ L MgCl₂ (1 M Sigma), and 0.1 μ L Template-switching oligos (TSO) (100 μ M AAGCAGTGGTATCAACGCAGAGTACrGrG+G). Next, RT reaction mixes were incubated at 42 °C for 90 min followed by 70 °C for 5 min and 10 cycles of 50 °C 2 min, 42 °C 2 min; finally ending with 70 °C for 5 min for enzyme inactivation. Pre-amplification of cDNA was performed by adding 12.5 μ L KAPA HiFi Hotstart 2x (KAPA Biosystems), 2.138 μ L H₂O, 0.25 μ L ISPCR primers (10 μ M, 5' AAGCAGTGGTATCAACGCAGAGT-3), 0.1125 μ L Lambda Exonuclease under the following conditions: 37 °C for 30 min, 95 °C for 3 min, 20 cycles of (98 °C for 20 sec, 67 °C for 15 sec, 72 °C for 4 min), and a final extension at 72 °C for 5 min. Libraries were then cleaned using AMPure bead (Beckman-Coulter) cleanup at a 0.7:1 ratio of beads to PCR product. Library was assessed by Bioanalyzer (Agilent 2100), using the High Sensitivity DNA analysis kit, and also fluorometrically using Qubit's DNA HS assay kits and a Qubit 4.0 Fluorometer (Invitrogen, Life Technologies) to measure the concentrations. Samples were normalized to 160 pg/ μ L. Sequencing libraries were constructed by using an in-house produced Tn5 transposase.⁹⁴ Libraries were barcoded with the Illumina Nextera XT (FC-131-1096, Illumina) and pooled, then went through three rounds of AMPure bead (Beckman-Coulter) cleanup at a 0.8:1 ratio of beads to library. Libraries were sequenced 2x100 reads base-pairs (bp) paired-end on Illumina HiSeq4000.

Single-cell suspension isolation from the human bones for proteomics

Bone samples were collected into formalin and were washed with PBS within 24 hours of fixation. Then, samples were placed in 20% EDTA (pH~8) in 37 °C. EDTA was changed every second day. When all bones reached a cuttable softness with scissors and a scalpel, the samples were washed with PBS overnight. 20 skull, vertebra and pelvis were dissected by carefully clearing the non-bone parts in the sample i.e., muscles and connective tissue. The same sizes of bones were cut into small pieces on a glass petri-dish with PBS. The resulting cell suspension was filtered through 40 μ m Falcon™ Cell Strainers into a 50 ml Falcon tube. The samples were centrifuged for 5 minutes in 12000g. The supernatant was discarded. The pellet was resuspended in 1 ml pbs and transferred to 1.5 ml Eppendorf tube (Eppendorf Safe-Lock Tubes, 1.5 mL, Eppendorf Quality™, 0030120086). The tubes were centrifuged for another 5 minutes in 12000g. PBS was discarded and samples were stored in -80 until all samples were acquired.

Single-cell isolation from human skull for scRNAseq

Sample was sectioned in the clinic with an electric saw to generate thinner, smaller pieces and was collected in DMEM + 10% FCS. The sample was brought to lab from the clinic on ice. Using a needle and a syringe, the bone marrow cells were flushed DMEM + 10% FCS (Gluc + /Glut +) into a 50 ml tube. Bone was further crushed using a mortar on ice in order to release more marrow cells into the cell suspension. Each sample was filtered through a 70 μ m strainer and centrifuged at 500 rcf for 5 mins at 4 °C. Supernatant was discarded. The pellet was resuspended in 10 ml chilled PBS / 2%BSA. Then, the cells were visually counted using trypan blue to assess the high viability. Next, the samples were washed again as above and resuspended for loading to the 10X Chromium.

scRNA sequencing – 10x Genomics

Samples were used for scRNA-seq if the fraction of dead cells determined by trypan blue staining was below 20%. Cell suspensions were diluted with PBS/2% FCS for mouse experiments and PBS/2% BSA for the human experiment, to a final concentration of 1000 cell/ μ L and 17.000 cells per sample were loaded onto 10x Chromium Single Cell RNA-seq chips to recover a target cell number of 10.000 cells per sample. Libraries were generated in three replicates for the mouse experiment. The 10x Chromium Single Cell 3' Library & Gel Bead Kit v3 for mouse and v3.1 for human was used following the manufacturer's protocol. Libraries were sequenced on an Illumina HiSeq 4000 (150 bp, paired end) for mouse experiment and NovaSeq6000 for human experiment.

Sample preparation for bulk RNA isolation

Mice were deeply anaesthetized with ketamine (120mg/kg) and xylazine (16mg/kg) and transcardiacally perfused with cold PBS. The necessary samples were quickly harvested and placed in ice-cold RNAlater solution in 1.5 ml tubes.⁹⁵ The samples were left in RNAlater solution for 24h in 4 °C. Next, the solution was discarded and samples were placed in -80 for storage until RNA isolation.

Bulk RNA isolation, library preparation and sequencing

The samples were processed 12 at a time. Samples were in a 2 ml Eppendorf tube. 1 ml of Trizol and a metal bead was added to each sample. Samples were then lysed in Tissue Lyser with 30 Hz frequency for 3 minutes. 200 μ L of Chloroform was added to each sample. After rigorous vortexing, samples were incubated at room temperature for 15 minutes. Next, samples were centrifuged at 10,000 g for 10 minutes at 4 °C. The upper phase of the sample was transferred into a new tube. 240 μ L, 100% seq-grade EtOH was added and samples were briefly vortexed. The samples were loaded into Econospin columns and were centrifuged at 13000 g for 30 seconds at room temperature. Flow-through was discarded. The samples were washed 3x with RPE buffer (Qiagen #1018013) and centrifuged at 13000 g for 30 seconds each time. After the last wash, sample was centrifuged dry. Next, columns were

transferred into new 1.5 ml tubes with open lids for 10 minutes. RNase free water was used to elute the sample in 30 μ l. Final centrifuge was performed at 9000 g for 2 minutes at room temperature. All samples were subjected to Nanodrop, Qubit and Bioanalyzer assays in order to determine quality and quantity of each sample. Samples were stored at -80 until all samples were processed. Only samples with RIN>8 were used. Illumina ligation stranded mRNA prep kit was used for library preparation and the sequencing of 95 samples were performed on a PE 2x100 flow cell.

Flow cytometry

Cell isolation and labeling

Cell isolations were prepared as previously described in “Single cell isolation for scRNAseq and proteomics” section. The suspended cells were centrifuged at 500g for 7 minutes at 4°C. The supernatant was discarded, and samples were resuspended in 1 ml FACS buffer. The 1 ml buffer with cells was transferred to a FACS tube. Tubes were spun down at 500 g 7 minutes at 4°C. The supernatant was discarded and each sample was resuspended in 50 μ l FACS buffer with 0.5 μ l FC blocker. The samples were incubated for 10 minutes, in dark on ice. Then 50 μ l of antibody mix was added to each sample: (1 μ l each from Ly-6G/Ly-6C (APC/Cyanine7, Biolegend, #108423), Cd11c (APC, Biolegend #117309), F4/80 (PerCP-Cy5, BD, #567202), CD45 (BUV395, BD, #565967), CD117(BV421, BD, #566290), I-A/I-E (Brilliant Violet 510, Biolegend, #107635), Ter-119 (BV650, Biolegend, #128035), NK-1.1 (Brilliant Violet 711, Biolegend, #108745), CD11b (Brilliant Violet, Biolegend, #101243), CD179a (PE, Biolegend, #143603), CD45R/B220 (PE-Cy5, BD, #553091), CD182 (CXCR2) (PE/Dazzle 594, Biolegend, 149317), Ly-6A/E (PE Cy 7, BD, #561021) and 1.5 μ l each from CD3 Alexa Fluor 700, BD, #561388), Ly-6C (Brilliant Violet 605, Biolegend, 128035), 34 μ l FACS buffer). Samples were incubated for 15 minutes on ice in dark. After the staining 3 ml of FACS buffer was added to each sample. The samples were centrifuged at 500 g 7 minutes at 4°C. After discarding the supernatant, samples were resuspended in 200 μ l of FACS buffer to be measured by the machine.

Proportions

Sample were recorded on a LSRFortessa (BD) and data were analyzed with FLOWJO software (Tree Star). Cell numbers were calculated as percentage of an appropriate gate. After gating out doublets, dead cells (SytoxGreen+) and red blood cells (Ter119+), white blood cell (CD45+) subpopulations were defined as follows: T-cells (CD3+), immature B-cells (B220dim I-A/I-Evar), mature B-cells (B220+ I-A/I-E+), NK-cells (NK1.1+), monocytes (F4/80+), eosinophils (Ly6G-, SSChigh), early neutrophils (Ly6G+, CXCR2-), late neutrophils (Ly6G+, CXCR2+) and hematopoietic stem-/progenitor cells (LSK cells, Lineage-, Sca-1+, c-Kit+).

Photoconversion KikGR

Mice were anesthetized with 1.5–2% isoflurane (vol/vol), delivered in medicine air, and maintained at 37 °C throughout the procedure. Briefly, a skin midline incision was made on the head of the mouse, and the skull was exposed. Photoconversion was performed with a defocused (5-mm beam diameter) violet laser source (405 nm, peak power 4.5 mW, ThorLabs) placed 5 cm above the skull of the brain ischemic region (ipsilateral) for 3 min. Mouse skin was then sutured and allowed to recover on a heating pad until responsive. One hour or six hours after photonconversion, mice were anesthetized with isoflurane and transcardially perfused with 20 ml cold PBS containing Heparin (2U/ml). Cell suspensions from brain and skull (ipsilateral and contralateral), spleen and femur were isolated as indicated below for flow cytometric analysis and the percentage of photoconverted red cells (KikGR+) was analyzed in the appropriate cell populations.

Cell isolation

Mice were deeply anaesthetized with ketamine (120mg/kg) and xylazine (16mg/kg) and transcardiacally perfused with cold PBS. The skull, femur, spleen and brain were immediately harvested and kept on ice. The olfactory bulb and cerebellum were discarded, and the brain was mechanically dissociated in RPMI media with a douncer homogenizer, followed by a Percoll gradient centrifugation. For the isolation of skull bone marrow, meninges were peeled from the skull cup under the microscope and not included in this study. The isolated calvarium was cut into small pieces and mechanically dissociated on top of a 40 μ m cell strainer with the end of a 1-mL syringe plunger. After centrifugation at 500g for 7 minutes, cell suspensions were washed with PBS or FACS buffer.

Flow cytometry of KikGR animals

For differentiation of live and dead cells we stained cells with the Zombie NIR (BioLegend). For surface marker analysis, nonspecific binding was blocked by incubation for 10 min at 4 °C with anti-CD16/CD32 antibody (Biolegend, 5 ng/ μ l) antibody and stained with the appropriate antibodies for 15 min at 4 °C. The following antibodies were used for extracellular staining: CD45 (clone 30-F11, eFluor450, Invitrogen # 48-0451-82), CD11b (clone M1/70, PE/Cy7, Invitrogen # 25-0112-82), Ly6C (clone HK1.4, PerCP/Cy5.5, BioLegend #128012), Ly6G (clone 1A8-Ly6g, PE-eFluor610, Invitrogen #61-9668-82), CD3 (Clone 17A2, APC, Invitrogen # 17-0032-82) and CD19 (eBio1D3, APC/eFluor780, Invitrogen # 47-0193-82).

Cells were washed with FACS buffer, resuspended in 200 μ l of FACS buffer and acquired using a Cytex® Northern Lights (Cytex® Biosciences, US) and analyzed using FlowJo software (Treestar, US). Isotype controls were used to establish compensation and gating parameters.

Multiplexed RNAscope smFISH

Large tissue section staining and fluorescent imaging were conducted largely as described previously.⁹⁶ Sections were cut from fixed frozen samples embedded in OCT at a thickness of 10 μ m using a cryostat, placed onto Hydrophilic Plus slides (BioSB) and stored at -80°C until stained.

Fixed frozen tissue sections were processed using a Leica BOND RX to automate staining with the RNAscope Multiplex Fluorescent Reagent Kit v2 Assay (Advanced Cell Diagnostics, Bio-Techne), according to the manufacturers' instructions. Probes may be found in [Table S1](#), tab 37. Prior to staining, sections were post-fixed in 4% paraformaldehyde in PBS at 4°C for 15 minutes, then dehydrated through a series of 50%, 70%, 100%, and 100% ethanol, for 5 minutes each. To maximize adhesion of sections, slides were then baked at 37°C for 30 minutes. Following manual pre-treatment, automated processing included digestion with Protease III for 10 minutes prior to probe hybridisation. Tyramide signal amplification with TSA Vivid 520, TSA Vivid 570, and TSA Vivid 650 (Tocris Bioscience) and TSA-biotin (TSA Plus Biotin Kit, Perkin Elmer) and streptavidin-conjugated Atto 425 (Sigma Aldrich) was used to develop RNAscope probe channels.

To reduce autofluorescence, slides were treated immediately post-staining with TrueBlack® Plus Lipofuscin Autofluorescence Quencher (Biotium) for 5 minutes, then washed several times with PBS before mounting with ProLong Gold Antifade Mountant (Thermo).

High-resolution imaging

Stained sections were imaged with a Perkin Elmer Opera Phenix Plus High-Content Screening System, in confocal mode with 2 µm z-step size, using a 40X (NA 1.1, 0.149 µm/pixel) water-immersion objective. Channels: DAPI (excitation 375 nm, emission 435-480 nm), Atto 425 (ex. 425 nm, em. 463-501 nm), TSA Vivid 520 (ex. 488 nm, em. 500-550 nm), TSA Vivid 570 (ex. 561 nm, em. 570-630 nm), TSA Vivid 650 (ex. 640 nm, em. 650-760 nm).

Image stitching

Confocal image stacks were stitched as two-dimensional maximum intensity projections using proprietary Acapella scripts provided by Perkin Elmer. Resulting images were viewed as OME-TIFFs using OMERO Plus (Glencoe Software).

Scanning electron microscopy

Human skull samples were freshly prepared, dissected and immersed into fixative (4% PFA and 2.5% glutaraldehyde in 0.1 M sodium cacodylate buffer, pH 7.4; Science Services). After decalcification in EDTA for 1 month at 4°C and 1 month at room temperature, skull samples were washed, further dissected into 1x2 mm slabs bearing dura and bone layers and immersion fixed for 24h in fixative. We applied a standard rOTO en bloc staining protocol including postfixation in 2% osmium tetroxide (EMS), 1.5% potassium ferricyanide (Sigma) in 0.1 M sodium cacodylate (Science Services) buffer (pH 7.4).⁹⁷ Staining was enhanced by reaction with 1% thiocarbonyldrazide (Sigma) for 45 min at 40°C. The tissue was washed in water and incubated in 2% aqueous osmium tetroxide, washed and further contrasted by overnight incubation in 1% aqueous uranyl acetate at 4°C and 2 h at 50°C. Samples were dehydrated in an ascending ethanol series and infiltration with LX112 (LADD). Blocks were screened for tunnel structures transversing from the bone to the dura on cross sections using sequential trimming (TRIM2, Leica) and light microscopy of semithin sections. Serial sections were taken with a 35° ultra-diamond knife (Diatome) on an ATUMtome (Powertome, RMC) at a nominal cutting thickness of 200 nm and collected on freshly plasma-treated (custom-built, based on Pelco easiGlow, adopted from M. Terasaki, U. Connecticut, CT), carbon coated Kapton tape (kindly provided by Jeff Lichtman and Richard Schalek). Tape stripes were assembled onto adhesive carbon tape (Science Services) attached to 4-inch silicon wafers (Siebert Wafer) and grounded by adhesive carbon tape strips (Science Services). EM micrographs were acquired on a Crossbeam Gemini 340 SEM (Zeiss) with a four-quadrant backscatter detector at 8 kV using ATLAS5 Array Tomography (Fibics). We acquired medium resolution (40-100 nm) images of the entire section and the region of interest and processed in Fiji.⁸²

Proteomics Sample Preparation

Sample preparation for proteomics analysis was performed as described previously with slight modifications.⁹⁸ Briefly, for mouse samples, SDC lysis buffer (2% SDC, 100 mM Tris-HCl pH 8.5) was used to lyse the cell pellets at 95°C for 45 min at 600 rpm in a thermoshaker. For human samples which were fixed in PFA, prior to the SDC lysis buffer step, the samples were first resuspended in 6% SDS buffer, heat denatured, sonicated and then precipitated using 80% acetone overnight in -20°C. Next day, these samples were centrifuged and the pellet was resuspended in SDC lysis buffer. After this, the procedure remains the same for both mouse and human samples. Naïve meninges samples from mice were lost during sample preparation. The samples in SDC buffer were sonicated in high mode for 15 cycles (30 sec OFF, 30 sec ON) (Bioruptor® Plus; Diagenode). The samples were again heated at 95°C for 45 min at 600 rpm in a thermoshaker. The extracted and solubilized protein concentration was estimated by BCA method and 25 µg of protein was further reduced and alkylated using a final concentrations of 10 mM TCEP and 40 mM CAA in dark, at 45°C for 10 min with 600 rpm in a thermoshaker. The protein samples were digested overnight with Trypsin and LysC (1:50, protease:protein ratio) at 37°C, 1,000 rpm shake. Resulting peptides were acidified with 1% TFA 99% isopropanol with 1:1 volume-to-volume ratio, vortexed and centrifuged to pellet residual particles. The supernatant was transferred to fresh tubes and subjected to in-house built StageTip clean-up consisted of three layers of styrene divinylbenzene reversed-phase sulfonate (SDB-RPS; 3 M Empore) membranes. Peptides were loaded on the activated (100% ACN, 1% TFA in 30% Methanol, 0.2% TFA, respectively) StageTips, run through the SDB-RPS membranes, and washed by EtOAc including 1% TFA, isopropanol including 1% TFA, and 0.2% TFA, respectively. Peptides were then eluted from the membranes via 60 µL elution buffer (80% ACN, 1.25% NH4OH) and dried using vacuum centrifuge

(40 min at 45°C). Finally, peptides were reconstituted in 10 μ L of loading buffer (2% ACN, 0.1% TFA) and peptide concentration was estimated using Pierce™ Quantitative Colorimetric Peptide Assay.

Liquid chromatography and mass spectrometry (LC-MS/MS)

The mass spectrometry data was acquired in data independent acquisition (DIA) mode. The LC-MS/MS analysis was carried out using EASY nanoLC 1200 (Thermo Fisher Scientific) coupled with trapped ion mobility spectrometry quadrupole time-of-flight single cell proteomics mass spectrometer (timsTOF SCP, Bruker Daltonik GmbH, Germany) via a CaptiveSpray nano-electrospray ion source. Peptides (50 ng) were loaded onto a 25 cm Aurora Series UHPLC column with CaptiveSpray insert (75 μ m ID, 1.6 μ m C18) at 50°C and separated using a 50 min gradient (5–20% buffer B in 30 min, 20–29% buffer B in 9 min, 29–45% in 6 min, 45–95% in 5 min, wash with 95% buffer B for 5 min, 95–5% buffer B in 5 min) at a flow rate of 300 nL/min. Buffer A and B were water with 0.1 vol% formic acid and 80:20:0.1 vol% ACN:water:formic acid, respectively. MS data were acquired in single-shot library-free DIA mode and the timsTOF SCP was operated in DIA/parallel accumulation serial fragmentation (PASEF) using the high sensitivity detection-low sample amount mode. The ion accumulation and ramp time was set to 100 ms each to achieve nearly 100% duty cycle. The collision energy was ramped linearly as a function of the mobility from 59 eV at $1/K_0 = 1.6$ Vs cm^{−2} to 20 eV at $1/K_0 = 0.6$ Vs cm^{−2}. The isolation windows were defined as 24 X 25 Th from m/z 400 to 1000.

Proteomics data processing

diaPASEF raw files were searched against the human uniprot database using DIA-NN.⁹⁹ Peptides length range from seven amino acids were considered for the search including N-terminal acetylation. Oxidation of methionine was set as a variable modification and cysteine carbamidomethylation as fixed modification. Enzyme specificity was set to Trypsin/P with 2 missed cleavages. The FASTA digest for library-free search was enabled for predicting the library generation. The FDR was set to 1% at precursor and global protein level. Match-between-runs (MBR) feature was enabled and quantification mode was set to “Robust LC (high precision)”. The Protein Group column in DIA-NN’s report was used to identify the protein group and PG.MaxLFQ was used to calculate the differential expression.

Small animal PET/MRI acquisition

All rodent PET procedures followed an established standardized protocol for radiochemistry, acquisition times and post-processing,^{100,101} which was transferred to a novel PET/MRI system.¹⁰² All mice were scanned with a 3T Mediso nanoScan PET/MR scanner (Mediso Ltd, Hungary) with a triple-mouse imaging chamber. A 15-minute anatomical T1 MR scan was performed at 45 min after [18F]-GE180 injection (head receive coil, matrix size 96 × 96 × 22, voxel size 0.24 × 0.24 × 0.80 mm³, repetition time 677 ms, echo time 28.56 ms, flip angle 90°). Injected dose was 13 ± 2 MBq delivered in 200 μ L saline via venous injection. PET emission was recorded at 60–90 min p.i. PET list-mode data within 400–600 keV energy window were reconstructed using a 3D iterative algorithm (Tera-Tomo 3D, Mediso Ltd, Hungary) with the following parameters: matrix size 55 × 62 × 187 mm³, voxel size 0.3 × 0.3 × 0.3 mm³, 8 iterations, 6 subsets. Decay, random, and attenuation correction were applied. The T1 image was used to create a body-air material map for the attenuation correction.

Human TSPO-PET imaging acquisition

All participants were scanned at the Department of Nuclear Medicine, LMU Munich, using a Biograph 64 PET/CT scanner (Siemens, Erlangen, Germany). Before each PET acquisition, a low-dose CT scan was performed for attenuation correction. Emission data of TSPO-PET were acquired from 60 to 80 minutes^{62,103} after the injection of 187 ± 11 MBq [18F]GE-180 as an intravenous bolus, with some patients receiving dynamic PET imaging over 90 minutes. The specific activity was >1500 GBq/ μ mol at the end of radiosynthesis, and the injected mass was 0.13 ± 0.05 nmol. All participants provided written informed consent before the PET scans. Images were consistently reconstructed using a 3-dimensional ordered subsets expectation maximization algorithm (16 iterations, 4 subsets, 4 mm gaussian filter) with a matrix size of 336 × 336 × 109, and a voxel size of 1.018 × 1.018 × 2.027 mm. Standard corrections for attenuation, scatter, decay, and random counts were applied. For the AD cohort, emission data of A β -PET were acquired from 90 to 110 minutes after injection of 188 ± 10 MBq [18F]flutemetamol. A β -PET was assessed by a visual read (one expert reader), and the decision of A β -positivity/negativity was supported by a software-driven approach implemented in HERMES Gold (V4.17, HERMES Medical Solutions AB, Stockholm, Sweden). One positive evaluated target region (frontal, temporal, parietal, posterior cingulate) defined the scan as positive.

QUANTIFICATION AND STATISTICAL ANALYSIS

Single-cell RNA data analysis

Count matrix generation

Count matrices were created using Cell Ranger (v. 3.0.2) aligning reads to the mouse genome mm10 (ensrel97). Spliced and un-spliced matrices for RNA-velocity⁴³ analysis were computed using the velocityto (0.17.17) pipeline. (n=3 pooled animals for sham and n=6 pooled animals for MCAO).

Quality control

Samples were jointly analyzed using scanpy⁸³ (v. 1.6) and anndata (v. 0.7.5) in Python 3.7. Different quality control filters¹⁰⁴ were used to account for the characteristics of the different samples: In bone samples, all cells with a mitochondrial read fraction higher than 0.2 were removed. In meninges and brain samples, thresholds were 0.3 and 0.6, respectively. Further, cells with less than 1000 UMI counts (bone samples) and 500 UMI counts (meninges, brain), and more than 50,000 UMI counts were removed. We did not apply a minimum gene filter per cell to retain erythroblasts. All genes expressed in less than 10 cells were removed. To estimate doublets, we used the tool scrublet with a doublet score threshold of 0.1 and removed cells with a higher doublet score. Additionally, we filtered out two small clusters that showed dendritic cell markers as well as markers from other cell types as they might also be doublets, and a sub cluster of early monocytes that showed an increased mitochondrial fraction. Finally, our filtered dataset contained 147,082 cells expressing 17,040 genes coming from 32 samples.

Data preprocessing

To normalize the data with scanpy,¹⁰⁵ size factors were determined as follows: data were first temporarily normalized by total with a target sum of 10,000 per cell followed by log+1-scaling. Then, for each cell, 30 nearest neighbors were computed and data were clustered with Leiden clustering at default resolution 1. Small clusters with less than 100 cells were merged with closely related clusters based on the PAGA graph. For PAGA graph calculations we used scanpy's implementation with default parameters.¹⁰⁶ Then, size factors were computed on these clusters and the UMI count data were divided by scanpy size factors for each cell and log+1-scaled. Then, mitochondrial reads were removed and 4,000 highly variable genes per sample were computed (highly_variable_genes with flavor "cell_ranger" in scanpy). Further, cell cycle scores were computed (score_genes_cell_cycle in scanpy). To evaluate batch effects, PC regression scores for the variance explained by cell cycle, anatomic region and condition were computed for the full dataset and the MCAo replicates, respectively. PC regression scores were lowest in the condition and replicate covariate, respectively, and therefore no batch effect correction was performed.

Dendrograms

With scanpy's dendrogram function SciPy's hierarchical linkage clustering was calculated on a Pearson correlation matrix over regions which was calculated for 50 averaged principal components.

Cell type annotations

Cell types were annotated according to a two-step procedure. In a first step a Leiden clustering was calculated on the log-normalized data. The Leiden clusters were annotated with coarse cell type labels according differentially expressed known markers. In the second step Leiden clustering with multiple resolutions were calculated for each coarse cell type. Based on differentially expressed known markers, as well as additional information like number of genes¹⁰⁷ and scVelo⁴³ implementation of RNA velocity⁴² the clusters were annotated with fine cell types, and coarse annotations were refined.

Variance explained by covariates and PC regression

To quantify how strong cell type populations of each region diverge from the other regions the explained variance was calculated by linear regression in PCA space. For each bone the cell type populations were grouped into the given bone vs the other bones. Scores were only calculated if there were at least 20 cells in each of both groups. 50 principal components were calculated for each cell type. A linear regression on the group variable was calculated for each PC component. R2 scores of the linear regression were multiplied by the eigenvalues of the pc components and normalized by the eigenvalue sum, and finally summed up to the variance explained. The significance of each obtained variance explained score was measured via a permutation test. The region annotations were permuted 1000 times. Scores with a p-value below 0.0001 were considered as significant. We decided to exclude scapula in further downstream analysis because we detected an overall decrease in log counts in this sample.

Combinatorial DE tests

For each gene, two t-tests were calculated to identify if the gene is upregulated in a group of bones. To define the two bone groups for a given gene, bones were ordered by the gene's mean expression and split in two groups at the highest mean expression gap. The first t-test was conducted on the two groups and the second on the two bones closest to the expression gap. The second test ensures that the expressions of the two closest bones of the two groups are significantly different. The maximal p-value and minimal log fold change of both tests were used to identify DEGs. The chosen thresholds are $p < 0.05$ and LF change > 1 (> 0.5 for neutrophils analysis).

Other differential expression tests

Differences of DAMP expressions and pro- and anti-inflammatory genes were measured with t-tests ($p < 0.05$, Benjamini-Hochberg correction). The distributions of each DAMP's expression over CD45+ cells of each bone in the scRNA-seq data were tested for significance differences between conditions. The pro- and anti-inflammatory genes were tested individually as well as the mean expression of pro- and anti-inflammatory gene sets respectively between groups of bones and conditions.

Ligand receptor (LR) interactions

For each bone ligand receptor interaction pairs between cell types were calculated with CellPhoneDB's³⁹ statistical analysis. An interaction is defined by four variables: ligand, receptor, ligand cell type and receptor cell type. For a fair comparison between bones, pairs were only calculated on cell types that had at least 10 cells in each bone. The statistical analysis was applied on log normalized counts. 400 cells per cell type were sampled to generate a uniform background distribution of the permutation test which otherwise would be skewed towards highly abundant cell types. Cell types with more than 400 cells were down sampled using geometric sketching¹⁰⁸ (geosketch v 1.2), while the other cell types were up sampled. Strict thresholds based on the CellPhoneDB p-values

were applied to reduce the number of false positives: Interactions were considered as significant for p-values equal to 0 (1000 permutations). Interactions were only considered unique to a bone group if the p-value difference between that group and the non-significant group was above 0.95.

Gene ontology enrichment

Enrichment of Gene ontology (GO) terms for biological processes were calculated using GProfiler.¹⁰⁹

RNA velocity

RNA velocity⁴² in its scVelo⁴³ (v 0.2.3) implementation was used as follows: the dataset with spliced and unspliced raw counts was reduced to the given cell type and condition. Then genes were filtered to 2000 genes with at least 20 counts each, and cells were normalized (filter_and_normalize function in scVelo). First and second order moments for velocity estimation with the scVelo's dynamical model were calculated with default parameters.

Pseudotime analysis

Diffusion pseudotime⁴⁴ was calculated to order cells along the neutrophil maturation trajectory. For naive, sham and MCAo a PCA and neighbors' graph were recalculated on the neutrophils population. The default parameters of scanpy's tl.dpt function was used. As root point we selected the most extreme pro-neutrophil cell from the umap. For cell density visualization along pseudotime⁴⁴ the cell count was smoothed with a Gaussian kernel according to the default parameters of seaborn's (v 0.11.1) kdeplot function. Densities were normalized for each region separately.

Donor Deconvolution based on SNPs

To enable statistical tests between different groups in the scRNA-seq data and validate the obtained cell type proportions we deconvolved the samples of pooled animals based on obtained SNPs profiles of the measured transcripts. For SNPs calling we used cellSNP-lite¹¹⁰ (v. 1.2.2). Based on the obtained SNPs of each cell vireo¹¹¹ (v. 0.2.3) was used to demultiplex the 3 animals in each pooled sample. Erythrocytes were removed from the analysis as they only express the hemoglobin genes which leads the deconvolution algorithm to identify Erythrocytes as one donor.

Correlation of proportions with flow cytometry data

Pearson-correlation between cell type proportions of scRNA-seq and flow cytometry was measured over all cell types obtained in flow cytometry. Since flow cytometry measurements are relative to gated subgroups, we transformed the proportions of scRNA-seq cell types relative to comparable coarse subgroups as well. The significance of proportion differences between bones or conditions were obtained by t-tests over flow cytometry samples and over SNPs based deconvolved animals of the pooled scRNA-seq samples. A few cell type proportion differences were observed consistently with statistical significance ($p < 0.05$) in both methods. E.g., we observed a significantly higher number of mature B-cells in sham-operated and MCAo operated compared to naïve animals (Table S1, tab 3). Other cell type differences were observed with either one of the methods, but did not always reach statistical significance in both (Table S1, tabs 3 and 4). Upon injury, B-cell progenitors were depleted in both the flow cytometry and the scRNAseq data. Moreover, mature neutrophils in the calvaria had a strong trend for an increased cell proportion that, however, did not reach significance (Table S1, tabs 1–4).

Other differential expression tests

Differences of DAMP expressions and pro- and anti-inflammatory genes were measured with t-tests ($p < 0.05$, Benjamini-Hochberg correction). The distributions of each DAMP's expression over CD45+ cells of each bone in the scRNA-seq data were tested for significance differences between conditions. The pro- and anti-inflammatory genes were tested individually as well as the mean expression of pro- and anti-inflammatory gene sets respectively between groups of bones and conditions.

Bulk RNA data analysis for 5xFAD dataset

BCL files were demultiplexed with the bcl2fastq software from Illumina. After quality control with FastQC, reads were aligned using rnaSTAR65 to the GRCm38 (mm10) genome with ERCC synthetic RNA added. Read counts were collected using the parameter "quantMode GeneCounts" of rnaSTAR and using the unstranded values. We filtered out data points with less than 6000 genes or a mitochondrial fraction above 0.0015. Data points were log-normalized by total counts. The significance of the *Tspo* difference between WT and 5xFAD was calculated with a t-test. Differentially expressed genes between bones were obtained from t-tests with Benjamini-Hochberg correction and a p-value threshold of 0.05. The PCA was calculated on log normalized counts. (n=3 5xFAD, 5 wildtype animals, 50 cells per sample, 69 samples in total: 37 wildtype, 32 5xFAD).

Bulk RNA data analysis for MCAo dataset

For the count matrix generation reads were aligned to the GRCm39 genome with Salmon¹¹² using the nf-core/rnaseq pipeline¹¹³ (v. 3.9). No sample was excluded after quality control. Differentially expressed genes between bones were obtained using the DESeq2 model.¹¹⁴ The UMAP was calculated based on a PCA on log-normalized counts (normalization by total counts). For the comparison with scRNA-seq mouse data the pearson-correlation between mean log raw counts over genes of single cell and bulk data of each bone was calculated. (n=5 naïve, 5 sham, 6 MCAo animals).

Statistical analysis of KikGR animals

Due to high penetration of UV laser, some Cd11b+ cells, that could be microglia were illuminated as well. To control for this offset, the percentage of microglia illuminated was subtracted from myeloid cells. Acquired data was analyzed and visualized using GraphPad

Prism (version 8.0) using two-tailed t-test. (Each dot represents a biological replicate, n=5 for 1h and n=4 animals for 6h, data represented as \pm SEM).

Image Analysis

2-Photon analysis

We analyzed the 2-photon image stacks as maximum intensity projected time-series (3 frames per batch). We trained a random forest pixel classifier (Ilastik¹¹⁵ with default settings) on 3 images of the green channel (LysM-eGFP) and used that for subsequent classification of the LysM-eGFP channel of each image stack. This gave 8-bit probabilities for each frame, which we then thresholded and watershed-segmented using ImageJ.⁸² We performed this procedure with the pixel count (=area) occupied by GFP+ cells. We normalized LysM+ cell density at each time point to the cell density at baseline for each ROI. To account for other influences such as laser skull exposure, laser illumination, and anesthesia we further normalized the fold changes in sham and MCAo to those observed in naïve animals at the same time point. The quantification graph was analyzed and visualized using GraphPad Prism (version 8.0) using two-tailed t-test and simple linear regression. (n=3 for naïve and sham and n=5 animals for MCAo, data represented as \pm SEM.)

Tissue cleared mouse head analysis

For quantification of the mouse heads, manual ROIs were drawn on the frontal and parietal skull bones. C57BL6/J mice has been used for naïve condition quantification. The areas above manually selected threshold based on bone marrow coverage were recorded. The quantification graph was analyzed and visualized using GraphPad Prism (version 8.0) (Ordinary one-way ANOVA with multiple comparisons). (n=3 per group, data represented as \pm SEM).

Nr4a1 analysis

Three naïve mice heads and femurs were labeled with *Nr4a1* antibody and propidium iodide (for nuclei staining) and high-resolution images were obtained for 20 ROIs from the mouse skulls and 14 ROIs from the femurs (Figure 2D). We then quantified the number of voxels with a signal above threshold and found that a significantly higher percentage of *Nr4a1* positive voxels in the mouse head (Figure 2E). For the quantification of *Nr4a1*, same-sized regions of interest (ROIs) of 12x scans of the *Nr4a1* channel was used. For each of these, an expert manually selected the signal activation threshold after visual inspection in an image analysis software (e.g., Fiji). These thresholds were then used in Python to obtain binary masks of active expression of the same size as the ROI. Pixels that have higher intensity than the threshold in the *Nr4a1* channel are assigned the value of 1 (positive pixels), and the rest, 0. The total amount of pixels above threshold in each ROI is the number of positive pixels in the binary mask, whereas the percentage of signal in the volume is calculated as the number of positive pixels divided by the number of total pixels in the ROI. The quantification was analyzed and visualized using GraphPad Prism (version 8.0) using two tailed t-test. (n=3 per group, data represented as \pm SEM).

Human skull segmentation and channel measurement

Segmentation of the skull channels network and measurement of skull meninges channels were performed by using syGlass (<https://www.syglass.io/>). This software allows to visualize the microscopic data of the light sheet microscopes in 3D in Virtual Reality (VR). To segment and measure the data, smaller ROIs were cut out in VR. In these ROIs the openings in the meninges connected to the skull meninges channels were segmented up to the channel network that connects to the first bone marrow chambers in the skull. Then the Virtual reality software was used to change visual settings in order to measure, segment and to generate videos in 3D. The quantification was analyzed and visualized using GraphPad Prism (version 8.0) using two tailed t-test. (n=7 post-mortem samples, 23 ROI in total, 522 channels, data represented as \pm SEM).

Graph Representation of the Skull Channels

In order to achieve an additional compact representation of the skull channels we extracted a graph representation from the human skull segmentation described above using VR. We used the *voreen* open-source software to generate a centerline representation and second a graph representation with edges and nodes. In total, the skull channel graph consists of 399 nodes, and 440 edges with an average node degree of 2.21. The images are rendered using the Syglass software (Figure S6R).

Proteomics data analysis

Both human and mouse samples were jointly analyzed using scanpy (v. 1.9.1) and anndata (v. 0.7.6) in Python 3.8 and follows similar analysis pipeline. (n=3 independent samples each for bones and brain for all conditions, n=3 for meninges MCAo and sham conditions.)

Quality control

All proteins expressed in less than half of the bone samples were filtered out. For mice, the meninges were excluded from the filtration criterion since we identify the least number of proteins.

Data preprocessing

The data was further log-transformed and normalised per sample. KNN imputation was our method of choice using KNNImputer (n_neighbors=5) from the sklearn package (v. 0.22).

Gene set enrichment analysis (GSEA)

Enrichment of Gene ontology (GO) terms for biological processes were analysed using GProfiler¹⁰⁹ and Enrichr.¹¹⁶

Weighted correlation network analysis (WGCNA)

To identify the different modules of correlated genes in our datasets, WGCNA were used [python version: PyWGCNA¹¹⁷]. This method is an unsupervised algorithms for finding clusters (modules) of highly correlated genes based on a graph where nodes represents genes/proteins and the adjacency matrix is calculated based on the co-expression similarity between the nodes. Modules are then identified as clustered of interconnected nodes (genes/proteins) using hierarchical clustering. Gene ontology enrichment is further applied for genes/proteins identified from each module are to determine the biological processes pathways related to these modules.

Dendrograms

With scanpy's dendrogram function scipy's hierarchical linkage clustering was calculated on a Pearson correlation matrix over regions which was calculated for 50 averaged principal components.

Differential expression tests

To identify differentially regulated genes across two conditions (e.g. one bone vs the rest), scanpy's method that ranks genes group using t-tests was used. The maximal p-value and minimal log fold change were used to identify differentially expressed proteins/genes (DEPs). The chosen thresholds are $p < 0.05$ and LF change > 1 . These DEPs were further used to plot the volcano plots.

Small animal PET/MRI analysis

To capture skull specific PET signal from the skull in three wildtype mice, immediately after in vivo TSPO-PET imaging of mice, the brain, blood (perfusion via PBS) and all tissue surrounding the skull bone was removed. The skull bone of each mouse was imaged via a second TSPO-PET session. The signal attributable to the skull in the in vivo TSPO-PET images were compared to the signal in the respective skull-only TSPO-PET as standard of truth. For this purpose, an in-house CT template to delineate the skull bone in PET was used and a cluster-based analysis (k-means clustering) was performed, dividing the skull into 50 regions of increasing PET signal intensity. We studied TSPO-PET images of 5xFAD mice ($n=6$) and wild-type mice ($n=6$), all female at an age of 4.5 months. Normalization of injected activity was performed by cerebellar scaling¹¹⁸ to ensure consistency with human data. TSPO labeling in the skull was obtained in each mouse from a fronto-parietal volume-of-interest (comprising 24 mm³) and from a temporal volume-of-interest (comprising 16 mm³), which were semi-automatically delineated using an in-house CT template. Fronto-polar skull was spared to avoid signal spill-over from regions with strong amyloidosis and microglial activation inside the brain. TSPO labeling of the skull was compared 5xFAD and wild-type mice. Voxel-wise differences were calculated to allow a volume-of-interest independent validation of elevated skull tracer binding in 5xFAD mice. The quantification and visualization was done using GraphPad Prism (version 8.0) using two-tailed t-test (data represented as \pm SEM) and correlation analysis.

Human TSPO-PET imaging analysis

All TSPO-PET data were analyzed using PMOD. Spatial normalization was performed to a tracer specific templates in the Montreal Neurology Institute (MNI) space which was acquired via MRI-based spatial normalization. All images were normalized by cerebellar grey matter scaling (defined by the Hammers atlas¹¹⁹) prior to analysis and a standardized-uptake-value (SUV) analysis served for pseudo-reference tissue independent validation.

For stroke, multiple sclerosis and 4R tauopathy patients we defined three target regions based on a voxel-wise exploratory analysis: temporopolar skull (comprising 18 cm³), skull base (comprising 97 cm³), and prefrontal skull (comprising 7 cm³). All regions were semi-automatically delineated using the human CT template available in PMOD. Region-based PET values were normalized to a composition of values of exactly age-matched (≤ 1 year difference) controls at the group level. Voxel-wise differences (% vs. age-matched controls) were calculated to allow a volume-of-interest independent validation of elevated skull tracer binding in all patient groups. Following the region-based approach, we used compositions of exactly age-matched controls for this calculation.

For the AD cohort, TSPO labeling in the calvaria was obtained in each participant from a large fronto-parietal volume-of-interest (comprising 66 cm³), which was semi-automatically delineated using the human CT template available in PMOD. Posterior and frontal calvaria was spared to avoid signal spill-over from sinuses and extracranial structures. Furthermore, we used a Brainnetome⁶⁶ atlas-based classification of cortical brain regions and corresponding calvaria regions to test for regional calvaria-brain associations. To this end, we increased the dimension of the atlas by a factor of 1.2 and we delineated all volumes-of-interest that were represented in the calvaria as defined by the CT template ($\geq 50\%$ of voxels included). This approach resulted in 64 individual calvaria-brain region pairs. TSPO labeling of the calvaria was compared between AD patients with β -amyloid pathophysiology (AD) and β -amyloid negative controls. Voxel-wise differences were calculated to allow a volume-of-interest independent validation of elevated calvaria tracer binding in patients with AD. TSPO labeling of the calvaria was correlated with age, sex, and cognitive testing (MMSE, CERAD, CDR) as well as with β -amyloid levels in CSF. Calvaria-brain associations of TSPO-PET were tested for the global calvaria volume-of-interest with Braak stage and β -amyloid related composite brain regions. Furthermore, calvaria-brain associations were tested by a correlation matrix of the predefined 64 volume-of-interest pairs. Single region increases in patients with AD vs. healthy controls were correlated between calvaria and brain regions.

As a validation of specificity, we performed an additional analysis of TSPO tracer uptake in the corpus vertebrae of C2. This bone was chosen as a negative control region since it was captured in nearly all acquisitions as the most remote bone structure relative to skull. The analysis was performed manually using HERMES Full Flex (V4.17, HERMES Medical Solutions AB, Stockholm, Sweden). A 1.0 mm³ sphere was placed in the center of C2 and SUV was extracted and normalized to cerebellar uptake (i.e. SUVr).

For longitudinal imaging, individual follow-up TSPO-PET SUVr of the fronto-parietal region were compared to baseline by a paired t-test for both patients of the AD continuum and controls. For patients with stroke, we used SUV normalization since distinct changes of tracer uptake in whole brain did not allow reference tissue normalization for the longitudinal analysis. Here, individual follow-up TSPO-PET SUV of the infarct region were compared to baseline by a paired t-test, as no 3 month follow-up scans were available for healthy controls. As a region independent analysis we used the skull template implemented in SPM (V12, University College of London, London, UK) running in Matlab version R2016 (MathWorks Inc., Natick, MA) and performed a voxel wise paired t-test analysis between baseline and follow-up images of patients of the AD continuum and controls (SUVr) as well as patients with stroke (SUV). A p value threshold of 0.05, incorrectly for multiple comparisons, was considered significant to obtain a pattern of changes rather than only peak clusters with the highest changes. Significant changes were displayed as a skull surface projection. The ActiGliA cohort also allowed to correlate changes of TSPO tracer uptake in brain with changes of TSPO tracer uptake in skull for patients of the AD continuum and controls (not feasible in stroke due to the individual locations of the lesion). Skull was treated as one region of interest as described for the longitudinal analysis above. Brain was parcellated into 246 regions of the brainnetome atlas.¹²⁰ Changes of all 246 brain regions were correlated with changes in skull separately for patients of the AD continuum and controls. An FDR correction for multiple comparisons was applied to the respective p values.

Statistics for human TSPO-PET imaging

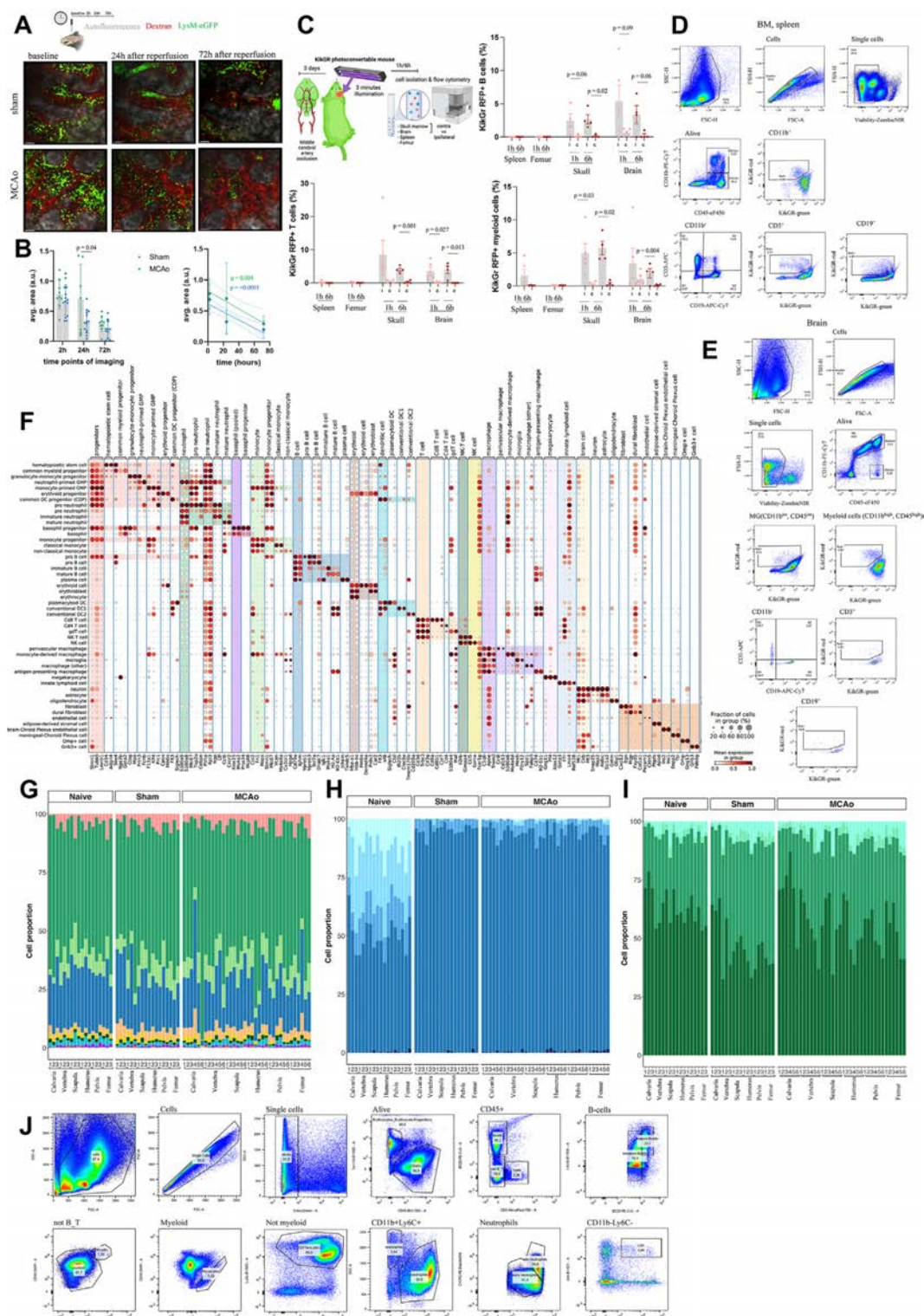
Group comparisons of VOI-based PET results between patient groups with mixed neurological disorders and controls (n=5 groups) were assessed by 1-way ANOVA and Bonferroni post hoc correction for multiple comparisons using IBM SPSS Statistics (version 22.0; SPSS). All data were controlled for age, sex and the TSPO single nucleotide polymorphism at the individual subject level.

Group comparison of Human TSPO-PET results between controls and AD patients were assessed by a two-tailed t-test in SPSS Statistics (version 22.0; SPSS), controlled for age, sex and the TSPO single nucleotide polymorphism. For correlation analyses, Pearson coefficients of correlation (R) were calculated. A threshold of P less than 0.05 was considered to be significant for the rejection of the null hypothesis. The visualization of the data was done using GraphPad Prism (version 8.0), (data represented as \pm SEM).

ADDITIONAL RESOURCES

Videos related to this work: <https://www.discotechnologies.org/Calvaria/>.

Supplemental figures



(legend on next page)

Figure S1. Assessment of skull cell dynamics and details of cell-type annotations, related to Figure 1

(A) Overview of the two-photon experiment and representative images from sham and MCAo groups. 2, 24, and 72 h after surgeries same ROIs were imaged. Per each imaging session, animals were given dextran for vessel labeling ($n = 3$ for naive and sham and $n = 5$ animals for MCAo). Scale bars, 50 μm .

(B) Quantification of changes in area between sham and MCAo conditions. LysM was quantified based on maximum intensity projected time series of 3 frames per batch. Average area of LysM cells in MCAo is less than sham in 24 h ($p = 0.04$) and both conditions have significant decrease of LysM cells over time ($p = 0.004$ for sham and $p < 0.0001$ in MCAo) Data represented as \pm SEM. (see [STAR Methods](#) for details).

(C) Photoconversion in KikGR mouse model to track cell trafficking from skull to brain 3 days after stroke. B cell (1 h, ipsi vs. contra skull, $p = 0.06$, brain, $p = 0.09$. 6 h ipsi vs. contra skull, $p = 0.02$, brain, $p = 0.06$), T cells (1 h, ipsi vs. contra brain, $p = 0.027$. 6 h ipsi vs. contra skull, $p = 0.001$, brain, $p = 0.013$), and myeloid cells (1 h, ipsi vs. contra skull, $p = 0.03$. 6 h ipsi vs. contra skull, $p = 0.02$, brain, $p = 0.004$) were analyzed within the skull and brain compartment at indicated time points. Data represented as \pm SEM.

(D and E) Gating strategy for B cells, T cells, myeloid cells in bone marrow and spleen (D) and in brain (E).

(F) Coarse and fine annotated cell types and their marker genes.

(G–I) Deconvolved pooled data using SNPs showing (G) coarse annotations, (H) B cell fine cell annotation, and (I) neutrophils fine cell annotations.

(J) Gating strategy for proportions: B cells, T cells, monocytes, neutrophils, eosinophils, erythroid cells, progenitors, NK cells, late neutrophils, B cell progenitors for flow cytometry experiment demonstrating proportions.

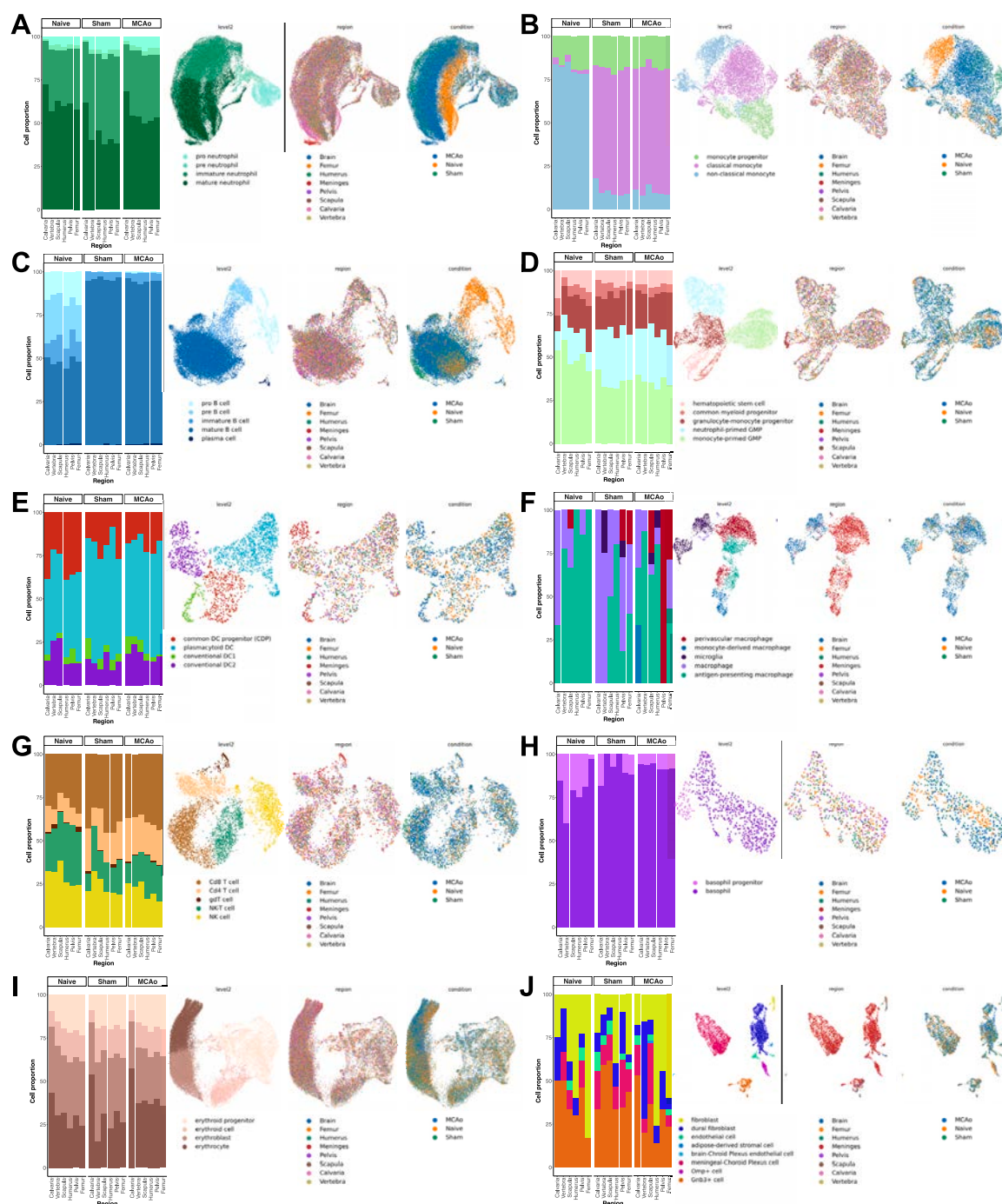


Figure S2. Proportions and UMAP of fine cell types over all conditions, related to Figure 1

Coarse cell types are shown separately with their fine cell-type proportion over three conditions, and their UMAP distribution for the cell-type, condition and region: (A) neutrophils, (B) monocytes, (C) B cells, (D) progenitors, (E) dendritic cells, (F) macrophages, (G) T and NK cells, (H) basophils, (I) erythroid cells, and (J) structural cells.

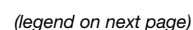


Figure S3. Analysis of skull cell numbers, neutrophil development, and inflammatory responses in different bones and the meninges, related to Figure 2

- (A) Whole head clearing of LysM mice in naive, sham, and MCAo (stroke on left side) condition.
- (B) Quantification of PI signal in the frontal and parietal bones show a strong trend ($F(2,6) = 5.027$, $p = 0.0522$) for increased PI signal in MCAo condition compared to sham ($p = 0.124$) and naive conditions ($p = 0.053$).
- (C) Quantification of PI signal in the contralateral parietal skull bone of show increase ($F(2,6) = 8.323$, $p = 0.019$) in PI signal in MCAo condition compared to sham ($p = 0.040$) and naive ($p = 0.022$) conditions ($n = 3$ per group); dpi, days post injury.
- (D) Expression of DAMP relevant genes in three conditions with their relative hierarchical clustering.
- (E) Comparison of naive vs. injury response of specific DAMP genes. Color code indicates significance ($p < 0.05$).
- (F) The unique LR pairs in the skull and vertebra in three different conditions. LR pairs that occur in at least 5 different cell-type pairs in a given bone group are shown. (permutation test, 1000 permutations, $p = 0$)
- (G) Pseudo-time analysis of naive, sham, and MCAo with normalized cell density in each condition for each region.
- (H) Phase portrait showing unspliced and spliced counts in neutrophils of gene *S100a6* for naive, sham and MCAo respectively.
- (I–K) Mean expressions of upregulated genes in meninges and in a single other group in (I) naive, (J) sham, and (K) MCAo.
- (L and M) Mean and standard deviation of (L) anti-inflammatory and (M) pro-inflammatory score over cells of all cell types, B cells, neutrophils, and monocytes in naive, sham, and MCAo (significance and LFC in [Table S1](#), tabs 29 and 30). Inflammatory score is based on the expression of *Il6*, *Il1a*, *Il1b*, *Ifng*, *Il11*, *Il7d*, *Il7f*, *Il18* and *Tnf* (pro-inflammatory) and *Il1rn*, *Tgfb1*, *Il4*, *Il10*, *Il12a*, and *Il13* (anti-inflammatory).

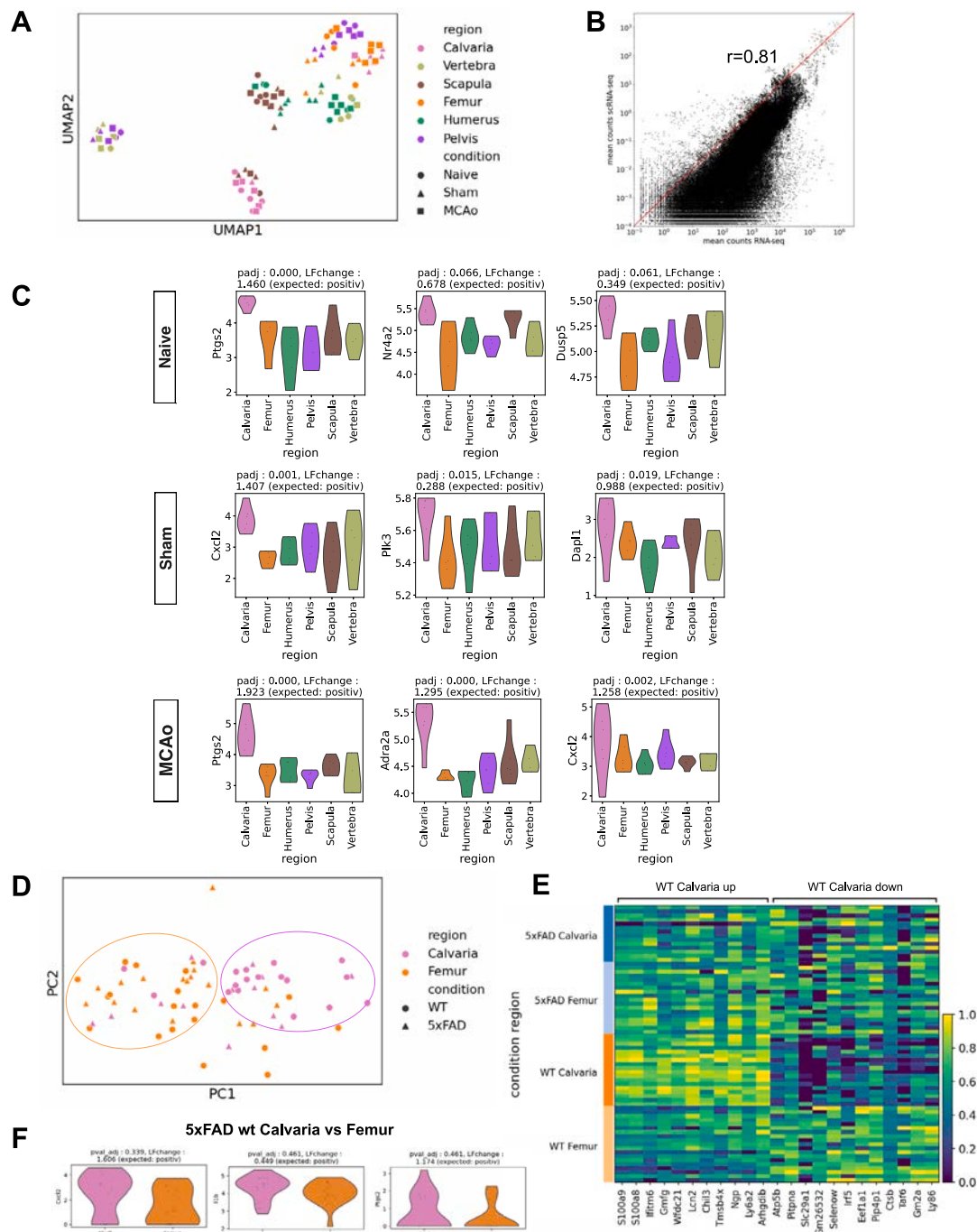


Figure S4. Analysis of bulk RNA-seq data of bone marrow cells, related to Figure 2

(A) PCA of calvaria, scapula, humerus, vertebra, pelvis, and femur from 5 naive, 5 sham, 6 MCAo animals. Color represents region and shape represents condition.

(B) Correlation between bulk RNA gene expression and scRNA-seq pseudobulked dataset. $r = 0.81$.

(C) Representative genes that show the same trend with scRNA-seq data for each condition. p values and log-fold changes are given on top of each violin plot (p < 0.001 for Ptgs2, p = 0.066 for Nr4a2, and p = 0.061 for Dusp5 in naive, p = 0.001 for Cxcl2, p = 0.015 for Plk3 and p = 0.019 for Dapl1 in sham, p < 0.001 for Ptgs2, p < 0.001 for Adra2a, and p = 0.002 for Cxcl2 in MCAo). Single-cell expression of these genes are given with "expected," positive means scRNA-seq data showed an increased trend of the given gene.

(legend continued on next page)

(D) PCA of femur and calvaria in 5xFAD model of Alzheimer's disease. 5xFAD animals are compared with their littermate controls. Colors represent different bones whereas shapes represent condition.

(E) Calvaria upregulated and downregulated genes in control case. There are no differentially expressed genes in AD case. The expression of the differentially expressed genes are shown in all groups for comparison. ($p < 0.05$)

(F) Selected upregulated genes that show the same trend in 5xFAD dataset. p values and log-fold change are given on top of each violin plot ($p < 0.339$ for Cxcl2, $p = 0.461$ for Il1b, and $p = 0.461$ for Ptgs2). Single-cell expression of these genes are given with expected, positive means scRNA-seq data showed an increased trend of the given gene.

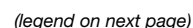
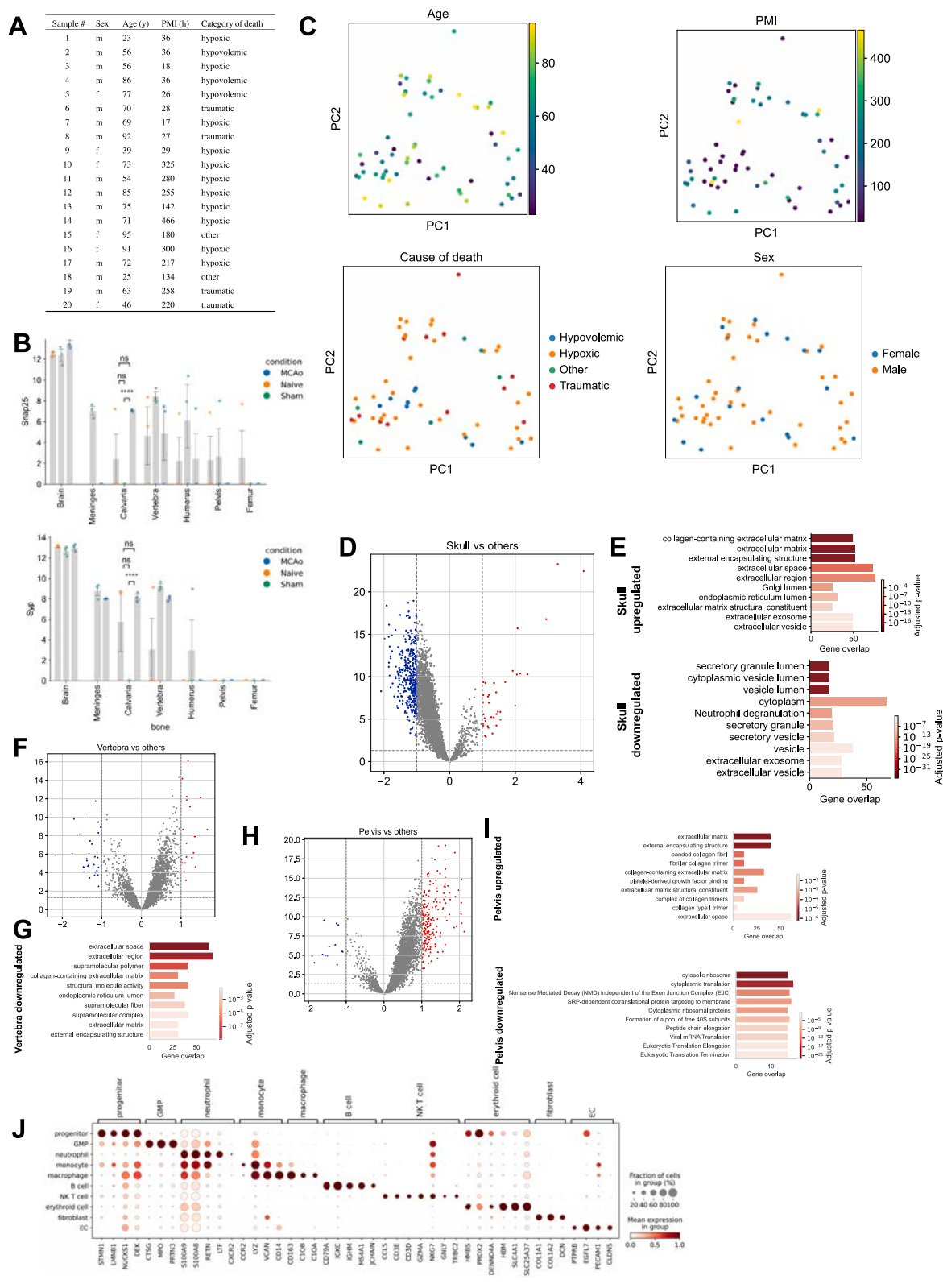


Figure S5. Details of the analysis of mouse proteome data and human skull-meninges channels, related to Figures 3 and 4

- (A) Number of proteins detected from each bone.
- (B) Number of common proteins and unique proteins detected from different bones for different conditions. Top: naive, middle: sham, and bottom: MCAo.
- (C) 10 top upregulated proteins for each region in each condition (LFC > 1, $p < 0.05$).
- (D) Dendrogram for each sample and condition is shown.
- (E) Volcano plot shows the difference between calvaria MCAo vs. sham. (LFC > 1, $p < 0.05$) Related GO terms are shown below.
- (F–K) Volcano plots are showing (F) naive calvaria vs. other bones, (H) sham calvaria vs. other bones and (J) MCAo calvaria vs. other bones, respectively. (LFC > 1, $p < 0.05$) (G–K) GO terms of upregulated calvaria proteins in (G) naive, (I) sham, and (K) MCAo conditions are provided below each volcano plot.
- (L) Correlation plot of module 2 of WGCNA neutrophil degranulation GO term proteins with scRNA-seq expression levels. Spearman correlation, $R = +0.42$, $p < 0.0001$.
- (M) Details for post-mortem tissue clearing and light-sheet fluorescent imaging experiments.
- (N) Channels connecting calvaria's bone marrow to the meninges with Iba1+ cells. Scale bars, 150 μm .
- (O) Human bone marrow labeled for cell nuclei (PI, in green), macrophage (Iba1, in magenta) is shown with calvaria bone (autofluorescence).
- (P) Skull channel diameter distribution based on each ROI quantified.
- (Q) Channel number per 1 cm^3 distribution over all ROIs and samples.
- (R) Annotated skull + dura ROI, bottom part shows dura with brown annotation, skull channels are annotated in green and bone marrow is annotated in gray. Annotated dura, skull and bone marrow mask. Graph extraction of human skull architecture, total length, and radius of the shortest path from skull marrow to the dural meninges in μm , respectively. Scale bars, 500 μm .
- (S–W) 200 nm thick scanning electron microscopy images of a SMC with zoom-ins. (S) shows different axial depths of the same channel.



(legend on next page)

Figure S6. Details of the analysis of the human proteome data, related to Figure 5

- (A) Post-mortem sample information, category of death is based on how death affects the brain.
- (B) Two proteins found uniquely in the human skull that show a similar trend in the mouse dataset. Snap25 and Syp expression in calvaria MCAo is higher than in sham ($p = 5.786\text{e-}08$ and $p = 2.000\text{e-}05$, respectively).
- (C) PCA of bones based on age, cause of death group, PMI, and sex, respectively; PMI, post-mortem interval.
- (D–I) Volcano plots among different bones: calvaria vs. others (D), vertebra vs. others (F), and pelvis vs. others (H) suggest there is a global downregulation in the skull compared to pelvis. ($\text{LFC} > 1$, $p < 0.05$) with GO terms for upregulated and downregulated for each bone (E), (G), and (I).
- (J) Cell-type annotation marker genes for scRNA-seq of human skull.

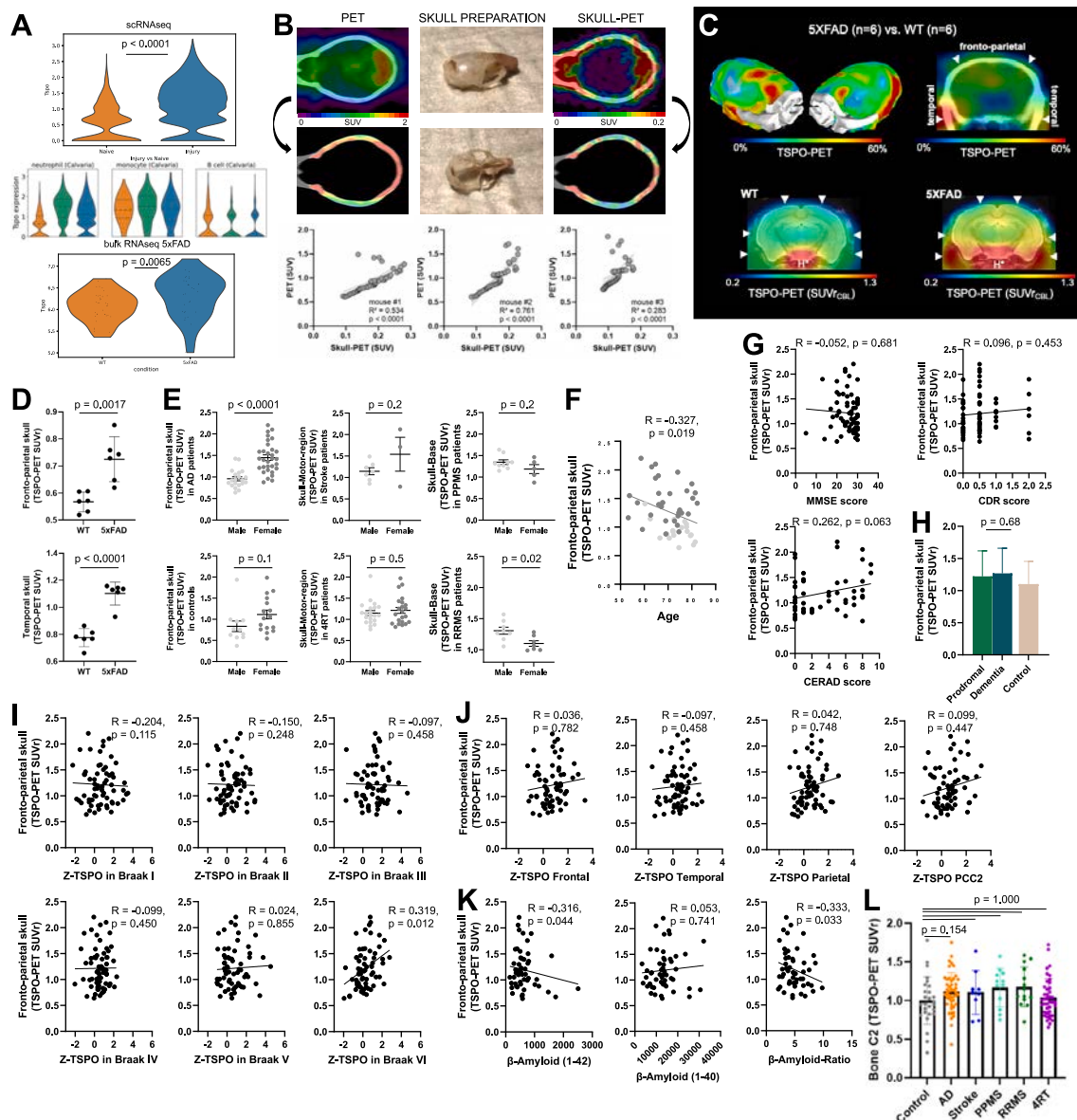


Figure S7. Influence of imaging method, and various covariates on TSPO-PET data, related to Figure 6

(A) TSPO RNA levels in naive vs. injury (MCAo + sham) ($p < 0.0001$) conditions in the skull from the scRNA-seq data. TSPO RNA levels in 5xFAD vs. wild type in the calvaria ($p = 0.0065$).

(B) *In vivo* TSPO-PET imaging of three wild-type mice, followed by a second scan after immediate removal of the brain, blood, and all tissue surrounding the skull bone. Signal attributable to the skull in the *in vivo* TSPO-PET images was compared to the signal in the respective skull-only TSPO-PET to delineate skull signal in mice (three replicates, $R^2 = 0.534, 0.761, 0.283, p < 0.0001$).

(C) Coronal slice upon a CT template shows %TSPO-PET differences between 5xFAD and wild-type mice at the group level. Images indicate increased TSPO labeling in the fronto-parietal and temporal skull of 5xFAD mice in contrast against age-matched wild-type mice. White arrows indicate spots with higher increases of skull TSPO labeling when compared to adjacent increases of brain TSPO labeling in 5xFAD. Axial slices upon an MRI template show TSPO-PET in an individual 5xFAD and an individual wild-type mouse. Elevated TSPO labeling in fronto-parietal and temporal skull is present (white arrows) in the 5xFAD mouse when compared to the wild-type mouse. H* = hypophysis with known strong TSPO-PET signal.

(D) Fronto-parietal skull, $p = 0.0017$, temporal skull, $p < 0.0001$ (two-tailed t test). Data represented as \pm SEM.

(E) Quantification of relevant skull signal sex differences for AD ($p < 0.0001$; controlled for age and TSPO-binding single nucleotide polymorphism), stroke ($p = 0.2$), PPMS ($p = 0.2$), RRMS ($p = 0.02$), 4RT ($p = 0.5$) patients and controls ($p = 0.1$). Data represented as \pm SEM.

(F) Quantification of fronto-parietal skull signal age associated patterns ($p = 0.019$, two-tailed t test, controlled for gender and TSPO-binding single nucleotide polymorphism) among 50 AD continuum patients. Data are means \pm SD. SUV_r, standardized uptake value ratio.

(G) Fronto-parietal skull TSPO signal from patients with AD show no significant correlation with clinical severity in MMSE ($p = 0.681$), CERAD ($p = 0.063$), and CDR ($p = 0.453$) scorings.

(legend continued on next page)

(H) Fronto-parietal skull TSPO signal in Alzheimer's disease compared to control patients (prodromal vs. dementia: $p = 0.63$, data represented as \pm SEM.).

(I) Fronto-parietal skull TSPO signal shows a positive association only with brain TSPO signal in the Braak VI stage region ($p = 0.115$ for Braak I, $p = 0.248$ for Braak II, $p = 0.458$ for Braak III, $p = 0.450$ for Braak IV, $p = 0.855$ for Braak V, and $p = 0.012$ for Braak VI).

(J) Fronto-parietal skull TSPO signal is not significantly associated with brain TSPO signal in any β -amyloid related regions: frontal ($p = 0.782$), temporal ($p = 0.458$), parietal ($p = 0.748$), and posterior cingulate cortex/precuneus ($p = 0.447$).

(K) Fronto-parietal skull TSPO signal is correlated with β -amyloid₄₂ ($p = 0.044$) but not β -amyloid₄₀ ($p = 0.741$) in cerebrospinal fluid, also reflected by the significant negative correlation of the β -amyloid ratio ($p = 0.033$).

(L) TSPO-PET signal quantifications in C2 bone of vertebra. One-way ANOVA with Bonferroni post hoc correction. See [STAR Methods](#) for details of normalization and statistical analysis. Significant differences of disease vs. controls are indicated ($p = 1.0$ for control vs. stroke, PPMS, RRMS, and 4RT, $p = 0.154$ for control vs. AD). Data represented as \pm SEM. Pairwise comparison of all groups can be found in [Table S3](#).

4.4 Study 4: Spatial proteomics in three-dimensional intact specimens.

The paper “Spatial proteomics in three-dimensional intact specimens.” was published in 2022 in the journal Cell as a resource article. The full citation is:

Harsharan Singh Bhatia*, Andreas-David Brunner*, Furkan Öztürk*, Saketh Kapoor, Zhouyi Rong, Hongcheng Mai, Marvin Thielert, **Mayar Ali**, ..., Fabian Theis, Matthias Mann, Ali Ertürk, "Spatial proteomics in three-dimensional intact specimens." Cell 185.26 (2022): 5040-5058. <https://doi.org/10.1016/j.cell.2022.11.021>

Summary:

Most spatial proteomics methods are limited in profiling to few proteins or 2-dimensional sections. However, studying proteome in three-dimensional large specimens (or even the whole body) is essential to capture the cellular function in pathological and physiological stages in an unbiased holistic view. In this study, we developed a technology that allows the proteome analysis of 3D large specimens by combining tissue clearing, imaging, robotic tissue extraction, and ultra-high-sensitivity mass spectrometry.

My collaborators developed DISCO-MS technology and applied it to cleared tissue using different techniques (3DISCO, uDISCO and vDISCO). They generated proteomics data from both fixed-fresh tissue (as control) and cleared tissues. Subsequently, my collaborators and I analysed the data to compare the composition, structure, and function of the entirety of expressed proteins between fresh and cleared tissues and showed that with DISCO-MS we can achieve high depth and quantitative accuracy comparable to that of fresh samples.

DISCO-MS was employed on various mouse models as well as human data. First, my collaborators utilised and validated the capabilities of DISCO-MS technology on mild traumatic brain injury (mTBI) mouse model. They generated proteomics data on isolated regions with locally activated microglia with known spatial locations extracted by laser capture microdissection (LCM). My collaborators and I analysed this data and identified several biomarkers of mTBI that were both novel and previously reported in literature which confirmed the power of DISCO-MS to analyse spatially resolved proteomics data in an unbiased manner.

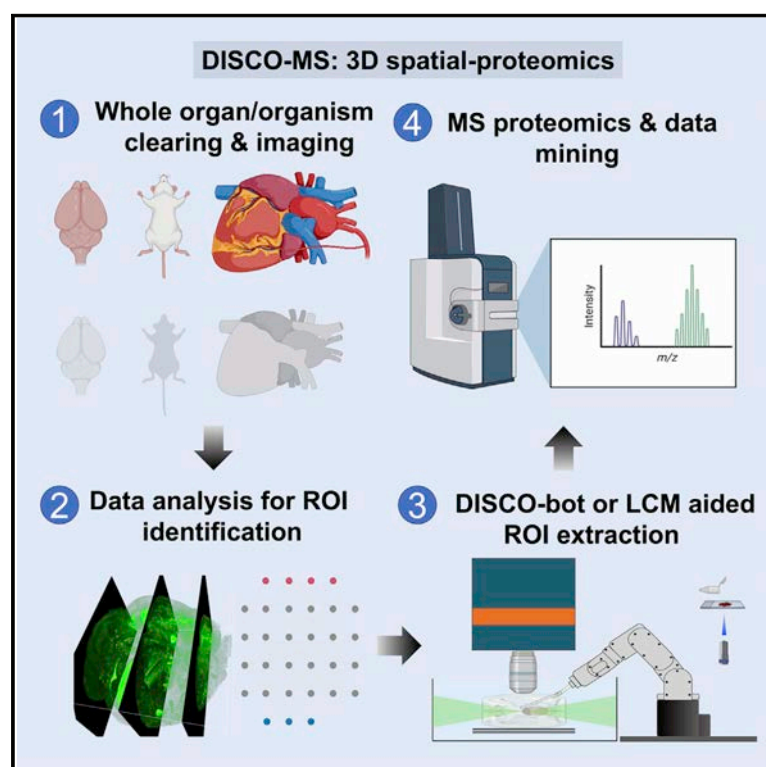
My collaborators further applied DISCO-MS on early-stage (6 weeks) and late-stage (6 months) Alzheimer's disease (AD) mouse models, identified the A β plaques in both time points using deep-learning models (U-Nets), extracted individual A β plaques using laser capture microdissection (LCM) and generated proteomics data for A β plaques at early and late AD stages. I further analysed the proteomics data of the isolated single-plaque microenvironments with the known spatial locations in whole brains and highlighted AD biomarkers at the early stages of the disease.

To apply DISCO-MS to larger cleared specimens (or even whole bodies), my collaborators developed a robotic tissue extraction tool (DISCO-BOT) to precisely extract small samples from specific locations. My collaborators generated proteomics data from cleared samples extracted via DISCO-BOT from mouse bone marrow and human heart tissue with acute myocardial infarction. My collaborators and I analysed these two sets of data and were able to identify perturbations in specific protein groups.

The development of DISCO-MS represents a significant advancement in 3-dimensional spatial proteomics, providing a new avenue to study the molecular profiles of tissues in an unbiased and holistic manner.

Spatial proteomics in three-dimensional intact specimens

Graphical abstract



Authors

Harsharan Singh Bhatia,
Andreas-David Brunner,
Furkan Öztürk, ..., Fabian Theis,
Matthias Mann, Ali Ertürk

Correspondence

mmann@biochem.mpg.de (M.M.),
erturk@helmholtz-muenchen.de (A.E.)

In brief

DISCO-MS and DISCO-bot allows for unbiased spatial proteome analysis of small tissue regions identified by panoptic imaging of large cleared samples, *in silico* reconstructions, and automated minimally invasive robotic tissue extraction.

Highlights

- DISCO-MS is a spatial proteomics technology in optically cleared whole specimens
- DISCO-MS is aided by AI and robotics and yields proteome similar to fresh samples
- DISCO-bot-aided DISCO-MS reveals spatial immune cell heterogeneity in mouse bones
- DISCO-bot-aided DISCO-MS reveals plaque heterogeneity in human coronary artery



Resource

Spatial proteomics in three-dimensional intact specimens

Harsharan Singh Bhatia,^{1,2,24} Andreas-David Brunner,^{3,4,24} Furkan Öztürk,^{1,24} Saketh Kapoor,¹ Zhouyi Rong,^{1,2,13} Hongcheng Mai,^{1,2,13} Marvin Thielert,³ Mayar Ali,^{1,5} Rami Al-Maskari,^{2,7,8} Johannes Christian Paetzold,^{1,7,8,10} Florian Kofler,^{7,8,9,12} Mihail Ivilinov Todorov,^{1,2} Muge Molbay,^{1,2,13} Zeynep Ilgin Kolabas,^{1,2,5} Moritz Negwer,¹ Luciano Hoeher,¹ Hanno Steinke,¹⁹ Alina Dima,^{7,8} Basavdatta Gupta,¹ Doris Kaltenecker,^{2,14} Özüm Sehnaz Caliskan,^{15,16} Daniel Brandt,^{15,16} Natalie Krahmer,^{15,16} Stephan Müller,^{17,18} Stefan Frieder Lichtenthaler,^{5,6,17,18} Farida Hellal,^{1,2} Ingo Bechmann,¹⁹ Bjoern Menze,^{7,8,11} Fabian Theis,^{20,21,22} Matthias Mann,^{3,23,*} and Ali Ertürk^{1,2,5,6,25,*}

¹Institute for Tissue Engineering and Regenerative Medicine (iTERM), Helmholtz Zentrum München, 85764 Neuherberg, Germany

²Institute for Stroke and Dementia Research, Klinikum der Universität München, Ludwig-Maximilians University Munich, 81377 Munich, Germany

³Department for Proteomics and Signal Transduction, Max Planck Institute of Biochemistry, 82152 Martinsried, Germany

⁴Boehringer Ingelheim Pharma GmbH & Co. KG, Drug Discovery Sciences, Birkendorfer Str. 65, D-88400 Biberach Riss, Germany

⁵Graduate School of Neuroscience (GSN), 82152 Munich, Germany

⁶Munich Cluster for Systems Neurology (SyNergy), 81377 Munich, Germany

⁷Center for Translational Cancer Research (TranslaTUM) of the TUM, 81675 Munich, Germany

⁸Image-Based Biomedical Modeling, Department of Informatics, Technical University of Munich, 85748 Garching, Germany

⁹Helmholtz AI, Helmholtz Zentrum München, 85764 Neuherberg, Germany

¹⁰Biomedical Image Analysis Group, Department of Computing, Imperial College London, London SW7 2AZ, UK

¹¹Department for Quantitative Biomedicine, University of Zurich, 8006 Zurich, Switzerland

¹²Department of Neuroradiology, Klinikum rechts der Isar, 81675 Munich, Germany

¹³Munich Medical Research School (MMRS), 80336 Munich, Germany

¹⁴Institute for Diabetes and Cancer, Helmholtz Zentrum München, 85764 Neuherberg, Germany

¹⁵Institute for Diabetes and Obesity, Helmholtz Zentrum München, 85764 Neuherberg, Germany

¹⁶German Center for Diabetes Research, Helmholtz Zentrum München, 85764 Neuherberg, Germany

¹⁷German Center for Neurodegenerative Diseases (DZNE), 81377 Munich, Germany

¹⁸Neuroproteomics, School of Medicine, Klinikum Rechts der Isar, Technical University of Munich, 81675 Munich, Germany

¹⁹Institute of Anatomy, University of Leipzig, 04109 Leipzig, Germany

²⁰Institute of Computational Biology, Helmholtz Zentrum München, 85764 Neuherberg, Germany

²¹TUM School of Life Sciences Weihenstephan, Technical University of Munich, 85354 Freising, Germany

²²Department of Mathematics, Technical University of Munich, 85748 Garching, Germany

²³NNF Center for Protein Research, Faculty of Health Sciences, University of Copenhagen, 2200 Copenhagen, Denmark

²⁴These authors contributed equally

²⁵Lead Contact

*Correspondence: mmann@biochem.mpg.de (M.M.), erturk@helmholtz-muenchen.de (A.E.)

<https://doi.org/10.1016/j.cell.2022.11.021>

SUMMARY

Spatial molecular profiling of complex tissues is essential to investigate cellular function in physiological and pathological states. However, methods for molecular analysis of large biological specimens imaged in 3D are lacking. Here, we present DISCO-MS, a technology that combines whole-organ/whole-organism clearing and imaging, deep-learning-based image analysis, robotic tissue extraction, and ultra-high-sensitivity mass spectrometry. DISCO-MS yielded proteome data indistinguishable from uncleared samples in both rodent and human tissues. We used DISCO-MS to investigate microglia activation along axonal tracts after brain injury and characterized early- and late-stage individual amyloid-beta plaques in a mouse model of Alzheimer's disease. DISCO-bot robotic sample extraction enabled us to study the regional heterogeneity of immune cells in intact mouse bodies and aortic plaques in a complete human heart. DISCO-MS enables unbiased proteome analysis of preclinical and clinical tissues after unbiased imaging of entire specimens in 3D, identifying diagnostic and therapeutic opportunities for complex diseases.



INTRODUCTION

At their early stages, many diseases have modest pathological changes in mostly unknown tissue regions, making them hard to identify and characterize. For example, early changes in dementia may include the activation of a few local inflammatory cells, changes in the microvasculature, and the appearance of just a few initial amyloid-beta plaques in uncharacterized brain regions.¹ Such small regional changes are extremely hard to identify using standard histology, limiting our ability to investigate initial stages of diseases for early diagnosis and therapy. Recent advances in tissue clearing technologies allow fluorescence imaging of complete biological tissues including mouse organs and whole bodies as well as intact human organs.^{2–4} After tissues are rendered transparent, end-to-end laser scanning microscopy reveals their cellular and subcellular details. Leveraging artificial intelligence (AI)-guided image analysis, even tiny changes in cellular structures, which otherwise would be missed, can be identified readily and quickly.^{5,6} However, visually pinpointing these regions alone does not answer mechanistic questions at the molecular level.

In parallel, enormous progress has been made to increase the throughput of single-cell transcriptomic technologies,^{7–9} even though some studies show that RNA expression may weakly correlate with the protein expression.^{10–13} More recently, single-cell analysis of proteomes has also become possible with the advent of ultra-high-sensitivity mass spectrometry (MS)-based approaches.^{10,14–17}

At the RNA level, it is possible to preserve the spatial context in two-dimensional (2D) samples as spatially resolved transcriptome analysis is quickly becoming a mainstay of the molecular biology toolkit.^{18–25} Methods for spatial proteome analysis are actively developed, but most methods are either limited to analyzing fewer than 100 proteins (e.g., highly multiplexed or multi-round immunostaining) or limited to 2D samples (e.g., MS-based spatial proteomics) or both.^{26–30} In addition, it has been unclear to what extent these methods can be made compatible with advanced whole-organ imaging of optically cleared tissue.

Here, we combine whole-organ and whole-mouse tissue clearing and imaging with ultra-high-sensitivity MS-based proteome analysis and can characterize the proteome of samples isolated from cleared tissue comprising fewer than 100 cells. We term this method three-dimensional (3D) imaging of solvent-cleared organs profiled by mass spectrometry, or DISCO-MS (Figure S1A). Using DISCO-MS, we successfully analyzed fluorescently labeled small target regions isolated from whole mouse or human organs to discover spatial-molecular profiles of initial pathological events in various disease models (Video S1). To facilitate sample extraction, we developed a robotic tissue extraction system (called DISCO-bot) for more challenging specimens including whole adult mouse bodies and whole human organs (Video S2). Combining DISCO-MS and DISCO-bot, we studied the spatial proteome heterogeneity of immune cell-enriched tissues from bone marrow niches of intact mice and aortic plaques from the human heart.

RESULTS

MS-based proteomics of solvent-cleared tissue

Tissue clearing is a chemical process that relies on tissue permeabilization and subsequent extraction of different biomolecules including water (organic-solvent-based methods) and lipids (in most clearing methods).³¹ Whether the proteome of tissues after these diverse extraction steps remains intact had been unclear. To investigate this, we employed MS-based proteomics, which can provide unbiased in-depth insights into the composition, structure, and function of the entirety of expressed proteins.³²

To this end, we subjected solvent-cleared samples to proteomics workflows with respect to protein recovery and qualitative and quantitative reproducibility. Using fresh-frozen tissues as controls, we started with 3DISCO and uDISCO clearing methods (Figures S1B–S1D), two commonly used methods that are quick and known to provide the highest tissue and organ transparency.³ We tested several protein-solubilization approaches and figured that the combination of SDS-based protein solubilization and tissue pulverization, followed by SDC resolubilization and protein digestion, yielded qualitatively and quantitatively very similar proteomes between fresh and solvent-based clearing methods (Figures S1B and S1C). We identified up to 5,500 proteins across conditions with Pearson correlation coefficients between 0.89 and 0.99 (Figure S1D).

While 3DISCO and uDISCO work well for fluorescent dye imaging, the signal of endogenous fluorescent proteins such as EGFP is rather unstable and decays with time.³³ To avoid this, we developed vDISCO, which uses fluorescent-dye-conjugated nanobodies to stabilize and enhance fluorescence signals.³⁴ As vDISCO includes several additional steps that might change proteome constitution, we also tested our proteomics workflow on these tissues. Identification of more than 6,000 proteins across all clearing conditions including vDISCO and replicates with Pearson correlations ranging from 0.85 to 0.94 confirmed the suitability of our workflow (Figure 1A). Next, we asked whether archived human brain tissues can be analyzed and cleared human brain tissue stored in formalin for more than 5 years with the DISCO and SHANEL methods.⁴ DISCO-MS identified more than 5,000 proteins in all clearing conditions very similar to paraformaldehyde (PFA)-fixed controls at high quantitative reproducibility ($R = 0.91–0.96$) (Figure 1B). We conclude that our sample preparation workflow allows the MS-based proteome analysis of cleared mouse and human specimens at high depth and quantitative accuracy comparable to fresh and PFA-fixed control samples.

High proteome yield in vDISCO cleared tissues

Next, we examined the in-depth proteomes of vDISCO-cleared tissues to investigate potential protein depletions introduced by the clearing process and compared with fresh-frozen samples. We identified close to 8,000 proteins, a very substantial proportion of the total proteome across conditions and biological replicates with a high quantitative reproducibility ($R = 0.94$; Figure 1C and S2A). Coefficients of variation (CVs) within fresh (non-perfused) and cleared (perfused and fixed) conditions were below 0.2, demonstrating that vDISCO clearing yields proteomes that are qualitatively and quantitatively similar to fresh tissue and highly reproducible across biological replicates.

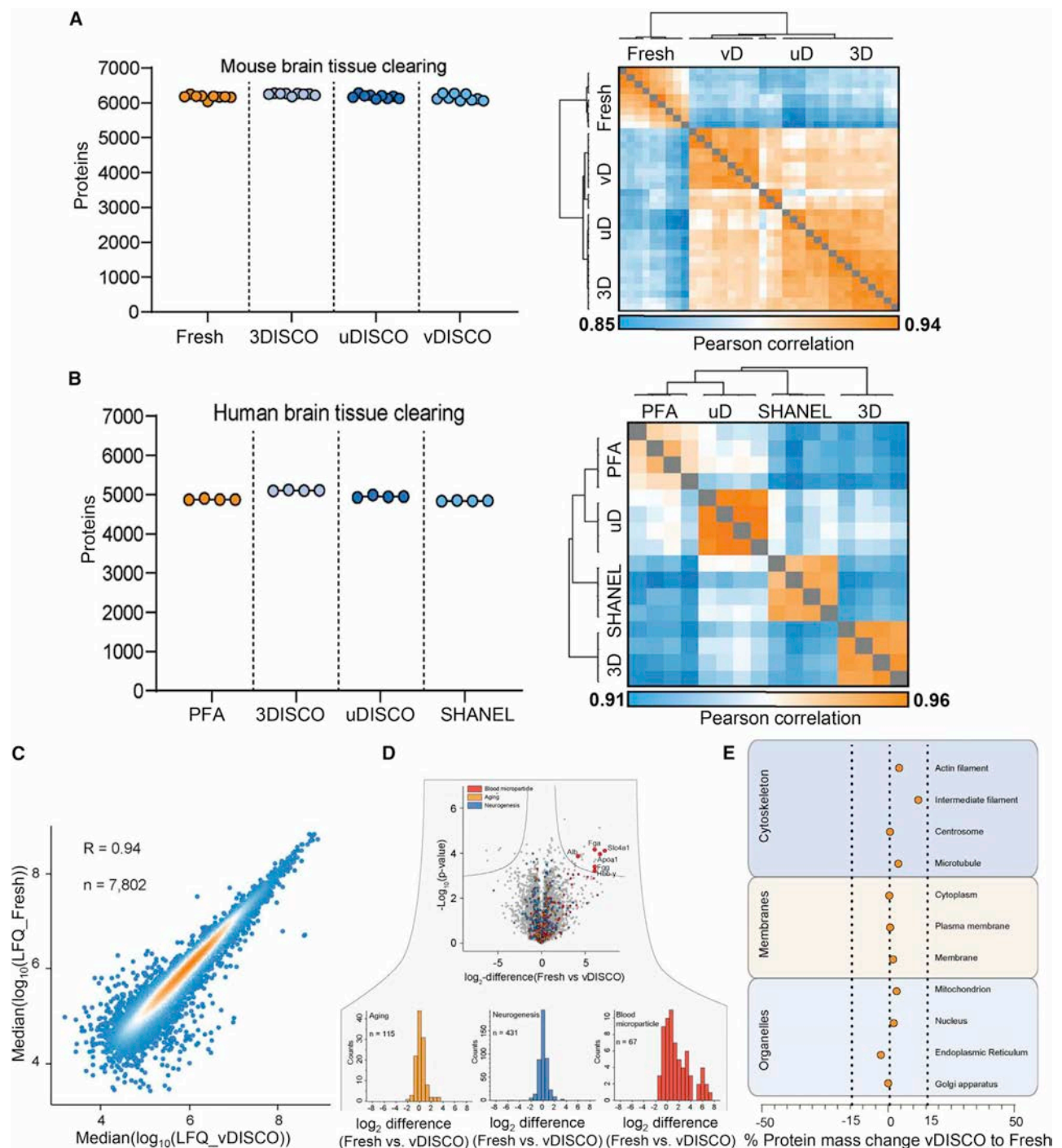


Figure 1. Proteome of cleared rodent and human tissues

(A) Proteome analysis from mouse brain tissues after different organic solvent-based tissue clearing methods vs. fresh controls. Protein identifications and proteome correlations across all clearing techniques and fresh tissue are shown. ($N = 3$ biological replicates, $n = 9$ total experimental replicates per condition). (B) Archived human brain cortex blocks cleared and number of detected protein groups with proteome correlations across all clearing methods are compared with the numbers in PFA fixed blocks. $n = 4$ experimental replicates.

(C) Quantitative reproducibility of vDISCO-cleared vs. fresh.

(D) DE analysis of vDISCO-cleared vs. fresh sample proteomes highlighting the expected change in “blood microparticle” due to blood perfusion step for tissue clearing in contrast to fresh samples. Otherwise, proteins in other GO groups were unchanged.

(legend continued on next page)

(Figures S2B–S2E). The only altered gene ontology (GO) term was “blood microparticle” proteins, not surprising as fresh tissues were not perfused. Other GO keywords are quantitatively and qualitatively preserved (Figure 1D and S2F). Next, we checked the protein mass distributions between fresh and vDISCO mouse brains for membrane, organelle, and cytoskeleton terms. We found that all percentage protein mass differences were well below 15% across sub-terms and that the protein mass change associated with all membrane-related terms was below 3% (Figure 1E). Moreover, we also looked at the specific membrane-bound protein class, which are plasma membrane proteins. The percentage total protein mass change was below 0.5%. As an example, we highlighted epidermal growth factor receptor (EGFR), a transmembrane receptor, between fresh and vDISCO-cleared brain samples (Figure S2G). In summary, even the strongest organic solvent-based tissue clearing approach, vDISCO, yields qualitatively and quantitatively very similar proteomes compared to the fresh tissue.

Proteomes of micro-dissected tissues imaged in 3D

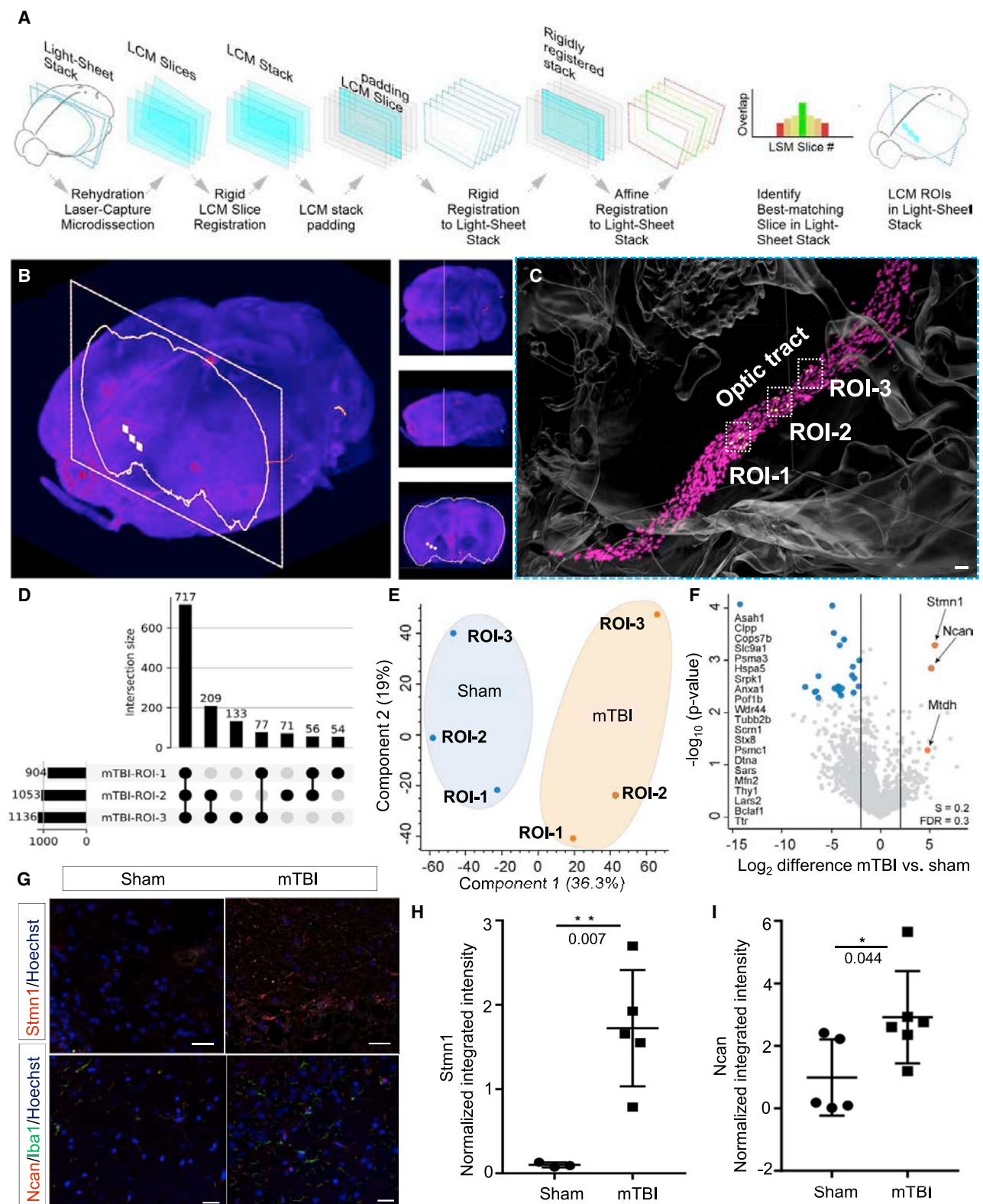
After establishing a high-quality and reproducible MS-compatible sample preparation workflow for solvent-cleared tissues, we turned to the unbiased proteome analysis of smaller target tissue regions ($\sim 0.0005 \text{ mm}^3$) previously imaged and located in 3D. We successfully met three major challenges: (1) reliable dissection of small tissue regions identified by 3D imaging of cleared tissues, (2) analysis of deep proteomes from only a few nanograms of dissected and rigid solvent-cleared tissue, and (3) registration of small tissue regions back onto a complete 3D light-sheet image stack. To solve the first challenge, we developed a series of steps to render cleared rigid tissue soft for precise cryo-sectioning and laser capture microdissection (LCM) without deformation. In short, we reversed the clearing protocol, rehydrated the cleared tissue stepwise, and cryo-preserved it. This workflow avoided rupturing of the tissue during cryo-sectioning and allowed us to laser micro-dissect tissue regions as small as 0.0005 mm^3 corresponding by volume to approximately 60 cells. Next, we miniaturized our sample preparation workflow and then performed MS-based proteome analysis on a modified trapped ion mobility MS platform developed for highest sensitivity down to the level of single cells.¹⁰ Lastly, we automated registration of the 2D LCM images back to the 3D light-sheet imaging stack (Figure 2A). Briefly, following light-sheet microscopy imaging, the cleared mouse brains were rehydrated, cryoprotected, sectioned, and imaged prior to cutting by LCM. These images were aligned (rigid registration) to produce a reconstructed 3D stack of LCM sections. These were then coordinated slice by slice to a subset of the light-sheet imaging stack (affine registration), and the highest-scoring section was subsequently used to project the regions of interest (ROIs) onto the 3D light-sheet imaging data (Figure 2B and S3Q; see Methods S1).

To explore the potential of our technology in biological applications, we first used a mild traumatic brain injury (mTBI) mouse model to identify and analyze proteomes of brain regions

containing discrete local inflammation. mTBI and concussions are common injuries that can lead to long-term morbidities such as sleep disorders, neuropsychiatric disorders, and even early onset of dementia.³⁵ They are characterized by chronic inflammation, which can induce neurodegeneration in selected brain regions, particularly along the stretched axonal tract.³⁶ We used a repetitive mTBI injury model on CX3CR1-EGFP mice (Figures S3A and S3B), in which all microglia are labeled with an EGFP-fusion construct. The mild nature of this injury was confirmed by behavioral test that showed no significant alterations after 8 weeks post injury in Barnes maze and beam-walk tests (Figures S3C and S3D). Brains of CX3CR1-EGFP mice were processed for vDISCO labeling and clearing 8 weeks post injury, showing microglia activation in discrete regions of whole brain. ClearMap quantification³⁷ identified activated microglia with enlarged morphology in diverse brain regions, especially along the axonal tracts including the optic tract and the corpus callosum when compared with sham-operated animals (Figures S3E–S3L). The same mTBI injury model on Thy1-GFP-M reporter mice (expressing GFP only in neurons) confirmed the axonal abnormalities in the same brain regions (Figures S3M–S3P).

We then used DISCO-MS on isolated ROIs including locally activated microglia with known spatial information (Figures 2B and 2C; Video S3). Analyzing three ROIs from the optic tract as small as 0.0005 mm^3 compared to corresponding regions in sham control animals, we quantified up to 1,400 proteins per ROI. Overall, we found 602 common proteins in all ROIs of mTBI and sham. Comparing ROIs from mTBI among themselves, we found a shared proteome signature comprising 717 proteins, with each ROI having unique sets of proteins (Figure 2D). Principal-component analysis (PCA) separated the proteomes of ROIs between mTBI and controls (Figure 2E). Interestingly, several proteins related to axonal damage and repair were strongly differentially regulated between conditions. For example, stathmin1 (Stmn1; 32-fold increase) is a protein involved in the regulation of microtubule filament system. Its overexpression has been shown to promote disassembly of microtubules in blast-induced mTBI.³⁸ Neurocan (Ncan; 30-fold increase) is a chondroitin sulfate proteoglycan involved in the modulation of cell adhesion and migration, which is upregulated in injured brains.³⁹ Eight proteins were uniquely detected in mTBI, including metadherin (Mtdh) present in glial cells but not yet been described in mTBI. Furthermore, we found many previously described proteins in the context of brain injury, providing positive controls, and many yet unknown proteins to be downregulated in the mTBI model. For example, acid ceramidase (aC-Dase, Asah1), an enzyme implicated in sphingolipid metabolism and in multiple diseases, was downregulated^{40–42} and has previously been associated with morphological defects in cultured neurons.⁴³ Our data now suggest its potential involvement in axonal deformity in mTBI. We also observed alterations in mitochondria proteins along the optical tract such as caseinolytic protease proteolytic subunit (Clpp), a mitochondrial matrix

(E) Percentage change of protein mass distribution between vDISCO-cleared vs. fresh samples. Percentage changes are shown as a median change within one group for organelles, membranes, and cytoskeleton GO terms (N = 3 biological replicates, n = 9 total experimental replicates per condition). See also Figures S1 and S2.



(legend on next page)

protease,⁴⁴ and mitofusin 2 (Mfn2), a mitochondrial membrane protein that participates in mitochondrial fusion and contributes to the maintenance and operation of mitochondrial network⁴⁵ (Figure 2F). We further validated the enrichment of Stmn1 and Ncan in mTBI brain tissues by immunofluorescence (Figures 2G–2I). Our data demonstrate that DISCO-MS is a powerful approach for obtaining unbiased proteomic information on heterogeneous tissue regions with known spatial locations.

Scalable and robust pathology identification using deep learning

One of the early hallmarks of Alzheimer's disease (AD) pathology is the accumulation of amyloid-beta (A β) plaques in the brain parenchyma.⁴⁶ We anticipated that the unbiased detection of A β plaques, followed by their equally unbiased proteome analysis using DISCO-MS, would provide valuable insights into the initial stages of AD. To this end, we used the 5xFAD mouse model of AD to identify Congo red labeled A β plaques in young mouse brains.

As the locations of these initial plaques are unknown, we developed a deep learning (DL) approach to identify all A β plaques rapidly and reliably in whole mouse brain scans. In short, our network architecture is based on U-Net, a well-established approach for biomedical image analysis⁴⁷ (Figure 3A). To assess our segmentation quality, we calculated a wide range of voxel-wise and A β plaque segmentation metrics. Our DL architecture for automated A β plaque detection showed high performance in volumetric accuracy (0.99 ± 0.00), volumetric (0.71 ± 0.06), and surface (0.94 ± 0.03) as well as overall Dice scores (0.89 ± 0.09) per A β plaque. After segmenting all plaques in the entire brain using DL, we registered our data to the Allen brain atlas to obtain region-wise quantifications for over a thousand brain subregions (Figure 3B).^{48,49} We then grouped them into the major brain regions as defined by the Allen mouse brain ontology for simplicity and visualized plaque volume per region in early and later stages of disease (Figures 3C and 3D) using brainrender—an open source Python package for interactive visualization.⁵⁰

Our DL model identified few A β plaques in 6-week-old mouse brains and identified several thousand at a later stage of the disease (6-month-old 5xFAD), (Video S4) whereas plaques were absent at 5 weeks of age. We also confirmed our finding of A β plaques in 6-week-old mice in the same brain regions by immunohistochemistry with anti-A β monoclonal antibodies (Figure S4A). To compare the plaques between 6-week- and 6-month-old 5xFAD mice in 1,238 different brain regions, we

grouped 72 major brain regions according to Allen brain atlas and plotted 27 disease-relevant regions. Some of the main brain regions with initial plaques were retrohippocampal region, medulla, molecular layer of cerebellar cortex, fiber tracts, subiculum areas, visual area, and hippocampal formation. The subiculum area and retrohippocampal region showed much larger number of plaques at later stage (6 months) of disease: 1,689 and 10,630, respectively (Figures 3E and 3F). We observed the largest plaques in the midbrain (motor related, $3,438 \mu\text{m}^3$) followed by temporal association areas ($2,880 \mu\text{m}^3$), posterior amygdalar nucleus ($2,450 \mu\text{m}^3$), and auditory areas ($2,366 \mu\text{m}^3$), with an average volume ranging between $2,000 \mu\text{m}^3$ and $3,500 \mu\text{m}^3$ in early stage (Figure 3G). Interestingly, the plaque volume of these regions were significantly reduced at 6 months, indicating a temporal change in plaque morphology, either caused by adverse biological effects by their surrounding microenvironments or potentially causing changes to it during disease progression.

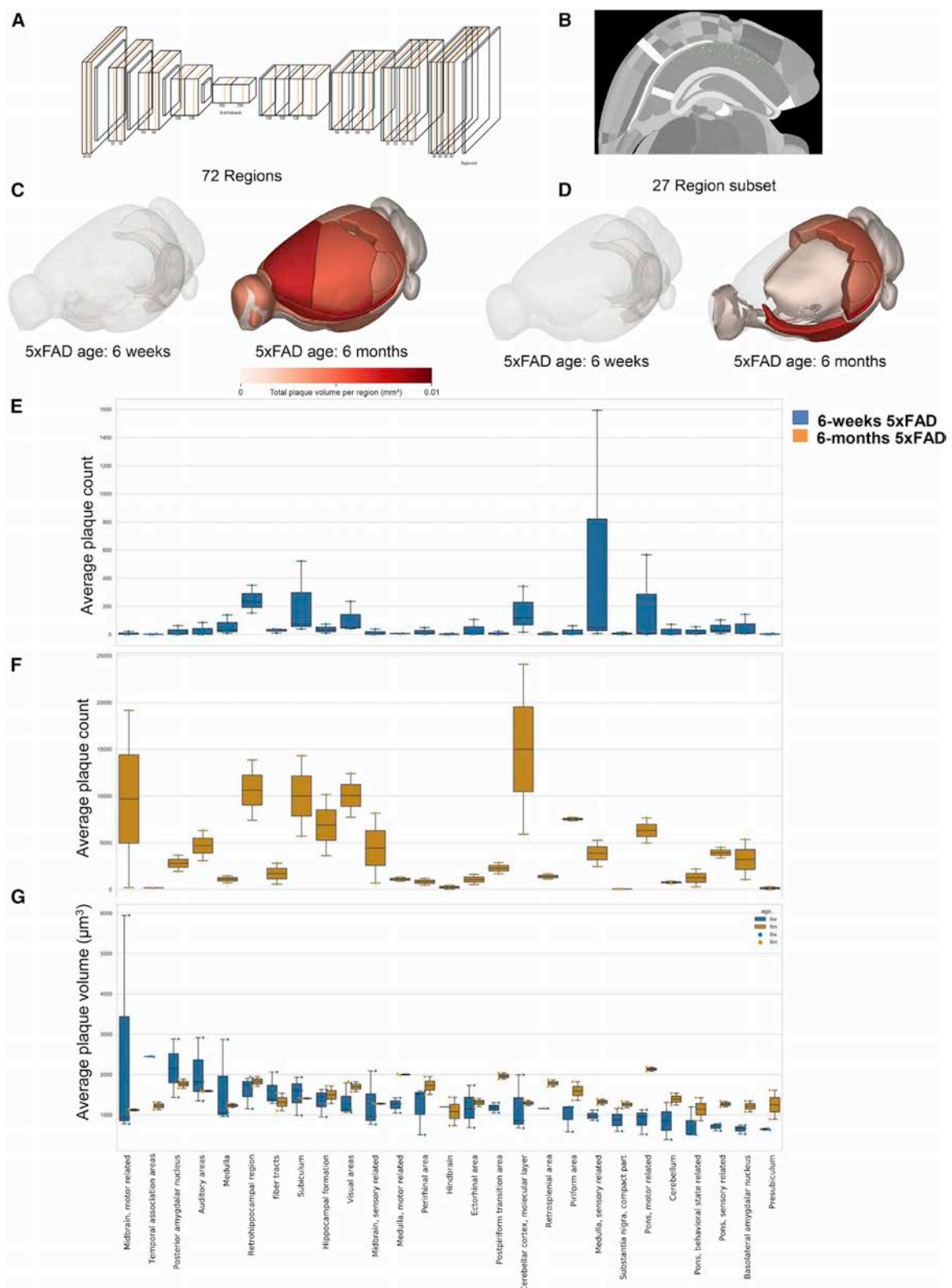
Following the DL-based identification of early A β plaques in the 5xFAD mouse model, we isolated four ROIs (volume: $\sim 0.0005 \text{ mm}^3$) from the hippocampal region vs. corresponding brain regions from the control mice and subjected them to MS-based proteomics (Figures 4A–4D). We compared $\sim 2,000$ proteins across replicates and PCA plot separated the ROIs with A β plaques from the control brain regions (Figure 4E). Differential expression (DE) analysis revealed that many well-characterized AD-associated proteins were enriched in 5xFAD ROIs including the A β precursor protein,^{46,51} (32-fold increase) and the thimet oligopeptidase 1 (8-fold increase) (Figure 4F). Apart from known and well-established AD-related proteins,^{52,53} we also detected less-characterized proteins in early-stage A β plaques such as a member of the calcium-binding protein family S100a11.

Moreover, we asked how similar the proteomes of our ROIs with early A β plaques were compared to each other. Plaques with more than 1,200 protein identifications each shared 768 proteins, defining a core proteome of early-stage A β plaque formation (Figure 4G). An abundance rank plot of the shared early-stage A β plaques' core proteome revealed several members of the Ywhaz (14-3-3) and the S100a protein family. In the early-stage A β plaque ROIs, we also found many other proteins involved in AD such as two isoforms of Mapt, namely Mapt-4 and Mapt-5, illustrating the specificity of MS-based proteomics (Figure S5A). Our proteomics data also highlight early-stage A β plaque variability (Figure S5B) with respect to well-characterized AD proteins (Mapt, Tmed10, App), proteins of the S100a family,

Figure 2. DISCO-MS reveals effects of mTBI in discrete regions of whole brain

- (A) Schematic representation of the alignment procedure.
 (B) Location of the LCM slice (outline) inside the light-sheet stack, with the dissected $200 \times 200 \mu\text{m}$ areas (white squares) inside the optic tract.
 (C) 3D reconstruction of stitched images of an exemplary CX3CR1-GFP/+ mouse brain after mTBI, highlighting substantial increase in activated microglia (in magenta) along optic tract region. 3 neighboring ROIs along optic tract were identified, laser captured, and subjected to proteomic analyses. Scale bar, $100 \mu\text{m}$.
 (D) The number of shared and unique set of proteins in mTBI.
 (E) PCA plot showing the distribution of individual ROIs from mTBI vs. ROIs from control (sham) with the same spatial location.
 (F) Volcano plot showing the significant enrichment of proteins.
 (G) Histological validation of the top 2 proteins in the optic tract: (1) stathmin (Stmn1) in red and nuclear marker Hoechst dye in blue, (2) neurocan (Ncan) shown in magenta along with microglia marker (Iba1) in green and Hoechst dye in blue. Scale bars, $20 \mu\text{m}$.
 (H and I) Intensity quantification of Stmn1 immunostaining signal ($p = 0.007$, $n = 3$ from total 8 sections) and Ncan immunostaining signal ($p = 0.044$, $n = 3$, animals from total 11 sections) in mTBI vs. sham, respectively (unpaired two-sided Student's t test, data presented as \pm SD).

See also Figure S3, Methods S1, and Video S3



(legend on next page)

peptidases (Thop1, Ppia), proteins of the Ywha family, and other structure-determining proteins including Nefm and Map2. Finally, we confirmed the presence of S100a11 and Thop1 in early-stage plaques of 5xFAD brain slices by immunofluorescence, whereas these proteins are absent from the respective regions in wild-type (WT) mice (Figures S4B–S4D).

We next compared plaque regions to neighboring non-plaque regions in the dorsal and ventral subiculum, where we observed initial plaque formations (Figures 4H and 4I). We found that 29 proteins were upregulated whereas 14 proteins were downregulated in these early plaque isolates. Among others, we found significant quantitative change of proteins related to vesicle fusion, vesicle-mediated transport, and secretory pathways (Bnip1, Cpd; >10-fold increase in both; $p < 0.0001$ for Bnip; $p < 0.05$ for Cpd), which are potential markers for an early AD onset (Figure 4K). Known plaque-associated proteins were regulated in a region-specific manner, which were previously identified only at the later stages of AD without precise spatial location (Figure 4L). For example, an increased expression of Manf had been reported in APP/PS1 transgenic mice only at later stages of the disease.⁵⁴ Actl6b is involved in transcriptional activation and repression of select genes by chromatin remodeling and has been investigated in the context of later-stage AD (6–15 months).⁵⁵ Mutations in human Actl6b have been associated with intellectual disability,⁵⁶ suggesting a role of this protein in the early stage of neurological conditions, including AD. Mbp, Cnp, and Plp1 have been associated with the structural integrity of the myelin sheath and its function in age-related AD.⁵⁷ In addition to many significantly enriched proteins in early plaques vs. non-plaque areas of the same region, we also found substantial subregional heterogeneity (Figures S5C–S5E). Furthermore, many of these proteins were uniquely distributed across these two subregions. These could potentially drive disease progression in a region-specific manner, a concept that has been little explored thus far due to technical limitations.

Next, we profiled the later-stage plaque (6 months) microenvironment in a region-specific manner and compared this with early plaque protein enrichments (Figures S5F and S5G). Dorsal subiculum data showed a significant upregulation of 49 proteins, whereas 21 proteins were downregulated. Among the upregulated proteins, we found proteins related to S100a family (S100a13), complement activation and microglia phagocytosis pathway (C1qa, C1qb, Itgb), and tau protein binding (ApoE, S100b, Clu). We also observed a distinct proteomic signature in dorsal vs. ventral subiculum at later stages, indicating region- and time-specific changes in the proteomic landscape around these plaques (Figures S5H and S5I).

Taken together, DISCO-MS allowed us to pinpoint early- and late-stage A β plaques from the whole brains in 3D and analyze

their spatial proteomic makeup. We recovered many known markers of A β plaques in AD as well as less-characterized proteins in AD pathogenesis. Our data also suggest the significant involvement of S100a, Ywhaz (14-3-3), vesicle fusion and transport, myelin sheath function, and the complement system related family members in early-stage A β plaque development.

DISCO-MS from large-volume samples by DISCO-bot tissue extraction

Next, we aimed to develop DISCO-MS for even larger samples including whole mouse bodies and whole human organs. As sectioning/imaging for LCM is impractical for large-volume samples at scale, we developed a robotic extraction system (named DISCO-bot), using biopsy needles to isolate ROIs for subsequent proteomics analysis (Figure 5A). This required (1) stabilization of whole mouse body for robotic extraction while imaging, (2) minimizing biopsy needle deflections during extractions, and (3) biopsy needles that can penetrate into hard cleared tissues.

Firstly, to stabilize the sample, we investigated different resins and agarose concentrations to modulate bed stiffness, compatibility with the clearing solutions, and imaging and figured that 2% agarose embedding was well suited for our purpose. Next, we customized different 3D-printed mouse holder adaptors and needle holders, according to their strength and force-deflection criteria and chose the one with the least deflection (Figure 5B–5E and S6). Last, we tested various needle sizes and shapes with stylet inside and found that needles size 18 gauge (G) and/or 22 G provided a good penetration and sample extraction precision without contamination of undesired tissue (Figure 5F; see details in STAR Methods). We further optimized the DISCO-bot to work concomitantly with the light-sheet microscope (Figures 5G–5I). The resulting DISCO-bot system allowed the extraction of small tissue regions from cleared samples while imaging, thereby enabling non-destructive and repetitive tissue isolation at scale for DISCO-MS (Figures 5J–5M; Video S5; see DISCO-MS Handbook as Methods S1).

To demonstrate the utility of the DISCO-bot in our DISCO-MS pipeline, we cleared LysM-eGFP mice using vDISCO. We co-labeled nuclei with propidium iodide (PI) to identify the ROIs for DISCO-bot extraction. Imaging of the whole body allowed us to spatially identify locations of all LysM-eGFP⁺ cells, which were mostly found to be in bone marrow niches (Figure 6A; Video S6). We then focused on the cranium and scapula, two bones with irregular 3D structures and thus hard to study with standard 2D sections. We chose three ROIs from the parietal cranium region and six ROIs from scapula (three from the lateral border (LysM-eGFP) and three ROIs from the medial border (LysM-eGFP⁺) [Figures 6B–6E]). DISCO-bot-extracted ROIs were then

Figure 3. Deep learning analysis of plaques in whole 5xFAD mouse brains

- (A) 3D U-Net architecture including layer information and feature sizes.
- (B) Segmented plaques overlaid on the hierarchically and randomly color-coded atlas to reveal annotated regions available.
- (C) Visualization of plaque volume per region in 72 regions.
- (D) Visualization of plaque volume per region in a subset of 27 major regions.
- (E) Quantification of the number of plaques in the major brain areas of 6-week-old mice ($n = 3$, \pm SD).
- (F) The number of plaques in the major brain areas of 6-month-old mice ($n = 2$, \pm SD).
- (G) Quantification of the plaque volume in 6-week-old mice (in blue, $n = 3$, \pm SD) and 6-month-old mice (in orange, $n = 2$, \pm SD).

See also Video S4

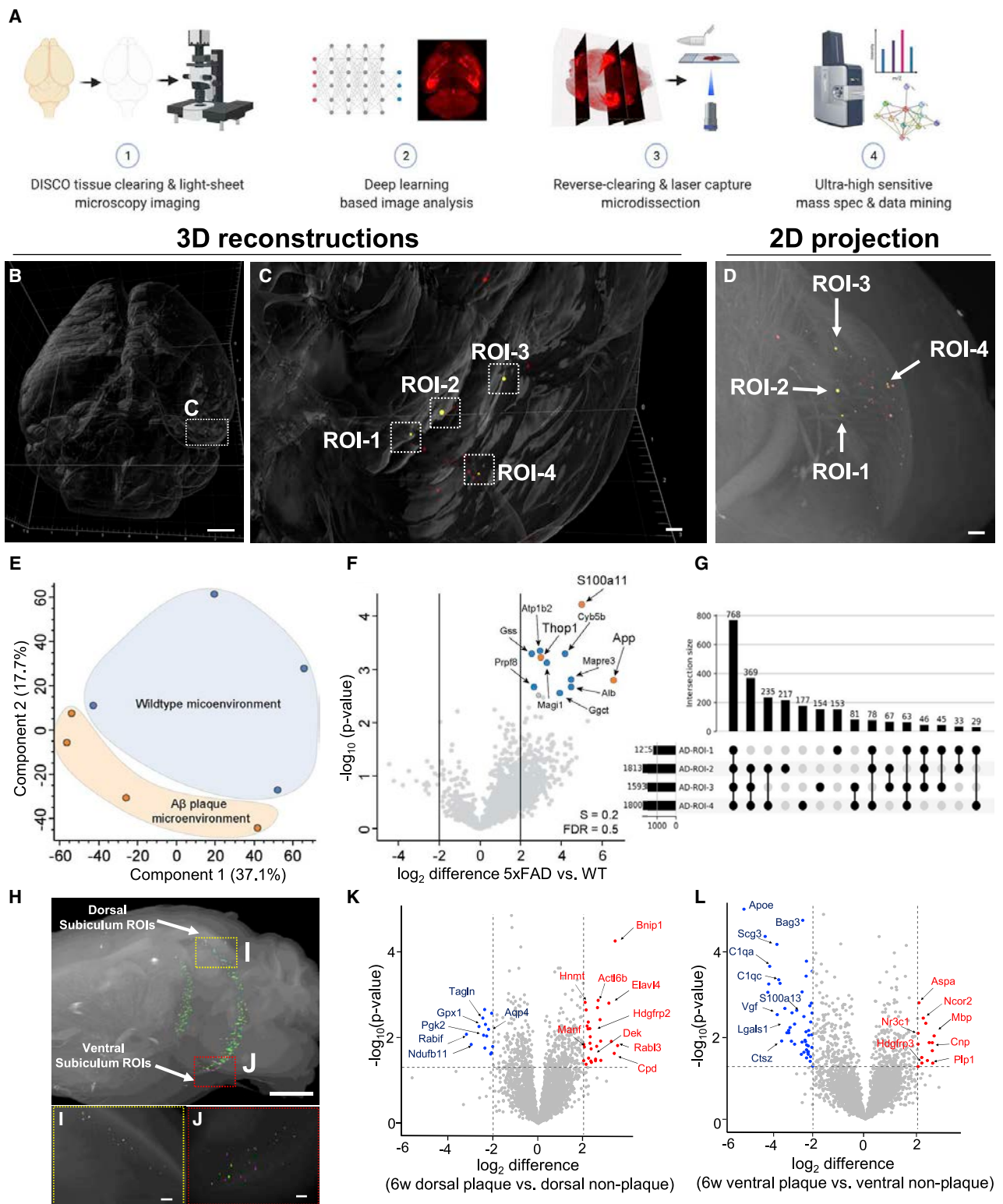


Figure 4. DISCO-MS unravels the single-plaque proteome in AD mouse model

(A) Major steps of DISCO-MS.

(B) 3D visualization of Aβ plaques (in red) in stitched images of 5xFAD mouse brains ($n = 4$ experimental replicates). Scale bar, 500 μm .

(legend continued on next page)

analyzed using the DISCO-MS pipeline as described above. In the cranium, we identified the shared signature of 1,984 proteins in all three ROIs with Pearson correlation between 0.72 and 0.76 (Figures 6F and 6G). To verify the precision of DISCO-bot extraction, we compared our results with proteomics of freshly isolated skull marrow cells.⁵⁸ We found ~2,200 shared proteins out of total 2,550 identified protein groups when compared with isolated skull-proteome, confirming the high precision of DISCO-bot extraction. Among others, seven protein groups identified here were earlier shown to be expressed both at transcript and proteome level in freshly isolated skull marrow, which further validates the extraction precision using robotic arm (Figure 6H). In the scapula, we observed distinct signal of LysM-eGFP in medial vs. lateral border bone. PCA clearly separated the two groups as well as the ROIs itself, particularly from medial border, indicating inter-regional and intra-regional heterogeneity among these extracts. We identified 1,250 proteins across conditions with high Pearson correlation coefficients (0.88–0.98) and found a common signature of 764 proteins between lateral and medial border bone, whereas 336 and 22 proteins were unique to the respective regions (Figures S7A–S7C). DE analyses showed up-regulation of ten proteins, including those related to the innate and adaptive immune system such as antigen-presenting molecule H2-L (MHC class1b), B cell/T cell receptor pathway-related proteins, and cytokine signaling proteins such as signal transducer and activator of transcription 3 (Stat3), which are involved in biological processes of inflammatory response regulation to antigenic stimuli. Among 33 downregulated proteins were signalosome-related proteins (Cops7a) and proteins related to actin filament network formation (Fhod1) (Figure 6I–6L and S7D). These results demonstrate that DISCO-MS can be applied to whole adult mouse bodies after end-to-end imaging to investigate spatial-molecular heterogeneity and diverse biology.

Spatial proteomics of coronary arteries in SHANEL-cleared human heart

Next, we tested our DISCO-bot-aided DISCO-MS approach in coronary artery disease (CAD). Acute myocardial infarction (MI) is the major contributor to cardiovascular mortality, the leading cause of deaths worldwide.^{59,60} It occurs when atherosclerotic plaques (largely made up of lipids and calcified tissue) slowly build up in the inner lining of a coronary artery and then suddenly rupture, causing thrombus formation, occluding the artery and ultimately prevent blood flow to other parts of body. Recent advances in single-cell RNA sequencing (scRNA-seq) technologies have provided a deeper understanding of cardiac cells in both health and disease^{61,62} but lack precise spatial information.

Moreover, transcript levels may weakly correlate with proteome data, even at the single cells.¹⁰

We obtained PFA-fixed human heart, labeled its vessels with dextran, and cleared the whole heart using SHANEL human organ clearing protocol (Figures 7A and 7B). This readily located the calcified atherosclerotic plaques of any size along regions without plaques in the same coronary artery. We extracted six ROIs around the large plaque-associated regions and six ROIs from the little-to-no plaque-associated regions, which could represent early plaque formation along the coronary artery of the same heart for DISCO-MS analysis (Figures 7C–7F; Video S7). We quantified 1,300 proteins in each ROI and found 53 downregulated and 6 upregulated proteins (Figure 7G). Systematic GO term and pathway analysis of regulated proteins suggests the regulation of hypertrophic cardiomyopathy, cardiac muscle contraction (TPM1, TPM2, MYL2, MYL3, MYH6, MYBPC3, DES), focal adhesion, blood coagulation, plasminogen activation, platelet aggregation, fibrinogen complex, blood-clotting cascade (SERPING1, FGA, FGG, FGB, FN1) (Figure 7H, S7E, and S7F). Some of these proteins were regulated in a region-specific manner including MYH10, MYH11, FGA, FGB, and FGG, which have already been reported to be associated with plaques (Figure 7I). Furthermore, we found upregulation (2.2-fold, $p < 0.05$) of myosin heavy chain (MYH8), a less-characterized protein in context of atherosclerotic plaque. As its related forms MYH10 and MYH11 were recently discovered as biomarker for atherosclerotic plaque formation,^{63,64} our findings of MYH8 in the context of CAD is encouraging and invites further investigation. We also observed a 2.5-fold ($p < 0.01$) increase in glyoxalase 1 (GLO1), a ubiquitous cellular enzyme that participates in the detoxification of methylglyoxal, a cytotoxic byproduct of glycolysis that induces protein modification (advanced glycation end products, AGEs), oxidative stress, and apoptosis. GLO1 and AGEs are implicated in the pathogenesis of aging and diabetes. A large-scale meta-analysis showed a gene network involved in antigen processing to be strongly associated with CAD.⁶⁵ Key drivers of this network included GLO1, which strengthens the potential role of this protein in reprogramming atherosclerotic plaque microenvironment. We also observed a significant enrichment (2.3-fold, $p < 0.01$) of carbonic anhydrase 6 (CA6), which might play a role in vascular calcification, hence plaque progression, and has not been associated with CAD before. CA are a group of isoenzymes that catalyze the reversible conversion of carbon dioxide into bicarbonate. CA isoenzymes were previously shown to be involved in the vascular calcification in humans.^{66,67} We further found perturbations in members of recently discovered myosin heavy-chain family

(C) Enlarged view of region marked in (B) 4 different ROIs (in yellow) from hippocampus, each containing single-plaque, selected and isolated for mass spectrometric measurements. Scale bar, 100 μ m.

(D) 2D projection of selected ROIs. Scale bar, 100 μ m.

(E) PCA plot of ROIs' proteome from 5x FAD vs. the same regions from control.

(F) Volcano plot showing the significantly enriched proteins.

(G) The number of shared and unique sets of proteins in 5x FAD.

(H) Selection of early plaque and non-plaque ROIs from 2 subregions of subiculum. Scale bar, 1,000 μ m.

(I and J) Enlarged view of regions marked in (H). Scale bar, 100 μ m.

(K) Volcano plot showing significantly enriched proteins in plaque vs non-plaque areas in dorsal region.

(L) In ventral region ($n = 14$ –20 ROIs per region).

See also Figures S4 and S5 and Video S1.

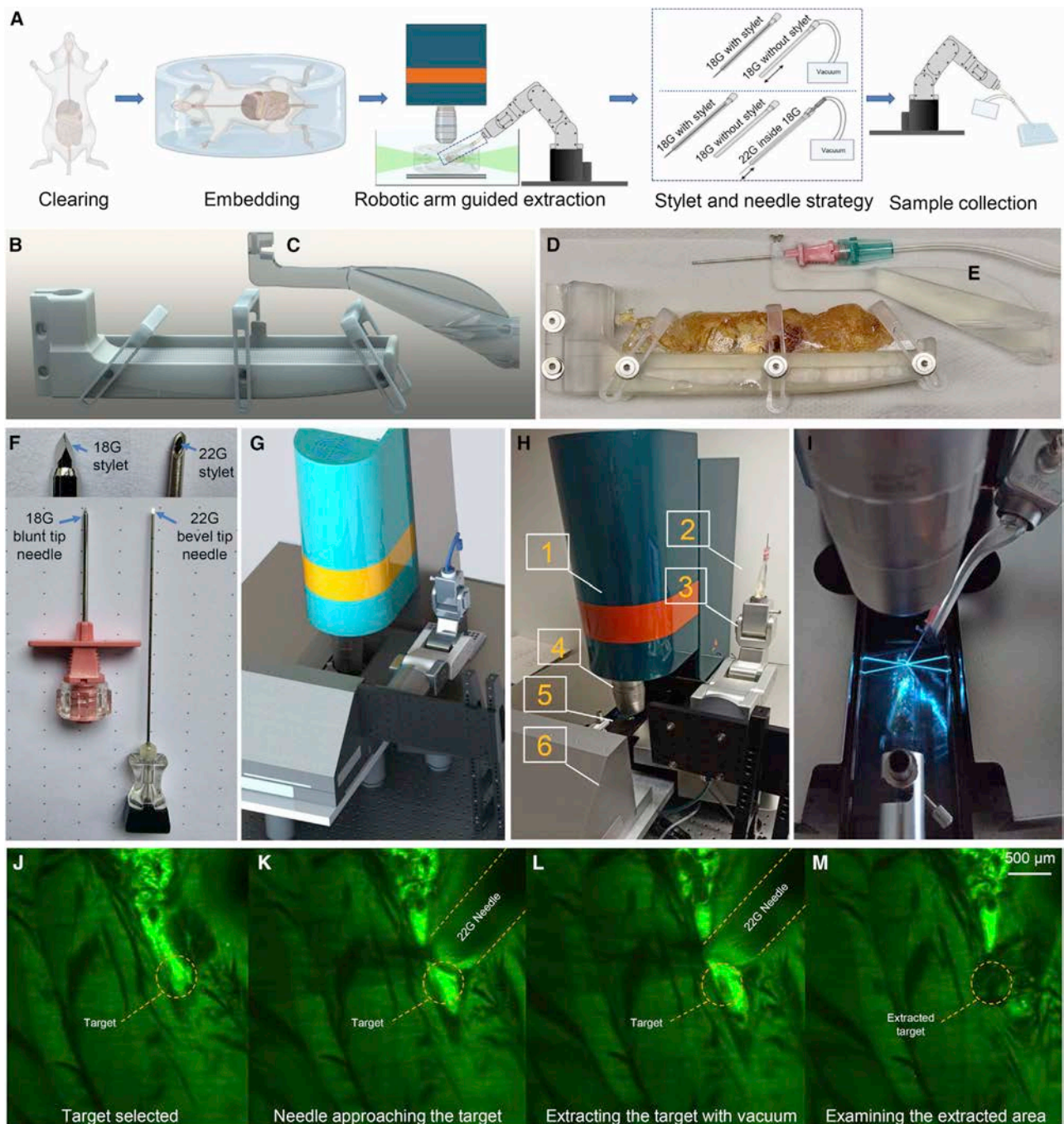


Figure 5. DISCO-bot enables non-destructive tissue extraction from large, cleared samples while imaging

(A) Schematic of robotic extraction.

(B) 3D model of the mouse holder.

(C) 3D model of needle holder.

(D) Cleared mouse on optimized mouse holder.

(E) Needle attached to the needle holder.

(F) The biopsy needles with sealing stylets.

(G) CAD model of microscope with robotic arm.

(H) Components of microscope and robotic setup annotated as (1) light-sheet microscope, (2) needle attached on the needle holder, (3) Meca500 6 DoF robotic arm with vacuum tube, (4) objective, (5) sample mounted on the mouse holder, (6) mouse holder stage.

(I) Meca500 robotic arm.

(legend continued on next page)

(MYH10, MYH11) biomarker and MYH6, a less-characterized form in the context of late-stage atherosclerotic plaque microenvironment. Moreover, we observed a significant reduction in the expression of MACROH2A.1 histone, which has been little studied in context of regulating autophagy and cholesterol efflux.⁶⁸

DISCUSSION

Deciphering tissue heterogeneity is essential to understand normal physiology and pathological processes. However, despite the enormous progress made in single-cell and spatially resolved -omics technologies,^{7–10,14–17} spatial-omics analysis of tissue regions imaged in whole organs and organisms remained challenging.

We addressed this challenge by developing and applying DISCO-MS for proteome analysis of small tissue regions identified by panoptic imaging of large samples, *in silico* 3D reconstructions using AI, and automated minimally invasive tissue isolation for large-volume tissues using robotics. Employing DISCO-MS, we identified brain regions affected by the early stages of A β plaque genesis in the brains of a young AD mouse model. Most of the initial plaques appeared in the retrohippocampal regions, including the entorhinal area, and some in hind-brain regions, including pons and medulla.⁶⁹ The proteome data provided by our work can facilitate the discovery of diagnostic and therapeutic approaches tailored for an early-stage intervention of AD. Future studies are warranted as, e.g., time course and molecular details might differ between the 5xFAD mouse model we used and other widely employed models such as the 3xTg-AD mice.⁷⁰ Our method also allows the analysis of human post-mortem samples to explore the clinical relevance of our findings.

Earlier studies obtained the proteomic profiles either from the lysed whole brains of AD mice⁷¹ or provided only average information on the plaque pathology from pre-selected brain regions without spatial details on the whereabouts of the plaques.^{72,73} Moreover, some of these studies were performed only on certain isolated cell types or brain sections,^{74,75} again missing the spatial context at the whole-organ level. More recently, attempts were made to characterize the plaques in whole brains of 5xFAD mice; however, these studies lack spatial proteome information.^{76,77} In contrast, we obtain the proteomic data on isolated single-plaque microenvironments with the known spatial locations in whole brains. Thus, we provide both molecular information related to single plaques, and their spatial location, which would be critical for localized targeted treatments.

Our technology performs equally well on mouse and human tissues and yields qualitative and quantitative proteomics data nearly indistinguishable from uncleared samples, even for the harshest organic solvent-based tissue clearing approaches. The broad compatibility with different tissues and organisms and the relative ease of the DISCO-MS procedure will allow benchmarking different animal models against human samples on the molecular and anatomical levels.

Although tissue clearing presumably removes the lipidic cast of membrane proteins, we observed that the plasma membrane protein GO class was hardly affected, suggesting that DISCO-MS can be used to identify surface markers for drug targeting. Beyond neuroscience, this technology may transform spatial molecular investigations in many other biomedical research areas including clinical samples. We already applied DISCO-MS to human heart samples with atherosclerotic plaques and identified molecules involved in CAD such as GLO1, CA6, MYH6, and MACROH2A.1. After SHANEL clearing, we quickly navigated through the whole coronary artery in 3D and pinpointed the spatial distribution of plaque-associated regions. Given the precision and sensitivity of our method, we were able to isolate and analyze neighboring tissue regions with and without pathology for comparison.

A key advantage of our approach is that the robot-guided extraction of tissue isolates directly from the cleared tissue makes it scalable, as no prior sectioning and registration is needed. This allows the quick streamlined isolation of many samples from identical specimens while retaining complete spatial information and allowing for the resampling of other parts of the same specimen in future analyses.

In conclusion, we present a spatial unbiased proteome profiling technology comprising complete 3D-imaging data of whole organs and organisms, enabling unbiased identification and automated extraction of interesting tissue regions and including subsequent molecular characterization. Notably, the DISCO-MS technology presented here is versatile across labeling and solvent-cleared methods for whole organs. It is not only applicable to reporter mouse lines but can also be utilized where reporter lines are unavailable. In those cases, deep tissue labeling with dyes and potentially antibodies can be performed against the antigen of interest, imaged as a whole organ, and subjected to MS-based proteome profiling. DISCO-MS should be of great interest to researchers with archived solvent-cleared organs and imaging data, where molecular data are missing. This method will further enable to interrogate the molecular basis of a pathological milieu located in a seemingly random manner to advance research in complex diseases.

Limitations of our study

Although we have demonstrated that DISCO-MS enabled us to perform unbiased proteome analysis after unbiased imaging of entire specimens in 3D, further developments would be needed to extract fewer cells for downstream proteome analyses. Our current method works well for down to about 60 cells and provides us with average molecular details of these cells and their microenvironments. While this is sufficient to study diverse biological questions such as plaque heterogeneity, it is still far from the single-cell level. Single-cell resolution is important to understand the cell compositions and cellular interactions in the biological processes under investigation. To reach that goal, the current protocol needs to be refined for smaller sample

(H and I) Coarse calibration with mouse in imaging chamber prior to extraction.

(J–M) Robotic extraction example: (J) target selection, (K) needle approaching the target, (L) extracting the target under vacuum, (M) evaluation of extracted region.

See also [Figure S6](#), [Methods S1](#), and [Videos S2](#) and [S5](#)

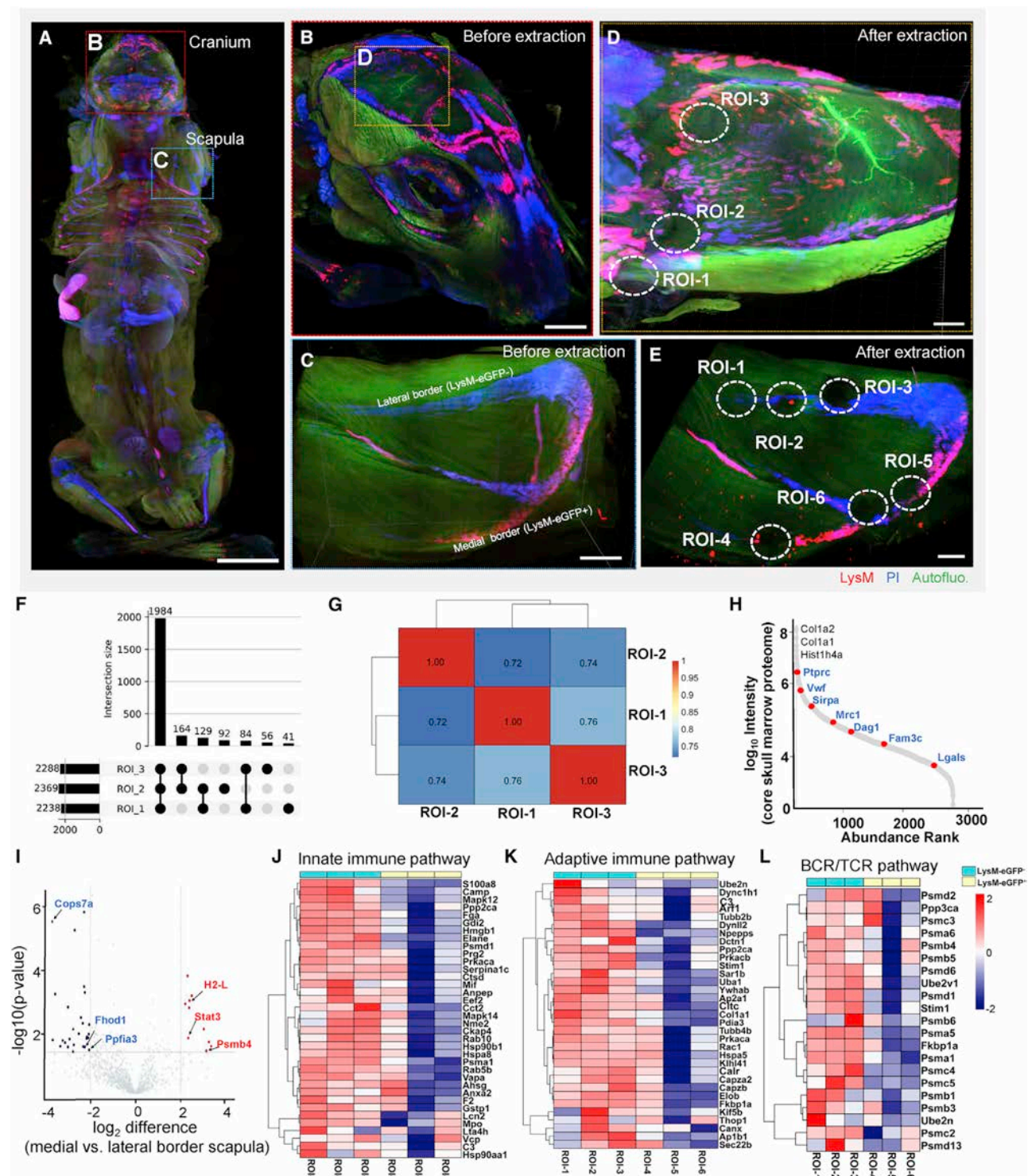


Figure 6. DISCO-bot-aided DISCO-MS on bone marrow niches of whole mouse bodies

(A) Stitched images of whole body of LysM-EGFP mouse after clearing and imaging (n = 4). Scale bar, 700 μ m.

(B) 3D visualization of stitched images of whole head zooming into parietal surface before extraction.

(C) 3D visualization of stitched images of right scapula showing lateral and medial borders before extraction (PI in blue, LysM in red). Scale bar, 500 μ m.

(D) Marked 3 ROIs in parietal surface after robotic extraction. Scale bar, 500 μ m.

(E) Marked 6 ROIs, 3 in lateral border and 3 in medial border after extraction. Scale bar, 500 μ m.

(legend continued on next page)

volumes to extract sub-nanogram tissues from the cleared samples. Furthermore, the proteomic sample preparation for cleared tissues could be miniaturized to the level of single cells or pooled cell states without losing proteomics depth.¹⁷

STAR★METHODS

Detailed methods are provided in the online version of this paper and include the following:

- **KEY RESOURCES TABLE**
- **RESOURCE AVAILABILITY**
 - Lead contact
 - Materials availability
 - Data and code availability
- **EXPERIMENTAL MODEL AND SUBJECT DETAILS**
 - Animals
 - Human samples
- **METHOD DETAILS**
 - Repeated closed head mild traumatic brain injury (mTBI)
 - Perfusion and tissue preparation
 - Congo red labeling of whole brains of 5xFAD animals
 - Clearing of brains using DISCO methods
 - vDISCO whole-brain passive immunostaining, clearing and imaging
 - vDISCO whole body immuno labeling, clearing and imaging
 - SHANEL sample preparation and clearing
 - Behavioral assessment
 - Immunofluorescence and confocal microscopy
 - Light-sheet microscopy and image processing
 - Registration of light-sheet and LCM images to correlate probe selection
 - Optimization of cleared tissue for cryopreservation and sectioning
 - Laser-capture microdissection
 - Automated robotic proteomic probe extraction from whole body
 - Precision and accuracy of sampling
 - Needle gauge
 - Specimen holder and needle holder strategy
 - Embedding of the whole mouse body
 - Manipulation system
 - Optimization of DISCO cleared sample preparation for mass spectrometry analysis
 - High-pH reversed-phase fractionation
 - Liquid chromatography and mass spectrometry (LC-MS)
- **QUANTIFICATION AND STATISTICAL ANALYSIS**

- ClearMap quantification
- Deep learning analyses
- Proteomics data processing
- Proteomics downstream data analysis

● ADDITIONAL RESOURCES

SUPPLEMENTAL INFORMATION

Supplemental information can be found online at <https://doi.org/10.1016/j.cell.2022.11.021>.

A video abstract is available at <https://doi.org/10.1016/j.cell.2022.11.021#mmc9>.

ACKNOWLEDGMENTS

A.-D.B. acknowledges support from the International Max Planck Research School for Life Sciences (IMPRS-LS). This work was supported by the Vascular Dementia Research Foundation, Deutsche Forschungsgemeinschaft (DFG, German Research Foundation) under Germany's Excellence Strategy within the framework of the Munich Cluster for Systems Neurology (EXC 2145 SyNergy, ID 390857198), the Bundesministerium für Bildung und Wissenschaft (BMBF) for Grant CLINSPECT-M (FKZ161L0214C, to S.F.L. and M.M.), ERC Consolidator Grant (AE, GA 865323), Nomis Heart Atlas Project Grant (Nomis Foundation), the Helmholtz AI program through grant Deeproad, and the Max Planck Society for the Advancement of Science. We thank our colleagues in the Department of Proteomics and Signal Transduction, Max Planck Institute of Biochemistry, for discussions and help. In particular, we thank I. Paron, A. Piras, and C. Deiml for technical support and J.B. Müller for column production. We thank Dr. Rupinder Kaur for her support. Some of the graphical illustrations used in the manuscript were prepared using BioRender.com. We thank Mr. Marin Bralo at iTERM for his technical support throughout this study.

AUTHOR CONTRIBUTIONS

A.E., M. Mann, H.S.B., and A.-D.B. conceptualized and designed the study. H.S.B., Z.R., and H.M. performed mice experiments, solvent-based organ clearing, light-sheet imaging procedures, and stitching of data. H.S.B. developed the LCM-based isolation procedure for target tissues from solvent-cleared organs. A.-D.B. developed the sample preparation workflow for proteomics analysis. A.-D.B., S.K., H.S.B., M. Molbay, and M.T. performed mass spectrometry-based proteomics analysis. R.A.-M., J.C.P., F.K., M.A., B.M., and F.T. developed deep learning models. M.A. and F.T. performed data analysis. M.I.T. performed atlas registration of 5xFAD brains. H.S.B. and D.K. performed ClearMAP analyses. A.E. conceptualized, and F.O. designed the robotic extraction system. Z.I.K. labeled, cleared, and imaged whole body of mouse. F.O., H.S.B., and S.K. extracted tissue from whole body and whole organs. S.K. performed mass spectrometry on robotic extracted samples. H.S.B. and S.K. analyzed the data. M.N., J.C.P., and A.D. performed 2D LCM registration to 3D data. S.M. and S.F.L. helped with the prototyping experiment. H.S.B., A.-D.B., M. Mann, and A.E. wrote the manuscript.

DECLARATION OF INTERESTS

F.T. reports receiving consulting fees from Roche Diagnostics GmbH and Cellarity, Inc., and ownership interest in Cellarity, Inc., and Dermagnostix. A.E.,

(F) The number of shared and unique set of proteins in cranium.

(G) Pearson correlation among cranium samples (n = 3 experimental replicates).

(H) Rank order of core protein abundance signals in cranium.

(I) Volcano plot showing the significantly enriched proteins in medial vs. lateral border of scapula.

(J) Heatmap showing the proteins related to innate immune system in medial vs. lateral border of scapula.

(K) Proteins related to adaptive immune system.

(L) Related to B cell receptor/T cell receptor pathway in scapula bone marrow niches.

See also [Figure S7](#) and [Video S6](#).

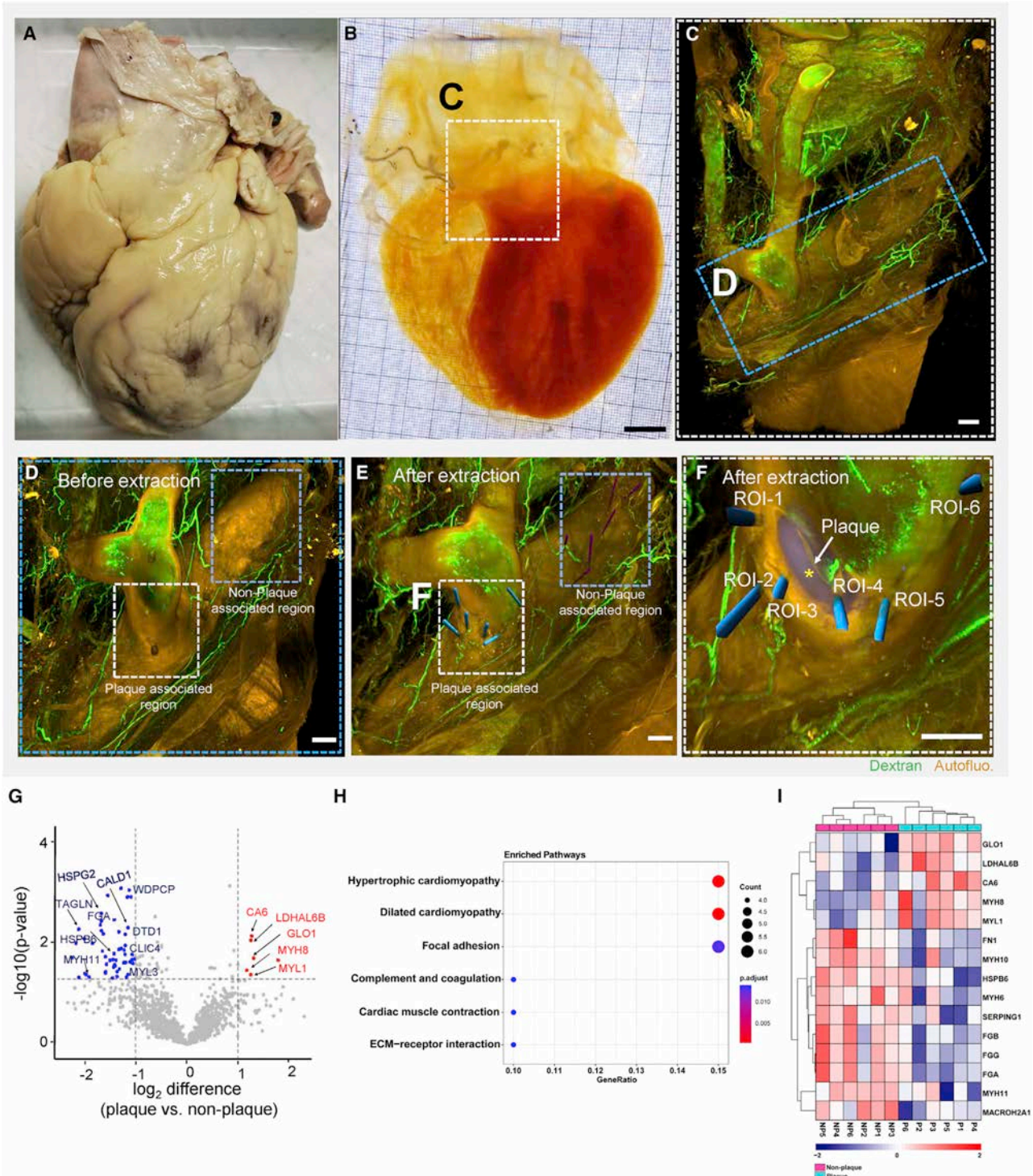


Figure 7. Human heart clearing, imaging, and proteomics from atherosclerotic plaques in coronary artery

(A) Image of whole human heart before clearing.

(B) Image of human heart after SHANEL clearing. Scale bar, 2 mm.

(C) 3D visualization of stitched images of portion of human heart showing dextran-labeled vessels (in green), plaques as autofluorescence (in gold). Scale bar, 1,000 μ m.

(D) Stitched images of coronal artery with atherosclerotic plaque-associated regions and non-plaque regions before robotic guided extraction. Scale bar, 1,000 μ m.

(legend continued on next page)

H.S.B., F.O., S.K., M.I.T., and M.N. have filed a patent related to robotics technologies presented in this work.

INCLUSION AND DIVERSITY

We support inclusive, diverse, and equitable conduct of research. We worked to ensure sex balance in the selection of non-human subjects. We worked to ensure diversity in experimental samples through the selection of the genomic datasets. One or more of the authors of this paper self-identifies as an under-represented ethnic minority in their field of research or within their geographical location. One or more of the authors of this paper self-identifies as a gender minority in their field of research. One or more of the authors of this paper self-identifies as a member of the LGBTQIA+ community. We avoided “helicopter science” practices by including the participating local contributors from the region where we conducted the research as authors on the paper.

Received: May 3, 2021

Revised: June 13, 2022

Accepted: November 18, 2022

Published: December 22, 2022

REFERENCES

1. Braak, H., Thal, D.R., Ghebremedhin, E., and Del Tredici, K. (2011). Stages of the Pathologic Process in Alzheimer Disease: Age Categories From 1 to 100 Years. *J. Neuropathol. Exp. Neurol.* 70, 960–969. <https://doi.org/10.1097/NEN.0b013e318232a379>.
2. Belle, M., Godefroy, D., Couly, G., Malone, S.A., Collier, F., Giacobini, P., and Chédotal, A. (2017). Tridimensional Visualization and Analysis of Early Human Development. *Cell* 169, 161–173.e12. <https://doi.org/10.1016/j.cell.2017.03.008>.
3. Ueda, H.R., Ertürk, A., Chung, K., Gradinaru, V., Chédotal, A., Tomancak, P., and Keller, P.J. (2020). Tissue clearing and its applications in neuroscience. *Nat. Rev. Neurosci.* 21, 61–79. <https://doi.org/10.1038/s41583-019-0250-1>.
4. Zhao, S., Todorov, M.I., Cai, R., Maskari, R.A., Steinke, H., Kemter, E., Mai, H., Rong, Z., Warner, M., Stanic, K., Schoppe, O., Paetzold, J.C., Gesierich, B., Wong, M.N., Huber, T.B., Duering, M., Bruns, O.T., Menze, B., Lipfert, J., Puelles, V.G., Wolf, E., Bechmann, I., and Erturk, A. (2020). Cellular and Molecular Probing of Intact Human Organs. *Cell* 180, 796–812.e19. <https://doi.org/10.1016/j.cell.2020.01.030>.
5. Moen, E., Bannon, D., Kudo, T., Graf, W., Covert, M., and Van Valen, D. (2019). Deep learning for cellular image analysis. *Nat. Methods* 16, 1233–1246. <https://doi.org/10.1038/s41592-019-0403-1>.
6. Sullivan, D.P., Winsnes, C.F., Åkesson, L., Hjelmare, M., Wiking, M., Schutten, R., Campbell, L., Leifsson, H., Rhodes, S., Nordgren, A., Smith, K., Revaz, B., Finnbogason, B., Szantner, A., and Lundberg, E. (2018). Deep learning is combined with massive-scale citizen science to improve large-scale image classification. *Nat. Biotechnol.* 36, 820–828. <https://doi.org/10.1038/nbt.4225>.
7. Ji, A.L., Rubin, A.J., Thrane, K., Jiang, S., Reynolds, D.L., Meyers, R.M., Guo, M.G., George, B.M., Mollbrink, A., Bergensträhle, J., Larsson, L., Bai, Y., Zhu, B., Bhaduri, A., Meyers, J.M., Rovira-Clave, X., Hollmig, S.T., Aasi, S.Z., Nolan, G.P., Lundeberg, J., and Khavari, P.A. (2020). Multimodal Analysis of Composition and Spatial Architecture in Human Squamous Cell Carcinoma. *Cell* 182, 497–514.e22. <https://doi.org/10.1016/j.cell.2020.05.039>.
8. Stuart, T., and Satija, R. (2019). Integrative single-cell analysis. *Nat. Rev. Genet.* 20, 257–272. <https://doi.org/10.1038/s41576-019-0093-7>.
9. VanHorn, S., and Morris, S.A. (2021). Next-Generation Lineage Tracing and Fate Mapping to Interrogate Development. *Dev. Cell* 56, 7–21. <https://doi.org/10.1016/j.devcel.2020.10.021>.
10. Brunner, A.D., Thielert, M., Vasilopoulou, C., Ammar, C., Coscia, F., Mund, A., Hoerning, O.B., Bache, N., Apalategui, A., Lubeck, M., Richter, S., Fischer, D.S., Raether, O., Park, M.A., Meier, F., Theis, F.J., and Mann, M. (2022). Ultra-high sensitivity mass spectrometry quantifies single-cell proteome changes upon perturbation. *Mol. Syst. Biol.* 18, e10798. <https://doi.org/10.15252/msb.202110798>.
11. Reimegård, J., Tarbier, M., Danielsson, M., Schuster, J., Baskaran, S., Panagiotou, S., Dahl, N., Friedländer, M.R., and Gallant, C.J. (2021). A combined approach for single-cell mRNA and intracellular protein expression analysis. *Commun Biol* 4, 624. <https://doi.org/10.1038/s42003-021-02142-w>.
12. Johnson, E.C.B., Carter, E.K., Dammer, E.B., Duong, D.M., Gerasimov, E.S., Liu, Y., Liu, J., Betarbet, R., Ping, L., Yin, L., Serrano, G.E., Beach, T.G., Peng, J., De Jager, P.L., Haroutunian, V., Zhang, B., Gaiteri, C., Bennett, D.A., Gearing, M., Wingo, T.S., Wingo, A.P., Lah, J.J., Levey, A.I., and Seyfried, N.T. (2022). Large-scale deep multi-layer analysis of Alzheimer’s disease brain reveals strong proteomic disease-related changes not observed at the RNA level. *Nat. Neurosci.* 25, 213–225. <https://doi.org/10.1038/s41593-021-00999-y>.
13. Wegler, C., Ölander, M., Wiśniewski, J.R., Lundquist, P., Zettl, K., Åsberg, A., Hjelmæsæth, J., Andersson, T.B., and Artursson, P. (2020). Global variability analysis of mRNA and protein concentrations across and within human tissues. *NAR Genom Bioinform* 2, lqz010. <https://doi.org/10.1093/nargab/lqz010>.
14. Budnik, B., Levy, E., Harmange, G., and Slavov, N. (2018). SCoPE-MS: mass spectrometry of single mammalian cells quantifies proteome heterogeneity during cell differentiation. *Genome Biol.* 19, 161. <https://doi.org/10.1186/s13059-018-1547-5>.
15. Cheung, T.K., Lee, C.-Y., Bayer, F.P., McCoy, A., Kuster, B., and Rose, C.M. (2021). Defining the carrier proteome limit for single-cell proteomics. *Nat. Methods* 18, 76–83. <https://doi.org/10.1038/s41592-020-01002-5>.
16. Cong, Y., Motamedchaboki, K., Misal, S.A., Liang, Y., Guise, A.J., Truong, T., Huguet, R., Plowey, E.D., Zhu, Y., Lopez-Ferrer, D., et al. (2021). Ultra-sensitive single-cell proteomics workflow identifies >1000 protein groups per mammalian cell. *Chem. Sci.* 12, 1001–1006. <https://doi.org/10.1039/D0SC03636F>.
17. Mund, A., Coscia, F., Kriston, A., Hollandi, R., Kovács, F., Brunner, A.-D., Migh, E., Schweizer, L., Santos, A., Bzorek, M., Naimy, S., Rahbek-Gjerdum, L.M., Dyring-Andersen, B., Bulkescher, J., Lukas, C., Eckert, M.A., Lengyel, E., Gnann, C., Lundberg, E., Horvath, P., and Mann, M. (2022). Deep Visual Proteomics defines single-cell identity and heterogeneity. *Nat. Biotechnol.* 40, 1231–1240. <https://doi.org/10.1038/s41587-022-01302-5>.
18. Alon, S., Goodwin, D.R., Sinha, A., Wassie, A.T., Chen, F., Daugharthy, E.R., Bando, Y., Kajita, A., Xue, A.G., Marrett, K., Prior, R., Cui, Y., Payne, A.C., Yao, C.C., Suk, H.J., Wang, R., Yu, C.C.J., Tillberg, P., Reginato, P., Pak, N., Liu, S., Punthambaker, S., Iyer, E.P.R., Kohman, R.E., Miller, J.A., Lein, E.S., Lako, A., Cullen, N., Rodig, S., Helvie, K., Abravanel, D.L., Waggle, N., Johnson, B.E., Klughammer, J., Slyper, M., Waldman, J., Jane-Valbuena, J., Rozenblatt-Rosen, O., Regev, A., IMAXT Consortium, Church, G.M., Marblestone, A.H., Boyden, E.S., Al Sa’id, M., Alon, S.,

(E) Stitched images of coronary artery after extraction of ROIs, extraction points are shown in blue (plaque region) and in magenta (non-plaque region). Scale bar, 1,000 μ m.

(F) Enlarged view of ROIs around the segmented plaque marked in (E). Scale bar, 1,000 μ m.

(G) Volcano plot showing the significantly enriched proteins in plaque (ROIs 1–6) vs. non-plaque areas.

(H) Pathway enrichment of differentially regulated proteins.

(I) Heatmap of differentially regulated proteins in each ROIs.

See also [Figure S7](#) and [Video S7](#).

- Aparicio, S., Battistoni, G., Balasubramanian, S., Becker, R., Bodenmiller, B., Boyden, E.S., Bressan, D., Bruna, A., Burger, M., Caldas, C., Callari, M., Cannell, I.G., Casbolt, H., Chormay, N., Cui, Y., Dariush, A., Dinh, K., Emenari, A., Eyal-Lubling, Y., Fan, J., Fatemi, A., Fisher, E., Gonzalez-Solares, E.A., Gonzalez-Fernandez, C., Goodwin, D., Greenwood, W., Grimaldi, F., Hannon, G.J., Harris, O., Harris, S., Jauset, C., Joyce, J.A., Karagiannis, E.D., Kovacevic, T., Kuett, L., Kunes, R., Kupcu Yoldas, A., Lai, D., Laks, E., Lee, H., Lee, M., Lerda, G., Li, Y., McPherson, A., Millar, N., Mulvey, C.M., Nugent, F., O'Flanagan, C.H., Paez-Ribes, M., Pearsall, I., Qosaj, F., Roth, A.J., Rueda, O.M., Ruiz, T., Sawicka, K., Sepulveda, L.A., Shah, S.P., Shea, A., Sinha, A., Smith, A., Tavare, S., Tietscher, S., Vazquez-Garcia, I., Vogl, S.L., Walton, N.A., Wassie, A.T., Watson, S.S., Weselak, J., Wild, S.A., Williams, E., Windhager, J., Whitmarsh, T., Xia, C., Zheng, P., and Zhuang, X. (2021). Expansion sequencing: Spatially precise in situ transcriptomics in intact biological systems. *Science* 371, eaax2656. <https://doi.org/10.1126/science.aax2656>.
19. van den Brink, S.C., Alemany, A., van Batenburg, V., Moris, N., Blotenburg, M., Vivié, J., Baillie-Johnson, P., Nichols, J., Sonnen, K.F., Martinez Arias, A., and van Oudenaarden, A. (2020). Single-cell and spatial transcriptomics reveal somitogenesis in gastruloids. *Nature* 582, 405–409. <https://doi.org/10.1038/s41586-020-2024-3>.
 20. Chen, W.-T., Lu, A., Craessaerts, K., Pavie, B., Sala Frigerio, C., Corthout, N., Qian, X., Laláková, J., Kühnemund, M., Voytyuk, I., Wolfs, L., Mancuso, R., Salta, E., Balusu, S., Snellinx, A., Munck, S., Jurek, A., Fernandez Navarro, J., Saido, T.C., Huitinga, I., Lundberg, J., Fiers, M., and De Strooper, B. (2020). Spatial Transcriptomics and In Situ Sequencing to Study Alzheimer's Disease. *Cell* 182, 976–991.e19. <https://doi.org/10.1016/j.cell.2020.06.038>.
 21. Liu, Y., Yang, M., Deng, Y., Su, G., Enniful, A., Guo, C.C., Tebaldi, T., Zhang, D., Kim, D., Bai, Z., Norris, E., Pan, A., Li, J., Xiao, Y., Halene, S., and Fan, R. (2020). High-Spatial-Resolution Multi-Omics Sequencing via Deterministic Barcoding in Tissue. *Cell* 183, 1665–1681.e18. <https://doi.org/10.1016/j.cell.2020.10.026>.
 22. Mahdessian, D., Cesnik, A.J., Gnann, C., Danielsson, F., Stenström, L., Arif, M., Zhang, C., Le, T., Johansson, F., Schutten, R., Backstrom, A., Axelsson, U., Thul, P., Cho, N.H., Carja, O., Uhlen, M., Mardinoglu, A., Stadler, C., Lindskog, C., Ayoglu, B., Leonetti, M.D., Ponten, F., Sullivan, D.P., and Lundberg, E. (2021). Spatiotemporal dissection of the cell cycle with single-cell proteogenomics. *Nature* 590, 649–654. <https://doi.org/10.1038/s41586-021-03232-9>.
 23. Rodrigues, S.G., Stickels, R.R., Goeva, A., Martin, C.A., Murray, E., Vanderburg, C.R., Welch, J., Chen, L.M., Chen, F., and Macosko, E.Z. (2019). Slide-seq: A scalable technology for measuring genome-wide expression at high spatial resolution. *Science* 363, 1463–1467. <https://doi.org/10.1126/science.aaw1219>.
 24. Ståhl, P.L., Salmén, F., Vickovic, S., Lundmark, A., Navarro, J.F., Magnusson, J., Giacomello, S., Asp, M., Westholm, J.O., Huss, M., Mollbrink, A., Linnarsson, S., Codeluppi, S., Borg, A., Ponten, F., Costea, P.I., Sahlen, P., Järnberg, J., Bergmann, O., Lundberg, J., and Frisen, J. (2016). Visualization and analysis of gene expression in tissue sections by spatial transcriptomics. *Science* 353, 78–82. <https://doi.org/10.1126/science.aaf2403>.
 25. Takei, Y., Yun, J., Zheng, S., Ollikainen, N., Pierson, N., White, J., Shah, S., Thomassie, J., Suo, S., Eng, C.-H.L., Guttman, M., Yuan, G.C., and Cai, L. (2021). Integrated spatial genomics reveals global architecture of single nuclei. *Nature* 590, 344–350. <https://doi.org/10.1038/s41586-020-03126-2>.
 26. Giesen, C., Wang, H.A.O., Schapiro, D., Zivanovic, N., Jacobs, A., Hattendorf, B., Schüffler, P.J., Grolimund, D., Buhmann, J.M., Brandt, S., Varga, Z., Wild, P.J., Gunther, D., and Bodenmiller, B. (2014). Highly multiplexed imaging of tumor tissues with subcellular resolution by mass cytometry. *Nat. Methods* 11, 417–422. <https://doi.org/10.1038/nmeth.2869>.
 27. Ko, J., Wilkovich, M., Oh, J., Kohler, R.H., Bolli, E., Pittet, M.J., Vinegoni, C., Sykes, D.B., Mikula, H., Weissleder, R., and Carlson, J.C.T. (2022). Spatiotemporal multiplexed immunofluorescence imaging of living cells and tissues with bioorthogonal cycling of fluorescent probes. *Nat. Biotechnol.* 40, 1654–1662. <https://doi.org/10.1038/s41587-022-01339-6>.
 28. Goltsev, Y., Samusik, N., Kennedy-Darling, J., Bhate, S., Hale, M., Vazquez, G., Black, S., and Nolan, G.P. (2018). Deep Profiling of Mouse Splenic Architecture with CODEX Multiplexed Imaging. *Cell* 174, 968–981.e15. <https://doi.org/10.1016/j.cell.2018.07.010>.
 29. Saka, S.K., Wang, Y., Kishi, J.Y., Zhu, A., Zeng, Y., Xie, W., Kirli, K., Yapp, C., Cicconet, M., Beliveau, B.J., Lapan, S.W., Yin, S., Lin, M., Boyden, E.S., Kaeser, P.S., Pihan, G., Church, G.M., and Yin, P. (2019). Immuno-SABER enables highly multiplexed and amplified protein imaging in tissues. *Nat. Biotechnol.* 37, 1080–1090. <https://doi.org/10.1038/s41587-019-0207-y>.
 30. Radtke, A.J., Kandov, E., Lowekamp, B., Speranza, E., Chu, C.J., Gola, A., Thakur, N., Shih, R., Yao, L., Yaniv, Z.R., Beuschel, R.T., Kabat, J., Croteau, J., Davis, J., Hernandez, J.M., and Germain, R.N. (2020). IBEX: A versatile multiplex optical imaging approach for deep phenotyping and spatial analysis of cells in complex tissues. *Proc. Natl. Acad. Sci. USA* 117, 33455–33465. <https://doi.org/10.1073/pnas.2018488117>.
 31. Ueda, H.R., Dodt, H.-U., Osten, P., Economo, M.N., Chandrasekar, J., and Keller, P.J. (2020). Whole-Brain Profiling of Cells and Circuits in Mammals by Tissue Clearing and Light-Sheet Microscopy. *Neuron* 106, 369–387. <https://doi.org/10.1016/j.neuron.2020.03.004>.
 32. Aebersold, R., and Mann, M. (2016). Mass-spectrometric exploration of proteome structure and function. *Nature* 537, 347–355. <https://doi.org/10.1038/nature19949>.
 33. Richardson, D.S., Guan, W., Matsumoto, K., Pan, C., Chung, K., Ertürk, A., Ueda, H.R., and Lichtman, J.W. (2021). TISSUE CLEARING. *Nat. Rev. Methods Primers* 1, 84. <https://doi.org/10.1038/s43586-021-00080-9>.
 34. Cai, R., Pan, C., Ghasemigharagoz, A., Todorov, M.I., Förstera, B., Zhao, S., Bhatia, H.S., Parra-Damas, A., Mrowka, L., Theodorou, D., Rempfler, M., Xavier, A.L.R., Kress, B.T., Benakis, C., Steinke, H., Liebscher, S., Bechmann, I., Liesz, A., Menze, B., Kerschensteiner, M., Nedergaard, M., and Ertürk, A. (2019). Panoptic imaging of transparent mice reveals whole-body neuronal projections and skull-meninges connections. *Nat. Neurosci.* 22, 317–327. <https://doi.org/10.1038/s41593-018-0301-3>.
 35. Langlois, J.A., Rutland-Brown, W., and Thomas, K.E. (2005). The incidence of traumatic brain injury among children in the United States: differences by race. *J. Head Trauma Rehabil.* 20, 229–238. <https://doi.org/10.1097/00001199-200505000-00006>.
 36. Ertürk, A., Mentz, S., Stout, E.E., Hedehus, M., Dominguez, S.L., Neumaier, L., Krammer, F., Llovera, G., Srinivasan, K., Hansen, D.V., Liesz, A., Searce-Levie, K.A., and Sheng, M. (2016). Interfering with the Chronic Immune Response Rescues Chronic Degeneration After Traumatic Brain Injury. *J. Neurosci.* 36, 9962–9975. <https://doi.org/10.1523/JNEUROSCI.1898-15.2016>.
 37. Renier, N., Adams, E.L., Kirst, C., Wu, Z., Azevedo, R., Kohl, J., Autry, A.E., Kadiri, L., Umadevi Venkataraju, K., Zhou, Y., Wang, V.X., Tang, C.Y., Olsen, O., Dulac, C., Osten, P., and Tessier-Lavigne, M. (2016). Mapping of Brain Activity by Automated Volume Analysis of Immediate Early Genes. *Cell* 165, 1789–1802. <https://doi.org/10.1016/j.cell.2016.05.007>.
 38. Chen, M., Song, H., Cui, J., Johnson, C.E., Hubler, G.K., DePalma, R.G., Gu, Z., and Xia, W. (2018). Proteomic Profiling of Mouse Brains Exposed to Blast-Induced Mild Traumatic Brain Injury Reveals Changes in Axonal Proteins and Phosphorylated Tau. *J. Alzheimers Dis* 66, 751–773. <https://doi.org/10.3233/JAD-180726>.
 39. Asher, R.A., Morgenstern, D.A., Fidler, P.S., Adcock, K.H., Oohira, A., Braistead, J.E., Levine, J.M., Margolis, R.U., Rogers, J.H., and Fawcett, J.W. (2000). Neurocan is upregulated in injured brain and in cytokine-treated astrocytes. *J. Neurosci.* 20, 2427–2438. <https://doi.org/10.1523/jneurosci.20-07-02427.2000>.
 40. Alaamery, M., Albesher, N., Aljawini, N., Alsuwailm, M., Massadeh, S., Wheeler, M.A., Chao, C., and Quintana, F.J. (2021). Role of sphingolipid metabolism in neurodegeneration. *J. Neurochem.* 158, 25–35. <https://doi.org/10.1111/jnc.15044>.

41. Gebai, A., Gorelik, A., Li, Z., Illes, K., and Nagar, B. (2018). Structural basis for the activation of acid ceramidase. *Nat. Commun.* 9, 1621. <https://doi.org/10.1038/s41467-018-03844-2>.
42. Parveen, F., Bender, D., Law, S.-H., Mishra, V.K., Chen, C.-C., and Ke, L.-Y. (2019). Role of Ceramidases in Sphingolipid Metabolism and Human Diseases. *Cells* 8, E1573. <https://doi.org/10.3390/cells8121573>.
43. Kyriakou, K., W Lederer, C., Kleanthous, M., Drousiotou, A., and Mal-ekkou, A. (2020). Acid Ceramidase Depletion Impairs Neuronal Survival and Induces Morphological Defects in Neurites Associated with Altered Gene Transcription and Sphingolipid Content. *Int. J. Mol. Sci.* 21, E1607. <https://doi.org/10.3390/ijms21051607>.
44. Rummyantseva, A., Popovic, M., and Trifunovic, A. (2022). CLPP deficiency ameliorates neurodegeneration caused by impaired mitochondrial protein synthesis. *Brain* 145, 92–104. <https://doi.org/10.1093/brain/awab303>.
45. Shi, Y., Yi, C., Li, X., Wang, J., Zhou, F., and Chen, X. (2017). Overexpression of Mitofusin2 decreased the reactive astrocytes proliferation in vitro induced by oxygen-glucose deprivation/reoxygenation. *Neurosci. Lett.* 639, 68–73. <https://doi.org/10.1016/j.neulet.2016.12.052>.
46. Meyer-Luehmann, M., Spiess-Jones, T.L., Prada, C., Garcia-Alloza, M., de Calignon, A., Rozkalne, A., Koenigsknecht-Talbot, J., Holtzman, D.M., Bacskai, B.J., and Hyman, B.T. (2008). Rapid appearance and local toxicity of amyloid-beta plaques in a mouse model of Alzheimer's disease. *Nature* 451, 720–724. <https://doi.org/10.1038/nature06616>.
47. Ronneberger, O., Fischer, P., and Brox, T. (2015). U-Net: Convolutional Networks for Biomedical Image Segmentation. <https://doi.org/10.48550/arXiv.1505.04597>.
48. Todorov, M.I., Paetzold, J.C., Schoppe, O., Tetteh, G., Shit, S., Efremov, V., Todorov-Völgyi, K., Düring, M., Dichgans, M., Piraud, M., Menze, B., and Erturk, A. (2020). Machine learning analysis of whole mouse brain vasculature. *Nat. Methods* 17, 442–449. <https://doi.org/10.1038/s41592-020-0792-1>.
49. Wang, Q., Ding, S.-L., Li, Y., Royall, J., Feng, D., Lesnar, P., Graddis, N., Naeemi, M., Facer, B., Ho, A., Dolbeare, T., Blanchard, B., Dee, N., Wake-man, W., Hirokawa, K.E., Szafer, A., Sunkin, S.M., Oh, S.W., Bernard, A., Phillips, J.W., Hawrylycz, M., Koch, C., Zeng, H., Harris, J.A., and Ng, L. (2020). The Allen Mouse Brain Common Coordinate Framework: A 3D Reference Atlas. *Cell* 181, 936–953.e20. <https://doi.org/10.1016/j.cell.2020.04.007>.
50. Claudi, F., Tyson, A.L., Petrucco, L., Margrie, T.W., Portugues, R., and Branco, T. (2021). Visualizing anatomically registered data with brainrender. *Elife* 10, e65751. <https://doi.org/10.7554/eLife.65751>.
51. Lichtenthaler, S.F. (2006). Ectodomain shedding of the amyloid precursor protein: cellular control mechanisms and novel modifiers. *Neurodegener. Dis.* 3, 262–269. <https://doi.org/10.1159/000095265>.
52. Meckelein, B., de Silva, H., Roses, A.D., Rao, P., Pettenati, M.J., Xu, P.T., Hodge, R., Glucksman, M.J., and Abraham, C.R. (1996). Human endopeptidase (THOP1) is localized on chromosome 19 within the linkage region for the late-onset alzheimer disease AD2 locus. *Genomics* 31, 246–249. <https://doi.org/10.1006/geno.1996.0041>.
53. Pollio, G., Hoozemans, J.J., Andersen, C.A., Roncarati, R., Rosi, M.C., van Haastert, E.S., Seredenina, T., Diamanti, D., Gotta, S., Fiorentini, A., Magnoni, L., Raggiaschi, R., Rozemuller, A.J., Casamenti, F., Caricasole, A., and Terstappen, G.C. (2008). Increased expression of the oligopeptidase THOP1 is a neuroprotective response to A β toxicity. *Neurobiol. Dis.* 31, 145–158. <https://doi.org/10.1016/j.nbd.2008.04.004>.
54. Xu, S., Di, Z., He, Y., Wang, R., Ma, Y., Sun, R., Li, J., Wang, T., Shen, Y., Fang, S., Feng, L., and Shen, Y. (2019). Mesencephalic astrocyte-derived neurotrophic factor (MANF) protects against A β toxicity via attenuating A β -induced endoplasmic reticulum stress. *J. Neuroinflammation* 16, 35. <https://doi.org/10.1186/s12974-019-1429-0>.
55. Arisi, I., D'Onofrio, M., Brandi, R., Felsani, A., Capsoni, S., Drovandi, G., Felici, G., Weitschek, E., Bertolazzi, P., and Cattaneo, A. (2011). Gene expression biomarkers in the brain of a mouse model for Alzheimer's disease: mining of microarray data by logic classification and feature selec-tion. *J. Alzheimers Dis* 24, 721–738. <https://doi.org/10.3233/JAD-2011-101881>.
56. Marom, R., Jain, M., Burrage, L.C., Song, I.-W., Graham, B.H., Brown, C.W., Stevens, S.J., Stegmann, A.P., Gunter, A.T., Kaplan, J.D., Gavrilova, R.H., Shinawi, M., Rosenfeld, J.A., Bae, Y., Tran, A.A., Chen, Y., Lu, J.T., Gibbs, R.A., Eng, C., Yang, Y., Rousseau, J., de Vries, B.B., Campeau, P.M., and Lee, B. (2017). Heterozygous variants in ACTL6A, encoding a component of the BAF complex, are associated with intellectual disability. *Hum. Mutat.* 38, 1365–1371. <https://doi.org/10.1002/humu.23282>.
57. Depp, C., Sun, T., Sasmita, A.O., Spieth, L., Berghoff, S.A., Steixner-Kumar, A.A., Subramanian, S., Möbius, W., Göbbels, S., Saher, G., Zampar, S., Wirths, O., Thalmann, M., Saito, T., Saido, T., Krueger-Burg, D., Kawaguchi, R., Willem, M., Haass, C., Geschwind, D., Ehrenreich, H., Stassart, R., and Nave, K.A. (2021). Ageing-associated myelin dysfunction drives amyloid deposition in mouse models of Alzheimer's disease. <https://doi.org/10.1101/2021.07.31.454562>.
58. Kolabas, Z.I., Kuemmerle, L.B., Perneczky, R., Förstera, B., Büttner, M., Caliskan, O.S., Ali, M., Rong, Z., Mai, H., Hummel, S., Bartos, L.M., Biechele, G., Zatzepin, A., Albert, N.L., Unterrainer, M., Gnorich, J., Zhao, S., Khalin, I., Rauchmann, B.S., Molbay, M., Sterr, M., Kunze, I., Stanic, K., Besson-Girard, S., Kopczak, A., Katzdobler, S., Palleis, C., Gokce, O., Lickert, H., Steinke, H., Bechmann, I., Buerger, K., Levin, J., Haass, C., Dichgans, M., Havla, J., Kumpfel, T., Kerschensteiner, M., Simons, M., Plesnila, N., Krahmer, N., Bhatia, H.S., Erturk, S., Hellal, F., Brendel, M., Theis, F.-J., and Erturk, A. (2021). Multi-omics and 3D-imaging reveal bone heterogeneity and unique calvaria cells in neuroinflammation. <https://doi.org/10.1101/2021.12.24.473988>.
59. Nabel, E.G., and Braunwald, E. (2012). A tale of coronary artery disease and myocardial infarction. *N. Engl. J. Med.* 366, 54–63. <https://doi.org/10.1056/NEJMr1112570>.
60. Wong, N.D. (2014). Epidemiological studies of CHD and the evolution of preventive cardiology. *Nat. Rev. Cardiol.* 11, 276–289. <https://doi.org/10.1038/nrcardio.2014.26>.
61. Fernandez, D.M., Rahman, A.H., Fernandez, N.F., Chudnovskiy, A., Amir, E.-A.D., Amadori, L., Khan, N.S., Wong, C.K., Shamailova, R., Hill, C.A., Wang, Z., Remark, R., Li, J.R., Pina, C., Faries, C., Awad, A.J., Moss, N., Björkegren, J.L.M., Kim-Schulze, S., Gnajatic, S., Ma'ayan, A., Mocco, J., Faries, P., Merad, M., and Giannarelli, C. (2019). Single-cell immune landscape of human atherosclerotic plaques. *Nat Med* 25, 1576–1588. <https://doi.org/10.1038/s41591-019-0590-4>.
62. Litviňuková, M., Talavera-López, C., Maatz, H., Reichart, D., Worth, C.L., Lindberg, E.L., Kanda, M., Polanski, K., Heinig, M., Lee, M., Nadelmann, E.R., Roberts, K., Tuck, L., Fasouli, E.S., DeLaughter, D.M., McDonough, B., Wakimoto, H., Gorham, J.M., Samari, S., Mahbubani, K.T., Saeb-Parsy, K., Patone, G., Boyle, J.J., Zhang, H., Zhang, H., Viveiros, A., Oudit, G.Y., Bayraktar, O.A., Seidman, J.G., Seidman, C.E., Nosedá, M., Hubner, N., and Teichmann, S.A. (2020). Cells of the adult human heart. *Nature* 588, 466–472. <https://doi.org/10.1038/s41586-020-2797-4>.
63. Meng, L.B., Li, J.Y., Xu, H.X., Wu, D.S., Shan, M.J., Chen, Y.H., Xu, J.P., Liu, L.T., Chen, Z., Li, Y.J., Gong, T., and Liu, D. (2022). A potential biomarker for clinical atherosclerosis: A novel insight derived from myosin heavy chain 10 promoting transformation of vascular smooth muscle cells. *Clin. Transl. Med.* 12, e672. <https://doi.org/10.1002/ctm2.672>.
64. Takahashi, L., Ishigami, T., Tomiyama, H., Kato, Y., Kikuchi, H., Tasaki, K., Yamashita, J., Inoue, S., Taguri, M., Nagao, T., Chikamori, T., Ishikawa, Y., and Yokoyama, U. (2021). Increased Plasma Levels of Myosin Heavy Chain 11 Is Associated with Atherosclerosis. *J. Clin. Med.* 10, 3155. <https://doi.org/10.3390/jcm10143155>.
65. Mäkinen, V.-P., Civelek, M., Meng, Q., Zhang, B., Zhu, J., Levian, C., Huan, T., Segrè, A.V., Ghosh, S., Vivar, J., Nikpay, M., Stewart, A.F.R., Nelson, C.P., Willenborg, C., Erdmann, J., Blakenberg, S., O'Donnell, C.J., Marz, W., Laaksonen, R., Epstein, S.E., Kathiresan, S., Shah, S.H., Hazen, S.L., Reilly, M.P., Lusis, A.J., Samani, N.J., Schunkert, H., Quertermous, T., McPherson, R., Yang, X., and Assimes, T.L. (2014). Integrative genomics reveals novel molecular pathways and gene networks for coronary

- artery disease. *PLoS Genet.* 10, e1004502. <https://doi.org/10.1371/journal.pgen.1004502>.
66. Adeva-Andany, M.M., Fernández-Fernández, C., Sánchez-Bello, R., Donapetry-García, C., and Martínez-Rodríguez, J. (2015). The role of carbonic anhydrase in the pathogenesis of vascular calcification in humans. *Atherosclerosis* 241, 183–191. <https://doi.org/10.1016/j.atherosclerosis.2015.05.012>.
 67. Yuan, L., Wang, M., Liu, T., Lei, Y., Miao, Q., Li, Q., Wang, H., Zhang, G., Hou, Y., and Chang, X. (2019). Carbonic Anhydrase 1-Mediated Calcification Is Associated With Atherosclerosis, and Methazolamide Alleviates Its Pathogenesis. *Front. Pharmacol.* 10, 766. <https://doi.org/10.3389/fphar.2019.00766>.
 68. Robichaud, S., Fairman, G., Vijithakumar, V., Mak, E., Cook, D.P., Pelletier, A.R., Huard, S., Vanderhyden, B.C., Figeys, D., Lavallée-Adam, M., Baetz, K., and Ouimet, M. (2021). Identification of novel lipid droplet factors that regulate lipophagy and cholesterol efflux in macrophage foam cells. *Autophagy* 17, 3671–3689. <https://doi.org/10.1080/15548627.2021.1886839>.
 69. Whitesell, J.D., Buckley, A.R., Knox, J.E., Kuan, L., Graddis, N., Pelos, A., Mukora, A., Wakeman, W., Bohn, P., Ho, A., Hirokawa, K.E., and Harris, J.A. (2019). Whole brain imaging reveals distinct spatial patterns of amyloid beta deposition in three mouse models of Alzheimer's disease. *J. Comp. Neurol.* 527, 2122–2145. <https://doi.org/10.1002/cne.24555>.
 70. Oddo, S., Caccamo, A., Shepherd, J.D., Murphy, M., Golde, T.E., Kaye, R., Metherate, R., Mattson, M.P., Akbari, Y., and LaFerla, F.M. (2003). Triple-transgenic model of Alzheimer's disease with plaques and tangles: intracellular Abeta and synaptic dysfunction. *Neuron* 39, 409–421. [https://doi.org/10.1016/S0896-6273\(03\)00434-3](https://doi.org/10.1016/S0896-6273(03)00434-3).
 71. Bai, B., Wang, X., Li, Y., Chen, P.-C., Yu, K., Dey, K.K., Yarbrough, J.M., Han, X., Lutz, B.M., Rao, S., Jiao, Y., Sifford, J.M., Han, J., Wang, M., Tan, H., Shaw, T.I., Cho, J.H., Zhou, S., Wang, H., Niu, M., Mancieri, A., Messler, K.A., Sun, X., Wu, Z., Pagala, V., High, A.A., Bi, W., Zhang, H., Chi, H., Haroutunian, V., Zhang, B., Beach, T.G., Yu, G., and Peng, J. (2020). Deep Multilayer Brain Proteomics Identifies Molecular Networks in Alzheimer's Disease Progression. *Neuron* 105, 975–991.e7. <https://doi.org/10.1016/j.neuron.2019.12.015>.
 72. Kim, D.K., Han, D., Park, J., Choi, H., Park, J.-C., Cha, M.-Y., Woo, J., Byun, M.S., Lee, D.Y., Kim, Y., and Mook-Jung, I. (2019). Deep proteome profiling of the hippocampus in the 5xFAD mouse model reveals biological process alterations and a novel biomarker of Alzheimer's disease. *Exp. Mol. Med.* 51, 1–17. <https://doi.org/10.1038/s12276-019-0326-z>.
 73. Neuner, S.M., Wilmott, L.A., Hoffmann, B.R., Mozhui, K., and Kaczorowski, C.C. (2017). Hippocampal proteomics defines pathways associated with memory decline and resilience in normal aging and Alzheimer's disease mouse models. *Behav. Brain Res.* 322, 288–298. <https://doi.org/10.1016/j.bbr.2016.06.002>.
 74. Boza-Serrano, A., Yang, Y., Paulus, A., and Deierborg, T. (2018). Innate immune alterations are elicited in microglial cells before plaque deposition in the Alzheimer's disease mouse model 5xFAD. *Sci. Rep.* 8, 1550. <https://doi.org/10.1038/s41598-018-19699-y>.
 75. Rangaraju, S., Dammer, E.B., Raza, S.A., Rathakrishnan, P., Xiao, H., Gao, T., Duong, D.M., Pennington, M.W., Lah, J.J., Seyfried, N.T., and Levey, A.I. (2018). Identification and therapeutic modulation of a pro-inflammatory subset of disease-associated-microglia in Alzheimer's disease. *Mol. Neurodegeneration* 13, 24. <https://doi.org/10.1186/s13024-018-0254-8>.
 76. Gail Canter, R., Huang, W.-C., Choi, H., Wang, J., Ashley Watson, L., Yao, C.G., Abdurrob, F., Bousleiman, S.M., Young, J.Z., Bennett, D.A., Delalle, I., Chung, K., and Tsai, L.H. (2019). 3D mapping reveals network-specific amyloid progression and subcortical susceptibility in mice. *Commun Biol* 2, 360. <https://doi.org/10.1038/s42003-019-0599-8>.
 77. Oblak, A.L., Lin, P.B., Kotredes, K.P., Pandey, R.S., Garceau, D., Williams, H.M., Uyar, A., O'Rourke, R., O'Rourke, S., Ingraham, C., Bednarczyk, D., Belanger, M., Cope, Z.A., Little, G.J., Williams, S.P.G., Ash, C., Bleckert, A., Ragan, T., Logsdon, B.A., Mangravite, L.M., Sukoff Rizzo, S.J., Territo, P.R., Carter, G.W., Howell, G.R., Sasner, M., and Lamb, B.T. (2021). Comprehensive Evaluation of the 5xFAD Mouse Model for Preclinical Testing Applications: A MODEL-AD Study. *Front. Aging Neurosci.* 13, 713726. <https://doi.org/10.3389/fnagi.2021.713726>.
 78. Percie du Sert, N., Hurst, V., Ahluwalia, A., Alam, S., Avey, M.T., Baker, M., Browne, W.J., Clark, A., Cuthill, I.C., Dimagli, U., Emerson, M., Garner, P., Holgate, S.T., Howells, D.W., Karp, N.A., Lazic, S.E., Lidster, K., MacCallum, C.J., Macleod, M., Pearl, E.J., Petersen, O.H., Rawle, F., Reynolds, P., Rooney, K., Sena, E.S., Silberberg, S.D., Steckler, T., and Wurbel, H. (2020). The ARRIVE guidelines 2.0: Updated guidelines for reporting animal research. *PLoS Biol.* 18, e3000410. <https://doi.org/10.1371/journal.pbio.3000410>.
 79. Kulak, N.A., Geyer, P.E., and Mann, M. (2017). Loss-less Nano-fractionator for High Sensitivity, High Coverage Proteomics. *Mol. Cell. Proteomics* 16, 694–705. <https://doi.org/10.1074/mcp.O116.065136>.
 80. Meier, F., Brunner, A.-D., Frank, M., Ha, A., Bludau, I., Voytik, E., Kaspar-Schoenefeld, S., Lubeck, M., Raether, O., Bache, N., Aebersold, R., Collins, B.C., Rost, H.L., and Mann, M. (2020). diaPASEF: parallel accumulation-serial fragmentation combined with data-independent acquisition. *Nat. Methods* 17, 1229–1236. <https://doi.org/10.1038/s41592-020-00998-0>.
 81. Schindelin, J., Arganda-Carreras, I., Frise, E., Kaynig, V., Longair, M., Pietzsch, T., Preibisch, S., Rueden, C., Saalfeld, S., Schmid, B., Tinevez, J.Y., White, D.J., Hartenstein, V., Eliceiri, K., Tomancak, P., and Cardona, A. (2012). Fiji: an open-source platform for biological-image analysis. *Nat. Methods* 9, 676–682. <https://doi.org/10.1038/nmeth.2019>.
 82. Silversmith, W. (2021). cc3d: Connected components on multilabel 3D & 2D images. <https://doi.org/10.5281/ZENODO.5535250>.
 83. Cox, J., Hein, M.Y., Luber, C.A., Paron, I., Nagaraj, N., and Mann, M. (2014). Accurate Proteome-wide Label-free Quantification by Delayed Normalization and Maximal Peptide Ratio Extraction, Termed MaxLFQ. *Mol. Cell. Proteomics* 13, 2513–2526. <https://doi.org/10.1074/mcp.M113.031591>.
 84. Bruderer, R., Bernhardt, O.M., Gandhi, T., Miladinović, S.M., Cheng, L.-Y., Messner, S., Ehrenberger, T., Zanotelli, V., Butscheid, Y., Escher, C., Vittek, O., Rinner, O., and Reiter, L. (2015). Extending the Limits of Quantitative Proteome Profiling with Data-Independent Acquisition and Application to Acetaminophen-Treated Three-Dimensional Liver Microtissues. *Mol. Cell. Proteomics* 14, 1400–1410. <https://doi.org/10.1074/mcp.M114.044305>.
 85. Callister, S.J., Barry, R.C., Adkins, J.N., Johnson, E.T., Qian, W.J., Webb-Robertson, B.-J.M., Smith, R.D., and Lipton, M.S. (2006). Normalization Approaches for Removing Systematic Biases Associated with Mass Spectrometry and Label-Free Proteomics. *J. Proteome Res.* 5, 277–286. <https://doi.org/10.1021/pr050300l>.
 86. Demichev, V., Messner, C.B., Vernardis, S.I., Lilley, K.S., and Ralser, M. (2020). DIA-NN: neural networks and interference correction enable deep proteome coverage in high throughput. *Nat. Methods* 17, 41–44. <https://doi.org/10.1038/s41592-019-0638-x>.
 87. Tyranova, S., Temu, T., Sinitcyn, P., Carlson, A., Hein, M.Y., Geiger, T., Mann, M., and Cox, J. (2016). The Perseus computational platform for comprehensive analysis of (pro)teomics data. *Nat. Methods* 13, 731–740. <https://doi.org/10.1038/nmeth.3901>.
 88. Wiśniewski, J.R., Hein, M.Y., Cox, J., and Mann, M. (2014). A “Proteomic Ruler” for Protein Copy Number and Concentration Estimation without Spike-in Standards. *Mol. Cell. Proteomics* 13, 3497–3506. <https://doi.org/10.1074/mcp.M113.037309>.

STAR★METHODS

KEY RESOURCES TABLE

| REAGENT or RESOURCE | SOURCE | IDENTIFIER |
|--|---------------------------------|---|
| Antibodies | | |
| Iba1 | Wako | Cat.# 019-19741; RRID: AB_839504 |
| Stathmin 1 | Novus Biologicals | Cat.# NBP1-76798; RRID:AB_11015725 |
| Neurocan | abcam | Cat.# ab31979; RRID:AB_2149711 |
| S100a11 | R&D | Cat.# MAB5167; RRID:AB_1207907 |
| Thop1 | Novus Biologicals | Cat.# NB400-146; RRID:AB_10128241 |
| MOAB2 | Novus Biologicals | Cat.# NBP2-13075; RRID:AB_2923428 |
| Goat anti-rabbit IgG Alexa Fluor 647 | Invitrogen | Cat.# A21245; RRID:AB_2535813 |
| Goat anti-Mouse IgG Alexa Fluor 488 | Invitrogen | Cat.# A11029; RRID:AB_2534088 |
| Goat anti-Mouse IgG Alexa Fluor 594 | Invitrogen | Cat.# A11032; RRID:AB_2534091 |
| Goat anti-Rat IgG Alexa Fluor 594 | Invitrogen | Cat.# A11007; RRID:AB_10561522 |
| Goat anti-Rat IgG Alexa Fluor 488 | Invitrogen | Cat.# A11006; RRID:AB_141373 |
| Atto647N conjugated anti GFP nanobooster | Chromotek | Cat.# gba647n-100; RRID:AB_2629215 |
| Chemicals, peptides, and recombinant proteins | | |
| Congo Red | Sigma-Aldrich | Cat.#C6277 |
| Propidium iodide (PI) | Sigma-Aldrich | Cat.#P4864 |
| Paraformaldehyde (PFA) | Sigma-Aldrich | Cat.#P6148 |
| Tetrahydrofuran (THF) | Sigma-Aldrich | Cat.# 186562 |
| tert-butanol | Sigma-Aldrich | Cat.# 360538 |
| Dichloromethane (DCM) | Sigma-Aldrich | Cat.# 270997 |
| Diphenyl ether (DPE) | Alfa Aesar | Cat.# A15791 |
| Vitamin E (DL-alpha-tocopherol) | Alfa Aesar | Cat.# A17039 |
| Benzyl benzoate | Sigma-Aldrich | Cat.#W213802 |
| Benzyl alcohol | Sigma-Aldrich | Cat.# 24122 |
| CHAPS | Carl Roth | Cat.# 1479.4 |
| N-Methyldiethanolamine | Sigma-Aldrich | Cat.# 471828 |
| Trypsin | Sigma-Aldrich | Cat.#T6567 |
| Formic acid | Sigma-Aldrich | Cat.# 64-18-6 |
| Acetonitrile | Sigma-Aldrich | Cat.# 75-05-8 |
| Experimental models: Organisms/strains | | |
| CX ₃ CR-1 ^{GFP} mice: B6.129P2(Cg)-Cx3cr1 ^{tm1Litt} /J | Jackson Laboratory | Strain # 005582; RRID: IMSR_JAX:005,582 |
| Thy1-GFP-M mice: Tg(Thy1-EGFP)MJrs/J | Jackson Laboratory | Strain # 007788; RRID: IMSR_JAX:007,788 |
| 5xFAD: B6.Cg-Tg(APP ^{Sw} FILon, PSEN1 ^{M146L} *L286V)6799Vas/Mmjax | Jackson Laboratory | Strain #034848-JAX; RRID: MMRRC_034848-JAX |
| LysM-eGFP: B6.129(Cg)-Lyz2 ^{tm1.1Graf} /Mmmh | MMRC | Strain #012039-MU; RRID: MMRRC_012039-MU |
| C57BL/6J mouse line | Jackson Laboratory | Strain #:000,664; RRID: IMSR_JAX:000,664 |
| Software and algorithms | | |
| ImSpector | Aberrior/LaVision | https://www.lavisionbiotec.com |
| Imaris | Bitplane AG | https://imaris.oxinst.com/ |
| Vision4D | Arivis | https://www.arivis.com/de/imaging-science/arivis-vision4d |
| Fiji | Schindelin et al. ⁸¹ | https://ImageJ.net/software/fiji/ |

(Continued on next page)

Continued

| REAGENT or RESOURCE | SOURCE | IDENTIFIER |
|---|------------------------------|---|
| syGlass VR | syGlass | https://www.syglass.io |
| Ansys Academic Research Mechanical | Ansys | https://www.ansys.com/academic |
| RoboDK 5.5 | RoboDK Software S.L. | https://robodk.com/ |
| MaxQuant (1.6.7.0) | Tyanova et al. ⁸⁷ | https://maxquant.org/ |
| Perseus (1.6.7.0) | Tyanova et al. ⁸⁷ | https://maxquant.org/perseus/ |
| GraphPad Prism(8.2.1) | GraphPad Software | https://www.graphpad.com |
| Code for 2D to 3D image registration | This Paper | Methods S1 |
| Deposited Data | | |
| Mass spectrometry raw data, libraries and outputs | This paper | https://www.ebi.ac.uk/pride/ ; ID# PXD034027 and PXD025316 |
| Others | | |
| 18G A-max paed Bone marrow biopsy needle 40,901,803 | HVM Medical Products GmbH | https://hvm-medical.com/produktkatalog-biopsie/ |
| 22G Chiba Fine Needle 07,742,208 | HVM Medical Products GmbH | https://hvm-medical.com/produktkatalog-biopsie/ |

RESOURCE AVAILABILITY**Lead contact**

Further information and requests for resources should be directed to and will be fulfilled by the Lead Contact, Ali Ertürk (erturk@helmholtz-muenchen.de).

Materials availability

This study did not generate new unique reagents.

Data and code availability

- All mass spectrometry raw data, libraries and outputs from each particular search engine analyzed in this study have been deposited to the ProteomeXchange Consortium via the PRIDE partner repository with the dataset identifier: Database: PXD034027 and Database: PXD025316.
- The source code for registration of 2D to 3D images is provided in supplemental information under [Methods S1](#).
- Any additional information required to reanalyze the data reported in this work paper is available from the Lead Contact upon request.

EXPERIMENTAL MODEL AND SUBJECT DETAILS**Animals**

We used the following animals in the study: mixed gender for CX3CR1-eGFP (10 months old), males only for Thy-1-GFPM (10 months old), mixed gender for 5xFAD (6 weeks and 6-months old), mixed gender for LysM-eGFP (3 months old) and mixed gender for C57Bl6/J (3 months old) from Jackson Laboratory. The animals were housed under a 12/12 h light/dark cycle. The animal experiments were conducted according to institutional guidelines: Klinikum der Universität München/Ludwig Maximilian University of Munich and after approval of the Ethical Review Board of the Government of Upper Bavaria (Regierung von Oberbayern, Munich, Germany) and the Animal Experiments Council under the Danish Ministry of Environment and Food (2015-15-0201-00535) and following the European directive 2010/63/EU for animal research. All data are reported according to the ARRIVE.⁷⁸ Sample sizes were chosen based on prior experience with similar models.

Human samples

Intact human brains from a 92 years-old female and intact heart from a 97 years-old female were taken from human body donors with no known neuropathological diseases. The donors gave their informed and written consent to explore their cadavers for research and educational purposes, when still alive and well. The signed consents are kept at the Anatomy Institute, University of Leipzig, Germany. Institutional approval was obtained in accordance to the Saxonian Death and Funeral Act of 1994. The signed body donor consents are available on request.

METHOD DETAILS

Repeated closed head mild traumatic brain injury (mTBI)

Before mTBI, tin foil was taped and tightened to the U-shaped stage made of clear plastic container ($38 \times 27 \times 27 \text{ cm}^3$) containing a sponge collection ($38 \times 25 \times 15 \text{ cm}^3$). Then, mice were pre-treated with buprenorphine (1:15 saline, 50 μl /20mg, ip) and anesthetized with 4% isoflurane using 1.0 L min^{-1} air until non-responsive to a paw or tail pinch. To ensure the head acceleration and rotation following the head impact, the mice were placed under an impact tip on the tin foil, which contains holes according to the shape of a mouse and can support the body weight of the mice. The mice were kept under light anesthesia with continued 2% isoflurane. mTBI was produced using a stereotaxic impactor device with a 5-mm round tip coated with 1mm thick rubber, which can preserve an intact skull after impact. The impact tip was placed and covered the scalp's area from just behind the eyes to the midline of the ears, the center of the tip at approximately midway along the sagittal suture. The injury was produced without skin incision (velocity of 5 m/s, depth of 0.5mm, and dwell time of 0.1 s). The mouse was removed quickly from the collection sponge and transferred to the recovery box maintained at 32°C . In total, mice received four hits with a 48 h interval in seven days. Sham mice receive identical handling and exposure to the same time length of anesthesia as the mTBI mice but receive no impact.

Perfusion and tissue preparation

Mice were anesthetized using a combination of midazolam, medetomidine and fentanyl (MMF) (1mL/100g of body mass for mice; i.p.). As soon as the animals did not show any pedal reflex, they were intracardially perfused with cold heparinized 0.1 M PBS (10 U/mL of Heparin, Ratiopharm; 100–125 mmHg pressure using a Leica Perfusion One system) for 5–10 min at room temperature until the blood was washed out, followed by ice-cold 4% paraformaldehyde (PFA) in 0.1 M PBS (pH 7.4) (Sigma) for 10 min. Then, the brains were extracted and post-fixed in 4% PFA for 1 day at 4°C and later washed with 0.1 M PBS for 10 min 3 times at room temperature. The whole brain clearing or nanoboosting procedure was started immediately. For the collection of fresh frozen samples, animals were sacrificed by cervical dislocation and brains were quickly snapped frozen in liquid nitrogen and stored in -80°C until further processing.

Congo red labeling of whole brains of 5xFAD animals

Whole brains were dehydrated with gradual addition of methanol in PBS (50% x1, 80% x1, 100% x2, each for 1 h). Overnight bleaching with 5% hydrogen peroxide in methanol was done at 4°C . Brains were then gradually rehydrated in 100%, 80%, 50% methanol in PBS (1 h for each step, followed by 2 additional washes in PBS). Detergent washing was then performed in PBS with 0.2% Triton X-100 for 2 h, brains were incubated overnight at 37°C in PBS with 0.2% Triton X-100 and 0.3 M glycine, followed by blocking in PBS with 0.2% Triton X-100 and 6% goat serum for 7 days. Following blocking, the tissue was washed for 1 h twice in PBS with 0.2% Tween 20 and 10 $\mu\text{g/mL}$ heparin (PTwH). Next, brains were incubated with 10 μM Congo Red (Sigma, C6277) at 37°C in PTwH for 5 days. After that, brains were washed in PTwH for 2 days with periodic solution changes and gradually dehydrated using 3DISCO clearing as described next.

Clearing of brains using DISCO methods

We followed the 3DISCO and uDISCO passive clearing protocol as described previously. In brief, dissected brains were placed in 5 mL tubes (Eppendorf, 0,030,119.401) and covered with 4.5 mL of clearing solution. All incubation steps were performed in a fume hood with gentle shaking or rotation, with the samples covered with aluminum foil to keep them in dark. To clear the samples using 3DISCO, gradient of tetrahydrofuran (THF) in distilled water (v/v %), 2 h for each step, was used as 50%, 70%, 90%, 100% and overnight 100% THF; after dehydration, the samples were incubated for 45 min in dichloromethane (DCM, Sigma, 270,997), and finally in BABB (benzyl alcohol + benzyl benzoate 1:2, Sigma, 24,122 and W213802) until transparency. Next for uDISCO a gradient of tert-butanol (Sigma, 360,538) in distilled water (v/v %) was used as 50, 70, 90, 100 twice at 32°C for 12 h each step, followed by immersion in DCM for 45 min at room temperature and finally incubated with the refractive index matching solution BABB-D15 containing 15 parts BABB, 1 part diphenyl ether (DPE) (Alfa Aesar, A15791) and 0.4% Vol vitamin E (DL- α -tocopherol, Alfa Aesar, A17039), for at least 6 h at room temperature until achieving transparency.

vDISCO whole-brain passive immunostaining, clearing and imaging

Passive vDISCO was performed on dissected organs as performed by Cai R et al. First, the post-fixed brains were pre-treated with permeabilization solution containing 1.5% goat serum, 0.5% Triton X-100, 0.5 mM of Methyl-beta-cyclodextrin, 0.2% *trans*-1-Acetyl-4-hydroxy-L-proline and 0.05% Sodium Azide 0.1 M for 2 days at 37°C with gentle shaking. Subsequently, the brains were incubated in 4.5 mL of this same permeabilization solution plus the nanobooster Atto647N conjugated anti-GFP (1:600, which is $\sim 5\text{--}8 \mu\text{g}$ of nanobooster in 4.5 mL) for CX3CR1-eGFP and Thy-1-GFPM brains for 12–14 days at 37°C with gentle shaking, then brains were washed for 2 h 3 times and once overnight with the washing solution (1.5% goat serum, 0.5% Triton X-100, 0.05% of sodium azide in 0.1 M PBS) at room temperature and in the end washed for 2 h 4 times with 0.1 M PBS at room temperature. The immunostained brains were cleared with 3DISCO clearing first they were put in the Eppendorf 5 mL tubes and then incubated at room temperature with gentle shaking in 4.5 mL of the following gradient of THF in distilled water (v/v %), 2 h for each step: 50, 70, 90, 100 THF and

overnight 100% THF; after dehydration, the samples were incubated for 45 min in DCM, and finally in BABB until transparency. During all the clearing steps, the tubes were wrapped with aluminum foil to keep them in dark.

vDISCO whole body immuno labeling, clearing and imaging

The detailed protocol of vDISCO was described previously.³⁴ The mouse bodies were placed inside a 300 mL glass chamber (Omnilab, 5,163,279), to be filled with the appropriate solution regarding the protocol to cover the entire body of the animal (~250–300 mL). A transcardial circulator system was established in order to allow peristaltic pumping of the solutions (ISMATEC, REGLO Digital MS-4/8 ISM 834; reference tubing, SC0266), with the pressure being set at 180–230 mmHg (50–60 rpm). The tubing was set to allow pumping of the solutions through the heart (attached to a perfusion needle (Leica, 39,471,024)) into the vasculature with the same entry point used for PBS and PFA perfusion steps described above. The other end of the tube was immersed into the chamber with a loose end to allow suction of the solution into the body. The samples were initially perfused with a decolorization solution (25% of CUBIC reagent 1 (55) which is composed of 25 wt % urea (Carl Roth, 3941.3), 25 wt % N,N,N',N'-tetrakis (2-hydroxypropyl) ethylenediamine (Sigma, 122,262) and 15 wt % Triton X-100 (AppliChem, A4975,1000) in 0.1 M PBS) for 2 days, refreshing the solutions every 12h. Samples were washed with PBS for 3 × 2h. Then, decalcification solution (10 w/v % EDTA in 0.01 PBS, pH~8–9, Carl Roth, 1,702,922,685) was perfused for 2 days followed by half a day with permeabilization solution composed of 0.5% Triton X-100, 1.5% goat serum (GIBCO, 16,210,072), 0.5 mM of Methyl-beta-cyclodextrin (Sigma, 332,615), 0.2% *trans*-1-Acetyl-4-hydroxy-L-proline (Sigma, 441,562), 0.05% sodium azide (Sigma, 71,290) in 0.01 M PBS. The setup was adjusted to initiate the PI labeling and boosting. The free end of the perfusion tube was connected to a 0.22 μm syringe filter (Sartorius, 16,532) and an infrared lamp (Beuer, IL21) was aimed at the chamber to enable the solution's temperature to be around 26–28°C. This setup was then left running for 6 days after the addition of 35 μL of nanobooster (stock concentration 0.5–1 mg/mL) and 290 μL of propidium iodide (stock concentration 1 mg/mL) which was added directly into the refreshed permeabilization solution. Next, the body was placed into a 50 mL tube (Falcon, 352,070), with the same permeabilization and labeling solution, and an extra 5 μL of nanobooster was added. The tube was then put on a shaker at RT for 2 additional days for labeling. Atto647N conjugated anti GFP nanobooster (Chromotek, gba647n-100) and propidium iodide (PI, Sigma, P4864) was used to boost the signal from the LysM-eGFP animals and stain cell nuclei respectively in the study. Then, the animals were placed back into the initial perfusion setup, where washing solution was perfused for 2 × 12h, which was composed of; 1.5% goat serum, 0.5% Triton X-100, 0.05% of sodium azide in 0.1 M PBS. 0.1 M PBS was used to wash the sample 3 × 2h. 3DISCO protocol was applied for whole body clearing. The animals were demounted from the perfusion system but kept in glass chambers and placed on top of shakers (IKA, 2D digital) at room temperature inside a fume hood. Glass chambers were sealed with parafilm and covered with aluminum foil along with the 3DISCO application. For dehydration, sequential immersion of tetrahydrofuran (THF) (Sigma, 186,562) (50 vol % THF, 70 vol % THF, 80 vol % THF, 100 vol % THF and again 100 vol % THF) was applied every 12 h. Then 3 h of dichloromethane (DCM) (Sigma, 270,997) immersion for delipidation was followed by indefinite immersion in BABB (benzyl alcohol + benzyl benzoate 1:2, Sigma, 24,122 and W213802) solution for refractive index matching.

SHANEL sample preparation and clearing

Archived human samples were obtained in PFA which were stored for a long period of time (>5 years) at 4°C and subjected to our previously published SHANEL clearing protocol with some modifications.⁴ Briefly, samples were dehydrated with EtOH/dH₂O series at RT: 50%, 70%, 100% for 1 h for each step, then incubated with 10 mL DCM/MetOH (2:1 v/v) (freshly prepared) for 6h at RT followed by rehydration with EtOH/dH₂O series at RT: 100%, 70%, 50%, dH₂O for 1 h each step then incubated with 0.5M acetic acid (30 mL/L) at RT for 2 h, then wash with dH₂O twice for 15 min and then incubated with 4M guanidine hydrochloride (382.12 g/L), 0.05M sodium acetate (4.1 g/L), 2% v/v Triton X-100 in dH₂O, (measure pH: 6.0) at RT for 2 h, then wash with dH₂O twice for 15 min each and wash with PBS twice for 15 min each. Afterward samples were incubated with 10% CHAPS, 25% N-Methyl diethanolamine in dH₂O at 37°C for 4 h and then washed with dH₂O twice for 15 min each. Since we did not perform any deep antibody labeling in these samples, we started clearing these samples without prior blocking or antibody labeling steps. Clearing was done with THF in water with dilutions (v/v %) of 50%, 70%, 90%, 100%, 1h each, 100% overnight, DCM 45 min and incubated in BABB until the samples were transparent.

Behavioral assessment

Barnes maze

Briefly, a maze consisting of a surface bright circular platform with an escape black box can be recessed and located at the bottom of one of the 20 holes. Visual shapes were placed on 3 walls of the room as cues. For all trials, mice were placed in a cylinder black start chamber in the center of the maze for 10 s. After the chamber lifted and the test started, mice were given 3 min to locate and enter the target box during the spatial acquisition time. For a period of 4 days, 4 trials were given per day with an inter-trial of 15 min. The trial ended when the mouse entered the escape box or after 3 min had elapsed. Mice were allowed to remain in the escape box for 1 min. A system (Ethovision XT) was used to continually track and record the movement of the mice. Escape latency was measured as the time taken for the mouse to enter the box.

Assessment of motor function

The mice were given 3 trials training per day for 3 days to walk along a 1 cm diameter and 100 cm long wood beam with a goal box on the end of the beam before mild TBI. The beam was placed 1 m above ground. The latency that it takes walking to cross the beam after 8 weeks from mild TBI were recorded. Mice that were unable to cross the beam were removed in the training.

Immunofluorescence and confocal microscopy

Briefly, mice were sacrificed after 8 weeks of injury or at six weeks of age following transcardial perfusion with PBS and with 4% cold PFA. Brains were post-fixed in 4% PFA at 4°C overnight. Either frozen sections or cleared-rehydrated frozen sections were treated with 0.2% Triton X-100 in PBS for 15 min, blocked for 1 h at room temperature with 10% serum in PBST. Then incubation with primary antibodies Iba1 (1:1000, Wako, 019-19741), Stathmin 1 (1:300, Novus, NBP1-76798), Neurocan (1:300, abcam, ab31979), S100a11 (1:300, R&D, MAB5167), Thop1 (1:300, Novus, NB400-146), MOAB2 (1:1000, Novus, NBP2-13075), at 4°C for overnight and Alexa conjugated secondary antibodies (1:1000, Goat anti-rabbit IgG Alexa Fluor 647, Invitrogen, A21245; Goat anti-Mouse IgG Alexa Fluor 488, A11029; Goat anti-Mouse IgG Alexa Fluor 594, A11032; Goat anti-Rat IgG Alexa Fluor 594, A11007; Goat anti-Rat IgG Alexa Fluor 488, A11006) were incubated for 1 h at room temperature. Slices were mounted after being stained with Hoechst 33,342 (Invitrogen). Images were acquired with 10x, 40x, and 63x objective of confocal microscope (ZEISS LSM880).

Light-sheet microscopy and image processing

Single plane illuminated (light-sheet) image stacks were acquired using an Ultramicroscope II (LaVision BioTec) and UltraMicroscope Blaze (Miltényi Biotec), featuring an axial resolution of 4 μm with following filter sets: ex 470/40 nm, em 535/50 nm; ex 545/25 nm, em 605/70 nm; ex 640/40 nm, em 690/50 nm. Whole brains were imaged individually using high magnification objectives: 4x objective (Olympus XLFLUOR 4x corrected/0.28 NA [WD = 10 mm]), LaVision BioTec MI PLAN 12x objective (0.53 NA [WD 10 = mm]) coupled to an Olympus revolving zoom body unit (U-TVCAC) kept at 1x. High magnification tile scans were acquired using 20-35% overlap and the light-sheet width was reduced to obtain maximum illumination in the field. Processing, data analysis, 3D rendering and video generation for the rest of the data were done on an HP workstation Z840, with 8 core Xeon processor, 196 GB RAM, and Nvidia Quadro k5000 graphics card and HP workstation Z840 dual Xeon 256 GB DDR4 RAM, nVidia Quadro M5000 8GB graphic card. We used Imaris (Bitplane), Fiji (ImageJ2), Vision 4D (Arivis) and syGlass (for 3D and 2D image visualization). Tile scans were stitched by Fiji's stitching plugin49.

Registration of light-sheet and LCM images to correlate probe selection

In order to map the proteomic samples to the whole brain light-sheet imaging we developed a registration protocol. The LCM method is acquired in order to select the ROI to be cut from the sample of brain tissue. The registration of light-sheet and LCM images is very challenging because it is a multimodal registration problem and the imaged tissue undergoes physical changes when the re-clearing process is applied after the light-sheet imaging, introducing scale differences and sometimes even damaged tissue. Moreover, the tissue contrast and lighting distribution are different.

For the purpose of registering the images, we acquired consecutive 2D LCM slices ($0.65 \times 0.65 \mu\text{m}^2$, slice thickness 12 μm) which correspond to the 3D light-sheet volume ($1.63 \times 1.63 \times 4 \mu\text{m}^3$). We down sampled all images to the largest dimension to achieve an isotropic resolution of 12 μm . We experimented with a multitude of registration steps, such as: 3D-3D volume registration, 2D-2D slice registration, various transformations (rigid, affine, BSpline), edge extraction, binary thresholding, normalization strategies, and similarity metrics. We found the best performance for the following protocol using elastix:

- 1) Pre-processing: Both LCM and light-sheet images were clipped to the relevant contrast ranges and normalized to the [0, 255] range. Additionally, the LCM slices undergo histogram equalization to mitigate the severe lighting differences, 2) first, a single LCM slice is rigidly registered to each 3D light-sheet slice 3) next, we calculate different image similarity scores between the registered LCM slice and its corresponding LS slice. We choose the most similar slices as an initial match in z-Dimension 4) then, we create a 3D LCM volume by padding the single LCM slice and then do a full 3D affine registration to the 3D light-sheet volume to account for scaling differences. These four steps lead to our registration result, where the two red boxes indicate a potential cut region of interest in the LCM image and its corresponding spatial location in the light-sheet image. We find that the registration of the individual LCM slices is very successful, whereby the equalization plays a crucial role. The rigid registration is also able to find a good initial-ization for the affine registration in the next step. The third step poses harder challenges, as the differences between the LCM and light-sheet images outlined above persist. For example, we observe that the brightness of the light-sheet image increases radially outwards, whereas in the LCM the light is more region-dependent. Furthermore, in the LCM images various regions are so hypo-intense, that even the extraction of low-level features such as edges is not very informative for the registration. These challenges particularly impact the registration of the LCM volume in the z direction. We are convinced that this registration problem is a highly non-trivial task and believe that future research will be of high relevance for the community beyond our application.

Optimization of cleared tissue for cryopreservation and sectioning

After acquiring the whole brain images from CX3CR1-eGFP, 5xFAD, C57BL/6J mice the brains were further optimized for cryopreservation and sectioning. The course of tissue clearing and imaging in BABB makes the tissue brittle and hard to process further. To solve this, we rehydrated the samples with the respective clearing solutions to be able to process samples for cryosectioning.

Thereafter, samples were washed with PBS twice for 15 min each and cryopreserved overnight with 30% sucrose solution in 4°C. To avoid any ice crystals formation, samples were further embedded in Optimal cutting temperature compound (OCT compound) under the chilled isopentane container placed on dry ice. Samples were stored in –80°C until cryosectioning.

Laser-capture microdissection

For the microdissection of cells and plaques, we used both the PALM Micro-Beam system (Zeiss) and Leica LMD 7000 (Leica). PALM Micro-Beam uses a focused laser beam to cut out and isolate the selected specimen without contact. The laser catapult quickly isolates the region of interest and uncontaminated in the adhesive cap mounted in the RoboMover upwards. The Leica system projects the samples downwards. Briefly, in case of the PALM system, after cryosectioning, sections were mounted on the polyethylene naphthalate (PEN, Zeiss) slides and were either stored at –80°C in 50 mL falcon tubes filled with molecular sieves (Sigma-Aldrich) or processed further for serial dehydration with ethanol and air dried for 15 min under the hood. Cells in the optic tract from mTBI/Sham brains and amyloid-beta plaques from the 5xFAD and from respective WT brain regions were micro-dissected by laser pressure catapulting (LPC) UV LCM system (Palm Zeiss Microlaser Technologies, Munich, Germany) consisting of an inverted microscope with a motorized stage, an UV laser and an X-Cite 120 fluorescence illuminator (EXFO). The microdissection process was visualized with an AxioCam ICc camera coupled to a computer and was controlled by Palm RoboSoftware (Zeiss, Germany). An area of approximately 200 × 200 μm (corresponding to 40–60 cells) were cut by laser using a 20× objective (LD Plan-Neofluar 20×/0.4 corr M27) and catapulted against gravity into the adhesive cap. Tissues were quickly lysed in 20 μL of lysis buffer, spun down and kept in dry ice or stored in –80°C. To avoid any uncertainties in capturing ROI, each time after catapulting as well as after lysing and spun down, the cap was examined under the camera.

Automated robotic proteomic probe extraction from whole body

The strategy applied in this study was image guided extraction of targeted samples in the bone marrow of scapula and cranium on whole mouse body with a precise robotic biopsy solution. The imaging takes place under the Ultramicroscope Blaze manufactured by Miltenyi Biotec. The robotic arm Meca500 R3 manufactured by Mecademic Robotics is used to control the motion of the needle sets to extract multiple targets. During the imaging, the embedded whole mouse body was placed on a bed designed for this study that holds the sample stable under the load applied by the needle. The Meca500 was mounted above the microscope to utilize the slim gap between the submerged lens and the walls of the sample bath for the operation on the mouse during live imaging. The extraction was conducted by using two sizes of biopsy needles with stylets sealing the shaft of the needle to prevent unwanted tissue contamination while approaching the target. The larger diameter needle was fixed on the robotic arm with a holder designed and manufactured to ensure the access of the finer needle to the target with precision.

Precision and accuracy of sampling

The most important problem to overcome in the deep tissue sampling in a whole mouse body is to achieve the required precision and accuracy of the sampling needle tip. Since the operation happens in toughened, inhomogeneous multilayer tissue, the forces acting on the needle and the tissue during the penetration are highly fluctuating and axially asymmetric. The borders of two different types of tissues e.g., bone and muscle, tend to deflect the needle in the direction of the muscle. These forces result in bending of the needle which leads to inaccuracies when approaching the target. Since it is problematic to move the needle sideways or rotate it inside the tissue due to high traction, it is complicated to compensate for the inaccuracy after the needle has penetrated into the tissue.

Providing precision and accuracy to the operation requires every component on the load path to remain as rigid as possible. The translational stage of the microscope is fixed on the main structure and holds the mouse bed, the mouse bed supports the agarose embedding around the mouse and the agarose embedding supports the whole mouse body including the extremities and inner organs. On the other end of the setup the robotic arm was fixed on the main structure. The needle holder is screwed on the last actuator of the robot arm. The needle is fixed on the needle holder with a screw. The load transfer mechanism can be reduced to some basic components to model the bending behavior of the structure and calculate the deflections. The total deflection of all these components under load is optimized to provide an accurate positioning of the needle deep in the tissue.

Needle gauge

The needle gauge plays a key role in the total deflection. The needle can be considered as a cylindrical cantilever beam and the maximum deflection on the needle caused by a concentrated load at the tip is defined by the formula:

$$\delta_{max} = \frac{Pl^3}{3EI}$$

In this equation the maximum deflection δ_{max} is proportional to the force applied on the tip P , proportional to the cube of the length of the needle l and inversely proportional to the Young's modulus of the needle's material E and the static moment of inertia I .

The needle's deflection in the deep tissue is not only caused by the concentrated force applied on the piercing tip, but also by the distributed load on the needle, for which case the deflection at the tip is defined by the formula: $\delta_{max} = \frac{\omega l^4}{8EI}$.

In this case the maximum deflection δ_{max} is proportional to the distributed load applied on the needle ω , proportional to the 4th power of the length of the needle l and inversely proportional to the Young's modulus of the needle's material E and the static moment of inertia I . The static moment of inertia I can be calculated as:

$$I_y = I_z = \frac{\pi(R^4 - r^4)}{4}$$

For both of these equations the static moment of inertia I is proportional to the difference of the 4th power of the outer R and inner r radii of the needles. These calculations suggest a 22G needle would deflect around 9 times further away from target in comparison to an 18G needle.

Although a larger needle is more accurate meeting the target due to lower deflection, there are also disadvantages such as collecting a larger sample including unwanted neighboring tissue. Furthermore, since the penetration area is larger with a larger needle, the force required to achieve the penetration stress on the tissue is also larger. Occasionally, it becomes impossible to apply the necessary force for penetration, since the tissue cannot support such loads and the harder bone tissue gets pushed into the softer muscle tissue. We found that the optimum solution to this problem was using two needles in combination. The procedure applied in this study was to extract bone marrow with 18G blunt tip biopsy needle A-MAX PAED and 22G Chiba biopsy needle. Both of these needles include a stylet to block the hollow shaft of the needle until the biopsy target is reached. Initially the 18G needle was fixed on the needle holder on the Meca500 and the coordinates of the tip of the needle are calibrated under the microscope. The needle is advanced with the Meca500 axially to the coordinates where the stylet is about to touch the target. Then the 18G stylet is removed to create an open channel for the 22G needle to move until the target without any resistance or deflection. As soon as the 22G needle reaches the target the 22G stylet is removed from the needle and the target is sucked in to the needle's shaft with the slight vacuum supplied by a syringe and the chopping motion of the beveled needle tip around the target. When the target's acquisition is confirmed observing the light sheet image, the needle is retracted without stopping or increasing the vacuum applied by the syringe and the sample is deployed into a low binding 0.5 mL Eppendorf tube with some extra ECi (ethyl-cinnamate) to make sure any remaining pieces of the sample in the needle is flushed before the next target.

Specimen holder and needle holder strategy

During the imaging process the sample and the lens are submerged into an imaging solution with a refractive index of 1.56. The common options for this medium are mostly ECi or benzyl benzoate and benzyl alcohol (BABB) solution with a 2:1 ratio. The mouse holder and needle holder are manufactured using the clear resin on a Form3 manufactured by Formlabs. This process provides agile prototype iterations but the manufactured parts lose their integrity and start falling apart upon contact with BABB. Therefore, these experiments are conducted under ECi. The mouse bed and the needle holder are modeled using finite elements method (FEM) to simulate their behavior under loading using Ansys Academic Research Mechanical 2022 R2. Using the stresses and deflections calculated from the static FEM analyses, an iterative method was employed to optimize the structures of the mouse bed and the needle holder. The mass of the mouse bed was reduced to around 80 g and the needle tip to around 20 g, while the simulated total deflection of both pieces combined was reduced to less than a millimeter from an initial total deflection around 7mm under extreme load conditions such as 40 N axial load applied on the needle and the same amplitude applied on the mouse bed in the direction of needle's approach.

Embedding of the whole mouse body

Although the whole mouse body is cleared and fixed, it still deflects far enough for the needle to miss the target. Especially when the target is in a bone, the forces required for penetration go beyond 10N with the 18G needle. Embedding the body with a gel or resin is crucial to limit the deformation of the mouse body. The uneven structure of the internal organs, gaps in the chest cavity and curved outer surfaces create incalculable sources for tissue and needle deflection. To stabilize the cleared mouse bodies during robotic tissue extraction, they had to be embedded in a block of agarose. To do this, we prepared a 2% (w/v) solution of agarose by dissolving the agarose powder in deionized water. This mixture was heated in a microwave until the agarose had completely dissolved. Then, the mixture was allowed to cool until it had reached a temperature of about 50–60°C. This cooled agarose solution was then poured onto the sample, and it was left to cool until it had completely solidified. After it had solidified, excess parts of agarose around the samples were carefully trimmed away using a sharp scalpel.

To clear the agarose and prepare it for light sheet imaging, the sample was dehydrated in a serial dilution of tetrahydrofuran (ROTISOLV, Carl Roth). The dilutions used were as follows: (v/v) 20%, 30%, 50%, 70%, 90%, 100% -2x. After the sample had completely dehydrated, it was immersed in a solution of BABB which is a mixture of benzyl alcohol and benzyl benzoate to complete the clearing process. The sample was immersed in these solutions for a minimum of 24 h at every stage.

Manipulation system

A common solution for micrometer accurate targeting is a micromanipulator but in this study the target was located deep in the hardened and tough tissue. Considering the force required in case of a bone penetration is in the range of 10 N and micromanipulators operate in the range of hundreds of mN, the standard solution would not suffice for this specific problem.

For the image guided sample extraction, a robot arm with harmonic drives was selected. The advantages in comparison to a micro-manipulator or a piezo electric stage system is the level of applicable force without compromising accuracy. The Meca500 can apply a force of 110N and still remain within a precision tolerance of 5 μm . Being able to control such a force with high precision in a large working envelope with 260mm reach in 6 degrees of freedom, provided us the freedom to conduct experiments with various assembly positions, tool designs, needle dimensions delivering repeatable results.

The system is controlled via the programming and simulation software for industrial robots RoboDK. The 3D models of the optical table, microscope and other structural parts are assembled corresponding to their real locations in a 3D CAD software and exported as STEP file to the RoboDK environment. From that point on Meca500 is controlled over TCP/IP socket communication with ASCII commands. Having the whole environment in the control software, paths are calculated in segments to avoid any collision. Any misalignment with the needle tip in real world and computer model is also calibrated in the software before sample extraction.

Optimization of DISCO cleared sample preparation for mass spectrometry analysis

Several conditions and combinations of solubilizing agents for the isolation of proteins from tissue cleared mouse brain, heart, and lung samples were initially evaluated for protein extraction efficiency, peptide recovery, and qualitative and quantitative reproducibility keeping fresh or PFA-fixed as reference. Our goal was to establish a workflow that recovers proteomes that are as similar as possible to non-cleared tissue and is universal for all tissue clearing techniques.

Cleared organs or cryosections were removed from the refractive index matching solution BABB and washed five times with 1x PBS solution. The organ was then flash-frozen and pulverized in a Covaris CP02. Afterward, the samples were resuspended in different protein solubilizing solutions (6% SDS 500 mM TrisHCl, pH 8.5 (SDS buffer); 2% Sodium deoxycholate, 100 mM TrisHCl pH 8.5, 10 mM Tris-(2-carboxyethyl)-phosphine (TCEP), 40 mM Chloroacetamide (SDC buffer); 50% Trifluoroethanol, 100 mM TrisHCl, pH 8.5 (TFE buffer), followed by protein extraction at 95°C, 1,000rpm for 45 min. Then the samples were subjected to sonication (Branson) at maximum frequency for 30 cycles at 50% output, followed by another heating step at 95°C, 1,000 rpm for 45 min. From here on, processing steps diverged for each protocol.

Proteins solubilized in the SDS buffer were precipitated with ice-cold acetone at 80% v/v ratio overnight at –80°C, followed by centrifugation at max. g for 15 min at 4°C. The supernatant was removed, the pellet was washed with 5 mL ice-cold 80% v/v Acetone/ddH₂O, followed by 30 min precipitation on dry ice. The acetone wash steps were repeated two times for a total of three washes. Proteins solubilized in the TFE buffer, were subjected to solvent evaporation in a SpeedVac at 45°C until dryness before further processing.

In case of SDS-SDC or TFE-SDC protocol, in which SDS or TFE protein extraction was coupled to an SDC-based protein digestion, SDS- or TFE-solubilized proteins were resuspended in 1mL of SDC buffer and heated to 95 °C at 1,000 rpm for 10 min to denature proteins, reduce cysteine bridges and alkylate free cysteine residues. Afterward, samples were sonicated for 15 cycles each 30 s at max power in a Bioruptor, followed by another heating step for 10 min at 95°C, 1,000 rpm in a Thermoshaker.

SDC-only, SDS-SDC, TFE-SDC solubilized protein solutions were cooled down to room temperature, diluted 1:1 with 100 mM TrisHCl, pH 8.5, followed by protein concentration estimation by Nanodrop. Extracted and solubilized proteins were digested overnight at 37°C and 1,000 rpm, with trypsin and LysC at a protein to enzyme w/w ratio of 1:50. Next day, trypsin and LysC were added again at a protein to enzyme w/w ratio of 1:50 and proteins were digested further for 4 h at 37°C, 1,000 rpm. Resulting peptides were acidified with 1% TFA 99% Isopropanol in a 1:1 ratio and vortexed, followed by centrifugation at 22,000 xg RT to pellet residual particles. The supernatant was transferred into a fresh tube and subjected to StageTip clean-up via SDB-RPS. 20 μg of peptides were loaded on two 14-gauge stage-tip plugs. Peptides were washed twice with 200 μL 1% TFA 99% ddH₂O followed by 200 μL 1% TFA 99% isopropanol in an in-house-made StageTip centrifuge at 2,000 xg. Peptides were eluted with 100 μL of 5% Ammonia, 80% ACN into PCR tubes and dried at 45°C in a SpeedVac centrifuge (Eppendorf, Concentrator plus). Peptides were resuspended in 0.1% TFA, 2% ACN, 97.9% ddH₂O.

After evaluation of protein extraction efficiency, all sample preparation for Fresh, PFA-fixed, uDISCO-, 3DISCO-, SHANEL-cleared tissue was performed following the SDS-SDC protocol. For LCM sample preparation, LCM samples were caught on PCR tubes with adhesive caps and successful isolation was verified by visual inspection. 20 μL of SDS-buffer was added to each tube. The tube was closed and vortex for 30 s, followed by centrifugation for 5 min in a table-top centrifuge to ‘catch’ the LCM sample in the protein solubilization buffer, which was confirmed afterward by visual inspection. Sample preparation was performed as described for the SDS-SDC protocol, except for the following modifications: No shaking during cooking steps; Instead of a Branson sonicator, a Bioruptor was used for each sonication step; No Covaris CP02 was used for crushing the sample; Acetone precipitation was performed at 100 μL total volume; SDC resuspension and protein digestion was performed in a 20 μL volume.

High-pH reversed-phase fractionation

To generate a deep library of experiment-specific precursors, peptides were fractionated at pH 10 with the spider-fractionator.⁷⁹ 50 μg of purified peptides were separated on a 30 cm C₁₈ column in 96 min and concatenated into 16 or 24 fractions with 2 min exit valve switches. Peptide fractions were dried in a SpeedVac and reconstituted in 2% ACN, 0.1% TFA, 97.9% ddH₂O for LC-MS analysis.

Liquid chromatography and mass spectrometry (LC-MS)

LC-MS was performed on an EASY nanoLC 1200 (Thermo Fisher Scientific) coupled online either to a quadrupole Orbitrap mass spectrometer (Q Exactive HFX, Thermo Fisher Scientific), or a trapped ion mobility spectrometry quadrupole time-of-flight mass spectrometer (timsTOF Pro, Bruker Daltonik GmbH, Germany) via a nano-electrospray ion source (Captive spray, Bruker Daltonik GmbH). Peptides were loaded on a 50 cm in-house packed HPLC-column (75 μ m inner diameter packed with 1.9 μ m ReproSil-Pur C18-AQ silica beads, Dr. Maisch GmbH, Germany). Sample analytes were either separated using a linear 100min gradient from 5 to 30% B in 80 min followed by an increase to 60% for 4 min, and by a 4 min wash at 95%, a decrease to 5% B for 4 min, and a re-equilibration step at 5% B for 4 min, or separated on a linear 120 min gradient from 5 to 30% B in 90 min followed by an increase to 60% for 10 min, and by a 5 min wash at 95%, a decrease to 5% B for 5 min, and a re-equilibration step at 5% B for 5 min (Buffer A: 0.1% Formic Acid, 99.9% ddH₂O; Buffer B: 0.1% Formic Acid, 80% CAN, 19.9% ddH₂O). Peptides derived from LCM and matching libraries were separated using a linear 70 min gradient from 3 to 30% B in 45 min followed by an increase to 60% for 5 min, an increase to 95% in 5min, followed by 5 min at 95% B, a decrease to 5% B for 5 min, and an equilibration step at 5% B for 5 min. Flow-rates were constant at 300 nL/min. The column temperature was kept at 60°C by an in-house manufactured oven.

Mass spectrometry analysis for the evaluation of sample preparation on a Q Exactive HFX was performed in data dependent scan mode. For full proteome measurements, MS1 spectra were acquired at 60,000 resolution and an m/z range of 300–1,650 with an automatic gain control (AGC) target of 3E6 ions and a maximum injection time of 20 ms. The top 15 most intense ions with a charge of two to eight from each MS1 scan were isolated with a width of 1.4 Th, followed by higher-energy collisional dissociation (HCD) with a normalized collision energy of 27% and a scan range of 200–2,000 m/z. MS/MS spectra were acquired at 15,000 resolution with an AGC target of 1E5, a minimum AGC target of 2.9E3, and a maximum injection time of 28 ms. Dynamic exclusion of precursors was set to 30 s.

Deep proteomes and comparisons of clearing conditions with the SDS-SDC protocol were acquired on a standard timsTOF Pro in a data-dependent PASEF mode with 1 MS1 survey TIMS-MS and 10 PASEF MS/MS scans per acquisition cycle. Ion accumulation and ramp time in the dual TIMS analyzer was set to 100 ms each and we analyzed the ion mobility range from $1/K_0 = 1.6 \text{ Vs cm}^{-2}$ to 0.6 Vs cm^{-2} . Precursor ions for MS/MS analysis were isolated with a 2 Th window for $m/z < 700$ and 3 Th for $m/z > 700$ in a total m/z range of 100–1,700 by synchronizing quadrupole switching events with the precursor elution profile from the TIMS device. The collision energy was lowered linearly as a function of increasing mobility starting from 59 eV at $1/K_0 = 1.6 \text{ Vs cm}^{-2}$ to 20 eV at $1/K_0 = 0.6 \text{ Vs cm}^{-2}$. Singly charged precursor ions were excluded with a polygon filter (otof control, Bruker Daltonik GmbH). Precursors for MS/MS were picked at an intensity threshold of 2,500 a.u. and re-sequenced until reaching a 'target value' of 20,000 a.u taking into account a dynamic exclusion of 40 s elution.

Peptides derived from LCM samples were acquired on a timsTOF Pro modified for highest ion transmission and sensitivity, as described in Brunner et al., in a data-dependent or data independent acquisition PASEF mode.¹⁰ In DDA, 1 MS1 survey TIMS-MS and 5 PASEF MS/MS scans represents one acquisition cycle. Ion accumulation and ramp time in the dual TIMS analyzer was set to 50 ms each and we analyzed the ion mobility range from $1/K_0 = 1.6 \text{ Vs cm}^{-2}$ to 0.6 Vs cm^{-2} . Precursor ions for MS/MS analysis were isolated with a 2 Th window for $m/z < 700$ and 3 Th for $m/z > 700$ in a total m/z range of 100–1,700 by synchronizing quadrupole switching events with the precursor elution profile from the TIMS device. The collision energy was lowered linearly as a function of increasing mobility starting from 59 eV at $1/K_0 = 1.6 \text{ Vs cm}^{-2}$ to 20 eV at $1/K_0 = 0.6 \text{ Vs cm}^{-2}$. Singly charged precursor ions were excluded with a polygon filter (otof control, Bruker Daltonik GmbH). Precursors for MS/MS were picked at an intensity threshold of 1,500 a.u. and re-sequenced until reaching a 'target value' of 20,000 a.u taking into account a dynamic exclusion of 40 s elution. For DIA analysis, we made use of the correlation of ion mobility (IM) with m/z and synchronized the elution of precursors from each IM scan with the quadrupole isolation window. We used the short-gradient diaPASEF method as described in Meier et al.⁸⁰ but performed five consecutive diaPASEF cycles before the next MS1 scan. The collision energy was ramped linearly as a function of the IM from 59 eV at $1/K_0 = 1.6 \text{ Vs cm}^{-2}$ to 20 eV at $1/K_0 = 0.6 \text{ Vs cm}^{-2}$.

QUANTIFICATION AND STATISTICAL ANALYSIS

ClearMap quantification

To quantify microglia distribution in whole brains of mTBI and sham animals, we used ClearMap. As the script was originally developed for quantification of the cFos⁺ cells, to comply with the offered method, we performed the following pre-processing steps on our microglia data using Fiji before ClearMap:

1. Background equalization to homogenize intensity distribution and appearance of the microglia cells over different regions of the brain, using pseudo-flat-field correction function from Bio-Voxxel toolbox.
2. Convolved background removal, to remove all particles bigger than relevant cells. This was done with the median option in the Bio-Voxxel toolbox.
3. Two-dimensional median filter to remove remaining noise after background removal. The filter radius was chosen to ensure the removal of all particles smaller than microglia cells.

4. Unshapen mask to amplify the high-frequency components of a signal and increase overall accuracy of the cell detection algorithm of ClearMap.

After pre-processing, ClearMap was applied by following the original publication and considering the threshold levels that we obtained from the pre-processing steps. As soon as the quantification was completed, the data was exported as an Excel file for further analysis.

Deep learning analyses

The segmentation of the stained A β plaques represents a key step toward a reliable quantification thereof. We develop a customized, three-dimensional deep learning approach to optimize segmentation of A β plaques in the whole brains of 5xFAD animals. Our network architecture is inspired by the well-established U-Net architecture. Our loss function is an equally weighted combination of Dice and binary cross entropy loss. We use the Ranger optimizer, which combines Rectified Adam, gradient centralization and LookAhead. Annotation of our dataset was performed in Fiji and double checked by multiple experts.⁸¹ Our dataset consists of 98 image volumes (300 \times 300 \times 300 voxel) from one Alzheimer brain; where 34 vol include A β plaques, and 64 vol do not contain any plaques. An ensemble of experts including the scientist who imaged the brains labeled all images. We randomly sampled our training set of 85 vol (21 with AD plaques, 64 without AD plaques), our validation set of seven volumes and our separate test set of six volumes. During training and testing we applied suitable data augmentation protocols. In order to assess the quality of our segmentation we calculate a wide range of voxel-wise and A β plaque wise segmentation metrics. Based on the reliable segmentation of individual A β plaques we continued toward a statistical evaluation of the number and size of A β plaques per brain region. First, we registered all of our brains to the Allen brain Atlas, enabling a single voxel assignment to brain structures. For whole brain segmentation we extracted the single connected components using cc3d,⁸² which represent our individual segmented A β plaques and calculate their total size in voxels as a biomarker. Using this registration and biomarker, we calculated per brain region statistics for the presence and size of A β plaques across the whole brain.

Proteomics data processing

Raw files were either searched against the mouse Uniprot databases (UP00000589_10090.fa, UP00000589_10090_additional.fa) or human Uniprot databases (UP000005640_9606.fa, UP000005640_9606_additional.fa). For DDA raw file analysis, we used the MaxQuant version 1.6.7.0 which extracts features from four-dimensional isotope patterns and associated MS/MS spectra. False-discovery rates were controlled at 1% both on peptide spectral match (PSM) and protein level. Peptides with a minimum length of seven amino acids were considered for the search including N-terminal acetylation and methionine oxidation as variable modifications and cysteine carbamidomethylation as fixed modification, while limiting the maximum peptide mass to 4.600 Da. Enzyme specificity was set to trypsin cleaving c-terminal to arginine and lysine. A maximum of two missed cleavages were allowed. Maximum precursor tolerance in the first search and fragment ion mass tolerance were searched as default for TIMS-DDA data. Main search tolerance was set to 20 ppm. The median absolute mass deviation for the dataset was 1.57 ppm for precursors. Peptide identifications by MS/MS were transferred by matching four-dimensional isotope patterns between the runs with a 0.7 min retention-time match window and a 0.05 1/ K_0 ion mobility window. Label-free quantification was performed with the MaxLFQ algorithm, and a minimum ratio count of 1.⁸³ For DIA data analysis of the 5xFAD samples isolated from different brain regions, a hybrid library containing all single-shot DIA files and region-specific libraries (16 fractions each) were created using the Spectronaut software suite (version 14.10.201222.47784; Biognosys AG, Schlieren, Switzerland).⁸⁴ All files were searched against the mouse Uniprot databases (UP00000589_10090.fa, UP00000589_10090_additional.fa) of canonical and isoform sequences. For DIA single-shot analysis, a minimum of three fragments per peptide, and a maximum of six fragments were included for data extraction. Searches used protein N-terminal acetylation and methionine oxidation as variable modifications. Protein intensities were normalized using the “Local Normalization” (Q-value = 0.2) algorithm based on a local regression model.⁸⁵ A protein and precursor FDR of 1% was used. Default settings were used for other parameters. Within our regional brain tissue FAD comparison, after filtering and before performing statistical analysis, our data were filtered for at least 3,500 protein identifications per samples and at least 50% data completeness per protein. This resulted in a total of 4,296 protein identifications across 60 samples at a data completeness of above 95%. For downstream analysis, the 5% missing values were imputed from a downshifted normal distribution. For DIA analysis of human heart samples, library free approach was used and the data was analyzed using DIA-NN (Version 1.).⁸⁶

Proteomics downstream data analysis

Proteomics data analysis was performed in the Perseus environment (version 1.6.7.0),⁸⁷ Prism (GraphPad Software, version 8.2.1). MaxQuant output tables were filtered for ‘Reverse’, ‘Only identified by site modification’, and ‘Potential contaminants’ before further processing. Protein and peptide identifications were reported after filtering as described above. Proteome correlations across technical/analytical/biological replicates were performed after log₁₀-transformation. Coefficients of variation (CVs) were calculated across the full dataset or within experimental groups on raw intensity levels for shared observations of more than one. Hierarchical clustering was performed in Perseus with default parameters and Pearson correlation as distance parameters. Before DE analysis, data were filtered for at least two observations in one group to be compared, followed by log₂-transformation and imputation from a normal distribution modeled as the dataset with a downshift of 1.8 standard deviations and a width of 0.3 standard deviations. Deep

proteomes of biological replicates from fresh or vDISCO cleared tissue were tested for differences by a two-sided t-test. False-discovery rate control due to multiple hypothesis testing was performed by a permutation-based model and SAM-statistic with an S_0 -parameter of 0.2 and an FDR of 0.01. Ontologies for cellular compartment assignment and keywords was performed with the mainAnnot.Mus_musculus.txt.gz followed by \log_2 -fold difference frequency counts for the terms 'Extracellular space', 'Blood micro-particle', 'Neurodegeneration', 'Aging', 'Neurogenesis', 'Receptor', 'Virus-Host', 'Immunity', 'Wound healing' and 'Cell migration'. 1D enrichment analysis was performed on the two-sided t-test difference and only enriched terms with a size of larger than ten were displayed in the comparison of fresh versus vDISCO deep proteomes. CVs rank plots were calculated within each of the deep proteome groups and plotted against the median abundance of each protein within each group after \log_{10} -transformation.

For the calculation of systematic ontology-related protein mass shifts, total protein copy number estimations of the deep fresh and vDISCO cleared proteomes of biological replicates were calculated using the Perseus plugin 'Proteomic ruler'.⁸⁸ Protein copy numbers were calculated with the following settings: Averaging mode: 'All columns separately', Molecular masses: 'Molecular weight [kDa]', Scaling mode: 'Histone proteomic ruler', Ploidy: '2', Total cellular protein concentration: '200 g/L'. Proteins were annotated with regards to their cellular compartment by gene ontology from the mainAnnot.mus_musculus.txt.gz. For protein mass estimates, we multiplied the resulting protein copy number by its protein mass for each conditional replicate and summed up all protein masses to obtain the total protein mass for each representative proteome reflecting 100% of the protein mass. To calculate the subcellular protein mass contribution, we calculated the protein mass proportion for the GOCC terms related to the cytoskeleton: 'Actin filament', 'Intermediate filament', 'Centrosome', 'Microtubule'; Membranes: 'Cytoplasm', 'Plasma membrane', 'Membrane'; Organelles: 'Mitochondrion', 'Nucleus', 'ER', 'Golgi apparatus'. For calculating the organellar change between the respective Fresh and vDISCO sub-proteomes, individual protein mass contributions were normalized by its total proteome mass first, followed by ratio calculation to obtain the percentage shift of protein mass between Fresh and vDISCO brains.

For PCA of both LCM applications (mTBI and FAD), data were grouped according to their condition, filtered for at least 760 or 900 proteins for the FAD or mTBI experiment respectively and at least 2 observations within one of the two conditions, column-wise median normalized, and missing values were imputed from a normal distribution with a width of 0.3 standard deviations that was down-shifted by 1.8 standard deviations. DE analysis for the FAD and mTBI experiment was performed by two-sided Welch's t-test on LFQ or IBAQ data respectively. False-discovery rate control due to multiple hypothesis testing was performed by a permutation-based model and SAM-statistic with an S_0 -parameter of 0 or 0.2 and an FDR of 0.3 or 0.5 for the mTBI and FAD comparison, respectively.

ADDITIONAL RESOURCES

- Videos related to DISCO-MS work: <http://discotechnologies.org/DISCO-MS/>
- Further details on the vDISCO protocol: <http://discotechnologies.org/vDISCO/>
- Videos related to workshops: <http://discotechnologies.org/workshop/>

Supplemental figures

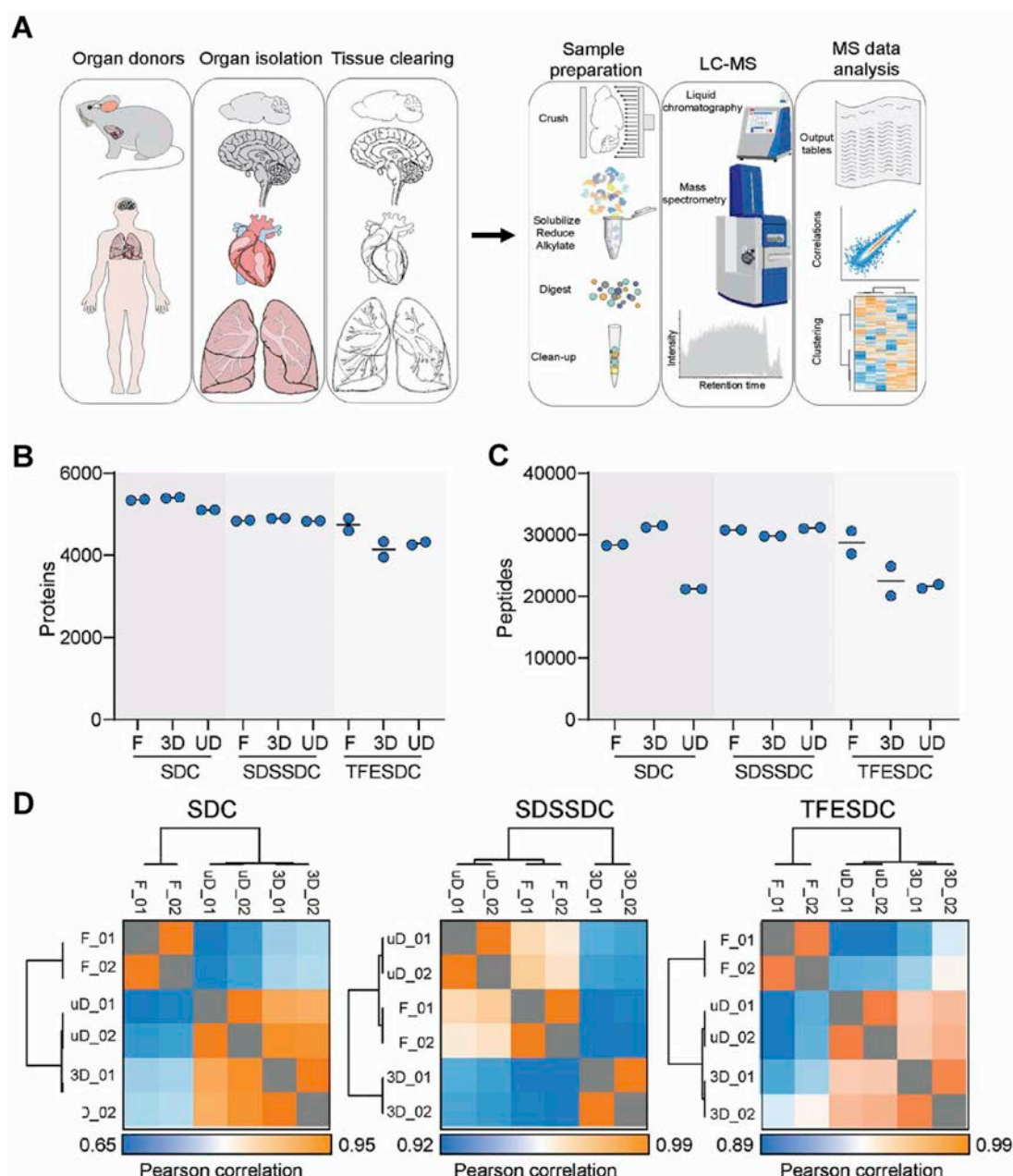


Figure S1. Optimization of sample preparation from cleared tissues, related to Figure 1

(A) The workflow for optimization of DISCO-MS from clearing bulk tissue to mass spectrometry. Organs can be isolated from any organism followed and cleared by any organic solvent-based tissue clearing. The cleared tissues then subjected to sample preparation workflow we developed for the mass spectrometry analysis. In short: the tissues were solubilized, reduced and alkylated, digested into tryptic proteins and cleaned up ready for liquid chromatography coupled to mass spectrometry (LC-MS) analysis. (B) Protein identifications across analytical duplicates for SDC, SDSSDC, or TFESDC preparations coming from fresh or cleared mouse brains (3D, uD: 3DISCO and uDISCO clearing methods, respectively). (C) Peptide levels of the samples shown in (B). (D) Proteome correlation matrices for measurements presented in (B) and (C). High Pearson correlations indicate very similar proteomes across conditions in SDSSDC and TFESDC.

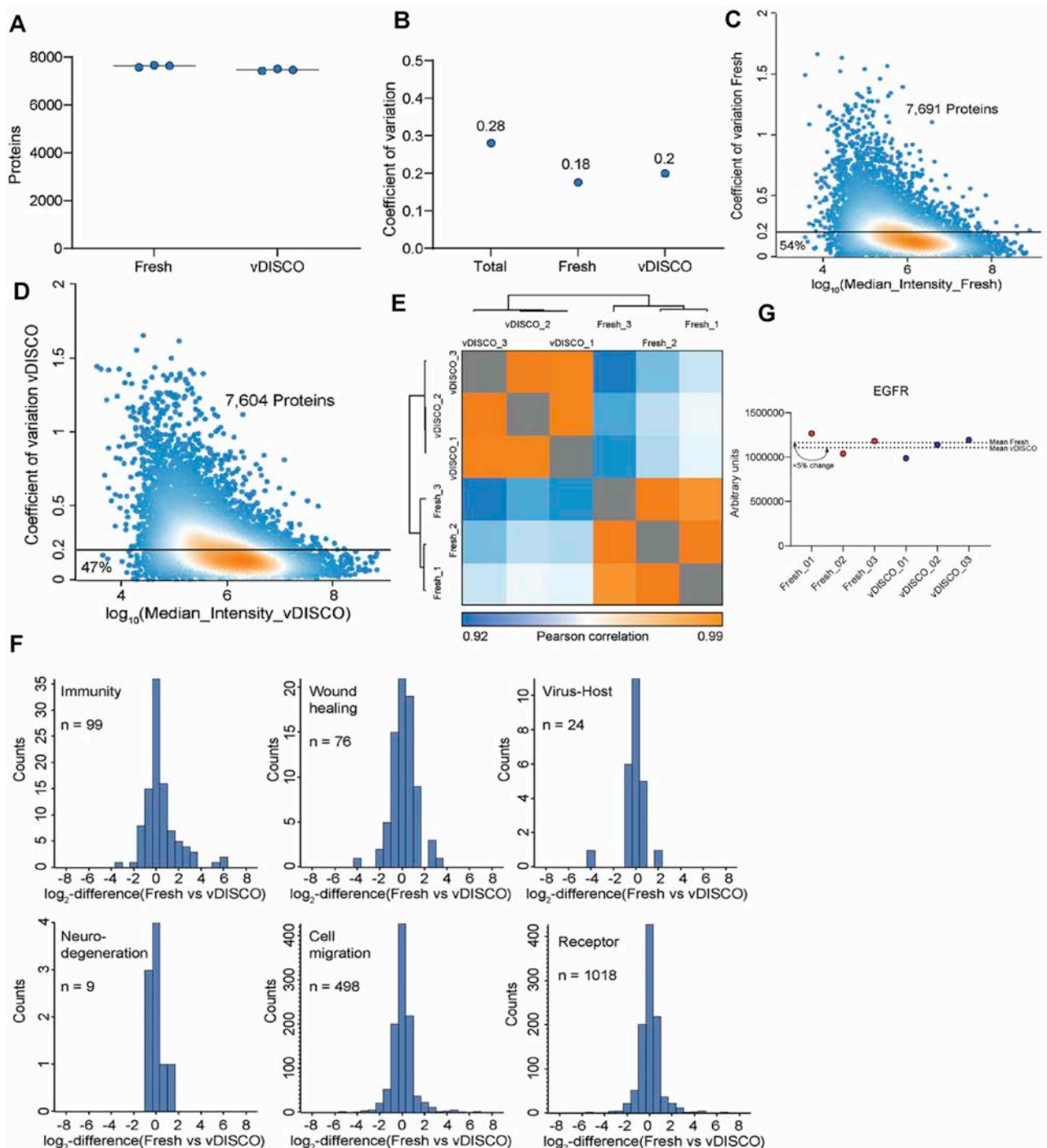


Figure S2. Quantitative assessment of proteome and gene ontologies in vDISCO-cleared and fresh mouse brain tissues in biological triplicates, related to Figure 1

(A) Proteins identified across all three biological replicates for either fresh or vDISCO-cleared tissue. (B) Coefficients of variation (CV) for either the total dataset including fresh and vDISCO cleared tissue, or fresh/vDISCO only. Note that CVs across biological replicates are low and that CVs across biological triplicates are very similar for fresh and for vDISCO highlighting that proteome of vDISCO-cleared organs is highly reproducible. (C) Abundance to CV rank plot for either fresh tissue (left; 7,691 proteins in total; 54% of all proteins are below CV = 0.2) or (D) vDISCO cleared tissue (right; 7,604 proteins in total; 47% of all proteins are below CV = 0.2). (E) Protein intensity correlation plot for all six biological replicates (3x fresh and 3x vDISCO-cleared). (F) Log₂-fold changes for the terms 'Immunity' (99 proteins), 'Wound healing' (76 proteins), 'Virus-Host' (24 proteins), 'Neurodegeneration' (9 proteins), 'Cell migration' (498 proteins) and 'Receptor' (1,018 proteins) between fresh and vDISCO-cleared biological triplicates. (G) Mean intensity difference in one of the plasma membrane-associated proteins in fresh and vDISCO cleared brains (N = 3).

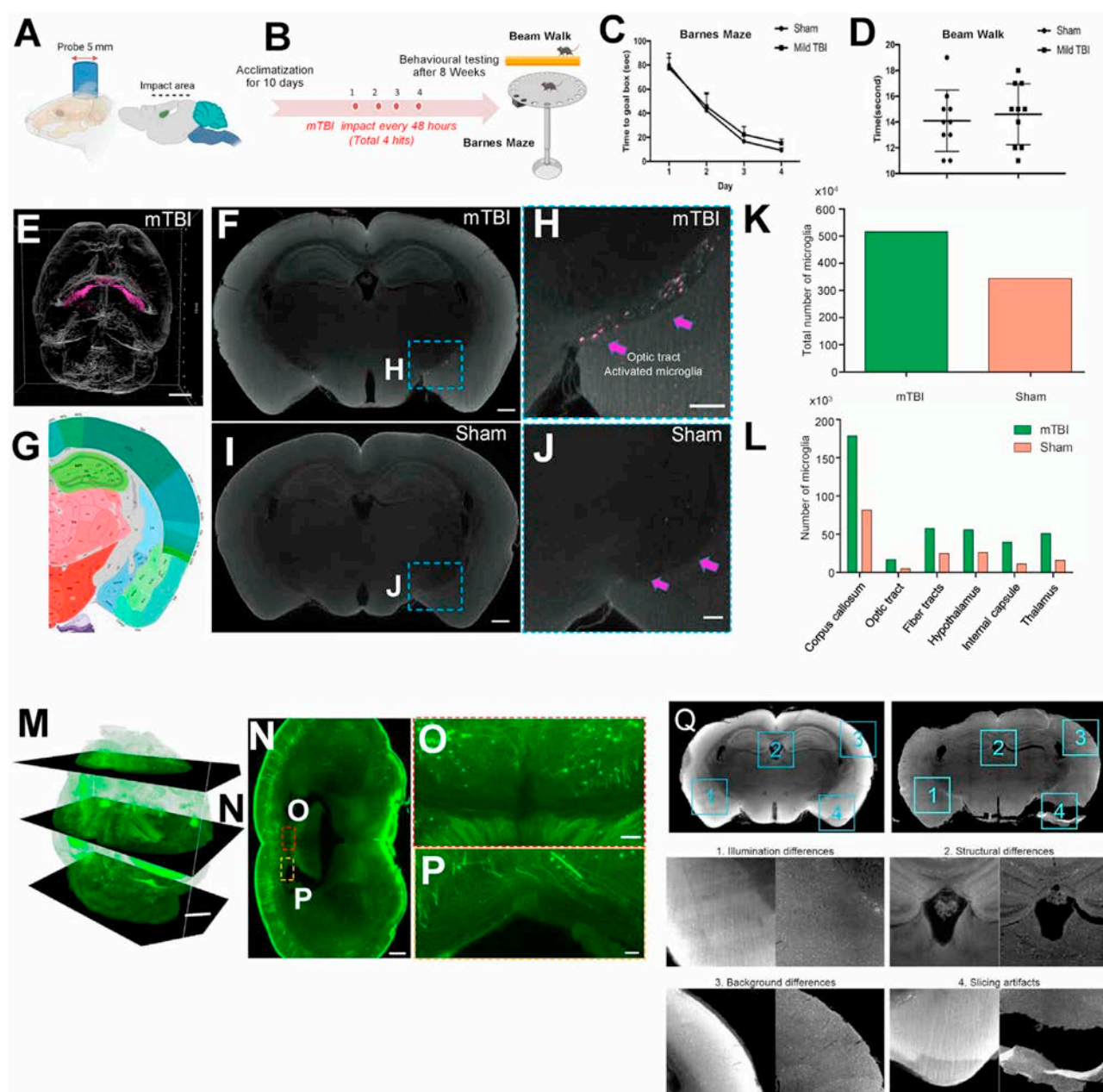


Figure S3. mTBI model validation by behavior and axonal morphology, related to Figure 2

(A) Depicting the mTBI impact area on the intact skull. (B) Schematic plan of the repetitive mTBI experimental mouse model (red points indicate each impact time point). (C) Barnes maze test in sham vs. mTBI animals. $n = 10$ animals per group. (D) Beam walk test in sham and mTBI animals. $n = 10$ animals per group. No significant behavior change detected—confirming the “mild” nature of our TBI model. (E) 3D-reconstruction of stitched data of an exemplary CX3CR1GFP+ mouse brain after mTBI. Segmented microglia shown in magenta. Scale bar, 500 μ m. (F) Stitched images of coronal optical slices showing optic tract with activated microglia. Scale bar, 400 μ m. (G) Corresponding brain regions (coronal view) shown in Allen Brain atlas. (H, J) High magnification image of optic tract in mTBI brain from (F) vs. the same region from sham control brain from (I) showing the activated microglia morphology in mTBI brain compared to control brain. Scale bar, 200 μ m. (K) Quantification of total number of microglia in mTBI vs. Sham animals. (L) Quantification of microglia numbers in mTBI vs. sham mice using ClearMap method. Only the regions with major changes are shown. (M) 3D view of stitched images of whole brain from a Thy1-GFP-M mouse after mTBI. Scale bar, 1000 μ m. (N) 2D orthoslice of stitched images showing the axonal swellings in corpus callosum (white matter areas). Scale bar, 500 μ m. (O, P) High magnification images marked in (N). Scale bar, O, 100 μ m and P, 50 μ m. (Q) Overview of potential hurdles when registering light-sheet z-planes (left) and LCM sections (right) from the same brain. 1: Light-sheet illumination can produce striping artifacts and uneven illumination. 2: Small, loosely attached structures such as the choroid plexus inside the ventricles will change shape during slicing. 3: Bulk tissue generates stronger autofluorescence, leading to e.g., uneven background illumination across the cortex. 4: During cryosectioning into 12 μ m sections, regions may tear.

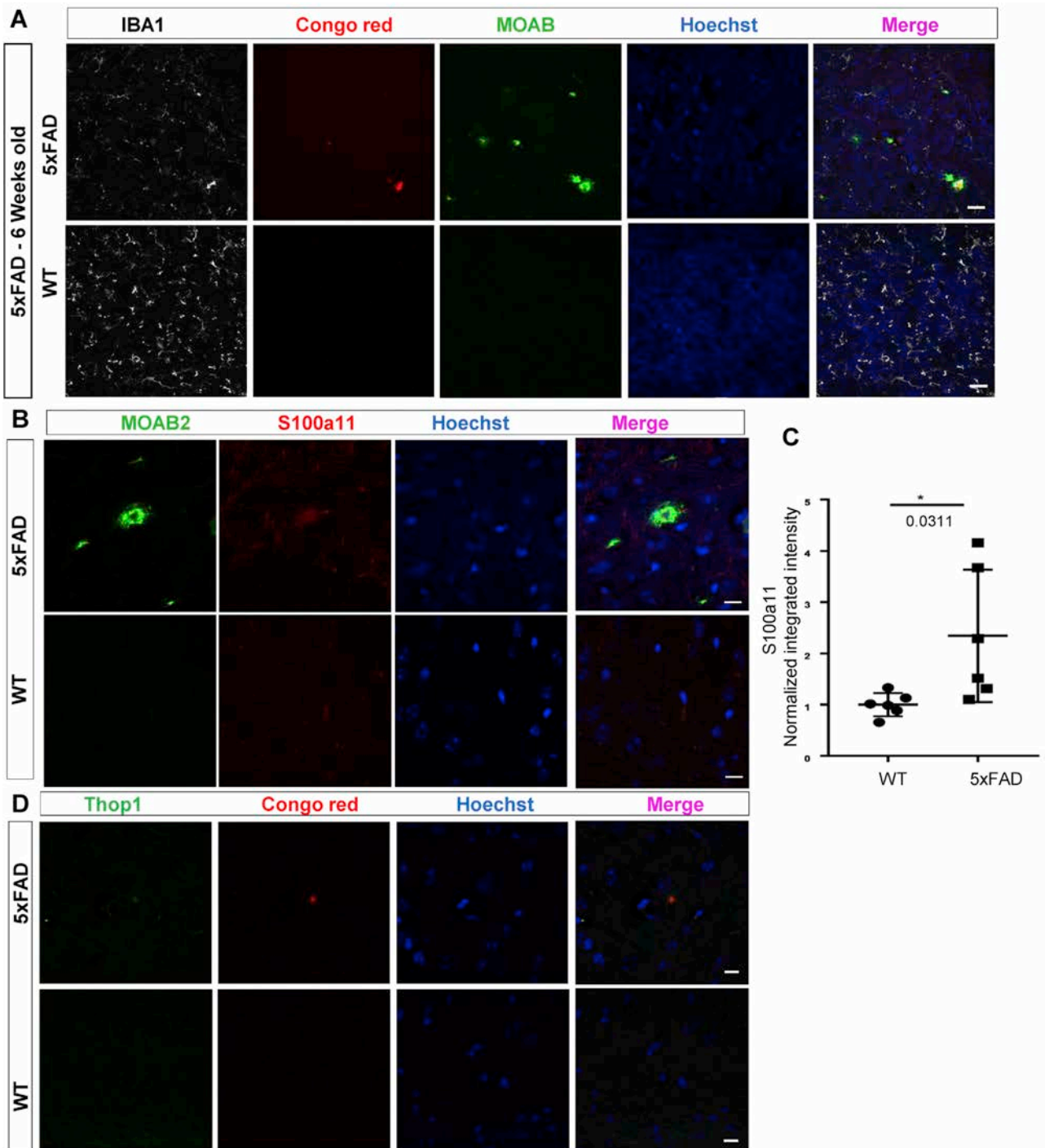


Figure S4. Histological validation of A β plaques and DISCO-MS hits in 5xFAD brains, related to Figure 4

(A) Tissue histology validation of Congo red plaque staining with a plaque-specific monoclonal antibody (MOAB, green). Furthermore, the microglia were stained using IBA1 antibody (in white) and nuclei using Hoechst dye (in blue). Microglia activation around the plaques of 5xFAD mouse brain is apparent. Scale bars, 20 μ m. (B) Histological validation of DISCO-MS hit S100a11 (red) in hippocampal region using antibody immunostaining in 6 weeks old mice. The plaques were co-labeled using the MOAB2 antibody (in green). (C) Intensity quantification of S100a11 (N = 3 animal per group from total 12 sections; unpaired two-sided Student's *t* test; $p = 0.0311$; data are presented as average \pm SD). (D) Histological validation of DISCO-MS hit Thop1 (in green) in hippocampal region of 5xFAD animals along with Congo red-labeled (in red) plaques in 6-weeks old mice. Scale bars, 10 μ m.

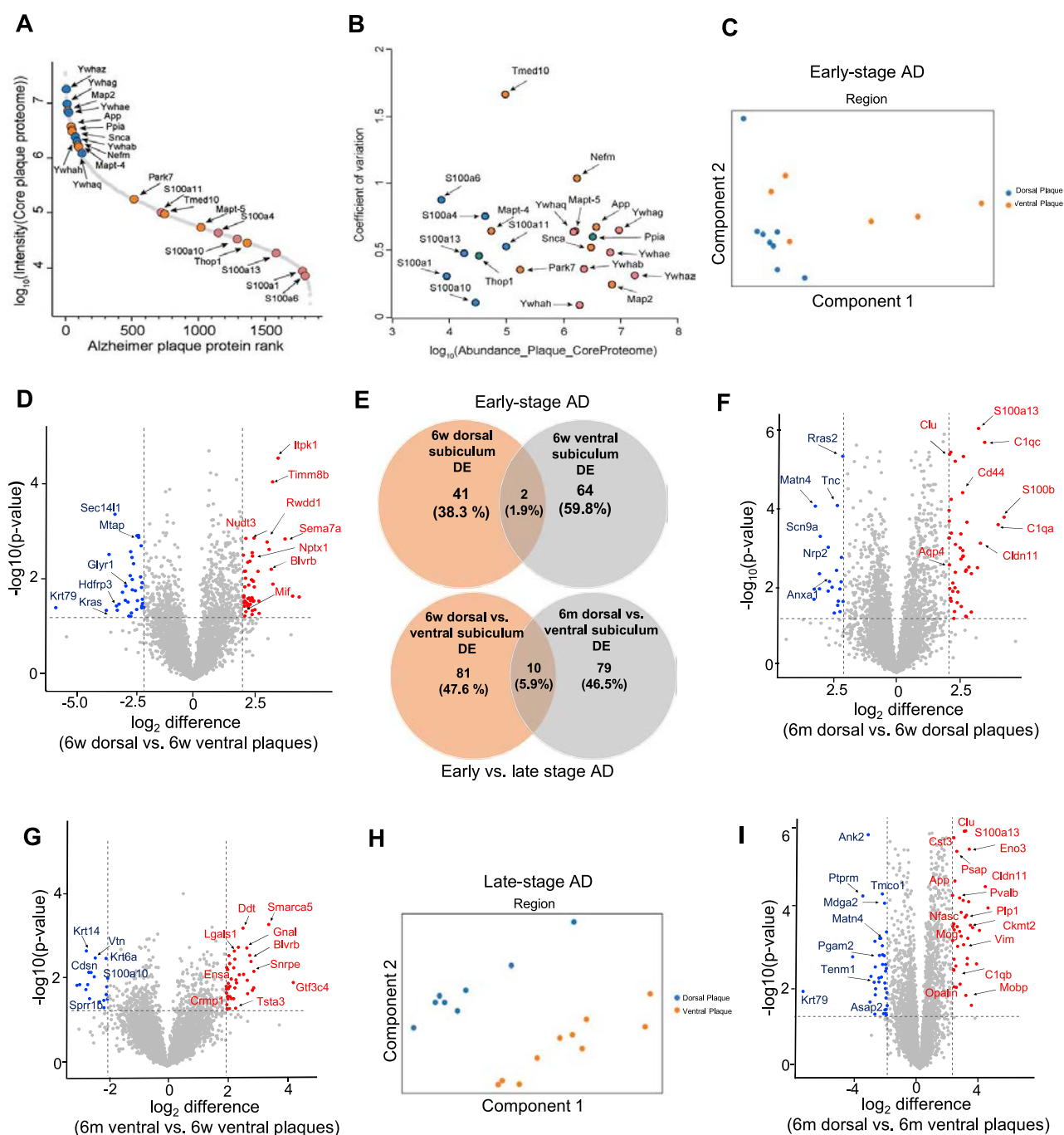
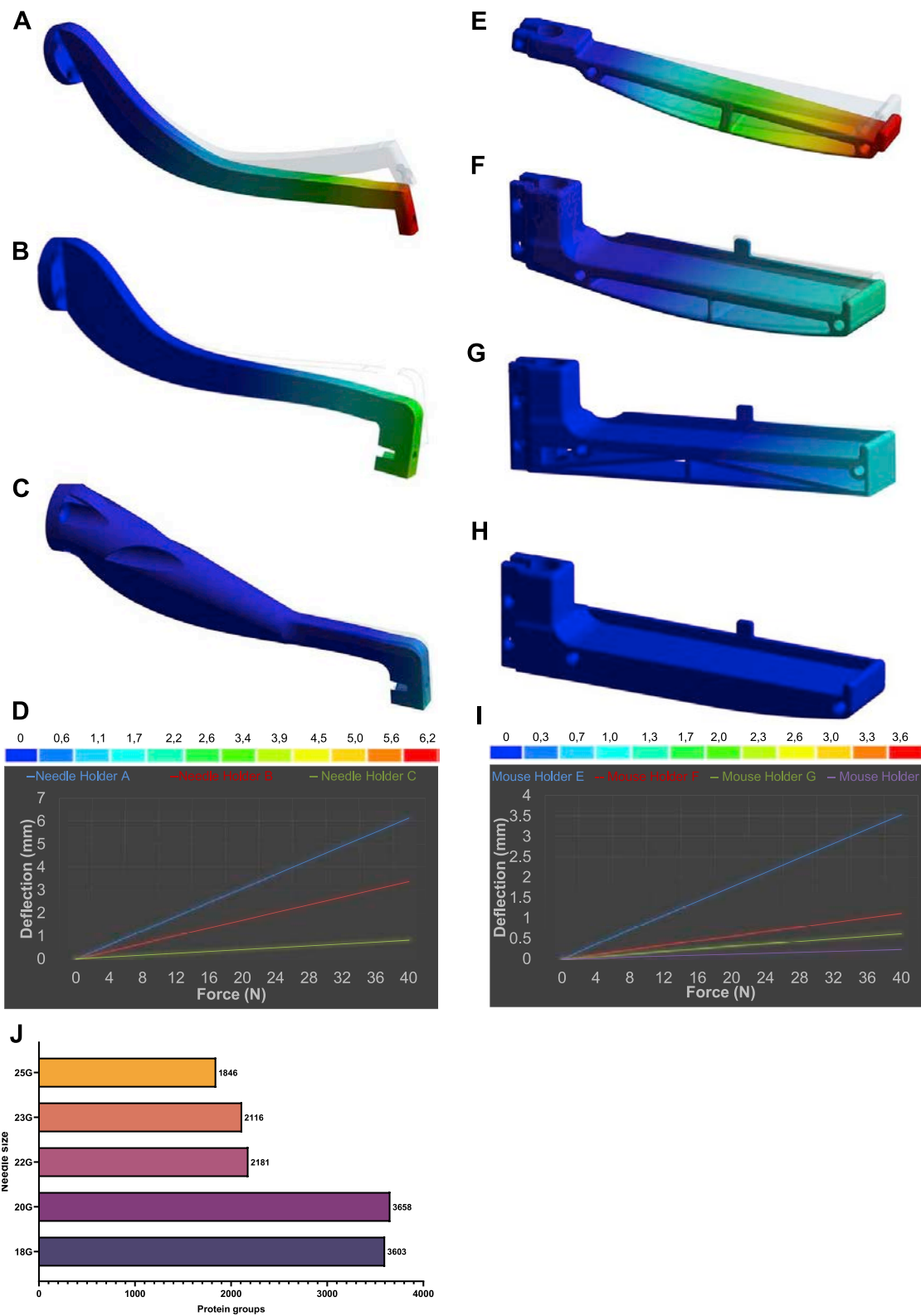


Figure S5. DISCO-MS unravels the spatiotemporally regulated single-plaque proteome in AD mouse model, related to Figure 4

(A) Rank order of core protein signals in a single plaque microenvironment. (B) Log10 abundance distribution of selected proteins and protein families as a function of their coefficient of variation (CV) across the core A β plaque proteomes. Dynamic range coverage is up to four orders of magnitude. CVs indicate variability in the shared plaque core proteome, among proteins known to play a role in Alzheimer's disease. (C) Principal component analyses (PCA) in early stage AD. (D) Volcano plot showing the significantly enriched proteins in 6w dorsal vs. 6w ventral plaques. (E) The number of shared and unique set of differentially expressed (DE) proteins in 6w and 6m regions. (F) Volcano plot showing the significantly enriched proteins in 6m dorsal plaque vs. 6w dorsal plaque. (G) In 6m ventral plaque vs. 6w ventral plaque region. (H) PCA in later stage regions. (n = 8–10 ROIs per region). (I) Inter-regional enrichment at later stage plaque.



(legend on next page)

Figure S6. Optimization of needle and mouse holders for robotic extraction from whole body, related to Figure 5

(A) The iterative development of the models using finite element analysis method to evaluate the approximate deflection of 6.2 mm for needle holder A, (B) 2.6mm for needle holder B and (C) 0.8 mm for needle holder C. (D) Deflection levels are color coded and plotted to comparatively present the iterative development of the needle holder design. "Images used in A-D courtesy of ANSYS, Inc.". (E) On the other side the maximum deflection levels for the mouse holder (E) is 3.6 mm, for the (F) 1.1 mm, for the (G) is 0.6 mm and for the mouse holder (H) is 0.2 mm. (I) Plot to comparatively present the iterative development of the mouse holder design for the precision of targeting. (J) Showing number of protein groups obtained with various needle gauge size. Note, that in addition to 18G and 22G needles we used here in biological applications (Figures 6 and 7), we could also obtain >1800 proteins with even smaller size needles.

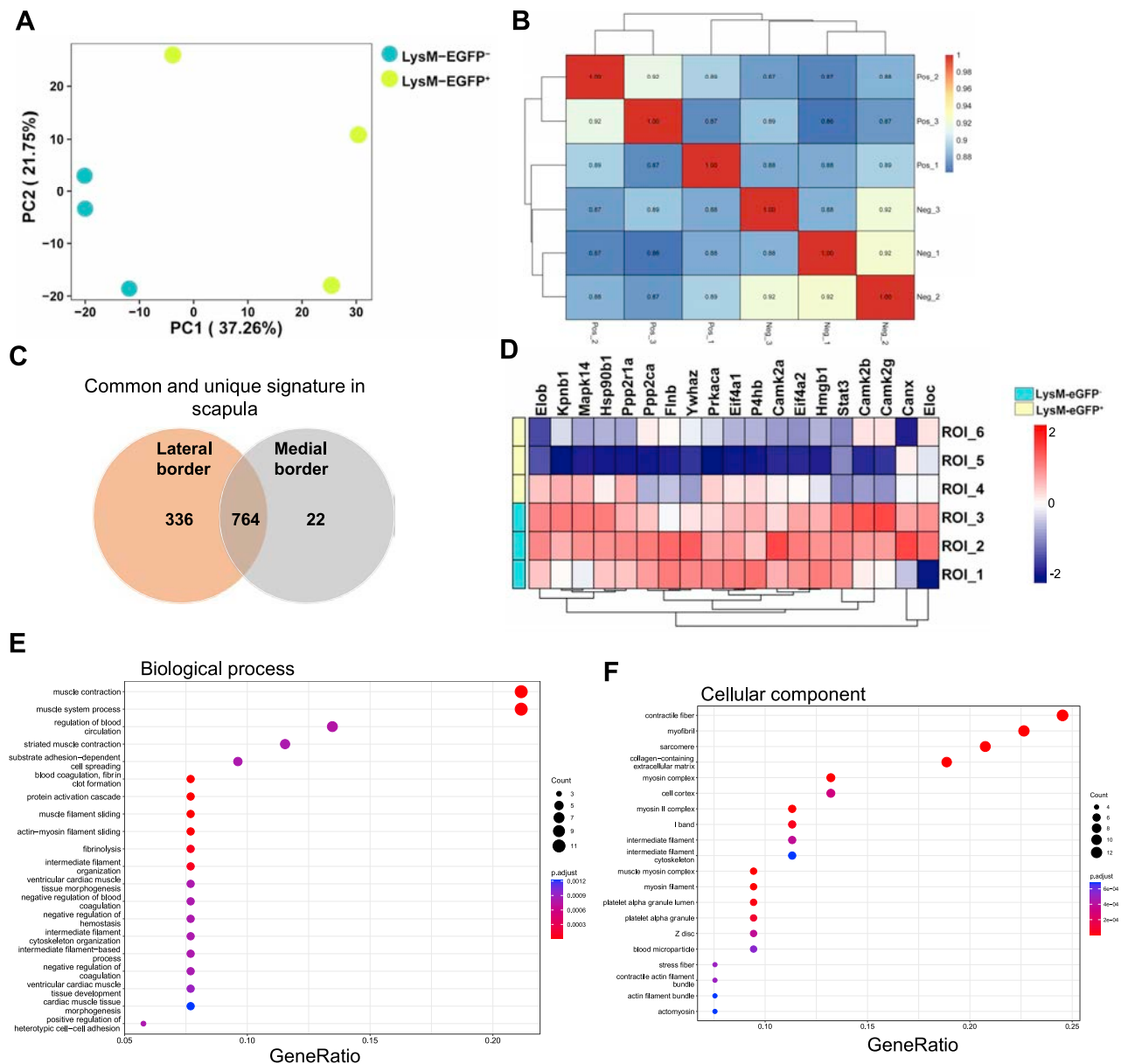


Figure S7. Spatial proteomics from DISCO and SHANEL cleared samples, related to Figures 6 and 7

(A) Principal component analyses (PCA) showing distribution of ROIs in medial and lateral border of scapula bone marrow. (B) Protein intensity correlation plot for all 6 ROIs from LysM-EGFP⁺ and LysM-EGFP⁻. (C) Venn diagram showing shared and unique proteins in medial vs. lateral border of mouse scapula. (D) Heatmap showing the proteins related to cytokine pathway in LysM-EGFP⁺ and LysM-EGFP⁻ scapula samples. (E) Biological process terms associated with regulated proteins in plaques vs. non-plaques regions in human right coronary artery. (F) Cellular component terms associated with regulated proteins.

5 General Discussion

Throughout this thesis, I have demonstrated how omics technologies, particularly spatial omics, can be leveraged to address cell and tissue biology across various pathological and physiological states. The thesis comprises three main parts: In the first part I developed statistical and machine learning approaches to study spatial cell arrangements in tissue under different conditions leveraging spatial omics data from various technologies. We developed these tools to help scientists utilise this data to uncover insights into diverse biological systems. The second part examines the role of the skull in brain diseases through unbiased holistic omics analysis. In the third part, we extended the spatial proteomics techniques into three dimensions by combining our imaging and mass spectrometry-based approaches, developing a new technique to better represent the tissue microenvironment.

To maintain a logical flow and accommodate the increasing complexity of the technologies, I will order the studies to reflect this progression and align with the aims of the thesis. I will begin with an analysis of bulk proteomics data to study the uniqueness of the molecular profiles of the skull bone marrow (Kolabas *et al.*, 2023). This will be followed by a shift to single-cell or spot molecular profiles combined with spatial information (in 2-dimensional slices) to study changes in cellular organisation and tissue architecture (Ali *et al.*, 2024; Fischer *et al.*, 2022). Finally, I will discuss our extension of spatial proteomics into 3-dimensional space using tissue clearing, 3D imaging techniques, and ultra-high-sensitivity mass spectrometry to develop a novel 3D spatial proteomics technique, particularly focusing on its application in Alzheimer's disease (Bhatia *et al.*, 2022).

5.1 Main findings

Here, I will briefly highlight the main findings from each of the studies presented in this thesis before expanding on them in the discussion of key implications, limitations and outlook.

5.1.1 Skull bone marrow molecular profile differs from other bones

Using optimised tissue clearing and imaging, we previously unravelled physical connections between the skull and dura matter through skull-meninges channels (SMCs) (Cai *et al.*, 2019). In our resource paper (Kolabas *et al.*, 2023), we combined cutting-edge technologies omics, tissue clearing and TSPO-PET imaging technologies and demonstrated the molecular distinctiveness of skull bone marrow compared to other bones and its therapeutic implication in brain diseases in mice and humans. Notably, we observed minimal proteomic changes in skull bone marrow under pathological conditions, indicating that its role may be more specialised than previously thought. In human samples, we detected synaptic vesicle membrane proteins unique to the skull, suggesting potential communication pathways with the brain. This distinction persisted regardless of pathological state, pointing to fundamental differences in the skull's biological function.

5.1.2 GraphCompass uncovers cellular organisation and tissue architecture across different conditions

Moving to the spatial space with higher molecular profiling resolution and by representing spatial omics data as graphs of cells, we have the flexibility to utilise the graph learning theories and adapt them to the omics domain. In our paper (Ali *et al.*, 2024), we adapted graph comparison metrics and developed `GraphCompass` packages to compare the cellular organisation of tissues at various abstraction levels: cell types, niches and samples across different pathological and physiological states. This package can aid in answering some key biological questions such as how cellular organisation and tissue architecture differ across conditions and what spatial patterns are indicators of specific conditions. We demonstrated the capabilities of `GraphCompass` in providing a quantitative framework for analysing tissue architecture across different conditions. When applied to breast cancer progression, our analysis revealed that increased immune cell co-occurrence in non-progressor samples may explain the protection against invasive breast cancer progression consistent with previous literature (Risom *et al.*, 2022). `GraphCompass` supported the finding that myocardial infarction can cause changes in the cellular organisation beyond the site of the injury (Kuppe *et al.*, 2022), and highlighted some cell types organisation that has been successfully restored after a brain injury in the axolotl brain such as dorsal pallium excitatory neurons (dpEX) and Sfrp+ ependymal glial cells (sfrpEGC) (Wei *et al.*, 2022). `GraphCompass` provides a comprehensive package of graph comparison methods that can empower both computational and experimental scientists to analyse the tissue architecture across various conditions.

5.1.3 Graph neural networks reveal tissue traits and predictive factors across pathological stages using spatial omics

We extended the same representation of tissue as a graph of cells in our manuscript (Fischer *et al.*, 2022) and applied more complex models, namely graph neural networks, to investigate the emergent properties of tissues in the various pathological stages. To achieve this, we conducted a multimodal ablation study on both the molecular and cell-type feature spaces. Our results showed that molecular features effectively encode spatial information and are predictive of patient outcomes. However, in the cell type feature space, the predictive factors varied across cancer data sets, whether the cellular organisation, the proportion of immune cells, or tissue architecture was more predictive of patient outcomes. In addition, we developed interpretation methods for the graph models to highlight specific regions within individual tissues that contribute to colorectal cancer staging and were able to capture tissue-level phenotypes, such as survival analysis in breast cancer, that the model had not been explicitly trained on.

5.1.4 DISCO-MS: advances in 3D spatial proteomics

In our effort to extend the spatial omics domain to capture the three-dimensional nature of the cells in whole tissues (or even full body), in our other resource paper (Bhatia *et al.*, 2022), we developed DISCO-MS which is a new technique that combines the cutting-edge technologies of tissue clearing, imaging, and mass spectrometry. DISCO-MS enabled several significant discoveries in Alzheimer's disease research. We detected amyloid-beta ($A\beta$) plaques in 5xFAD transgenic mice modelling Alzheimer's disease at 6 weeks, earlier than previously reported (Jawhar *et al.*, 2012; Uras *et al.*, 2023). The technology identified novel proteins in early-stage plaques, including S100a11, and revealed distinct regional differences in plaque composition between the dorsal and ventral subiculum. We further observed region-specific gene regulation patterns that affect synaptic plasticity and immune response, suggesting local microenvironments play a crucial role in disease progression. Lastly, with the development of the advanced robotic tissue extraction tool (DISCO-BOT), we demonstrated the capability of the DISCO-MS

technique to be applied to whole mouse bodies and large human heart tissues, and using our proteomics analysis pipeline, we were able to identify changes in various protein groups across different conditions. This new development introduces a new approach for examining cellular functional changes across conditions in an unbiased three-dimensional holistic manner.

5.2 Key implications

5.2.1 Skull bone marrow molecular profiles differ from other bones

The primary goal of our study (Kolabas *et al.*, 2023) was to investigate the potential molecular differences between the skull bone marrow and other bones driven by the recent discoveries of skull-meninges channels connecting the skull bone marrow and the brain meninges (Cai *et al.*, 2019). This led us to two questions: (1) How does the skull differ from other bones in the body under both healthy and pathological conditions? and (2) What role does the skull play in both healthy and pathological brain function? In our attempt to answer these questions, we employed a range of technologies and followed two distinct pathways. The first pathway involved studying molecular changes at transcriptome and proteome levels across various bones. We used single-cell RNA sequencing and mass spectrometry-based proteomics to analyse different flat and long bones in comparison to the skull, meninges, and brain, across three conditions: naïve, sham-operated, and stroke in mice and three bones including skull in human samples with various causes of death. The second pathway leveraged tissue clearing and light-sheet imaging to investigate the spatial dynamics of immune responses. For this discussion, I will focus on my contributions to the analysis and interpretation of the proteomics data.

Our key goal in investigating the mouse proteome from various bone types and conditions was to understand how the skull bone marrow differs from other bones in both health and disease. With this in mind, we posed two key questions when analysing the data: (1) Is the skull distinct from other bones, and if so, how? and (2) How does the skull proteome change under pathological conditions, i.e. does it become more similar to or more distinct from other bones? The proteomics data supported our hypothesis that the skull is indeed distinct from other bones. However, I observed less prominent changes than expected between the pathological condition and the naïve state. Further investigation revealed distinct proteins in the skull bone marrow in mice, particularly in modules of proteins, related to neutrophil degranulation pathways, which are downregulated in the skull. This result was also supported by single-cell RNA-seq data. This downregulation may indicate that the skull bone marrow is more tightly regulated in terms of the immune response, potentially due to its proximity to the CNS, to prevent excessive inflammation that could harm the brain.

To answer the second question, the results offer several insights into the skull compared to other bones, both in its naïve state and after brain injury. The subtle proteomic changes in skull bone marrow under pathological conditions might be due to various factors which we can only hypothesise and focusing primarily on immune cells may also limit our understanding of what makes the skull unique. First, bone marrow across different bones might function more collectively than expected, as no studies have specifically examined their response to disease. Our findings suggest that the differences between bone marrows may not be as significant. Second, each bone marrow might have specialised roles. The skull's role may not be to act as a broad immune reservoir but rather to closely monitor the brain's immune state, maintaining a lower level of mRNA activity and being prepared to respond if needed. Third, more substantial changes could occur at the epigenomic level or through protein modifications, which are known to affect bone homeostasis and disease progression.

In human samples, I compared the proteome profiles of the skull with the vertebra and pelvis from 20 human samples with various causes of death. Our reasoning behind choosing these two bones is one would expect either the vertebra to be more similar to the skull due to their proximity to the central nervous system (CNS) or that the pelvis and skull are more alike since they are both classified as flat bones. Surprisingly, neither proximity to the CNS nor bone type appeared to influence the bone marrow significantly. Instead, the vertebra and the pelvis showed more similarity to each other than the skull. Most notably, I detected synaptic vesicle membrane protein (SYN) in the skull marrow, suggesting possible communication via peripheral nerves or brain antigens passed through the meninges. These findings lay the groundwork for further experimental work to understand the origin of these pre-synaptic proteins and the mechanistic distinction of the skull from other bones.

This study provides a comprehensive framework for understanding the unique molecular and functional features of the skull bone marrow and further serves as a benchmark for future research of bone marrow biology and its relationship with brain health.

5.2.2 Spatial omics as graphs - what we can learn about cellular organisation in different conditions

Moving to spatial omics, with the increase in molecular profiling resolution up to the single-cell level and the addition of spatial information, our research (Ali *et al.*, 2024; Fischer *et al.*, 2022) aimed to understand the cellular organisation and tissue architecture differences across samples in various pathological and physiological states, while developing methods to guide future research. This work addresses a crucial gap in the spatial omics domain, where existing tools often lack the ability to quantitatively compare tissue architectures across conditions and explain the emergent tissue traits that drive patient outcomes. Two key questions drove our efforts: How do cellular organisation and tissue architectures differ under various conditions, and what tissue traits are most predictive of patient outcomes? To tackle these, we worked on two approaches. First, we adapted graph similarity metrics to quantitatively compare samples at multiple levels of abstraction: cell types, tissue niches, and entire samples (Ali *et al.*, 2024). Second, we utilised graph models that can incorporate both spatial and molecular information and conducted a multilevel ablation study to examine the tissue trait influencing patient outcomes (Fischer *et al.*, 2022). I will discuss in detail the key implications of each of the methods below. It is worth mentioning that for both approaches, we represented spatial omics data as graphs of cells or spots, a representation that has been used in the spatial domain (Palla *et al.*, 2022a) (Section 2.2).

5.2.2.1 Spatial omics-adapted graph comparison metrics revealed biological insights

Recent studies have shown that cellular organisation plays an important role in determining the pathological or physiological state of the tissue and that tissue architecture changes with disease progression or during developmental stages (Schürch *et al.*, 2020; Jackson *et al.*, 2020; Wang *et al.*, 2023). This led us to an important question: how can we quantitatively capture these spatial changes across different conditions? To tackle this challenge, we developed `GraphCompass` package (Ali *et al.*, 2024), a comprehensive tool that collects omics-adapted graph similarity metrics, which can be easily used to unravel biological insights about the differential neighbourhood composition and tissue architecture across different conditions. Our choice of graph comparison metrics was driven by their interpretability, adaptability, and ability to handle data sets with varying sample sizes, which are common in spatial omics, especially those involving different conditions. This is due to the emerging nature of the field and the high experimental cost. With spatial omics data represented as graphs of cells or spots (Palla *et al.*, 2022a), this structure serves as a foundation for differential analysis, enabling the comparison

of specific cell type sub-graphs, neighbourhood composition, and entire graphs between disease states, developmental stages, and experimental conditions.

In selecting the metrics for the package, we prioritised interpretability, versatility and ease of use. For each of the abstraction levels: cell type, niches and samples, we chose metrics that were most suited to the information provided at each level and adapted them to the spatial omics data. We included metrics that capture the essence of tissue topology, tissue homogeneity, and both local and global views of tissue architecture. Some of the metrics we used were foreign to the omics field, such as filtration curves O’Bray *et al.* (2021) and Wasserstein Weisfeiler-Lehman graph kernels (Togninalli *et al.*, 2019). We developed the `GraphCompass` package on top of widely-used spatial omics analysis packages `Squidpy` (Palla *et al.*, 2022b) and `AnnData` (Virshup *et al.*, 2021), making it easy to extend to more metrics.

To test our package, we gathered spatial omics data from three different studies, each with different conditions, representing distinct disease stages, physiological regions, and regenerative states across various organs, all obtained using different spatial omics technologies of different resolutions. These data sets can serve as benchmarks for further differential method developments. The three data sets include breast cancer progression, myocardial infarction from different sites of the heart after ischaemic injury, and the regeneration stages of the axolotl brain after injury. Our results from applying `GraphCompass` to the different data sets were largely confirmatory of previously reported findings in the literature, while also offering explanations for some intriguing new observations. For example, in the breast cancer data set, we confirmed the unexpected finding of (Risom *et al.*, 2022), that myoepithelial cells in patients who progressors to invasive breast cancer (IBC) showed greater similarity to control samples than those who did not progressor to IBC. To further explore the immune environments of progressor and non-progressor patients in comparison to control samples, we used `GraphCompass`’s neighbourhood analysis metrics. We observed an increased co-occurrence of immune cells in non-progressor samples, suggesting that the thinner myoepithelial barrier in these patients may have influenced the immune environment, potentially offering protection against the progression to IBC (Galon *et al.*, 2010; Fridman *et al.*, 2017). This example shows how `GraphCompass` can serve as a hypothesis-generating tool; however, validation experiments will be necessary to confirm these findings.

With these different applications, our results showed the capabilities of our `GraphCompass` tool as a differential toolkit to compare samples across different conditions and at various abstraction levels, as well as its generalisability to the different spatial omics technologies and biological systems. `GraphCompass` closes a gap in differential spatial omics tools by providing a comprehensive suite of graph metrics, which is likely to be further extended in the future to cover more metrics, for studying spatial cellular arrangement and tissue architecture changes across conditions.

5.2.2.2 Ablation study to understand emergent tissue properties

Another intriguing question we were eager to explore was: What tissue traits contribute to patient outcomes? By tissue traits, I mean properties of the tissue such as cellular organisation, the proportion of immune cells in case of cancerous tissues, or overall tissue architecture regardless of cell states. Recent studies have demonstrated the power of graph neural networks in correctly identifying different patient outcomes and examining the tumour microenvironment, particularly in cancer data sets (Schürch *et al.*, 2020; Wang *et al.*, 2023). However, to our knowledge, no studies have directly focused on identifying the specific tissue traits that contribute to patient outcomes, a gap that we aimed to fill in our study (Fischer *et al.*, 2022).

To tackle this, we took a deep learning approach, utilising graph models to uncover the underlying predictive features of disease states. In an extensive multimodal ablation study, we explored spatial and molecular information from spatial omics technologies and benchmarked graph models against traditional machine learning models to capture tissue-level phenotypes. This analysis was particularly challenging due to the complexity of the models and the need for large data sets, hundreds of images, to avoid overfitting. Given that spatial omics is still an emerging field, finding data sets large enough for our study was difficult. Fortunately, for our study, we could access three cancer data sets with a couple hundred images, one for colorectal cancer and two data sets for breast cancer data sets.

To explore the different tissue traits, we investigated our models on two feature spaces, molecular expressions and cell types. When we focused on molecular information, we found that spatial data is indeed encoded within the molecular profiles, as permuting the nodes in the graph models did not affect performance. This has been reported in recent studies (Fischer *et al.*, 2023) and suggests that, while spatial omics data provides a valuable layer of detail, its spatial features may be implicitly captured by molecular markers alone. However, by investigating the graph embedding, we were able to obtain further insights which show that graph models could extract deeper layers of information from the data patterns and relationships beyond what the models were explicitly trained on, such as survival analysis. This highlights the potential of graph neural networks to learn more than just the obvious features and their ability to uncover hidden biological insights.

Even though global gene expression seems to be predictive of patient outcomes, we wanted to investigate whether spatial patterns and other tissue traits such as cell type frequencies also contribute to patient outcomes. Therefore, we switched to examining the cell type information, and indeed we noticed that the graph models outperformed other baseline models. The difference in performance between graph models and baselines was mostly obvious in colorectal cancer and therefore, based on prior studies, we anticipated that cellular organisation would play a key role (Schürch *et al.*, 2020). However, our intriguing results showed that even when we permuted the nodes, or even when we removed the cell-type features, the models still performed remarkably well. This suggests that it might not be cellular organisation driving the patient outcome, but the tissue architecture regardless of the cell states.

Interestingly, the breast cancer data sets revealed more complex patterns, with each of the two data sets showing different levels of importance for cellular organisation as a predictive factor for patient outcomes. This variation reflects the heterogeneity of breast cancer, a disease known for its complexity and diverse behaviour across patients. Our findings align with the literature, illustrating the impact of tissue structure and cell types in driving disease outcomes (Jackson *et al.*, 2020; Ali *et al.*, 2020).

To the best of our knowledge, our multimodal ablation study is the most comprehensive in the field. Notably, we invested considerable time in training strong baseline models. These baseline models provided a robust point of comparison and highlighted the strengths and potential of graph neural networks in capturing different aspects of tissue traits. We believe that, with more data, graph models will continue to prove their power in unravelling the complexities of tissue architecture traits and patient outcomes.

5.2.3 Spatial proteomics goes 3D

Most current spatial omics technologies are performed on two-dimensional slices, limiting our understanding of three-dimensional cells and tissue structures. This limitation is particularly significant in spatial proteomics, a relatively new field where high-resolution spatial methods

are currently two-dimensional and have limited proteome coverage (Giesen *et al.*, 2014; Goltsev *et al.*, 2018), while common mass spectrometry methods with broader proteome coverage lack spatial information (as discussed in Section 1.4.2). Our DISCO-MS technique was developed to address this gap Bhatia *et al.* (2022).

To demonstrate DISCO-MS's capabilities, we applied it across multiple disease models and organs. In this discussion, I will highlight its application in detecting the early onset of Alzheimer's disease in the 5xFAD mouse model. We focused on three key questions: (1) How early can A β plaques be detected in the brain? (2) What differences exist between early- and late-stage A β plaques? (3) How do A β plaques vary across different locations within the subiculum region, a region where these plaques first appear?

Our findings revealed that A β plaques are detectable at 6 weeks, significantly earlier than the reported 2-3 months threshold (Uras *et al.*, 2023; Kim *et al.*, 2019). Motivated by this detection of A β plaques at 6 weeks, I expanded our investigation to explore the proteomic profiles of these early-onset plaques (6 weeks) in comparison to both control regions and the more widely studied late-stage plaques at 6 months, which in turn addresses our second research question. DISCO-MS technique using laser capture microdissection (LCM) enabled us to extract single A β plaques and run mass spectrometry on them. From the results of early-stage A β plaques, we were able to identify proteins that were not previously reported in Alzheimer's disease studies, including S100a11, a calcium-binding protein family implicated in inflammation and cell cycle regulation and have been reported to influence trace metal homeostasis in the brain (Cristóvão and Gomes, 2019), both of which may play key roles in the early development of Alzheimer's pathology. While I successfully identified Apoe, a well-established marker associated with Alzheimer's disease progression at the late stage of AD, its absence in the early stage suggests its involvement may emerge at later stages of plaque development.

Further, I investigated the regional differences between A β plaques in the dorsal and ventral subiculum, an early site of plaque formation, and revealed distinct molecular profiles. We observed that certain genes were differentially regulated between the dorsal and ventral regions such as Tspan7 and Negr1, involved in synaptic plasticity and maintenance, and Mif, a gene linked to immune regulation, suggesting region-specific responses to plaque development (Zhang *et al.*, 2019). From this finding, we can hypothesise that the local microenvironment within each subregion might play a crucial role in shaping plaque composition and development. It might be the case that region-specific differences in cellular populations, metabolic activity, or protein expression create distinct environments that influence the form and development of A β plaques. These findings highlight the importance of local context in Alzheimer's disease progression and suggest that plaques may not develop uniformly across different regions of the brain, especially in early stages. Further investigation into these regional differences could provide new insights into how Alzheimer's disease progresses and why certain areas of the brain are affected more severely than others.

Our study highlights the potential of DISCO-MS for spatial proteomics, particularly in detecting early A β plaques, at 6 weeks in 5xFAD model which has not been reported before, as well as revealing regional differences in the brain. Although we applied DISCO-MS to other disease models, they are beyond the scope of this discussion. In addition, our findings suggest that A β plaque formation is influenced by local microenvironments, providing new insights into Alzheimer's pathology and the need for further investigation into regional variations in disease progression.

5.3 Limitations

While our studies provide valuable insights into utilising omics data, particularly proteomics, to understand biological systems, applying graph approaches to the spatial omics domain and extending spatial proteomics to the 3-dimensional space, as with any other studies several limitations need to be acknowledged. The diversity of technologies used introduces additional methodological and computational challenges, as each method comes with its constraints and variability. In this section, I will highlight the various technical and biological limitations of the technologies and computational approaches used throughout the studies presented in this thesis.

5.3.1 Technical limitations

In this part, I will discuss the technical limitations that arise from the various technologies used to acquire the data, as well as the constraints and challenges of the different computational approaches utilised to preprocess, analyse, and interpret the diverse omics data sets. This includes issues related to data acquisition techniques, preprocessing variability, and computational methods applied to extract meaningful biological insights from the data.

5.3.1.1 Mass spectrometry proteomics data acquisition and processing

Mass spectrometry proteomics presents several challenges in data acquisition and processing. The lack of standardised protocols introduces variability in both acquisition methods and preprocessing pipelines. For proteomics data acquisition, the two main methods that are used are data-dependent acquisition (DDA) and data-independent acquisition (DIA). While DDA selects peptides based on abundance, it often overlooks lower abundance proteins. DIA on the other hand, which was used in our studies, scans a broader spectrum of proteins, however, this comes at the cost of increased noise and decreased sensitivity for low-abundance peptides. Therefore, the choice of data acquisition method may affect the outcome by missing important biological insights or introducing false positives.

Another source of variability or limitation when dealing with mass spectrometry proteomics data is the absence of consensus on a best-practice preprocessing pipeline. Several key steps in the preprocessing pipeline can introduce variability, including the order of normalisation and log transformation, as well as the method used for imputing missing data. These methods usually vary across different studies, with each researcher choosing what suits their data, and may therefore distort biological signals. A problem associated with proteomics data, unlike RNA-sequencing data, is the presence of a large amount of missing values (ranging from 10-50% of missing values). There are multiple sources for missing values, where some are missing at random due to technical errors, while others are not random, meaning they may have low abundance below the detection threshold of the machine (Jin *et al.*, 2021). As a result, proper imputation methods are applied to correct for these missing values, which can introduce variability and bias into the data. For our studies, we applied k-nearest neighbours (kNN) imputation to address the missing values. kNN imputation can be effective by filling in gaps based on the similarity of nearby data points, however, it has its limitations. One key limitation is that it assumes similar samples have similar missing values, which may not always hold true in biological data. Moreover, kNN imputation can introduce bias, particularly when the missing values are not randomly distributed or when the nearest neighbours themselves contain noise, potentially distorting the biological signals further.

These technical limitations in acquisition and preprocessing could influence the biological interpretations drawn in this thesis. For instance, the use of DIA may have introduced background

noise or masked low-abundance proteins relevant to disease pathways. Similarly, kNN imputation, while practical, may have affected downstream analyses by introducing biases, especially in heterogeneous tissue types. Therefore, while the insights presented are robust within the applied frameworks, they must be interpreted with awareness of these underlying methodological constraints.

5.3.1.2 Tissues as graphs of cells and graph neural networks: model complexity and data constraints

When it comes to utilising graphs for spatial omics across different conditions, we face limitations in various aspects of modelling, such as data constraints, representation, and model complexity, which may affect the biological insights we can obtain from our methods.

In our methods papers (Ali *et al.*, 2024; Fischer *et al.*, 2022), we are relying on the representation of tissues as graphs of cells, with edges representing the proximity of cells. While this proximity-based method effectively captures local cellular interactions, it may overlook important long-range connections between cells that are not solely dependent on spatial proximity. These long-range connections, such as those involved in signalling pathways or immune responses, can be critical to understanding biological processes. With our focus proximity alone to determine if two cells are communicating, the model risks missing key cellular interactions, thereby limiting the insights gained from the graph. In addition, in our paper (Fischer *et al.*, 2022), we use a distance-based approach to determine whether two cells are connected, which introduces further limitations. This method requires hyperparameter tuning to define the distance threshold at which two cells are considered neighbours. Therefore, it adds a layer of complexity to the modelling process, and choosing an inappropriate threshold can either overestimate or underestimate the true biological connections, leading to biased or incomplete interpretations of the tissue.

The use of graph neural networks (GNNs) presents both opportunities and challenges when applied to spatial omics data. While GNNs are powerful tools for capturing the relationships between cells, their complex implementation comes with certain limitations. In our study (Fischer *et al.*, 2022), we utilised well-established graph models such as Graph Convolutional Networks (GCNs) and Graph Isomorphism Networks (GINs), which rely on aggregation functions to aggregate feature information from neighbouring nodes. One limitation of this approach is the nature of the aggregation functions. For instance, GCNs use a weighted average to aggregate features from neighbouring cells, which works well in homogeneous environments but may oversimplify the heterogeneity of the tissues. On the other hand, GINs utilise a summation-based aggregation that is better at distinguishing between graph structures, but they can be sensitive to sparsity in nodes, especially in small data sets. We conducted experiments on the aggregation functions of GCNs and GINs and indeed observed differences in model performance when altering the aggregation methods. In addition, both models rely on local neighbourhood information, which limits their ability to capture long-range interactions between cells.

Another limitation of GNNs, as with other deep learning models, is the need for a large amount of data. Since our problem involves graph classification, we required a substantial number of tissue samples with various conditions. This poses a significant challenge in the field of spatial omics due to the limitations and high costs of the technologies. However, even with the couple hundred sample data sets we were able to obtain, the model's complexity may have led to overfitting, especially in the colorectal cancer data set that was too small to allow for a proper validation split.

5.3.1.3 3D spatial proteomics: technological barriers

Our DISCO-MS, and 3-dimensional spatial proteomics technologies in general, provide a great promise to understand tissue architecture and cellular organisation. However, it is a new field and still faces multiple technical limitations.

One of the limitations of our technology is the lack of single-cell resolution. Although we were able to reach the resolution of dozens of cells, achieving single-cell resolution remains a challenge, not just in 3-dimensional spatial proteomics, but even in non-spatial mass spectrometry. This is due to the requirement for a specific amount of tissue material to generate a detectable signal. In addition to the challenges in sample preparation and instrumental limitations.

Despite DISCO-BOT's development, tissue extraction remains labour-intensive and cannot match the precision of laser capture microdissection, potentially introducing sampling bias.

5.3.2 Biological limitations

In the following section, I will discuss the biological limitations that arise from the inherent complexity of the tissues and systems studied, as well as the challenges associated with interpreting proteomic and spatial omics data. These limitations include issues related to tissue heterogeneity, the variability of protein abundances, and the dynamic nature of biological processes that may not be fully captured in our analyses.

5.3.2.1 Tissue heterogeneity

Tissue heterogeneity poses significant challenges, particularly in bone marrow and tumour analysis. Although we aim to capture a wide range of cellular behaviour, the variability in cell populations, such as rare immune or structural cells, might be under-represented, especially given the focus on certain cell types, for example, immune cells in our study of skull bone marrow (Kolabas *et al.*, 2023). This diversity within tissues can complicate our ability to draw broad conclusions and may limit the scope of our insights.

Furthermore, this heterogeneity may also affect the reproducibility of the findings across different data sets, as the composition and interactions of cell types may vary from sample to sample. This makes it more challenging to generalise the findings and increases the risk of missing key biological processes that are crucial in other contexts.

5.3.2.2 Protein abundances in tissue

Proteomic analysis is based on relative abundance and therefore introduces its challenges. Because protein levels can fluctuate between tissues and conditions, the use of relative abundance might obscure the role of low-abundant proteins that could be biologically significant. These proteins, although present in small amounts, may play critical roles in processes like signalling or immune responses. The reliance on relative abundance makes it difficult to determine the true impact of these proteins, potentially leading to incomplete or skewed interpretations. In addition, this limitation can affect our understanding of disease progression, where even small shifts in the expression of low-abundant proteins could have major biological consequences. By focusing primarily on more abundant proteins, we may overlook subtle but critical molecular changes that are key to understanding complex biological processes.

In summary, these limitations provide context for interpreting our findings and highlight areas for future technological and methodological improvements. By addressing these constraints, we can work towards more comprehensive and accurate models of biological systems.

5.4 Outlook

In this thesis, I have demonstrated the use of existing omics technologies to study different biological systems, specifically skull biology. I have also highlighted our efforts in developing computational graph methods for spatial omics technologies to explore cellular organisation, tissue architecture, and the different tissue traits across various conditions. Moreover, I contributed to the development of novel technology aimed at extending the spatial proteomics field to three dimensions. However, this work opens up many future research directions that can be explored to further deepen our understanding and refine these methodologies. Here, I outline multiple areas that could significantly extend this work. Future research opportunities arise from this work in several key areas:

5.4.1 Leveraging multi-omics and spatial omics for a deeper understanding of the brain-skull axis and disease targeting

This study (Kolabas *et al.*, 2023) has a large collection of molecular data from both single-cell RNA-seq and proteomics, which contributes to our understanding of skull biology. However, RNA is relatively more dynamic than protein, and factors such as time delays and other experimental or processing influences may have impacted the results. Therefore, it would be valuable to perform a multi-omics approach to study both RNA and protein simultaneously from the same cells. This combined analysis could provide a more complete picture of cellular differences and offer further insights into skull biology. This in turn can make the study more robust when comparing the skull bone marrow under various conditions and therefore enhances our understanding of the brain-skull axis.

In addition to single-cell RNA-seq and proteomics, incorporating spatial omics would offer another layer of information. Spatial omics provides insight into the spatial context of cellular organisation and tissue architecture. This could reveal how molecular interactions vary across different regions of the skull and provide clues to how specific regions interact with the brain, particularly in response to brain pathologies like neuroinflammation.

Furthermore, the use of proteomics to identify key protein targets in specific diseases could open new therapeutic avenues. By identifying disease-specific proteins, we can pinpoint molecular targets that are crucial for pathological processes. With tools like AlphaFold (Abramson *et al.*, 2024) and RFdiffusion (Watson *et al.*, 2023), these proteins could be further analysed to design peptides or drugs that specifically bind to and modify their function which can be used for targeted treatments. This could be especially valuable for diseases linked to the brain-skull axis, such as neurodegenerative diseases, where modulating skull-related immune responses could influence disease progression.

5.4.2 Advancing graph-based methods in spatial omics

For our two graph-based papers (Ali *et al.*, 2024; Fischer *et al.*, 2022), several future directions can significantly extend the scope and power of these methods, offering deeper insights into tissue organisation, cell-cell interactions, and disease mechanisms.

For the `GraphCompass` package (Ali *et al.*, 2024), future work can focus on expanding the range of graph metrics to study more complex cellular interactions. One potential direction is the addition of long-range neighbourhood analysis, which could help capture more distant cellular interactions. Many spatial omics tools focus on immediate cellular neighbourhoods, but extending the analysis to consider cells further apart could uncover signalling pathways or structural relationships that are otherwise overlooked.

Another interesting future direction to extend the metrics is to adopt methods such as persistent homology or other topological data analysis (TDA) techniques (Ballester and Rieck, 2023) that could help capture underlying topological structures that standard graph metrics might miss. Persistent homology approaches are foreign to the spatial omics field. However, they can provide insights into the shape and structure of cellular networks across different scales, which could be crucial for understanding tissue heterogeneity or complex pathologies such as cancer progression and developmental stages.

The currently available spatial omics data sets have small sample sizes, a of maximum a few hundred, which makes it rather challenging for graph neural networks not to overfit. However, I believe that with the continuous development of the field, larger data sets will be available and therefore graph models will be more powerful and less prone to overfitting. Therefore, once these large data sets are available, we should expand our work (Fischer *et al.*, 2022) to include such data sets which can allow the graph models to capture more complex tissue architectures and subtle patterns of cellular organisation that might be difficult to detect with smaller data sets.

Another direction would be to enhance the architecture of graph models and integrate other approaches. First, by incorporating transformer-based graphs. Transformer models, which excel at capturing long-range dependencies and relationships, could potentially reveal new insights into tissue organisation by learning more complex interactions between distant cells. The self-attention mechanism in transformers may enable the model to focus on the most important connections, providing a better understanding of how different parts of the tissue, along varying distances, can influence patient outcomes. Another architectural enhancement would be the introduction of topological graphs, which focus on preserving the hidden topological structure within the data. This additional layer of information could offer further insights into the overall organisation of tissues. By capturing both the geometric and topological properties of cell distributions, topological graphs could help uncover latent features or hidden structures within tissues that may not be detected by traditional graph-based models.

Further studies should also focus on validating the findings from GNNs through experimental approaches, ensuring that the predicted tissue-level traits align with biological reality. In particular, applying these models to different cancer types or brain-related diseases could highlight the ability of graph-based approaches to understand a wide range of pathologies.

5.4.3 Combining 3D spatial proteomics and graph models

A promising future direction for DISCO-MS (Bhatia *et al.*, 2022) lies in its integration with graph models to explore complex tissue microenvironments. By combining graph-based approaches with DISCO-MS, which is a bulk proteomics technique, it would be possible to extract A β plaques and form graphs representing their spatial relationships and molecular profiles. This could provide critical insights into how A β plaques are organised and their molecular characteristics in early-stage Alzheimer's disease. In addition, this approach could be extended to study tumour microenvironments, where it would help in understanding the molecular profiles of metastases and why some are successfully targeted while others are not. This could open new avenues for targeted therapeutic strategies aimed at disrupting key cellular interactions in the metastatic process.

Another exciting prospect is extending 3D spatial proteomics to the single-cell level and mapping it onto a graph. Achieving this would offer a comprehensive view of how individual cells are organised and interact in three-dimensional space, providing an unprecedented understanding

of tissue architecture in both healthy and diseased states. While this remains technically challenging, it would represent a significant leap forward in the spatial omics field that can allow for detailed cellular resolution in a 3D representation of tissue.

The studies discussed in this thesis, though focused on different areas, are deeply connected and point toward an exciting future for biological research. These developments collectively form a unified framework for advancing both research and therapeutic development. The combination of different omics approaches with graph models and DISCO-MS technology holds promise for transforming our understanding of complex diseases like Alzheimer's disease and cancer.

5.5 Conclusion

In this thesis, I have explored several cutting-edge approaches to studying biological systems, ranging from skull biology to graph-based analysis of tissue organisation, and novel techniques for advancing spatial proteomics. We leveraged existing omics technologies to gain new insights into the molecular and cellular landscape of the skull and its relationship to brain health. The development of graph models enabled us to quantitatively compare tissue architectures and study the emergent tissue traits across various conditions. Furthermore, extending spatial proteomics into three dimensions through DISCO-MS has opened new possibilities for capturing detailed molecular profiles in a three-dimensional context, for example in diseases like Alzheimer's disease.

Each project contributed unique perspectives to our understanding of tissue organisation and molecular changes. Together, these approaches create a richer view of biological processes, from molecular dynamics in the skull to complex cellular patterns and detailed spatial molecular profiles in different biological systems.

The thesis achieved two primary goals, (1) to develop tools and methodologies to address the gaps in spatial omics technologies to study differential cellular organisation and tissue traits across different conditions, and (2) to investigate complex biological systems at a holistic view. Our focus on cellular organisation and molecular profiles across various pathological and physiological conditions has advanced our understanding of how these variations influence tissue structure and contribute to disease. While these projects may appear distinct, they form a cohesive foundation for future research in neuroscience and cancer research. By bridging these technologies and methodologies, this work sets the stage for significant advances in understanding tissue and systems biology.

Bibliography

- Abramson, J., J. Adler, J. Dunger, R. Evans, T. Green, A. Pritzel, O. Ronneberger, L. Willmore, A. J. Ballard, J. Bambrick *et al.*, “Accurate structure prediction of biomolecular interactions with alphafold 3”, *Nature* pp. 1–3 (2024).
- Aebersold, R. and M. Mann, “Mass spectrometry-based proteomics”, *Nature* **422**, 6928, 198–207 (2003).
- Ali, H. R., H. W. Jackson, V. R. Zanotelli, E. Danenberg, J. R. Fischer, H. Bardwell, E. Provenzano, O. M. Rueda, S.-F. Chin *et al.*, “Imaging mass cytometry and multiplatform genomics define the phenogenomic landscape of breast cancer”, *Nature Cancer* **1**, 2, 163–175 (2020).
- Ali, M., M. Kuijs, S. Hedyeh-Zadeh, T. Treis, K. Hrovatin, G. Palla, A. C. Schaar and F. J. Theis, “Graphcompass: spatial metrics for differential analyses of cell organization across conditions”, *Bioinformatics* **40**, Supplement_1, i548–i557 (2024).
- Alon, S., D. R. Goodwin, A. Sinha, A. T. Wassie, F. Chen, E. R. Daugharthy, Y. Bando, A. Kajita, A. G. Xue, K. Marrett *et al.*, “Expansion sequencing: Spatially precise in situ transcriptomics in intact biological systems”, *Science* **371**, 6528, eaax2656 (2021).
- Alves de Lima, K., J. Rustenhoven and J. Kipnis, “Meningeal immunity and its function in maintenance of the central nervous system in health and disease”, *Annual review of immunology* **38**, 1, 597–620 (2020).
- Angelo, M., S. C. Bendall, R. Finck, M. B. Hale, C. Hitzman, A. D. Borowsky, R. M. Levenson, J. B. Lowe, S. D. Liu, S. Zhao *et al.*, “Multiplexed ion beam imaging of human breast tumors”, *Nature medicine* **20**, 4, 436–442 (2014).
- Ballester, R. and B. Rieck, “On the expressivity of persistent homology in graph learning”, *arXiv preprint arXiv:2302.09826* (2023).
- Bandura, D. R., V. I. Baranov, O. I. Ornatsky, A. Antonov, R. Kinach, X. Lou, S. Pavlov, S. Voro-biev, J. E. Dick and S. D. Tanner, “Mass cytometry: technique for real time single cell multi-target immunoassay based on inductively coupled plasma time-of-flight mass spectrometry”, *Analytical chemistry* **81**, 16, 6813–6822 (2009).
- Bandyopadhyay, S., M. P. Duffy, K. J. Ahn, J. H. Sussman, M. Pang, D. Smith, G. Duncan, I. Zhang, J. Huang, Y. Lin *et al.*, “Mapping the cellular biogeography of human bone marrow niches using single-cell transcriptomics and proteomic imaging”, *Cell* **187**, 12, 3120–3140 (2024).
- Benjamini, Y. and Y. Hochberg, “Controlling the false discovery rate: a practical and powerful approach to multiple testing”, *Journal of the Royal statistical society: series B (Methodological)* **57**, 1, 289–300 (1995).
- Bennett, H. M., W. Stephenson, C. M. Rose and S. Darmanis, “Single-cell proteomics enabled by next-generation sequencing or mass spectrometry”, *Nature Methods* **20**, 3, 363–374 (2023).

- Bhatia, H. S., A.-D. Brunner, F. Öztürk, S. Kapoor, Z. Rong, H. Mai, M. Thielert, M. Ali, R. Al-Maskari, J. C. Paetzold *et al.*, “Spatial proteomics in three-dimensional intact specimens”, *Cell* **185**, 26, 5040–5058 (2022).
- Black, S., D. Phillips, J. W. Hickey, J. Kennedy-Darling, V. G. Venkataaaman, N. Samusik, Y. Goltsev, C. M. Schürch and G. P. Nolan, “Codex multiplexed tissue imaging with dna-conjugated antibodies”, *Nature protocols* **16**, 8, 3802–3835 (2021).
- Bressan, D., G. Battistoni and G. J. Hannon, “The dawn of spatial omics”, *Science* **381**, 6657, eabq4964 (2023).
- Brioschi, S., W.-L. Wang, V. Peng, M. Wang, I. Shchukina, Z. J. Greenberg, J. K. Bando, N. Jaeger, R. S. Czepielewski, A. Swain *et al.*, “Heterogeneity of meningeal b cells reveals a lymphopoietic niche at the cns borders”, *Science* **373**, 6553, eabf9277 (2021).
- Brunner, A.-D., M. Thielert, C. Vasilopoulou, C. Ammar, F. Coscia, A. Mund, O. B. Hoerning, N. Bache, A. Apalategui, M. Lubeck *et al.*, “Ultra-high sensitivity mass spectrometry quantifies single-cell proteome changes upon perturbation”, *Molecular systems biology* **18**, 3, e10798 (2022).
- Butler, J. E., “Enzyme-linked immunosorbent assay”, *Journal of immunoassay* **21**, 2-3, 165–209 (2000).
- Cai, R., Z. I. Kolabas, C. Pan, H. Mai, S. Zhao, D. Kaltenecker, F. F. Voigt, M. Molbay, T.-I. Ohn, C. Vincke *et al.*, “Whole-mouse clearing and imaging at the cellular level with vdisco”, *Nature Protocols* **18**, 4, 1197–1242 (2023).
- Cai, R., C. Pan, A. Ghasemigharagoz, M. I. Todorov, B. Förstera, S. Zhao, H. S. Bhatia, A. Parra-Damas, L. Mrowka, D. Theodorou *et al.*, “Panoptic imaging of transparent mice reveals whole-body neuronal projections and skull–meninges connections”, *Nature neuroscience* **22**, 2, 317–327 (2019).
- Carson, M. J., J. M. Doose, B. Melchior, C. D. Schmid and C. C. Ploix, “Cns immune privilege: hiding in plain sight”, *Immunological reviews* **213**, 1, 48–65 (2006).
- Chen, A., S. Liao, M. Cheng, K. Ma, L. Wu, Y. Lai, X. Qiu, J. Yang, J. Xu, S. Hao *et al.*, “Spatiotemporal transcriptomic atlas of mouse organogenesis using dna nanoball-patterned arrays”, *Cell* **185**, 10, 1777–1792 (2022).
- Chen, A., Y. Sun, Y. Lei, C. Li, S. Liao, J. Meng, Y. Bai, Z. Liu, Z. Liang, Z. Zhu *et al.*, “Single-cell spatial transcriptome reveals cell-type organization in the macaque cortex”, *Cell* **186**, 17, 3726–3743 (2023a).
- Chen, J., Y. Wang and J. Ko, “Single-cell and spatially resolved omics: Advances and limitations”, *Journal of Pharmaceutical Analysis* **13**, 8, 833 (2023b).
- Chen, K. H., A. N. Boettiger, J. R. Moffitt, S. Wang and X. Zhuang, “Spatially resolved, highly multiplexed rna profiling in single cells”, *Science* **348**, 6233, aaa6090 (2015).
- Chen, X., Y.-C. Sun, G. M. Church, J. H. Lee and A. M. Zador, “Efficient in situ barcode sequencing using padlock probe-based baristaseq”, *Nucleic acids research* **46**, 4, e22–e22 (2018).
- Codeluppi, S., L. E. Borm, A. Zeisel, G. La Manno, J. A. van Lunteren, C. I. Svensson and S. Linnarsson, “Spatial organization of the somatosensory cortex revealed by osmfish”, *Nature methods* **15**, 11, 932–935 (2018).

- Cristóvão, J. S. and C. M. Gomes, “S100 proteins in alzheimer’s disease”, *Frontiers in Neuroscience* **13**, 463 (2019).
- Cugurra, A., T. Mamuladze, J. Rustenhoven, T. Dykstra, G. Beroshvili, Z. J. Greenberg, W. Baker, Z. Papadopoulos, A. Drieu, S. Blackburn *et al.*, “Skull and vertebral bone marrow are myeloid cell reservoirs for the meninges and cns parenchyma”, *Science* **373**, 6553, eabf7844 (2021).
- Cui, M., C. Cheng and L. Zhang, “High-throughput proteomics: a methodological mini-review”, *Laboratory investigation* **102**, 11, 1170–1181 (2022).
- Dries, R., Q. Zhu, R. Dong, C.-H. L. Eng, H. Li, K. Liu, Y. Fu, T. Zhao, A. Sarkar, F. Bao *et al.*, “Giotto: a toolbox for integrative analysis and visualization of spatial expression data”, *Genome biology* **22**, 1–31 (2021).
- Efremova, M., M. Vento-Tormo, S. A. Teichmann and R. Vento-Tormo, “Cellphonedb: inferring cell–cell communication from combined expression of multi-subunit ligand–receptor complexes”, *Nature protocols* **15**, 4, 1484–1506 (2020).
- Eng, C.-H. L., M. Lawson, Q. Zhu, R. Dries, N. Koulana, Y. Takei, J. Yun, C. Cronin, C. Karp, G.-C. Yuan *et al.*, “Transcriptome-scale super-resolved imaging in tissues by rna seqfish+”, *Nature* **568**, 7751, 235–239 (2019).
- Enniful, A., Z. Zhang, D. Klymyshyn, H. Zong, Z. Bai, N. Farzad, G. Su, A. Baysoy, J. Nam, M. Yang *et al.*, “Integration of imaging-based and sequencing-based spatial omics mapping on the same tissue section via dbitplus”, *bioRxiv* pp. 2024–11 (2024).
- Ertürk, A., K. Becker, N. Jährling, C. P. Mauch, C. D. Hojer, J. G. Egen, F. Hellal, F. Bradke, M. Sheng and H.-U. Dodt, “Three-dimensional imaging of solvent-cleared organs using 3disco”, *Nature protocols* **7**, 11, 1983–1995 (2012).
- Fischer, D. S., M. Ali, S. Richter, A. Ertürk and F. Theis, “Graph neural networks learn emergent tissue properties from spatial molecular profiles”, *bioRxiv* pp. 2022–12 (2022).
- Fischer, D. S., A. C. Schaar and F. J. Theis, “Modeling intercellular communication in tissues using spatial graphs of cells”, *Nature Biotechnology* **41**, 3, 332–336 (2023).
- Fridman, W. H., L. Zitvogel, C. Sautès-Fridman and G. Kroemer, “The immune contexture in cancer prognosis and treatment”, *Nature reviews Clinical oncology* **14**, 12, 717–734 (2017).
- Galon, J., M. Dieu-Nosjean, E. Tartour, C. Sautès-Fridman, W. Fridman *et al.*, “Immune infiltration in human tumors: a prognostic factor that should not be ignored”, *Oncogene* **29**, 8, 1093–1102 (2010).
- Giesen, C., H. A. Wang, D. Schapiro, N. Zivanovic, A. Jacobs, B. Hattendorf, P. J. Schüffler, D. Grolmund, J. M. Buhmann, S. Brandt *et al.*, “Highly multiplexed imaging of tumor tissues with subcellular resolution by mass cytometry”, *Nature methods* **11**, 4, 417–422 (2014).
- Goltsev, Y., N. Samusik, J. Kennedy-Darling, S. Bhate, M. Hale, G. Vazquez, S. Black and G. P. Nolan, “Deep profiling of mouse splenic architecture with codex multiplexed imaging”, *Cell* **174**, 4, 968–981 (2018).
- Guo, G., H. Wang, D. Bell, Y. Bi and K. Greer, “Knn model-based approach in classification”, in “On The Move to Meaningful Internet Systems 2003: CoopIS, DOA, and ODBASE: OTM Confederated International Conferences, CoopIS, DOA, and ODBASE 2003, Catania, Sicily, Italy, November 3-7, 2003. Proceedings”, pp. 986–996 (Springer, 2003).

- Heumos, L., A. C. Schaar, C. Lance, A. Litinetskaya, F. Drost, L. Zappia, M. D. Lücken, D. C. Strobl, J. Henao, F. Curion *et al.*, “Best practices for single-cell analysis across modalities”, *Nature Reviews Genetics* **24**, 8, 550–572 (2023).
- Hu, Y., J. Rong, Y. Xu, R. Xie, J. Peng, L. Gao and K. Tan, “Unsupervised and supervised discovery of tissue cellular neighborhoods from cell phenotypes”, *Nature Methods* **21**, 2, 267–278 (2024).
- Jackson, H. W., J. R. Fischer, V. R. Zanotelli, H. R. Ali, R. Mechera, S. D. Soysal, H. Moch, S. Muenst, Z. Varga, W. P. Weber *et al.*, “The single-cell pathology landscape of breast cancer”, *Nature* **578**, 7796, 615–620 (2020).
- Jawhar, S., A. Trawicka, C. Jenneckens, T. A. Bayer and O. Wirths, “Motor deficits, neuron loss, and reduced anxiety coinciding with axonal degeneration and intraneuronal $\alpha\beta$ aggregation in the 5xfad mouse model of alzheimer’s disease”, *Neurobiology of aging* **33**, 1, 196–e29 (2012).
- Jeong, S., “Molecular and cellular basis of neurodegeneration in alzheimer’s disease”, *Molecules and cells* **40**, 9, 613–620 (2017).
- Jin, L., Y. Bi, C. Hu, J. Qu, S. Shen, X. Wang *et al.*, “(2021) a comparative study of evaluating missing value imputation methods in label-free proteomics”, *Sci. Rep* **11**, 1, 11 (2021).
- Kim, D. K., D. Han, J. Park, H. Choi, J.-C. Park, M.-Y. Cha, J. Woo, M. S. Byun, D. Y. Lee, Y. Kim *et al.*, “Deep proteome profiling of the hippocampus in the 5xfad mouse model reveals biological process alterations and a novel biomarker of alzheimer’s disease”, *Experimental & molecular medicine* **51**, 11, 1–17 (2019).
- Kipf, T. N. and M. Welling, “Semi-supervised classification with graph convolutional networks”, *arXiv preprint arXiv:1609.02907* (2016).
- Kirschner, M. W., “The meaning of systems biology”, *Cell* **121**, 4, 503–504 (2005).
- Kolabas, Z. I., L. B. Kuemmerle, R. Perneczky, B. Förster, S. Ulukaya, M. Ali, S. Kapoor, L. M. Bartos, M. Büttner, O. S. Caliskan *et al.*, “Distinct molecular profiles of skull bone marrow in health and neurological disorders”, *Cell* **186**, 17, 3706–3725 (2023).
- Kuppe, C., R. O. Ramirez Flores, Z. Li, S. Hayat, R. T. Levinson, X. Liao, M. T. Hannani, J. Tanevski, F. Wünnemann, J. S. Nagai *et al.*, “Spatial multi-omic map of human myocardial infarction”, *Nature* **608**, 7924, 766–777 (2022).
- Larsson, C., I. Grundberg, O. Söderberg and M. Nilsson, “In situ detection and genotyping of individual mrna molecules”, *Nature methods* **7**, 5, 395–397 (2010).
- Lee, D.-T. and B. J. Schachter, “Two algorithms for constructing a delaunay triangulation”, *International Journal of Computer & Information Sciences* **9**, 3, 219–242 (1980).
- Lee, J. H., E. R. Daugharthy, J. Scheiman, R. Kalhor, T. C. Ferrante, R. Terry, B. M. Turczyk, J. L. Yang, H. S. Lee, J. Aach *et al.*, “Fluorescent in situ sequencing (fisque) of rna for gene expression profiling in intact cells and tissues”, *Nature protocols* **10**, 3, 442–458 (2015).
- Leimkühler, N. B. and R. K. Schneider, “Inflammatory bone marrow microenvironment”, *Hematology 2014, the American Society of Hematology Education Program Book* **2019**, 1, 294–302 (2019).
- Li, X. and C.-Y. Wang, “From bulk, single-cell to spatial rna sequencing”, *International journal of oral science* **13**, 1, 36 (2021).

- Liu, Y., M. Yang, Y. Deng, G. Su, A. Enniful, C. C. Guo, T. Tebaldi, D. Zhang, D. Kim, Z. Bai *et al.*, “High-spatial-resolution multi-omics sequencing via deterministic barcoding in tissue”, *Cell* **183**, 6, 1665–1681 (2020).
- Liu, Z., M. Y. Gerner, N. Van Panhuys, A. G. Levine, A. Y. Rudensky and R. N. Germain, “Immune homeostasis enforced by co-localized effector and regulatory t cells”, *Nature* **528**, 7581, 225–230 (2015).
- Lubeck, E. and L. Cai, “Single-cell systems biology by super-resolution imaging and combinatorial labeling”, *Nature methods* **9**, 7, 743–748 (2012).
- Lubeck, E., A. F. Coskun, T. Zhiyentayev, M. Ahmad and L. Cai, “Single-cell in situ rna profiling by sequential hybridization”, *Nature methods* **11**, 4, 360–361 (2014).
- Macosko, E. Z., A. Basu, R. Satija, J. Nemesh, K. Shekhar, M. Goldman, I. Tirosh, A. R. Bialas, N. Kamitaki, E. M. Martersteck *et al.*, “Highly parallel genome-wide expression profiling of individual cells using nanoliter droplets”, *Cell* **161**, 5, 1202–1214 (2015).
- Mahmood, T. and P.-C. Yang, “Western blot: technique, theory, and trouble shooting”, *North American journal of medical sciences* **4**, 9, 429 (2012).
- Marconato, L., G. Palla, K. A. Yamauchi, I. Virshup, E. Heidari, T. Treis, W.-M. Vierdag, M. Toth, S. Stockhaus, R. B. Shrestha *et al.*, “Spatialdata: an open and universal data framework for spatial omics”, *Nature Methods* pp. 1–5 (2024).
- Marx, V., “Method of the year: spatially resolved transcriptomics”, *Nature methods* **18**, 1, 9–14 (2021).
- Moffitt, J. R., D. Bambah-Mukku, S. W. Eichhorn, E. Vaughn, K. Shekhar, J. D. Perez, N. D. Rubinstein, J. Hao, A. Regev, C. Dulac *et al.*, “Molecular, spatial, and functional single-cell profiling of the hypothalamic preoptic region”, *Science* **362**, 6416, eaau5324 (2018).
- Moffitt, J. R., J. Hao, D. Bambah-Mukku, T. Lu, C. Dulac and X. Zhuang, “High-performance multiplexed fluorescence in situ hybridization in culture and tissue with matrix imprinting and clearing”, *Proceedings of the National Academy of Sciences* **113**, 50, 14456–14461 (2016).
- Molbay, M., Z. I. Kolabas, M. I. Todorov, T.-L. Ohn and A. Ertürk, “A guidebook for disco tissue clearing”, *Molecular Systems Biology* **17**, 3, e9807 (2021).
- Mund, A., F. Coscia, A. Kriston, R. Hollandi, F. Kovács, A.-D. Brunner, E. Migh, L. Schweizer, A. Santos, M. Bzorek *et al.*, “Deep visual proteomics defines single-cell identity and heterogeneity”, *Nature Biotechnology* **40**, 8, 1231–1240 (2022).
- Nat, “Method of the year 2024: spatial proteomics”, *Nature Methods* **21**, 12, 2195–2196, URL <https://doi.org/10.1038/s41592-024-02565-3> (2024).
- O’Bray, L., B. Rieck and K. Borgwardt, “Filtration curves for graph representation”, in “Proceedings of the 27th ACM SIGKDD Conference on Knowledge Discovery & Data Mining”, pp. 1267–1275 (2021).
- Palla, G., D. S. Fischer, A. Regev and F. J. Theis, “Spatial components of molecular tissue biology”, *Nature Biotechnology* **40**, 3, 308–318 (2022a).
- Palla, G., H. Spitzer, M. Klein, D. Fischer, A. C. Schaar, L. B. Kuemmerle, S. Rybakov, I. L. Ibarra, O. Holmberg, I. Virshup *et al.*, “Squidpy: a scalable framework for spatial omics analysis”, *Nature methods* **19**, 2, 171–178 (2022b).

- Pan, C., R. Cai, F. P. Quacquarelli, A. Ghasemigharagoz, A. Loubopoulos, P. Matryba, N. Plesnila, M. Dichgans, F. Hellal and A. Ertürk, “Shrinkage-mediated imaging of entire organs and organisms using udisco”, *Nature methods* **13**, 10, 859–867 (2016).
- Pan, C., O. Schoppe, A. Parra-Damas, R. Cai, M. I. Todorov, G. Gondi, B. von Neubeck, N. Böğürçü-Seidel, S. Seidel, K. Sleiman *et al.*, “Deep learning reveals cancer metastasis and therapeutic antibody targeting in the entire body”, *Cell* **179**, 7, 1661–1676 (2019).
- Pan, S., R. Hu, G. Long, J. Jiang, L. Yao and C. Zhang, “Adversarially regularized graph autoencoder for graph embedding”, *arXiv preprint arXiv:1802.04407* (2018).
- Petrosius, V., P. Aragon-Fernandez, N. Üresin, G. Kovacs, T. Phlairaharn, B. Furtwängler, J. Op De Beeck, S. L. Skovbakke, S. Goletz, S. F. Thomsen *et al.*, “Exploration of cell state heterogeneity using single-cell proteomics through sensitivity-tailored data-independent acquisition”, *Nature Communications* **14**, 1, 5910 (2023).
- Pijuan-Sala, B., J. A. Griffiths, C. Guibentif, T. W. Hiscock, W. Jawaid, F. J. Calero-Nieto, C. Mulas, X. Ibarra-Soria, R. C. Tyser, D. L. L. Ho *et al.*, “A single-cell molecular map of mouse gastrulation and early organogenesis”, *Nature* **566**, 7745, 490–495 (2019).
- Polychronidou, M., J. Hou, M. M. Babu, P. Liberali, I. Amit, B. Deplancke, G. Lahav, S. Itzkovitz, M. Mann, J. Saez-Rodriguez *et al.*, “Single-cell biology: what does the future hold?”, (2023).
- Qiu, S., Y. Hu, Y. Huang, T. Gao, X. Wang, D. Wang, B. Ren, X. Shi, Y. Chen, X. Wang *et al.*, “Whole-brain spatial organization of hippocampal single-neuron projectomes”, *Science* **383**, 6682, ead9198 (2024).
- Quake, S. R., “The cell as a bag of rna”, *Trends in Genetics* **37**, 12, 1064–1068 (2021).
- Ransohoff, R. M., P. Kivisäkk and G. Kidd, “Three or more routes for leukocyte migration into the central nervous system”, *Nature Reviews Immunology* **3**, 7, 569–581 (2003).
- Rao, A., D. Barkley, G. S. França and I. Yanai, “Exploring tissue architecture using spatial transcriptomics”, *Nature* **596**, 7871, 211–220 (2021).
- Regev, A., S. A. Teichmann, E. S. Lander, I. Amit, C. Benoist, E. Birney, B. Bodenmiller, P. Campbell, P. Carninci, M. Clatworthy *et al.*, “The human cell atlas”, *elife* **6**, e27041 (2017).
- Renier, N., Z. Wu, D. J. Simon, J. Yang, P. Ariel and M. Tessier-Lavigne, “idisco: a simple, rapid method to immunolabel large tissue samples for volume imaging”, *Cell* **159**, 4, 896–910 (2014).
- Risom, T., D. R. Glass, I. Averbukh, C. C. Liu, A. Baranski, A. Kagel, E. F. McCaffrey, N. F. Greenwald, B. Rivero-Gutiérrez, S. H. Strand *et al.*, “Transition to invasive breast cancer is associated with progressive changes in the structure and composition of tumor stroma”, *Cell* **185**, 2, 299–310 (2022).
- Rodrigues, S. G., R. R. Stickels, A. Goeva, C. A. Martin, E. Murray, C. R. Vanderburg, J. Welch, L. M. Chen, F. Chen and E. Z. Macosko, “Slide-seq: A scalable technology for measuring genome-wide expression at high spatial resolution”, *Science* **363**, 6434, 1463–1467 (2019).
- Sanger, F., S. Nicklen and A. R. Coulson, “Dna sequencing with chain-terminating inhibitors”, *Proceedings of the national academy of sciences* **74**, 12, 5463–5467 (1977).
- Schürch, C. M., S. S. Bhate, G. L. Barlow, D. J. Phillips, L. Noti, I. Zlobec, P. Chu, S. Black, J. Demeter, D. R. McIlwain *et al.*, “Coordinated cellular neighborhoods orchestrate antitumoral immunity at the colorectal cancer invasive front”, *Cell* **182**, 5, 1341–1359 (2020).

- Solár, P., A. Zamani, L. Kubičková, P. Dubový and M. Joukal, “Choroid plexus and the blood–cerebrospinal fluid barrier in disease”, *Fluids and Barriers of the CNS* **17**, 1–29 (2020).
- Sountoulidis, A., A. Lontos, H. P. Nguyen, A. B. Firsova, A. Fysikopoulos, X. Qian, W. Seeger, E. Sundström, M. Nilsson and C. Samakovlis, “Screenshot enables spatial mapping of cell states in tissue sections with single-cell resolution”, *PLoS biology* **18**, 11, e3000675 (2020).
- Ståhl, P. L., F. Salmén, S. Vickovic, A. Lundmark, J. F. Navarro, J. Magnusson, S. Giacomello, M. Asp, J. O. Westholm, M. Huss *et al.*, “Visualization and analysis of gene expression in tissue sections by spatial transcriptomics”, *Science* **353**, 6294, 78–82 (2016).
- Stickels, R. R., E. Murray, P. Kumar, J. Li, J. L. Marshall, D. J. Di Bella, P. Arlotta, E. Z. Macosko and F. Chen, “Highly sensitive spatial transcriptomics at near-cellular resolution with slide-seq2”, *Nature biotechnology* **39**, 3, 313–319 (2021).
- Stubbington, M. J., O. Rozenblatt-Rosen, A. Regev and S. A. Teichmann, “Single-cell transcriptomics to explore the immune system in health and disease”, *Science* **358**, 6359, 58–63 (2017).
- Svensson, V., S. A. Teichmann and O. Stegle, “Spatialde: identification of spatially variable genes”, *Nature methods* **15**, 5, 343–346 (2018).
- Togninalli, M., E. Ghisu, F. Llinares-López, B. Rieck and K. Borgwardt, “Wasserstein weisfeiler-lehman graph kernels”, *Advances in neural information processing systems* **32** (2019).
- Uras, I., M. Karayel-Basar, B. Sahin and A. T. Baykal, “Detection of early proteomic alterations in 5xfad alzheimer’s disease neonatal mouse model via maldi-msi”, *Alzheimer’s & Dementia* **19**, 10, 4572–4589 (2023).
- Varrone, M., D. Tavernari, A. Santamaria-Martínez, L. A. Walsh and G. Ciriello, “Cellcharter reveals spatial cell niches associated with tissue remodeling and cell plasticity”, *Nature Genetics* **56**, 1, 74–84 (2024).
- Veličković, P., G. Cucurull, A. Casanova, A. Romero, P. Lio and Y. Bengio, “Graph attention networks”, *arXiv preprint arXiv:1710.10903* (2017).
- Virshup, I., S. Rybakov, F. J. Theis, P. Angerer and F. A. Wolf, “anndata: Annotated data”, *BioRxiv* pp. 2021–12 (2021).
- Wang, C., D. Acosta, M. McNutt, J. Bian, A. Ma, H. Fu and Q. Ma, “A single-cell and spatial rna-seq database for alzheimer’s disease (ssread)”, *Nature Communications* **15**, 1, 4710 (2024).
- Wang, X. Q., E. Danenberg, C.-S. Huang, D. Egle, M. Callari, B. Bermejo, M. Dugo, C. Zagni, M. Thill, A. Anton *et al.*, “Spatial predictors of immunotherapy response in triple-negative breast cancer”, *Nature* **621**, 7980, 868–876 (2023).
- Watson, J. L., D. Juergens, N. R. Bennett, B. L. Trippe, J. Yim, H. E. Eisenach, W. Ahern, A. J. Borst, R. J. Ragotte, L. F. Milles *et al.*, “De novo design of protein structure and function with rfdiffusion”, *Nature* **620**, 7976, 1089–1100 (2023).
- Wei, X., S. Fu, H. Li, Y. Liu, S. Wang, W. Feng, Y. Yang, X. Liu, Y.-Y. Zeng, M. Cheng *et al.*, “Single-cell stereo-seq reveals induced progenitor cells involved in axolotl brain regeneration”, *Science* **377**, 6610, eabp9444 (2022).
- Wolf, F. A., P. Angerer and F. J. Theis, “Scanpy: large-scale single-cell gene expression data analysis”, *Genome biology* **19**, 1–5 (2018).

- Wu, Z., A. E. Trevino, E. Wu, K. Swanson, H. J. Kim, H. B. D'Angio, R. Preska, G. W. Charville, P. D. Dalerba, A. M. Egloff *et al.*, "Graph deep learning for the characterization of tumour microenvironments from spatial protein profiles in tissue specimens", *Nature Biomedical Engineering* **6**, 12, 1435–1448 (2022).
- Xu, K., W. Hu, J. Leskovec and S. Jegelka, "How powerful are graph neural networks?", *arXiv preprint arXiv:1810.00826* (2018).
- Yuan, Y. and Z. Bar-Joseph, "Gcng: graph convolutional networks for inferring gene interaction from spatial transcriptomics data", *Genome biology* **21**, 1–16 (2020).
- Zeng, Z., Y. Li, Y. Li and Y. Luo, "Statistical and machine learning methods for spatially resolved transcriptomics data analysis", *Genome biology* **23**, 1, 83 (2022).
- Zhang, M., S. W. Eichhorn, B. Zingg, Z. Yao, K. Cotter, H. Zeng, H. Dong and X. Zhuang, "Spatially resolved cell atlas of the mouse primary motor cortex by merfish", *Nature* **598**, 7879, 137–143 (2021).
- Zhang, S., J. Zhao, Y. Zhang, Y. Zhang, F. Cai, L. Wang and W. Song, "Upregulation of mif as a defense mechanism and a biomarker of alzheimer's disease", *Alzheimer's research & therapy* **11**, 1–12 (2019).
- Zhao, E., M. R. Stone, X. Ren, J. Guenthoer, K. S. Smythe, T. Pulliam, S. R. Williams, C. R. Uytingco, S. E. Taylor, P. Nghiem *et al.*, "Spatial transcriptomics at subspot resolution with bayesspace", *Nature biotechnology* **39**, 11, 1375–1384 (2021).
- Zhao, S., M. I. Todorov, R. Cai, A.-M. Rami, H. Steinke, E. Kemter, H. Mai, Z. Rong, M. Warmer, K. Stanic *et al.*, "Cellular and molecular probing of intact human organs", *Cell* **180**, 4, 796–812 (2020).
- Zhou, J., G. Cui, S. Hu, Z. Zhang, C. Yang, Z. Liu, L. Wang, C. Li and M. Sun, "Graph neural networks: A review of methods and applications", *AI open* **1**, 57–81 (2020).

List of Publications

Accepted Publications

Jie Luo, Muge Molbay, Ying Chen, Izabela Horvath, Karoline Kadletz, Benjamin Kick, Shan Zhao, Rami Al-Maskari, Inderjeet Singh, **Mayar Ali** et al. "Nanocarrier imaging at single-cell resolution across entire mouse bodies with deep learning." *Nature Biotechnology* (2024, in press)

Zhouyi Rong, Hongcheng Mai, Gregor Ebert, Saketh Kapoor, Victor G. Puelles, Jan Czogalla, Senbin Hu, Jinpeng Su, Danilo Prtvar, Inderjeet Singh, Julia Schadler, Claire Delbridge, Hanno Steinke, Hannah Frenzel, Katja Schmidt, Christian Braun, Gina Bruch, Viktoria Ruf, **Mayar Ali**, Kurt-Wolfram Suhs, et al. "Persistence of spike protein at the skull-meninges-brain axis may contribute to the neurological sequelae of COVID-19." *Cell Host & Microbe* (2024).

Mayar Ali, Merel Kuijs, Soroosh Hedyeh-Zadeh, Tim Treis, Karin Hrovatin, Giovanni Palla, Anna C. Schaar, and Fabian J. Theis. "GraphCompass: spatial metrics for differential analyses of cell organization across conditions." *Bioinformatics* 40, no. Supplement_1 (2024): i548-i557.

Zeynep Ilgin Kolabas, Louis B. Kuemmerle, Robert Perneczky, Benjamin Förster, Selin Ulukaya, **Mayar Ali**, Saketh Kapoor et al. "Distinct molecular profiles of skull bone marrow in health and neurological disorders." *Cell* 186, no. 17 (2023): 3706-3725.

Harsharan Singh Bhatia, Andreas-David Brunner, Furkan Öztürk, Saketh Kapoor, Zhouyi Rong, Hongcheng Mai, Marvin Thielert, **Mayar Ali** et al. "Spatial proteomics in three-dimensional intact specimens." *Cell* 185, no. 26 (2022): 5040-5058.

Submitted for Publications

Doris Kaltenecker, Izabela Horvath, Rami Al-Maskari, Zeynep Ilgin Kolabas, Ying Chen, Luciano Hoehner, Mihail Todorov, Saketh Kapoor, **Mayar Ali** et al. "Deep Learning and 3D Imaging Reveal Whole-Body Alterations in Obesity." *bioRxiv* (2024): 2024-08.

David S. Fischer, **Mayar Ali**, Sabrina Richter, Ali Ertürk, and Fabian Theis. "Graph neural networks learn emergent tissue properties from spatial molecular profiles." *bioRxiv* (2022): 2022-12.

Curriculum Vitae

Education

| | |
|-------------------|--|
| 11.2020 - Present | PhD Candidate Graduate School of Systemic Neurosciences Ludwig Maximilian University of Munich |
| 10.2017 - 03.2020 | Computational Neuroscience, MSc Bernstein Center for Computational Neuroscience Berlin |
| 03.2016 - 09.2016 | Semester abroad Dual Hochschule Baden Württemberg, Stuttgart |
| 10.2012 - 07.2017 | Computer Science and Engineering, BSc German University in Cairo |

Work Experience

| | |
|-------------------|--|
| 03.2021 - Present | PhD Candidate and Research Associate iBIO institute Helmholtz Munich |
| 04.2022 - Present | Machine Learning Engineer (Part time) Knowing01 GmbH, Munich |
| 05.2020 - 10.2020 | Data Scientist biotx.ai GmbH, Potsdam |
| 10.2017 - 04.2020 | Data Engineer Scout24 AG, Berlin |

Acknowledgements

To everyone who has been part of my journey — a journey filled with challenges and opportunities, highs and lows, achievements and disappointments, belief and self-doubt, laughter and tears — each moment has shaped who I am today, and for that, I am deeply grateful.

To my supervisors: Ali, for his belief in me, trust, support, and ambitious goals that pushed me to learn, develop, and grow. And Fabian, for his insightful discussions, collaborative spirit, and constant drive to challenge me. They both made me a better scientist, and for that, I am profoundly thankful.

To my mentors: Farida, for the endless support, comforting presence during tough times, and invaluable encouragement that kept me going, I am thankful. And David, for his guidance at the beginning of this journey, when I felt lost, helping me find my path, I am truly grateful.

To my Thesis Advisory Committee: For the time, thoughtful input, and commitment to my progress, I am thankful.

To all my collaborators: Merel, David, Sabrina, Ilgin, Louis, Harsh, and everyone who contributed, who made each project an enriching experience and who have taught me skills that deepened my knowledge. Despite the challenges, the journey was enjoyable and for that I am grateful.

To the lab members: For their insights and the meaningful impact they had on my research. To the friendships forged in the lab, for the support and conversations that brought light to my struggles and made the tough days easier. To the support teams in the labs and at the GSN, for helping me navigate bureaucratic complexities and making my journey smoother. I am thankful.

To my friends: For their belief in me and unwavering support through the different stages. Every word of encouragement, every shared laugh, and every comforting conversation meant the world to me. I won't mention names here because, truly, the list is endless. For that, I am blessed and grateful.

To my family: Words cannot capture the depth of my gratitude. Mama and Loza, for their endless support and belief in me that carried me through, I truly would not be here without you. And to the one who planted strength and faith in me, whose presence I miss dearly, I hope I am making you proud.

And finally: To the challenges I conquered, the obstacles I overcame, and the setbacks that made me stronger. To the opportunities that brought me closer to my dream, the achievements that kept me motivated and the joyful moments that nurtured my inner child. I truly wouldn't have wished for a different journey.

Declaration of Author Contribution

Study 1: (Ali et al., 2024, Bioinformatics) GraphCompass: spatial metrics for differential analyses of cell organization across conditions.

Mayar Ali, Merel Kuijs, Soroor Hedyeh-zadeh, Tim Treis, Karin Hrovatin, Giovanni Palla, Anna C Schaar and Fabian J Theis

Contribution of authors: MA and MK conceived and led the study. MA and MK implemented the overall software and performed the analyses. MA, MK, SH and TT designed the methods. MA and MK wrote the manuscript. All authors reviewed the manuscript.

My contribution to this publication details: Together with my co-first author Merel Kuijs, I designed the initial graph comparison metrics used in the package, developed the package, collected the open-source datasets, performed the analyses and interpreted the data. I applied the cell-type distance-based and entire-graph kernel-based approaches. I co-led the project and co-wrote the manuscript with Merel Kuijs.

Herewith, I confirm the contributions to the manuscript.

Munich, December 8, 2024

Mayar Ali (1st author)

Merel Kuijs (1st author)

Ali Ertürk (supervisor)

Study 2: (Ali et al., 2022, bioRxiv) Graph neural networks learn tissue phenotypes from spatial molecular profiles.

Mayar Ali, David S. Fischer, Sabrina Richter, Ali Ertürk and Fabian Theis

Contribution of authors: DSF, MA, SR and FJT conceived the study. DSF, MA and SR implemented the overall software and performed the analyses. MA, DSF, SR, AE and FJT wrote the manuscript.

My contribution to this study details: Together with David S. Fischer and Sabrina Richter, I designed the project and models, performed the analyses, and interpreted the results. I further implemented the graph and baseline models, and we jointly conducted the interpretation experiments for the graph models and co-wrote the manuscript. I also designed and assembled the manuscript figures.

Herewith, I confirm the contributions to the manuscript.

Munich, December 8, 2024

Mayar Ali (1st author)

David S. Fischer (1st author)

Sabrina Richter (1st author)

Ali Ertürk (supervisor)

Study 3: (Kolabas et al., 2023, Cell) Distinct molecular profiles of skull bone marrow in health and neurological disorders.

Zeynep Ilgin Kolabas, Louis B. Kuemmerle, Robert Perneczky, Benjamin Förstera, Selin Ulukaya, **Mayar Ali**, Saketh Kapoor, Laura M. Bartos, Maren Büttner, Ozum Sehnaz Caliskan, Zhouyi Rong, Hongcheng Mai, Luciano Höher, Denise Jeridi, Muge Molbay, Igor Khalin, Ioannis K. Deligiannis, Moritz Negwer, Kenny Roberts, Alba Simats, Olga Carofiglio, Mihail I. Todorov, Izabela Horvath, Furkan Ozturk, Selina Hummel, Gloria Biechele, Artem Zatcepin, Marcus Unterrainer, Johannes Gnörich, Jay Roodselaar, Joshua Shrouder, Pardis Khosravani, Benjamin Tast, Lisa Richter, Laura Díaz-Marugan, Doris Kaltenecker, Laurin Lux, Ying Chen, Shan Zhao, Vanessa W.Y. Kan, Sabine Liebscher, Boris-Stephan Rauchmann, Michael Sterr, Ines Kunze, Karen Stanic, Vanessa W.Y. Kan, Simon Besson-Girard, Sabrina Katzdobler, Carla Palleis, Julia Schädler, Johannes C. Paetzold, Sabine Liebscher, Anja E. Hauser, Ozgun Gokce, Heiko Lickert, Hanno Steinke, Corinne Benakis, Christian Braun, Celia P. Martinez-Jimenez, Katharina Buerger, Nathalie L. Albert, Günter Höglinger, Johannes Levin, Christian Haass, Anna Kopczak, Martin Dichgans, Joachim Havla, Tania Kümpfel, Martin Kerschensteiner, Martina Schifferer, Mikael Simons, Arthur Liesz, Natalie Krahmer, Omer A. Bayraktar, Nicolai Franzmeier, Nikolaus Plesnila, Suheda Erener, Victor G. Puelles, Claire Delbridge, Harsharan Singh Bhatia, Farida Hellal, Markus Elsner, Ingo Bechmann, Benjamin Ondruschka, Matthias Brendel, Fabian J. Theis and Ali Ertürk

Contribution of authors: Conceptualization and management of whole project, A.E.; methodology, Z.I.K., L.B.K., B.F., B.T., L.R., I.H., and M.N.; software, L.B.K., M.A., M. Büttner, I.H., M.N., M.I.T., and J.C.P.; validation, Z.I.K., L.B.K., S.U., I.H., K.R., and O.A.B.; formal analysis, Z.I.K., L.B.K., M.A., M. Büttner, M. Brendel, N.F., L.M.B., G.B., S.H., J.G., M. Schifferer, A.S., L.H., I.H., M.N., M.I.T., L.L., J.C.P., S.U., S. Kapoor, O.S.C., and N.K.; investigation, Z.I.K., S.U., M. Sterr, I. Kunze, H.L., I.K.D., C.P.M.-J., M. Schifferer, A.S., O.C., L.D.-M., C. Benakis, A.L., P.K., K.R., O.A.B., D.J., M.M., F.O., J. Shrouder, J.R., A.E.H., S.Z., D.K., I. Khalin, N.P., B.F., H.S.B., Z.R., H.M., M.M., K.S., F.H., S.B.-G., O.G., S. Kapoor, O.S.C., N.K., V.W.Y.K., and S.L.; writing – original draft, Z.I.K., S.E., and A.E.; writing – review & editing, Z.I.K., M.E., and A.E.; funding acquisition, A.E.; visualization, Z.I.K., L.B.K., M.A., S.U., L.H., and A.Z.; resources, R.P., M. Brendel, H.S., I.B., C. Braun, C.D., J. Schädler, B.O., V.G.P., N.L.A., M.U., J.G., S. Katzdobler, C.P., A.K., K.B., J.L., C.H., M. Simons, M.D., G.H., J.H., T.K., and M.K.; project administration, Z.I.K.; supervision, F.H., S.E., H.S.B., F.J.T., M.E., and A.E.

My contribution to this publication details: I led the proteomics analysis part of the study. I designed, implemented and performed all the preprocessing and downstream analyses for the proteomics data for both mouse and human samples. I further interpreted the data with Zeynep Ilgin Kolabas. Figures 3, 5(B-H,L,M), S5(A-M) and S6(A-I), comprise all the data I contributed to this publication. In addition, I commented on the manuscript, particularly the proteomics part.

Herewith, I confirm the contributions to the manuscript.

Munich, December 8, 2024

Mayar Ali (co-author)

Zeynep Ilgin Kolabas (1st author)

Louis B. Kuemmerle (1st author)

Robert Perneczky (1st author)

Benjamin Förster (1st author)

Ali Ertürk (supervisor)

Study 4: (Bhatia et al., 2022, Cell) Spatial proteomics in three-dimensional intact specimens

Harsharan Singh Bhatia, Andreas-David Brunner, Furkan Öztürk, Saketh Kapoor, Zhouyi Rong, Hongcheng Mai, Marvin Thielert, **Mayar Ali**, Rami Al-Maskari, Johannes Christian Paetzold, Florian Kofler, Mihail Ivilinov Todorov, Muge Molbay, Zeynep Ilgin Kolabas, Moritz Negwer, Luciano Hoeher, Hanno Steinke, Alina Dima, Basavdatta Gupta, Doris Kaltenecker, Özüm Sehnaz Caliskan, Daniel Brandt, Natalie Krahmer, Stephan Müller, Stefan Frieder Lichtenhaler, Farida Hellal, Ingo Bechmann, Bjoern Menze, Fabian Theis, Matthias Mann, Ali Ertürk

Contribution of authors: A.E., M. Mann, H.S.B., and A.-D.B. conceptualized and designed the study. H.S.B., Z.R., and H.M. performed mice experiments, solvent-based organ clearing, light-sheet imaging procedures, and stitching of data. H.S.B. developed the LCM-based isolation procedure for target tissues from solventcleared organs. A.-D.B. developed the sample preparation workflow for proteomics analysis. A.-D.B., S.K., H.S.B., M. Molbay, and M.T. performed mass spectrometry-based proteomics analysis. R.A.-M., J.C.P., F.K., M.A., B.M., and F.T. developed deep learning models. M.A. and F.T. performed data analysis. M.I.T. performed atlas registration of 5xFAD brains. H.S.B. and D.K. performed ClearMAP analyses. A.E. conceptualized, and F.O. designed the robotic extraction system. Z.I.K. labeled, cleared, and imaged whole body of mouse. F.O., H.S.B., and S.K. extracted tissue from whole body and whole organs. S.K. performed mass spectrometry on robotic extracted samples. H.S.B. and S.K. analyzed the data. M.N., J.C.P., and A.D. performed 2D LCM registration to 3D data. S.M. and S.F.L. helped with the prototyping experiment. H.S.B., A.-D.B., M. Mann, and A.E. wrote the manuscript.

My contribution to this publication details: I led parts of the proteomics analysis in this study, focusing on Alzheimer's disease across different stages and multiple brain regions. I implemented and performed the preprocessing and downstream analyses for the proteomics data for the 5xFAD mouse samples and together with Harsharan Singh Bhatia interpreted the data. Figures 2A, 3(E-G), 4(G,K,L), 6F, 7A and S5(C-I) comprise all the data I contributed to this publication. In addition, I reviewed the manuscript, particularly the proteomics part I worked on.

Herewith, I confirm the contributions to the manuscript.

Munich, December 8, 2024

Mayar Ali (co-author)

Harsharan Singh Bhatia (1st author)

Andreas-David Brunner (1st author)

Furkan Öztürk (1st author)

Ali Ertürk (supervisor)

Affidavit

Herewith I certify under oath that I wrote the accompanying Dissertation thesis myself. Title: *Interpretable approaches for cellular organisation and molecular profiles using (spatial) omics data in health and disease*. In the thesis no other sources and aids have been used than those indicated. The passages of the thesis that are taken in wording or meaning from other sources have been marked with an indication of the sources (including the World Wide Web and other electronic text and data collections). Furthermore, all parts of the thesis that were de novo generated with the help of artificial intelligence tools were identified by footnotes/annotations at the appropriate places and the artificial intelligence tools used were listed. The prompts used were listed in the appendix. This statement applies to all text, graphics, drawings, sketch maps, and pictorial representations contained in the work.

All illustrations in this thesis have been generated designed and hand-drawn by me. All the text has been run through Grammarly for spelling check and some paragraphs through ChatGPT and Claude for optimisation. The manuscript "GraphCompass: spatial metrics for differential analyses of cell organization across conditions." has been reproduced with permission from Oxford University Press, Bioinformatics. The manuscript "Distinct molecular profiles of skull bone marrow in health and neurological disorders." and "Spatial proteomics in three-dimensional intact specimens." has been reproduced with permission from Elsevier.

Hiermit versichere ich an Eides statt, dass die vorliegende schriftliche Dissertation mit dem Titel *Interpretable approaches for cellular organisation and molecular profiles using (spatial) omics data in health and disease*. von mir selbstständig verfasst wurde und dass keine anderen als die angegebenen Quellen und Hilfsmittel benutzt wurden. Die Stellen der Arbeit, die anderen Werken dem Wortlaut oder dem Sinne nach entnommen sind, wurden in jedem Fall unter Angabe der Quellen (einschließlich des World Wide Web und anderer elektronischer Text- und Datensammlungen) kenntlich gemacht. Weiterhin wurden alle Teile der Arbeit, die mit Hilfe von Werkzeugen der künstlichen Intelligenz de novo generiert wurden, durch Fußnote/Anmerkung an den entsprechenden Stellen kenntlich gemacht und die verwendeten Werkzeuge der künstlichen Intelligenz gelistet. Die genutzten Prompts befinden sich im Anhang. Diese Erklärung gilt für alle in der Arbeit enthaltenen Texte, Graphiken, Zeichnungen, Kartenskizzen und bildliche Darstellungen.

Alle Abbildungen in dieser Dissertation wurden von mir entworfen und handgezeichnet. Der gesamte Text wurde zur Rechtschreibprüfung durch Grammarly und einige Absätze zur Optimierung durch ChatGPT und Claude laufen gelassen. Das Manuskript "GraphCompass: spatial metrics for differential analyses of cell organization across conditions." wurde mit Genehmigung von Oxford University Press, Bioinformatics, vervielfältigt. Das Manuskript "Distinct molecular profiles of skull bone marrow in health and neurological disorders." und "Spatial proteomics in three-dimensional intact specimens." wurde mit Genehmigung von Elsevier vervielfältigt.

Munich, December 12, 2024

(Location/date)

MAYAR ALI

(First and last name in block letters)

(Signature)